Novel Models to Image and Quantify Bone Drug Efficacy and Disease Progression In Vivo: Addressing the Fragility Phenotype

by

Rachel Kathleen Surowiec

A dissertation submitted in partial fulfillment
of the requirements for the degree of
Doctor of Philosophy
(Biomedical Engineering)
in the University of Michigan
2019

Doctoral Committee:

Associate Professor Kenneth M. Kozloff, Chair
Associate Professor Michelle S. Caird
Associate Professor Craig J. Galbán
Associate Professor Luis Hernandez-Garcia
Assistant Professor Noriaki Ono

Rachel K. Surowiec

rachelks@umich.edu

ORCID iD: 0000-0001-7614-4412

Dedication

For my husband and son; you guys are my heart and my world. Dakota, your grounding energy, love and humor made this all possible. Sebastian, your smile, inquisitiveness, energy and love got me through each day. Without you, Sebastian, this thesis may have been done sooner but I wouldn’t have enjoyed the process half as much. Can’t wait to read it to you at bedtime (I kid!).

Acknowledgements

When I left my career to return to school to pursue my PhD, I so naively thought that a person received this degree as a result of their hard work, determination and grit alone. What I quickly realized, at least in my case, is that I am here because I was fortunate to be surrounded by an immensely supportive, kind and patient mentor, an incredible dissertation committee who cheered me on while challenging me, the massively helpful research staff in the ORL and CMI, a few amazing undergraduate research assistants, and loving family and friends who have made this push possible, rich and meaningful.

I first and foremost want to sincerely thank my mentor, Ken Kozloff, for the guidance and support throughout this entire process. As a mentor, Ken challenged me beyond my self-perceived scientific capabilities and allowed me the room to pursue topics in which I was passionate about. As a result, I sit here writing my thesis about topics for which I am excited about and have many more scientific questions I hope to answer one day as a result. He mentored with kindness, patience and thoughtfulness; any one of these attributes would make a wonderful mentor and I am grateful that with Ken you get all three. These are things I hope to one day emulate as a future mentor in the next stages of my career.

I next want to express my gratitude to my committee- when I reached out to each of you and you agreed to serve and guide me during this process I joked that I really had the “dream team”. There turned out to be so much truth in that. I want to thank Craig Galban, a member of my committee, who took an enormous chance on me when I reached out to him shortly after I started at Michigan telling him about my ideas to MRI bone. Without hesitation, he provided me so much support to realize these goals- something that has made my experience here so rich. Craig continually offered his support and expertise time and time again and I have learned so much from him during my time here. I appreciate his enthusiasm for research and how he approaches research questions. I would also like to thank Dr. Michelle Caird. I am incredibly grateful for the opportunity to work with her on the first two projects I undertook in the Kozloff Lab. Her compassion to help her patients and her drive to answer some really amazing research questions was truly contagious.

This work truly would not be possible without the help and support of the amazing staff in the Orthopaedic Research Laboratories (ORL) and the Center for Molecular Imaging (CMI) and for that I am utterly grateful. The focus on student growth and success is apparent and what's more, is that it was always done with such kindness. And often a lot of laughs. The scientific conversations were great but the life conversations were even better. I am so grateful that I walk away from this experience with so many dear friends that happen to have been my work family. I am immensely thankful for the PIs who make up the Orthopaedic Research Laboratories. Each PI has offered so much support and sage advice during my journey. I want to thank my fellow graduate students Diana Olvera and Hsiao Sung, the incredible undergraduate students and staff (past and present) who made up the Kozloff Lab during my time here- I certainly could not have done this without each one of you. The talks and laughs back in the lab are something I will cherish forever and the continual support was so instrumental. For the members of the Galban Lab, I cannot thank you all enough for all the support you have given me and for all the friendship and laughs, I am incredibly grateful to know you guys.

An immense source of my growth as a scientist and future academic is due to the continual help and guidance that Stephen Schlecht provided me during my time in the ORL. He is an incredible teacher and so many of the techniques I used in this dissertation were the result of his teaching in the lab. He is always willing to lend a hand, offer advice, teach a technique and read a research statement and he does it all with a healthy dose of sarcasm. And for all of this I am truly grateful. Another sincere thank you goes to Lauren Battle who joined our lab and my research project as a sophomore student and without here none of this work would be possible. It has been nothing short of a pleasure working with her for these past three years; scientifically she has an incredible eye and attention to detail and can also so seamlessly see the "big picture" and personally she is a wonderful person and a joy to work with. While she joined our lab to learn about the project, I feel I have learned so much from her and am thankful she was willing to spend these years working through these projects. I would also like to thank Ferrous Ward who was so instrumental in helping me work through the beginnings of my time in the lab and who has become a tremendous friend.

I would like to sincerely thank those who collaborated with me on this project. A specific thank you goes to Djaudat Idiyatulin at the University of Minnesota who taught me so much about MR physics and troubleshooting and who developed the specific sequence I have employed in my last research study of this dissertation.

I am so unbelievably thankful for the friendships that I made at UM during this PhD process; those in the classroom, labs, through the GSC and beyond. I am especially and immensely grateful for Sydney Williams, Federica Cuomo and Mariana Masteling; I cannot believe I have made such amazing lifelong friends during this process. I cannot tell you how much your friendship and laughs have meant and all the support through the ups and downs and helping me through balancing a baby and grad school. These three engineers continually inspire me to be a better scientist and better person. I have an immense amount of gratitude for my friends from home; we have gone through so many beautiful life events together from growing up, college, moving and coming back, marriage and family. I am so proud and grateful to call each of these ladies not only my friend but my family. They have been here to pick me up and continually cheer me on; as I write this, I’m not so sure I have the words to extend the kind of thank you they all deserve.

I next want to thank Kapila Castoldi who has been such a beacon of light in my life here in Ann Arbor. She is not only an incredible physicist and academic mentor, she has been an incredible friend and like family to me and for that I am forever grateful. A tremendous amount of gratitude goes to my family and our family friends back home in Indiana. While we are small in number, the love and support are so huge and have helped me through so much. I continue to learn from you all and when we get the chance to see one another whether it be a holiday or otherwise, I nearly have to pinch myself; I feel that lucky.

I really hit the jackpot as they say with my incredible in laws who are truly my second family. With them I have gained a younger brother, grandparents and a tremendous mother and father in law. I am moved by the amount of love and support you have showered me with as I pursued this goal. I am so grateful to know you all and call you family.

I owe everything to my parents Janet and Gary; I would choose you both over and over again. I have learned so much by watching you both navigate life with grace, grit and a beautiful sense of humor. When you each went back to finish your diploma, I was quietly watching. It set into motion a fire to pursue school knowing that anything is possible; you reminded me that you can plow past your circumstance and achieve anything. I owe any of the strength and determination to you both. I’m so grateful to know you both on this journey of life and love you guys to the moon. I don’t think I’ll ever be finished telling you thank you.

To Dakota and Sebastian, my unbelievable husband and amazing son, thank you. Dakota, as I reflect over this decade, I can hardly believe all of the beautiful adventures we have embarked on. I am so grateful we get to walk through this life together. Your support, encouragement, grounding energy and humor makes each day all that much richer. I most certainly wouldn't be writing this dissertation if it weren't for you, you have made this entirely possible. Your support and sacrifice to see me through this; leaving Colorado to come back to school in Michigan, I'm not sure if I will ever find the vocabulary to tell you what that has meant but I will most certainly try. And Sebastian, Sebi Baby! I cannot believe I get the chance to know you! What an amazing, funny, smart, kind and loving little guy and I am so grateful to call you my son. You can't even say the word "bone" yet you have done more for me and my research than you will ever know. I love you both and thank you for being my family.

Table of Contents

List of Tables

List of Figures

Abstract

Bone is a composite biomaterial of mineral crystals, organic matrix, and water. Each contributes to bone quality and strength and may change independently, or together, with disease progression and treatment. Even so, there is a near ubiquitous reliance on ionizing x-ray-based approaches to characterize bone mineral density (BMD) which only accounts for ~60% of bone strength and may not adequately predict fracture risk. In a rare and severe bone disease such as osteogenesis imperfecta (OI), the hallmark genotypic and phenotypic variability makes clinical management particularly challenging. Treatment strategies rely on anti-resorptive bisphosphonates which address osteoclastic, but not osteoblastic deficiencies. Radiographic characterization of efficacy identifies structural, but not biomaterial-level alterations. Together, there is an unmet need for improved treatment strategies and means to longitudinally monitor treatment outcomes at the biomaterial-level to improve clinical management of bone disease.

This thesis will describe a novel model to understand and predict individual patient treatment response to an emerging therapeutic, sclerostin antibody (SclAb) prior to clinical exposure. We then challenge the current bone imaging gold-standard with the characterization of a novel zero echo time (ZTE) magnetic resonance imaging (MRI) technique that may hold promise in identifying matrix-level and biochemical changes characteristic of OI and other diseases.

SclAb has gained interest as a promising bone-forming therapeutic suggesting a novel treatment strategy through inhibition of endogenous sclerostin but effects in human pediatric OI bone remains unknown. We treated bone samples retrieved from pediatric OI patients during

surgery with SclAb *in vitro* and quantified transcriptional response of *Wnt*-related genes. Results demonstrated a bone-forming response in a manner paralleling pre-clinical experience. Factors inherent to the unique phenotypic/genotypic patient profile such as the patient's baseline cellular phenotype appear to govern response magnitude; OI patients with low untreated expression of osteoblast-related genes demonstrated the greatest magnitude of upregulation during treatment. To expand findings *in vivo*, we developed a novel OI xenograft model where bone was implanted into a host-derived microenvironment. The model was efficacious; bone was bioaccessible by the host and retained patient-derived bone cells throughout implantation. Treatment increased bone density and volume with a variable outcome between cortical and trabecular bone. Patients with low baseline osterix demonstrated robust human-derived osterix-expression with treatment supporting *in vitro* findings. The validated xenograft model can be used to establish patient-specific factors influencing treatment response suggesting a personalized medicine approach to managing OI.

Characterization of treatment efficacy for OI, as well as other metabolic bone diseases, is complicated by the lack of imaging modality able to safely monitor material-level and biochemical changes *in vivo*. To improve upon BMD, we tested the efficacy of a 3D ZTE-MRI approach in an estrogen-deficient (OVX) model of osteoporosis during growth. ZTE-MRI-derived BMD correlated significantly with BMD measured using the gold standard, µCT, which significantly increased longitudinally over the duration of the study. Growth appeared to overcome estrogen-deficient changes in bone mass yet ZTE-MRI detected significant changes consistent with estrogen deficiency by ten weeks in cortical water, cortical matrix organization (T_1) and marrow fat. Findings point to ZTE-MRI's ability to quantify BMD in good agreement with the gold standard and detect biochemical alterations consistent with disease independent of the mineral phase suggesting its value for bone imaging. Together, results from this thesis indicate a new treatment design and non-ionizing imaging strategy to improve management of bone diseases such as OI.

Chapter 1 Introduction

Motivation

Osteogenesis imperfecta (OI) is a rare and severe heritable collagen-related bone dysplasia characterized by low bone mass, fragility and poor bone quality with increased pathological fracture risk presenting most severely in childhood. [1] Heterogeneity is a hallmark of the disease[2] which can be classified into 18+ genetically unique types differing in modes of inheritance (dominant, recessive, X-linked) and affected gene loci resulting in a range of phenotypic presentation. [3] The type of disease-causing mutation and position along the collagen chain was once believed to dictate phenotype,[1] but studies have revealed divergent phenotypes in patients with identical, or near-identical genetic mutations and different symptoms have been reported among family members with the same mutation. [4] This spectrum of genotypic-phenotypic variability makes management of the disease especially challenging.

Current treatment approaches to manage OI include any combination of physical therapy, dietary intervention to improve body composition, corrective orthopaedic surgery and pharmacological treatment to address the fragility phenotype. While the goal of pharmacological management of OI is to reduce fracture incidence and increase bone density and mass, achieving this has been complicated. There is currently no United States Food and Drug Administration- or European Medicines Agency-approved therapy for OI. Therefore management relies, in part, on off-label therapies developed to treat osteoporosis, a metabolic bone dysplasia, which is not fully predictive of the clinical response in pediatric OI. Off-label use of bisphosphonates, a class of drugs which reduce osteoclast activity, represent the predominant treatment strategy for OI [5]. Yet bisphosphonates only partially correct the OI bone phenotype, and improvements in growth, functional ability and definitive fracture risk reduction have been inconclusive. [6, 7] The arrival of monoclonal sclerostin antibody (SclAb) has gained interest as a promising bone-forming therapeutic [8] suggesting an alternative treatment strategy through inhibition of sclerostin, an osteocyte-secreted negative regulator of bone formation. [9] Clinical trials have shown SclAb treatment to elicit a positive increase in bone density and mass,[10-12] reductions in fracture rate, [13] and improvements in mechanical strength using finite element analysis (FEA) models in post-menopausal osteoporotic women.[11, 14] Pre-clinical studies using transgenic murine models support the use of SclAb in treating OI, [15-20] but the magnitude of bone-forming response between mild, moderate and severe OI phenotypes in these models suggest genotype and phenotype variability influences the response. [15, 18-20] In humans, a Phase II clinical trial in adults with types I, III and IV OI treated with a form of SclAb demonstrated increased markers of bone formation, decreased markers of bone resorption, and increased lumbar areal bone mineral density. [21] However, the low number of patients enrolled in the trial prohibited analysis of response by OI phenotype. To date, results in the pediatric OI patient remain unknown and is confounded by the difficulty of performing clinical trials in this young and heterogeneous population. [22]

In addition to the complications surrounding investigations focused on the interaction of pharmacologic treatments and bone disease in children, imaging strategies to diagnose and longitudinally manage bone disorders such as OI and osteoporosis are incomplete. Current clinical practice relies primarily on ionizing x-ray-based approaches to characterize the mineral phase of bone. [23-25] When patients are treated for their low bone mass in the clinic, response is monitored *in vivo* using these x-ray based techniques.[26] Clinical trials for emerging therapeutics aimed to address low bone mass and fracture risk utilize baseline and end-point dual-energy X-ray absorptiometry (DXA) to quantify treatment efficacy by quantifying bone mineral density (BMD). [27] Finally, pre-clinically there is a reliance on these same ionizing techniques [e.g. micro-computed tomography, (μCT)], often at higher radiation dose, to quantify mineral density and the bone microarchitecture with precision. [28]

While mineral is the focus of DXA measures, it is understood that bone is a composite material composed of ~35-45% mineral crystals composed of hydroxyapatite, ~40% organic matrix including type I collagen, proteoglycan (PG) and glycosaminoglycan (GAG), and ~15-25% water existing as free (in Haversian and Volkmann's canals) and bound (hydrostatically bound to organic matrix constituents), by volume. [29] Each are critical components to bone quality and fragility and may change independently, or together, with disease progression and ultimately with treatment. [30, 31] Even so, there is a near ubiquitous reliance on BMD to predict mechanical properties and ultimately serve as an *in vivo* surrogate for treatment efficacy, while ignoring these other important contributors of bone strength.[23] The literature largely supports that BMD is an incomplete measure since it accounts for only ~60% of bone strength and may not adequately predict fracture risk.[32, 33]

Because these imaging techniques come at a cost of radiation, longitudinal *in vivo* imaging analysis, particularly in the clinic and during clinical trials, is limited in the number of acquisitions that can safely be acquired. As a result, the earliest and intermediate biological changes due to treatment can go uncharacterized. In the case of pediatric OI patients who sustain numerous fractures annually and undergo frequent corrective fluoroscopic-guided surgery, clinicians often forego radiographic imaging in an attempt to reduce the lifetime radiation exposure and mitigate the long-term consequences that radiation exposure has on bone. There is an urgent need to identify alternative or adjuvant imaging methods that could reduce the radiation cost in diagnostic, pre-clinical and clinical trial imaging while improving sensitivity to factors contributing to bone strength that are not recognized by the present imaging technology.

The ability to non-invasively measure biochemical and molecular processes *in vivo* as they relate to bone pathophysiology represents a powerful tool to guide therapeutic development and subsequent clinical trials [34] where the desire for non-destructive imaging biomarkers is wildly immense and equally unmet. When quantifying metrics beyond the mineral phase in bone, traditional pre-clinical targets typically involve end-stage tissue resection to perform histology. This requires study design to include matched treatment/control groups (cross-sectional) limiting longitudinal *in vivo* analysis and adding both cost and use of animal. Thus the cost and time to employ these studies is immense and there are limitations in assuming groups are comparable in the entropic biological system. [35, 36] Non-ionizing quantitative imaging biomarkers for bone quality, as such, may be the turning point for increasing pre-clinical, clinical and clinical trial efficacy and efficiency.

There are a number of clinically available imaging modalities whose application in bone appear promising but have not yet been fully exploited. [37, 38] One such clinically available modality, magnetic resonance imaging (MRI), is gaining interest for its sensitivity to biochemical composition and its rich dynamic range. However, bone appears as a signal void in conventional MRI bone since it is unable to “capture” bone’s inherently ultra-short transverse relaxation time (T_2) due to MRI time domain constraints (echo time, TE and repetition time, TR). In bone, proton signal intensity is drawn from a limited hydrogen pool which includes water residing in microscopic Haversian canals and lacunae-canaliculi systems (free water, $T_2 > 1$ ms), matrix water bound to collagen (bound water, $T_2 << 1$ ms) and protons of the collagen backbone/sidechain (T2 < 0.1 ms). [29, 39] The extremely short T_2 relaxation times for these three pools are directly related to the movement allotted by the protons following excitation in MRI.[40] In recent years, a number of remarkable advances have been proposed for both the qualitative and quantitative evaluation of short T_2 species such as bone with the advent of ultra-short and zero echo time MRI. [41, 42]

Thesis Outline and Contributions

The studies that will be presented in this work have been approached using two distinct yet equally important models of altered bone remodeling to describe the impact of genetic and phenotypic variability on treatment response (Chapter 3 and Chapter 4) and to describe an efficacious set of non-invasive imaging biomarkers to quantify bone quality surrogates, in addition to mineral density, in bone (Chapter 5). In order to cover this breadth of topics, Chapter 2: Background will first review bone structure, OI and its phenotypic and genotypic features, and pharmacological treatments aimed to address the fragility phenotype of the disease. Chapter 2 will also briefly discuss osteoporosis, current clinical and pre-clinical imaging approaches to characterize the bone and discuss the utility of BMD as the most commonly reported imaging outcome (and its inherent limitations). We will next introduce additional measurable “quality” components of bone that can be captured using the novel MR imaging technique we present in Chapter 5. As such, Chapter 2 includes a review of MRI with a focus on ultra-short and zero echo time techniques, an important concept for this thesis.

We believe that genotypic and phenotypic variability, including baseline fragility, pre-existing trabecular phenotype, and perhaps yet undescribed mechanisms may impact treatment response in OI. In pursuit of this hypothesis, Chapter 3 will describe how individual patient genotype and baseline cellular phenotype influence treatment response *in vitro*.

The *in vitro* environment provides a safe and reductionist method to evaluate human OI tissue response to SclAb but we recognize the environment is limited in biokinetic and metabolic factors inherent to the more complex *in vivo* environment. As such, in Chapter 4 we build upon and extend findings from Chapter 3 *in vivo* using a solid-tissue isolate xenograft model OI patient tissue is implanted into a nude mouse to study the effects of SclAb in its target tissue, *in vivo*.

The work to uncover factors influencing treatment response in Chapter 3 and Chapter 4 has inspired the pursuit of an imaging technique that is able to quantify constituents making up bone's dynamic, composite structure. We believe the ability to non-invasively characterize bone quality using quantitative imaging biomarkers represents an extraordinarily powerful tool that can impact the field where the safe longitudinally characterization of the entire composite bone, not just the mineral, could improve clinical trials and management of bone disease. As such, in Chapter 5 we used a novel 3D radial zero echo time (ZTE) MRI sequence that can achieve virtually simultaneous excitation and signal acquisition in order to image the bone *in vivo*. Using the technique, we sought to develop a comprehensive (although not exhaustive) set of MRI biomarkers to characterize aspects of bone quality that go "missed" when using gold-standard bone imaging approaches (e.g., DXA, µCT) that rely on ionizing radiation to attenuate the mineral phase in bone.

The contributions to the field for Body Chapters (3, 4, 5) are as follows:

Chapter 3 Gene Expression Profile and Acute Gene Expression Response to Sclerostin Inhibition in Pediatric Osteogenesis Imperfecta Bone

The work presented in Chapter 3 is the first description of the effects of a novel anabolic therapeutic, SclAb, in pediatric OI tissue retaining patient-specific, OI-causative genetic defect. When tissues isolated from OI patients during routine orthopaedic procedures were cultured and treated *in vitro*, SclAb stimulated an acute upregulation in downstream *Wnt* targets *WISP1* and *TWIST1* and a compensatory response in inhibitory regulators *DKK1* and *SOST*, paralleling experience in animal models treated with SclAb. We demonstrate that acute SclAb therapy is able to elicit a bone forming response through upregulation of osteoblast and osteoblast precursor genes *in vitro.* The magnitude of response was heterogeneous regardless of clinical phenotype or bone morphological type (trabecular, cortical). These data represent the first reports in the literature of human OI patient bone cell response to sclerostin antibody treatment.

Perhaps the most important contribution of Chapter 3 is the description of the effects of genotype, cellular phenotype and bone morphological type (using the untreated condition) on treatment response in pediatric OI bone tissue. Pediatric OI patient samples with low untreated expression of osteoblast and osteoblast precursor genes demonstrated the greatest magnitude of upregulation in these genes with SclAb treatment. Conversely, patients with high untreated expression of osteoblast and osteoblast precursors demonstrated little to no additional upregulation following sclerostin inhibition, suggesting that amount of osteoblast activity at the time of treatment may help govern the potential for bone-forming response in an inverse relationship. Therefore, understanding the patient's baseline osteoblast and osteoblast progenitor pool may be predictive of response magnitude to SclAb.

The *in vitro* results presented in Chapter 3 provide evidence that pediatric OI bone cells are responsive to acute SclAb treatment in a manner parallel to the pre-clinical experience and that factors inherent to the unique phenotypic and genotypic patient profile appear to govern magnitude of treatment response. We believe this work takes the field one step closer to identifying which patients are best suited for SclAb treatment and has the potential to stratify responders verses non-responders prior to treatment.

Chapter 4 A Xenograft Model to Evaluate the Bone Forming Effects of Sclerostin Antibody in Human Bone Derived from Pediatric Osteogenesis Imperfecta Patients

Clinical trials to establish the effects of emerging and promising therapeutics in the pediatric OI population is uniquely challenging due to low patient numbers coupled with high disease heterogeneity and the desire for treatment naive patients. As such there is a near ubiquitous reliance on OI animal models to understand the *in vivo* response of emerging therapeutics, yet these models do not comprehensively cover all genetically unique types of the disease and may not be fully predictive of patient response. In an effort to evaluate SclAb in pediatric OI bone *in vivo*, Chapter 4 contributes to the field through the description of a patient-derived xenograft approach as an alternative or adjuvant to genetically modified OI mouse models. In this xenograft model, pediatric OI bone tissue can be implanted directly into a biologically rich host-derived microenvironment to quantify treatment efficacy *in vivo*.

In our xenograft model, we demonstrated that 1) implanted OI bone tissue becomes bioaccessible by the host 24 hours after implantation, allowing the drug to access the implant, 2) implanted bone cells undergo minimal apoptosis up to 12 weeks of implantation, and 3) implanted OI bone remains rich with human-derived bone cells throughout the implantation period. We also successfully demonstrated that pediatric OI bone cells respond positively, yet differentially, to SclAb in an *in vivo* condition. While treatment increased bone density and volume over time, response was variable by bone type (trabecular, cortical) with the greatest magnitude obtained in trabecular implants following four weeks of treatment. Baseline OI osterix expression dictated magnitude of response supporting *in vitro* findings in Chapter 3. OI patients with low baseline osterix expression demonstrated robust human-derived osterix-expression with treatment. Interestingly, it appears that SclAb recruits human-derived, osterix expressing bone lining cells to the implant surface in comparison to untreated implants which had bone surfaces with host (mouse) derived osterix expressing bone lining cells. Taken together, we believe the successful implementation of the model in Chapter 4 contributes to the field by providing a safe and efficacious approach for identifying factors that influence treatment response without contraindications to the patient.

Chapter 5 In Vivo Quantitative Imaging Biomarkers of Bone Quality and Mineral Density using a Novel 3D Zero Echo Time Magnetic Resonance Imaging Approach

Central to the work in Chapter 5 is the focus on a non-invasive and non-destructive imaging technique that creates a clear path to clinical translation with patient safety in mind. We believe a significant contribution to the field is the direct quantification of mineral density using MRI in Chapter 5, while sequentially quantifying additional measures of bone quality including cortical water, bone marrow fat fraction and a surrogate for matrix organization using T_1 relaxation, *in vivo*. In doing so, we challenge the current gold standard which relies on harmful ionizing radiation to detect changes in bone mineralization through our implementation of a novel 3D zero echo time (ZTE) MRI, multi-band SWeep Imaging with Fourier Transformation (MBSWIFT), that is able to achieve a higher bandwidth compared to other MRI approaches and mitigate susceptibility artifact inherently present at bone's cortical/marrow and cortical/muscle borders. Because of the experimental MRI's ability to capture all pools of protons including those associated with the mineral phase, we directly derived BMD using MRI and compared to µCT, the preclinical gold standard. Both MRI and µCT BMD detected significant longitudinal *in vivo* changes in the measure by two weeks. Furthermore, MRI BMD significantly correlated to BMD derived from µCT.

MRI distinguished significant decreases in cortical water, increases in marrow fat and cortical volumetric T_1 relaxation (a tissue specific biomarker where measures are related to tissue organization) consistent with OVX by 10 weeks. Cortical water fraction quantified using MBSWIFT significantly correlated to water loss (% by volume) during sequential drying. Findings point to ZTE MRI's ability to detect biochemical alterations occurring in the system following estrogen deficiency and detect alterations in BMD in a manner correlating to the gold standard suggesting the utility of an imaging modality able to characterize both the mineral- and quality measures beyond the mineral phase of bone.

It is my aim that the work presented in this thesis contributes to an overarching goal to safely improve upon clinical management of bone disease. This goal was pursued using two separate yet equally important approaches to 1) establish a model to safely evaluate drug efficacy in the target bone tissue and 2) describe a non-invasive imaging technique to quantify imaging biomarkers of bone quality, in addition to mineral density, without the use of harmful ionizing radiation. Together, the work can be used to establish patient-specific factors influencing treatment response where material-level and biochemical changes can be quantified and monitored safely *in vivo*.

Chapter 2 Background

Bone

Bone is a complex, heterogeneous and dynamic tissue that, through the interplay of different cells responsible for remodeling, respond to environmental factors, mechanical loading and internal needs based on location and function. [43] The macrostructure of bone is comprised of ~ 80% cortical and ~20% trabecular architecture. The cortical bone forms the outer "shell" which encases the bone marrow and blood vessels of the system and largely makes up the shaft of the extremities and the trabecular bone is comprised of a network of interconnected plates and rods and is dominant in the vertebrae. The tissue itself is a composite biomaterial made up of ~35-45% mineral crystals composed of hydroxyapatite, ~40% organic matrix including type I collagen, proteoglycan (PG) and glycosaminoglycan (GAG), and ~15-25% water existing as free (in Haversian and Volkmann's canals) and bound (hydrostatically bound to organic matrix constituents), by volume, with each component contributing to bone quality. [29, 44, 45] These materials seemingly made up of opposite qualities (organic, inorganic) provide flexibility, toughness and elasticity and are essential to understanding the quality of the tissue where changes in composition can occur during aging, disease progression and in response to treatment, all of which affect mechanical behavior.[30]

Bone is uniquely dynamic; the tissue possesses the ability to self-repair through a process known as bone remodeling. [46] The remodeling process is the continuous, life-long interplay of bone resorption (removal of old or damaged bone) and formation of new bone which is guided by osteoclasts and osteoblasts, each essential for maintaining optimal bone quality, strength and maintaining mineral homeostasis. [47, 48] The third bone cell, the osteocyte, is the most abundant of the bone cells. The osteocyte differentiates from osteoblasts and are embedded within the bone matrix during cycles of the modeling and remodeling processes. [49] The balance of activities between bone-forming osteoblasts and bone-resorbing osteoclasts determine bone mass where the mechanosensing-osteocyte appears to play a role in regulation of this process through signal transmission.[50, 51] Under normal conditions, bone remodeling is tightly coupled to ensure there are no major net alterations in bone mass or decreases in mechanical strength. When resorption or formation becomes impaired the bone undergoes phenotypical alterations marked by changes in composition, structure and function which can lead to fragility, decreased bone quality and increases in fracture risk. The imbalance in remodeling and turnover can be metabolic, genetic or secondary to disease, treatment or environmental factors.[52] The focus of this dissertation will be on two distinct bone diseases: osteogenesis imperfecta (OI), a rare and severe genetic disorder of bone fragility, and metabolic osteoporosis, the most common disorder of altered bone remodeling.

Osteogenesis Imperfecta

Osteogenesis imperfecta (OI) is a genetic bone dysplasia marked by low bone mass, high bone fragility and increased incidence of fracture which is especially burdensome during childhood. The name osteogenesis imperfecta, literally meaning ‘imperfect bone formation’ in Latin, was first coined by Professor Willem Vrolik in the 1840’s when describing an infant with a poorly mineralized skeleton, tubular bones, and multiple fractures who only survived three days postnatal. [53] OI is extremely rare with an overall prevalence of approximately 1:20,000 births [54] affecting between 25,000 and 50,000 individuals in the U.S. [55] The disease is both genetically and clinically heterogeneous [56] but has several common phenotypic features such low bone mass, sustained recurrent fractures following minor trauma, short stature, vertebral compression, bone pain, long bone bowing and laxity in connective tissue. [3] Of these, the liability to fracture is often considered the most critical clinical feature to manage in patients.

The first classification of OI was created using clinical features and patterns of inheritance.[2] The system has become known to the community as the ‘Sillence’ classification system and began with four autosomal dominant OI types ranging in severity from mild (OI type I), perinatal lethal (OI type II), severe (OI type III), and moderate (OI type IV). [56] An expanded Sillence classification system was proposed to include four additional types (V-VIII).[57] This included an autosomal dominant moderate form (OI type V),[58] having distinct clinical and histological characteristics such as hyperplastic callus formation, radial head dislocation and interosseous membrane calcification of the forearm. [59] The next two types include an autosomal recessive severe OI (type VI) and an autosomal recessive severe form (type VII) which, in some cases, can be lethal. [57, 60] In 2007, Cabral et al. described an autosomal recessive OI (type VIII) characterized by severe growth retardation, undermineralization of the skeleton and bulbous metaphysis.[61] However, in 2010 the International Nomenclature group for Constitutional Disorders of the Skeleton (INCDS) published a consensus to group OI into five groups; keeping the original four described by Sillence and including the addition of OI V in an attempt to return to a more descriptive grouping based on clinical characteristics and patterns of inheritance. [62]

As discussed, OI is generally autosomal dominant but can be autosomal recessive and even X-linked in modes of inheritance.[3] The disease is caused by autosomal dominant mutations in *COL1A1* or *COL1A2* encoding the α1 or α2 chain of type I collagen, respectively, in up to 85% percent of cases resulting in an underproduction of normal collagen, secretion of defective collagen chains or a quantitative loss of the α1 chain depending on the mutation. [63-65] Other *COL1A1* or *COL1A2* mutations resulting in structural defects in the collagen triple helix are related to glycine substitutions in the endoplasmic reticulum. [64] The remaining 15% of cases include genes beyond *COL1A1* or *COL1A2* (15+ and growing) that are recessive, dominant and even X-linked in origin. [3] Of the new genes, two in particular, CRTAP and PLOD2, altered prior conceptions through the discovery that the disease can be caused by changes in collagen post-translational modifications. [66, 67] This finding lead to a cascade of discoveries involving other collagen chaperones. [68, 69] While the exhaustive list of 15+ genes will not be discussed in detail here, the reader should refer to Marini et al. 2017 for further information. [3]

The mutation type and position of the mutation was once accepted to dictate phenotype,[1] but variability in clinical presentation can exist within genotype. Studies have revealed divergent phenotypes in patients with identical, or near-identical genetic mutations and different symptoms have been reported among family members with the same mutation [4]. This spectrum of genotypic-phenotypic variability makes both diagnosis and management of the disease challenging. It remains unclear how mutation type, location and affected gene contribute to OI bone fragility and ultimately response to treatment.

Pharmacological treatment of Osteogenesis Imperfecta

There is currently no cure for OI nor a United States Food and Drug Administration- or European Medical Agency- approved treatment therapy. Instead, clinical treatment strategies include any combination of physical therapy, orthopaedic surgery and pharmacological management. Often, pharmacological treatment strategies for OI evolve from approaches developed to treat osteoporosis, a metabolic bone disease (which will be discussed in the following section). Numerous pharmacological treatment strategies have been proposed for OI but results across patients have been inconsistent highlighting an opportunity to explore factors related to treatment response in this highly heterogeneous disease.

OI is marked by increased osteoclastic bone resorption and as such, off-label use of anti-resorptive bisphosphonates have been the primary clinical treatment strategy for OI for the last decade. [5] However, bisphosphonates only partially correct the OI phenotype as they do not actively build bone tissue and do not address osteoblasts harboring the OI-causing collagen mutation. [6, 7] Clinical results have been variable and are dependent on OI type, severity and bone site. [6, 70, 71] Concerns regarding prolonged suppression of bone-turnover coupled with the long half-life of bisphosphonates raises questions about its long-term use in the pediatric population.[72, 73] Denosumab, a monoclonal RANKL antibody that inhibits osteoclast maturation, has received approval for use in osteoporotic adults [74] and because denosumab acts on the osteoclast, it has gained interest for use in patients with OI. In a prospective pilot trial in four children with type VI who had poor response to bisphosphonates, denosumab significantly decreased markers of bone resorption yet two patients sustained fractures during the trial.[75] In ten children with types I, III, and IV OI, denosumab improved BMD but also demonstrated decreased osteocalcin levels and four patients sustained fracture during trial. [76, 77] Other experience with denosumab in OI has been equivocal with no clinical improvement in BMD. [78] Concerns regarding hypercalciuria development during active treatment and pre-clinical therapy has limited its use. [79, 80]

Anabolic treatment strategies are gaining interest for their potential use in OI in part because the primary underlying genetic defect of OI often affects collagen type I which is synthesized by osteoblasts. Growth hormone therapy in pediatric OI successfully elicited linear bone growth yet these effects were only observed in half of the patients.[81] With intermittent teriparatide, a recombinant humanized parathyroid hormone, treatment responders versus non-responders in adults could be stratified by their OI type.[82] However, results of teriparatide treatment in pediatric OI remain unknown due to concerns over osteosarcoma development in rats.[83] Recently, the advent of sclerostin monoclonal antibody (SclAb) represents a different treatment strategy to increase bone mass and reduce fracture occurrence.[8] While bisphosphonates focus on preventing bone resorption, SclAb increases bone formation by inhibiting sclerostin, an osteocyte-secreted protein that negatively regulates osteoblast bone formation through *Wnt* signaling.[9]

SclAb has elicited positive increases in bone quality and mechanical strength during clinical trial for the treatment of post-menopausal osteoporosis. [10-12, 84-86] Pre-clinical results in animal models of OI overall support its use in the disease [15-20], but the magnitude of bone-forming response between mild, moderate and severe murine models of OI suggest the impact of genotypic and phenotypic variability. [15, 18-20] SclAb stimulated markers of bone formation, reduced bone resorption and increased lumbar spine areal BMD in a phase II clinical trial in adults with types I, III, and IV OI. [21] Because of low group numbers, response to SclAb could not be stratified by OI type. Clinical trial for pediatric OI is particularly challenging due to the rarity of the disease, stark heterogeneity and desire for treatment-naïve individuals [22] and while response to SclAb has been promising, experience in the pediatric OI patient and across all types and severity of the disease remain unknown.

Osteoporosis

While OI is a rare and severe genetic bone dysplasia,[87] osteoporosis represents the most common bone disorder with a prevalence of over 200 million people worldwide. [88] The disease is a multi-factorial metabolic bone disorder characterized by decreased BMD, decreased bone quality, disruption of bone microarchitecture and bone function all leading to compromised bone strength and increased fracture risk. [89] Even with such a high prevalence and accompanying reduction in quality of life, associated morbidity and increased mortality, the disease often remains “silent” until the development of fracture which is both clinically and socioeconomically burdensome. [90-92]

Osteoporosis can be classified as primary or secondary depending on the factors affecting altered bone metabolism. Primary osteoporosis includes two subgroups: osteoporosis type I and osteoporosis type II. Type I, also known as post-menopausal osteoporosis, is caused by estrogen deficiency and is the most common cause of primary osteoporosis. Estrogen deficiency leads to increased cytokine production in the bone marrow environment stimulating bone resorption either through increasing the number or activity of osteoclasts and impairing osteoblast function.[93] The trabecular bone in type I is particularly altered as a result of estrogen deficiency.[94] Primary osteoporosis type II, also referred to as senile osteoporosis, is loss of bone mass due to the aging process.[94-96] Secondary forms of osteoporosis account for ~10% of all cases and can be caused as a result of a recognized disease, medication and environmental/lifestyle factors. [97] Osteoporosis can also be observed in adolescence. In children, osteoporosis is often secondary to disease or treatment, [98, 99] but more rarely can be idiopathic where there is severe demineralization. [100] Because the classification of osteoporosis includes ‘bone loss that is extensive enough to increase fracture risk’, the Osteogenesis Imperfecta Foundation (OIF) reports that nearly all OI patients also have osteoporosis. This can confound OI symptoms and become particularly challenging during aging.

Pre-clinical models of osteoporosis represent an invaluable system to evaluate altered bone remodeling. As postmenopausal osteoporosis is the most common form of osteoporosis, animal models utilizing ovariectomy (OVX) to achieve estrogen deficient bone loss represent the most popular animal model of osteoporosis. The OVX procedure involves the bilateral removal of the ovaries at the distal uterine horn,[101] and is the gold standard to initiate an estrogen deficiency bone loss [102] through enhanced resorption.[103] In human postmenopausal osteoporosis, bone loss is most significant in the trabecular bone and on the endocortical surfaces. [104] Therefore an efficacious animal model for the disease should mirror these effects. As such, the rat is often the choice animal for OVX models and is recommended by the Food and Drug Administration [105] because its remodeling of the trabecular network occurs in a manner similar to humans during menopause.[106] In mature rats, OVX bone loss at the tibial metaphysis can be observed as early as 14 days but can range to 100 days before significant changes are observed.[107] The time of OVX initiation has been studied in rats as early as three weeks of age [108] and in rats up to two years old.[109] Young rats create a unique system where estrogen-deficient bone loss is competing with the elevated modeling/remodeling associated with growth while older rats (+ two years) are slow to induce changes because they may have reached anovulation prior to OVX.[110]

Bone Mineral Density

Bone mineral density (BMD) refers to the amount of mineral in bone tissue or, more specifically, the mass of mineral per volume of bone. BMD is highly, yet imperfectly, correlated to bone strength [111-114] which is determined by relative amount of mineral, the properties of the apatite and mineral crystal organization. [115-118] The mineral phase of bone can change with age or during disease such as osteoporosis where smaller mineral crystals grow in size to become larger crystals that are more brittle.[119, 120] Because of this knowledge coupled with large epidemiological characterization studies and the ease, availability and low cost of x-ray based imaging techniques to assess BMD, the measure is used in near ubiquity to characterize bone disease and as an outcome during clinical trial for therapeutics targeting low bone mass.[13, 121-124] Reporting changes in BMD during clinical trial gives treating clinicians a framework when implementing these pharmaceuticals to their own patients. Further, positive increases between pre- and post- DXA aBMD measures may have a beneficial role in encouraging patients to continue treatment.

In the next sections, we will describe the clinical and pre-clinical imaging methods to obtain BMD, how the measure is used to inform diagnosis of disease and then discuss the limitations of the measure. Finally we will review the effects of radiation exposure inherent to the imaging modalities used to characterize BMD and discuss potential alternative bone quality targets for imaging.

Imaging modalities to assess bone mineral density

Both clinically and pre-clinically, the mineral phase of bone is measured using ionizing x-ray based techniques. This is because the high atomic mass number associated with calcium (Z=20) gives rise to a higher photoelectric absorption compared to that of soft tissue providing excellent contrast in x-ray and computed tomography (CT). [125] Historically, plain skeletal radiographs were used in the clinical to measure bone density, however bone demineralization is not apparent until >40% of loss has occurred making it too insensitive for clinical reliance. In 1989, duel x-ray absorptiometry (DXA) was introduced and represents a projection-based technique that measures x-ray beam attenuation as they pass through tissues (that vary in density) in 2D.[126] The resultant measure is the bone mineral content (expressed in g) and the planar area of the projected bone tissue (measured in cm^2) which are used to derive the “areal” BMD (aBMD) expressed in g/cm^2. DXA aBMD is most commonly measured at the hip and spine but is not able to distinguish between cortical and trabecular bone.

Osteoporosis is diagnosed when a fragility fracture has been sustained or by the patient's DXA-derived aBMD. Clinically, the aBMD is converted to a T- and/or Z-score to give some meaningful context in relation to various populations. The T-score is defined as the difference between the person's measured aBMD and the mean aBMD of young individuals (age 20-29 years, the reference population) divided by the standard deviation of the reference population. The subsequent "score" represents the number of standard deviations above or below the average peak bone mass of young adults (the reference). The Z-score is the number of standard deviations above or below the average aBMD of a person of the same age, sex, and ethnicity.[127] Using the T-score, an aBMD equal to or less than 2.5 standard deviations (SD) below the mean for a young individual of the same sex meets the diagnostic criteria for osteoporosis.[128] A reduction in T-score of 1 SD increases fracture risk by 1.5-2 times and a reduction of 2.5 SD is the threshold where fractures can be predicted [129] and is generally used as the prescribing criteria for antiresorptive bisphosphonates. A Z-score below -2.5 SD is indicative of secondary osteoporosis because the measure is calculated against the mean aBMD of a person of the same age and sex. [128]

BMD is also acquired in the growing skeleton. It is understood that bone health in the growing skeleton has long term effects during adulthood because up to 50% of the skeleton is laid down during adolescence.[130, 131] As such, BMD is used to assess bone health in children at risk for early bone mass derangement [132] in order to optimize bone mass accrual and prevent onset of primary osteoporosis or secondary as a result of chronic illness or treatment.[133, 134]

In pre-clinical research, micro-CT (µCT) has allowed for 3D measures of the bone with enhanced resolution from the use of microfocused x-ray tubes.[135] As a result, volumetric BMD can be derived using phantoms made of calcium hydroxyapatite (CHA, $Ca_{10}(PO_4)_6(OH)_2$) which makes up the mineral in bone. These CHA phantoms are essential to determine specimen-specific volumetric BMD measures [136] where µCT BMD is calculated using the voxel-wise Hounsfield unit compared to the known densities of the CHA calibration standard and water.[137] Because of the correlation between apparent bone density (mass of bone without marrow divided by bone volume including bone pores) and bone mechanical properties, [138] µCT BMD can be converted to apparent bone density and used in finite element (FEA) models to determine fracture risk under mechanical loading conditions.[139] Beyond volumetric BMD, µCT permits measurements of bone microarchitecture where individual trabecular structures can be resolved with remarkable precision. [140]

More recently, high resolution peripheral quantitative computed tomography (HR-pQCT) has been introduced as an *in vivo* µCT scanner for humans that allows for rapid scanning with high resolutions (82 µm) where volumetric BMD, in addition microarchitecture, can be derived.[141] HR-qQCT measures are taken at peripheral sites such as the tibia and wrist and, because of the higher resolution compared to DXA, can derive separate densitometry measures in the cortical and trabecular compartments. Volumetric BMD from HR-pQCT has demonstrated good correlation (R^2=0.69) with DXA aBMD and allows the user to obtain additional indices such as connectivity density and FEA-derived measures to determine fracture risk under loading conditions. [142]

Limitations of bone mineral density

While there is an association between a low aBMD and an increased risk of fracture,[143] there are a number of limitations with this technique.[32] Bala and Seeman refer to bone density as an ambiguous and incomplete measure where the “completeness of mineralization, its spatial distribution, porosity, and other factors” are missed.[31]

In the aging population, declines in bone strength are disproportionally steeper than concurrent decreases in BMD and therefore can only partially explain bone strength.[144] Other age-related changes including the presence of osteophytes can hinder the interpretation of results. In post-menopausal osteoporosis, Sornay-Rendu et al. reported that fracture incidence was associated with bone resorption rate in a manner that was independent of BMD.[145] More than 50% of postmenopausal women who sustained a hip fracture had a BMD score that did not meet the conventional -2.5 standard deviations below the reference. Both adults and children with small bones or those with extremely low bone density, long bone bowing, have metal rods or have compression fracture may get an inaccurate measure of BMD. BMD has further associated problems in the growing skeleton. The 2D nature of DXA is unable to capture the inherent non-uniform bone growth which occurs in 3D during adolescence.[146, 147] Pre-clinically, BMD in the growing skeleton can be challenging, too where studies suggest that changes in BMD may be attributable to growth and miss underlying alterations indicative of altered bone remodeling.[148-150]

In OI, increases in BMD and overall increases in bone mineralization may be independent of OI severity and the associated collagen mutation.[151, 152] Characterizing OI using BMD can therefore be challenging. For Type I OI, a mild phenotype, diagnosis of the disease cannot be excluded by a BMD score in the normal range.[153] Paterson et al. determined that in a cohort of 58 patients with either Type I or Type IV OI, 70% had BMD values within the reference interval.[154] In 154 adults with OI (ages 25-83 and OI types I, III, and IV) only 10% of the adults demonstrated T-scores within the osteoporotic range as measured by DXA yet had three-fold higher fracture risk compared to the normative population.[155] Thus a measure that relies solely on the mineral appear to fall short in fully characterizing this collagen-related bone disorder.

BMD can be an incomplete target to quantify treatment response of drugs aiming to target diseases of low bone mass. For example, anti-resorptive alendronate induced improvements in spinal BMD but this improvement could only be attributable to 16% of the risk reduction in vertebral fractures suggesting that improvements in BMD during antiresorptive treatment accounts for a predictable yet small fracture risk reduction. [156] Some drugs aiming to improve bone strength and decrease fracture risk have demonstrated promising results independent of an increase in BMD. Anabolic parathyroid hormone demonstrated early increases in total bone area, cortical porosity and hypomineralized new bone which resulted in little-to-no change in BMD in postmenopausal osteoporosis.[157] The pitfalls of relying on BMD alone are particularly highlighted in studies using raloxifene, a selective estrogen receptor modulator. Vertebral fracture risk reduction was documented in osteoporotic patients treated with raloxifene which was documented without concurrent improvements in BMD.[158] Sarkar et al. estimated that BMD could explain only 4% of the fracture risk reduction associated with raloxifene therapy while the remaining 96% was attributable to BMD/mineral-independent properties.[159] Pre-clinically, raloxifene demonstrated improvements in bone material and mechanical properties without increasing bone mass and BMD. These pre-clinical studies suggest that raloxifene improves mechanical properties through a non-cellular mediated mechanism independent of hydroxyapatite.[160-163] Another drug target of osteoporosis, strontium ranelate, is thought to increase bone strength by increasing bone water. Increases in mechanical outcomes were lost when bone from rats treated with strontium ranelate were dehydrated.[164] Where raloxifene did not result in substantial alterations in BMD, strontium ranelate demonstrated strong increases at the spine and hip. [165] This increase, however, may be artificial. Strontium ranelate has been shown to overestimate BMD up to 10%. [166] This may be attributable to the high atomic number of strontium (Z=38) which is even higher than calcium which would more intensely attenuate x-ray.[167]

Radiation exposure from imaging modalities to assess bone mineral density

While x-ray based techniques remain the current clinical and pre-clinical imaging gold standard for bone, these approaches deliver ionizing radiation to the subject/patient tissue which can harm the very structure we aim to study. Bone has a higher linear attenuation coefficient than soft tissue and experiences local radiation doses ~3-5 times higher compared to these tissues, such as the lung, as a result.[168-170] Further, there is a punishing relationship between the desire to achieve greater resolution to resolve microarchitecture in the bone at the cost of increasing radiation dose.[171] When reporting radiation dose parameters, the effective dose expressed in millisieverts (mSv) is commonly used. The effective dose is calculated from information regarding absorbed dose to the organ (expressed in grays, (Gy), and is the energy per unit mass deposited) and the radiation risk assigned to each of these organs.[172] Bone densitometry measured via DXA gives an effective radiation dose to the patient of 0.001 mSv (comparable to 3 hours of natural background radiation where the average annual U.S. background radiation is 3.6 mSv). While DXA has substantially decreased radiation doses compared to other techniques, this projection based method is unable to directly derive true volume densities and has demonstrated difficulty in resolving small changes in longitudinal studies of osteoporosis.[173, 174] When acquiring an x-ray of the long bone, the effective radiation dose increases to 1.5 mSv and is comparable to 6 months of background radiation. For a CT of the same long bone, the dose increases to 3 mSv and can go up to 7 mSv (or two years of background radiation). At the increased radiation dose, CT increases achievable resolution and is therefore able to derive 3D microarchitecture.[175] The advent HR-pQCT has allowed for 3D high-resolution acquisition with a substantially reduced radiation cost compared to CT yet remains higher than DXA (HR-pQCT: 0.01 mSv).[176, 177] For each imaging modality, it should be noted that radiation exposure depends on many factors including the device itself, duration of the scan, size of the individual and sensitivity of the target tissue.[175]

It is well understood that exposure to high levels of ionizing radiation, on the order of 1-2 Gy, can result in rapid increases in osteoclast number and osteoclast resorbing surfaces within the metabolically active trabecular bone leading to loss of structural integrity.[178-181] An early (4 hr) and persistent (24 hr) rise in the expression of RANKL, a marker of bone resorption, was observed in mice following a single large (2 Gy) dose of radiation.[182] Radiation exposure at lower doses commonly used in the clinic have negative and lasting long-term effects, too. Much attention has been focused on the potential risk of radiation-induced cancer as a result from diagnostic radiology, especially CT, where one abdominal CT can have the radiation equivalent of nearly 750 chest x-rays. Sodickson et al. quantified the potential cancer risk from CT in 31,462 patients over 22 years; as a whole, the increase was slight (0.7%) but when patients who had multiple CTs, this risk increased and ranged from 2.7%-12%.[183] This ionizing radiation exposure limits their use in longitudinal *in vivo* studies where multiple follow-up imaging acquisitions to monitor disease progression or response to treatment become unfeasible and unethical. In sensitive populations such as pediatric OI patients who endure multiple fractures annually, treating physicians often forego x-ray based imaging studies in order to limit the child's lifetime radiation exposure.

Bone Quality Measures beyond the Mineral: Potential Imaging Targets

We have discussed that BMD is an incomplete measure accounting for only ~60% of bone strength in humans and animals, [32, 33, 184, 185]; thus it is apparent that the remaining 40% comprise important bone quality factors that go "missed" using traditional imaging approaches. There are currently no accepted approaches to measure bone quality, non-invasively, in the clinical setting. [127] In the next section, we will review additional bone quality measures that we believe could serve as potential imaging biomarkers for bone diseases of altered remodeling. This list is not exhaustive and does not include all potential bone quality measures; instead we discuss targets that are relevant to Chapter 5 of this thesis. Here, we will highlight important pre-clinical work in the framework of osteoporosis that supports the development of non-invasive biomarkers to characterize these components.

Organic matrix

The bone extracellular matrix includes the organic matrix, or organic phase, which is made up of 90% type I collagen laid down by osteoblasts during formation. The remaining organic extracellular matrix is comprised of non-collagenous components such as osteopontin and osteocalcin. [186] The assembly and density of these molecules gives important insight to the amount of elasticity and deformation the bone can endure. [187] As a result, alterations in the proportion and assembly can be indicative of disease where in fragile bones, the matrix composition is shown to be compromised. [188] We can begin to grasp the critical role collagen has in determining bone strength when considering OI where deficient collagen substantially increases fracture risk. [55] Patients with osteoporosis have altered expression of type III and IV collagen compared to healthy individuals [189] and collagen from premenopausal women who sustained low trauma fractures had higher ratios of non-reducible to reducible collagen crosslinks compared to controls. [190] While preclinical *ex vivo* techniques such as atomic force microscopy can resolve these nanoscalar molecules (>1 mm in lengthy and 20-50 nm wide), [191], capturing bone collagen *in vivo* remains challenging. Techniques such as second harmonic generation imaging take advantage of the fact that collagen can absorb low energy incident photons and re-emit them where the interaction between two low-energy photons, specifically, can be quantified [192] with demonstrated success in live animals. [193] This technique, as well as other optical techniques not discussed in this thesis, are limited by depth of achievable tissue penetration which needs to be resolved prior to realization of clinical use in bone. [194] Again, exploiting the fact that collagen can provide endogenous absorption contrast in the near-infrared spectrum,[195] label-free *in vivo* characterization of tendon using photoacoustic imaging has demonstrated promise [196] and may have application in bone. Depth penetration may limit the non-invasive technique clinically in bone. Exploitation of organic phase organization however, may be achievable using indirect measures of collagen organization derived from clinically available non-invasive imaging modalities such as magnetic resonance imaging (MRI) and will be discussed in the following sections. [197, 198]

Cortical water

Water is an integral constituent of bone. While mineral is related to stiffness and in part strength [115] and the organic matrix influences toughness,[199, 200] the interaction of water with each of these phases is just as critical to bone mechanical properties. [201] Water's role in bone mechanics has been documented following dehydration of the tissue where water removal decreases strain, energy to fracture, and increases stiffness, tensile strength and hardness. [201-205] Water changes as a function of skeletal age, too. During growth, water in bone decreases along with progressive mineralization. [206, 207] As aging continues, the decrease in water is correlated to a reduction in bone ductility. [201]

Water in bone exists in two primary compartments; the “free” and “bound” water pools. Water existing as “free” is found in intra-cortical pores including the Haversian and Volkmann’s canals and the lacuno-canalicular system. [206] This fraction of water is directly related to cortical bone porosity; as porosity increases with age, strength is impaired. [208] Further, the free water fraction has been shown to be negatively correlated to peak stress. [209] Because some of collagen’s residues are hydrophilic, water molecules associate themselves to collagen within the matrix and comprises the “bound” pool of water and makes up ~ 20% of cortical bone’s wet weight. [210] Bound water influences the three dimensional structure of the organic matrix and a reduction in this water pool decreases cortical toughness and reduces collagen fibril diameter. [201, 211] Reduction in this pool can directly affect the mineral crystals, too. Decreases in water shortens the distance between lattices of mineral crystals reducing their size where smaller crystals are correlated with decreased mechanical stiffness. [212] But increases in mineralization which increase the size of crystals can also decrease water (diffusing it out).

Even with all the promise as a biomarker of strength and bone quality, Granke et al. in 2015 reasoned that water is arguably the “least studied constituent, even less than non-collagenous proteins and growth factors within the matrix of bone (~1% by volume)”.[29] We believe this is because, until recently, there were no straightforward and acceptable techniques to non-invasively quantify water in bone. Recently, work has been done to establish the utility of MRI to detect alterations in total, bound and free water fractions which will be discussed at length in the following sections.

Bone marrow fat content

Bone marrow is a highly vascular substance that occupies ~85% of the bone cavity with the remaining ~15% being comprised of trabecular bone. Bone marrow adipose cells are observed to have a role in regulation of hematopoiesis, bone turnover and metabolism and the alteration/derangement of marrow adipose cells are observed in metabolic bone diseases such as osteoporosis in addition to obesity and diabetes. [213]. It has long been observed that decreases in bone marrow volume are shown to correlate with increases in bone marrow fat in patient biopsies and animal models of osteoporosis and osteopenia. [214, 215] As such, quantification of marrow fat suggests a promising opportunity to diagnose and monitor disease. [216] Argawal observed that vertebral marrow fat was significantly increased in postmenopausal women with osteoporosis compared to women with osteopenia and healthy individuals; as BMD decreased marrow fat increased. [217] Higher marrow fat has been correlated with lower trabecular BMD as a result of age, too. [218] Because MRI signal in the biological system is derived primarily from water and fat protons, the fat fraction or the proportion of signal derived from fat protons has gained interest as a quantitative, objective image-based biomarker of disease. [219] As such, we will explore the utility of quantifying marrow fat *in vivo* using MRI in the following sections and in Chapter 5 of this thesis.

Magnetic Resonance Imaging

While clinical assessment of bone fragility relies on ionizing x-ray-based imaging techniques to <u>*assess*</u> bone mineral density and <u>*predict*</u> bone quality and fracture risk *in vivo*, mounting evidence suggests that additional markers, [220-222] including the composition of the organic extracellular matrix, [223-226] and the content of both bound and free water [201] and even the marrow fat, [227] contribute to overall bone health and strongly correlate with bone quality and strength. There remains a clear need to develop and implement an imaging tool that can derive quantitative biomarkers relevant to bone, non-invasively, to be utilized in the clinical setting and to aid in clinical trial. Di Iorgi et al. made an appeal that the ideal imaging instrument to be used in children should be able to perform measurements on skeletal sites where fractures are frequent and it should be ‘minimally invasive, accurate, precise and rapid’. [228] Magnetic resonance imaging (MRI) is a well-known tool that offers superior soft tissue contrast without harmful ionizing radiation.

Brief history

The advent of MRI for biological tissue has revolutionized the non-invasive characterization of the human body. Emerging from several fundamental inventions in the 1970s, MRI has underwent tremendous development over the past four decades and its capabilities have certainly not been fully exploited. With increases in field strength, novel multi-channel coil design, advancements in pulse-programming and innovative post processing and reconstruction techniques, the high spatial resolution and superior soft-tissue contrast inherent to conventional MRI has made it the gold standard modality for diagnostic imaging of numerous diseases such as cancer and stroke. Yet with all of these gains, its application beyond soft tissue and the identification of quantitative biomarkers is only beginning to be realized. This section provides a brief sampling of the principles of MRI from a biomedical imaging perspective with emphasis on zero echo time (ZTE) imaging to exploit short T_2 species and quantitative MRI tissue parameter mapping. Therefore this discussion is confined to the central aspects that are particularly relevant to Chapter 5 dissertation.

Nuclear magnetic resonance

The principle for MR is based on the interaction between external magnetic fields and the nonzero magnetic moment of the nuclei termed the nuclear magnetic resonance (NMR) effect.

Initially discovered and described by Purcell and Bloch in 1946, the NMR phenomenon was first elicited using a technique known as continuous-wave NMR and could be described by the Bloch equation. [229, 230] Soon after Hahn demonstrated that the NMR effect could be observed with a modified approach based on finite radio frequency (RF) pulses. The imaging area truly took off in 1973 when separate manuscripts by Lauterbur and Mansfield described the concept that if the external magnetic field is spatially varying, the Larmor frequency also becomes spatially varying. [231, 232] Ernst introduced a reconstruction method using Fourier transformation [233] and the first image of a living human was published by 1977. [234]

The NMR effect can be observed in ^{1}H, ^{13}C, ^{19}F, ^{16}O, ^{17}O, ^{23}NA and ^{31}P where the nuclei contain a nonzero spin quantum number and produce a large spin angular momentum, S. [235, 236] Most biological MRI experiments focus on the resonance effects of the hydrogen proton due to its abundance in biological tissue and its high gyromagnetic ratio. As a result hydrogen imaging has become the foundation for clinical MRI. The potential energy, E, of the magnetic moment in a magnetic field, B, is:

Equation 2.1

$$E = -\mu \cdot B = -\mu_z B_0 = \gamma S_z B_0$$

The magnetic field, B_0, is in the z-direction, μ_z and S_z are the magnetic dipolar moment and spin angular momentum in the z-direction, respectively. γ is the gyromagnetic ratio which is specific to each nuclei. The net magnetization sums over all nuclei in the unit volume, $M = \sum \mu$. The magnetic field exerts a torque on the net magnetization and the behavior of the net magnetization in the presence of an external magnetic field is given:

Equation 2.2

$$\frac{dM}{dt} = M \times \gamma B$$

The net magnetization angular frequency around the main magnetic field B can be solved as:

Equation 2.3

$$\omega_0 = \gamma B_0$$

Where ω_0 denotes the Larmor frequency. The Larmor frequency is known as the angular frequency of a proton where the energy is the difference between the two nuclear spin states; the transition of states is exploited in MR to produce a signal.

When a specimen/tissue is inserted into the scanner's static magnetic field (B_0), the protons align parallel or anti-parallel and the result is the net magnetization. To create the measurable signal, an RF electromagnetic pulse is applied perpendicular to the main magnetic field at the Larmor frequency which induces measurable transition between states. An inductive oscillator-driven coil is placed around specimen/tissue where the RF pulse initiates the precession of the protons as vectors. The RF pulse generates the 'transverse magnetization' perpendicular to the main magnetic field and the net magnetization behavior is described by the Bloch equation:

Equation 2.4

$$\frac{d\vec{M}}{dt} = \vec{M} \times \gamma\vec{B} - \frac{\vec{M}_{xy}}{T_2} - \frac{M_z - M_0}{T_1} Mz$$

where M is the net magnetization, γ is the gyromagnetic ratio of the proton, B is the external magnetic field, M_{xy} is the transverse magnetization, M_z is the z-component or longitudinal magnetization, and M_0 is the magnetization prior to the RF pulse application. T_1 is the spin-lattice or longitudinal relaxation time and T_2 is the spin-spin or transverse relaxation time (which will be discussed in detail in the next section).

Relaxation

The detectible signal declines rapidly via two processes: loss of phase between spins and the release of energy to the environment, each of which affect the net magnetization.[229] The first type of relaxation affecting the net magnetization is called spin-lattice or longitudinal relaxation, denoted by $T_{1,}$ and is the exponential recovery of the longitudinal magnetization following the RF pulse. The longitudinal relaxation effect is attributable to the energy exchange between protons and their local environment during the return of the excited system (from the RF pulse) to its equilibrium state. The second type of relaxation is the spin-spin or transverse relaxation, denoted by $T_{2,}$ which is the dephasing of the magnetic moments inside a volume. The transverse relaxation effect is attributable to frequency fluctuations caused by proton interactions.

The Bloch equation can now be solved for the longitudinal and transverse relaxation components observed by the protons following RF excitation. [237] The dynamic behavior of the magnetization (in the laboratory frame) is given by the following equations:

Equation 2.5

$$\mathrm{M_z(t) = M_0\left(1 - e^{-t/T_1}\right)}$$

Equation 2.6

$$\mathrm{M}_{xy}(\mathrm{t}) = \mathrm{M_{xy}(0)}e^{-\mathrm{i}\gamma B_0\,\mathrm{t}}\; e^{-t/T_2}$$

Where immediately following the RF pulse, Equation 2.5 describes the longitudinal magnetization recovery to equilibrium or the initial magnetization where T_1 determines the time of this return. Equation 2.6, the term $M_{xy}(0)$ represents the transverse magnetization following the RF pulse, $e^{-\mathrm{i}\gamma B_0\,\mathrm{t}}$ is the accumulated phase and indicates the angle between transverse magnetization and the positive x-axis and e^{-t/T_2} indicates that the transverse magnetization decays exponentially following RF excitation determined by T_2. Transverse magnetization is equivalent to the MR signal and its decay; the detected signal following the RF pulse in conventional MR pulse sequences decays with the T_2 relaxation time.

Protons do not respond to the RF pulse independent of their local environment; instead the response of the proton is highly affected by the surrounding macromolecules and elements in the tissue and this impact can be detected in the signal using multiple tissue specific parameters or contrasts. Damadian et al. first described the difference in T_1 and T_2 relaxation values of tumor tissue compared to that of normal, unaffected tissue exploiting the effects a disease may have on image contrast.[238] Thus T_1 and T_2 time constants directly represent the individual biological tissue of interest and changes to this microenvironment.

Signal localization and image formation

In its simplest form, a signal can be received (free induction decay (FID)) following the RF pulse but the resonating protons cannot be spatially resolved. Spatial localization of the protons is based on a linear combination of three magnetic gradient fields in the xyz-directions:

Equation 2.7

$$G_x(t) = \frac{\mathrm{d}B_z(t)}{\mathrm{d}x}, \quad G_y(t) = \frac{\mathrm{d}B_z(t)}{\mathrm{d}y} \quad \text{and} \quad G_z(t) = \frac{\mathrm{d}B_z(t)}{\mathrm{d}z}$$

These gradients, which are applied in a deliberate sequence parallel to the main magnetic field in a specific spatially differing pattern produce a changing z-component which varies by a few hundred to a few thousand Hz. This pattern can then be used to resolve the location of the tissue with respect to the isocenter of the magnet (which is designed to be zero). This allows a link from the Larmor frequency we "capture" to the spatial location in the scanner where frequency localization can be used for slice selection (2D) and spatial position encoding. [231]

With the gradients on after RF excitation, the Larmor frequency becomes spatially encoded:

Equation 2.8

$$\omega_0(r,t) = \gamma(B_0 + G(t) \cdot r)$$

where r denotes the spatial coordinates x, y, z and G(t) is the gradient vector. Now the magnetization, with its time-dependent components, can be written as:

Equation 2.9

$$\mathrm{M}(\mathrm{r},\mathrm{t}) = \mathrm{M}_0(\mathrm{r}) e^{-\mathrm{i}\gamma \mathrm{G}(\mathrm{t}) \cdot rt} \, e^{-t/T_2}$$

Integration of the equation over all excited locations of the specimen gives the signal equation for MRI; the equation demonstrates how over time in the presence of gradients traces the Fourier transformation of the magnetization distribution along a path. This is denoted by the variable k(t). Solving the signal at each k position in the distribution of the collected data followed by taking the inverse Fourier transformation will, in principle, obtain an image. Coordinates in Fourier space have been historically denoted by k; because of this, data collected in MRI is referred to as k-space data.

K-space trajectories

The k-space in MRI is sampled by modulating the gradients. The very first MR images were acquired using spokes and gave rise to the radial trajectory. This is where a point in k-space is measured moving in a straight line through the center of k-space or from the center of k-space moving outwards. [231] This sampling pattern creates a disc shape in 2D and a sphere in 3D. More commonly employed, however, is a Cartesian trajectory where sampling is done by creating a line-by-line pattern of k-space which produces a Cartesian grid. Data sampled using the Cartesian trajectory has become popular because analysis and reconstruction is relatively simple compared to radial sampling which requires additional steps such as regridding. Radial sampling provides many benefits over Cartesian sampling such a robustness to motion artifact and reduction in scan time and is used by the sequence in Chapter 5 of this dissertation.

Summary

In summary, the bulk magnetization of the protons from a specimen align in the positive z-direction when placed in the magnetic field for imaging. For each experiment, the specimen must be placed within a coil. Proton magnetization can be tipped to the xy-plane by emitting an RF pulse at the Larmor frequency generated by the coil perpendicular to the static magnetic field. This tipped magnetization precesses at the Larmor frequency in the xy-plane and acts like a gyroscope. This precession induces an alternating voltage within the coil which is proportional to its transverse component. This transverse component decays exponentially with the T_2 relaxation time while the longitudinal component relaxes with the T_1 relaxation time back to equilibrium. The use of gradients in the xyz direction spatially encodes the protons in the sample and the collected signal is processed taking into account the k-space sampling pattern.

Magnetic Resonance Imaging and Bone

For musculoskeletal imaging, the application of MRI is in its infancy compared to the gold standard clinical radiographs and preclinical CT. Conventional MRI is superb for visualization of soft tissue such as cartilage and marrow yet tissues such as bone appear as a signal void. This void has been exploited to interpolate trabecular microarchitecture where the hyperdense marrow signal is detected via MRI and the blank space is quantified as an indirect measure of trabecular bone. [239] By taking the inverse gray scale and applying this to the image, the bone, which was once void of signal is now bright and the marrow is the lower intensity background allowing for quantification of trabecular bone volume fraction (BV/TV), trabecular thickness (Tb.Th.) and trabecular number (Tb.N.) in skeletal sites such as the distal extremities, proximal tibia, proximal femur and proximal hip. [240-245] The approach is limited to morphological measures, thus rich and tissue specific biochemical information embedded in tissue contrast cannot be examined.

Conventional MRI is unable to image bone, which has a limited hydrogen pool, due to what was once thought to be a technical limitation of the hardware. The signal detected at the induction coil terminals decays exponentially on the order of microseconds making the time between RF excitation and signal acquisition crucial. The echo time (TE) is the measure of time between these two events (RF excitation and signal acquisition). The repetition time (TR) is the time between successive RF pulses applied to the same slice; a long TR allows the protons in all tissues to return to equilibrium while a short TR will result in the protons from some tissues not having relaxed fully to equilibrium before the signal is acquired, thus decreasing signal from these tissues. The shortest TE and TR achievable using conventional MRI remains greater than a few milliseconds. Even with TEs on the order of a few milliseconds, some protons in bone have returned to equilibrium before signal acquisition has even initiated, thus completely missing a fraction, or in some cases all of the protons in a tissue.

In recent years, a number of remarkable advances have been proposed for both the qualitative and quantitative MRI evaluation of biological tissues such as bone with limited and highly restricted hydrogen pool. We will focus the discussion on a category of methods focused on special pulse sequences that manipulate or nearly eradicate the time elapse between signal excitation and acquisition events (TE). These pulse sequences include the ultra-short echo time (UTE) sequence, the zero-echo time (ZTE) sequence and SWeep Imaging with Fourier Transformation (SWIFT) sequence. Each sequence in the UTE and ZTE family comes with its pros and cons which will be discussed. Further, it remains unknown which sequence is the optimal pre-clinical and clinical choice; direct comparisons are difficult because not all are supported/available simultaneously by a scanner vendor or may not be feasible to employ due to system hardware limitations. A schematic focusing on the achievable reduction in TE can be appreciated in Figure 2.1 along with a conventional MRI sequence, which is discussed in the next paragraph for comparison.

In order to understand the advances of UTE, ZTE and SWIFT, the conventional gradient recall echo sequence (GRE) should be discussed. The GRE was first described by Haase et al. and is one of the simplest pulse sequences in MRI consisting of an RF excitation pulse followed by spatial encoding.[246] For the GRE sequence, the TE is specifically defined as the time from the center of the RF pulse to the center of the signal acquisition or essentially the point in which the center of k-space has been crossed (Figure 2.1A). This is because the first frequency encoding gradient moves the sampling measurement point to the edge of k-space prior to the acquisition event and this accounts for the time it takes to cross the center of k-space. After each acquisition, the GRE takes advantage of a spoiler gradient which is applied to strongly diphase or halt transverse magnetization leaving only longitudinal relaxation until the next TR event. In a conventional GRE sequence, the TE ranges from 2-25 ms where the shorter TEs are achieved on pre-clinical scanners with high performing gradients.

In order to gain signal in bone using MRI we will elucidate why, biologically, bone is difficult to image. We will next discuss UTE and ZTE and work that has been performed in the context of bone. Then we will discuss SWIFT and the advent of multi-band SWIFT which will be utilized in the work presented in Chapter 5 of this dissertation.

Short T_2 species

Biological specimens can be classified into two types based on their T_2 values which reflects both the size and molecular motion of the molecule: long T_2 species and short T_2 species. Long T_2 species are those specimens in which the current clinical application of MR is focused and includes materials such as the brain, muscles, cartilage, marrow and lipids. These long T_2 species have T_2 relaxation times ranging from a few milliseconds to hundreds of milliseconds. MR imaging of long T_2 species can be achieved by applying conventional pulse sequences where the characteristic time delay between RF excitation and signal acquisition is appropriate to capture this relaxation time. Conversely, short T_2 species are those biological tissues which have T_2 relaxation times that can be as short as a few microseconds (μs). These short T_2 tissues include tendon, ligament, teeth, and bone and the approximate T_2 relaxation time for a number of these short T_2 tissues in human can be appreciated in Table 2.1.

For bone, the proton signal intensity is drawn from water residing in microscopic Haversian canals and lacunar-canalicular systems (free water, $T_2 > 1$ ms),[247] matrix water which is bound to collagen (bound water, $T_2 << 1$ ms) and the protons of the collagen backbone/sidechain and other matrix proteins ($T_2 < 0.1$ ms). [40] The T_2 relaxation times for these three pools are directly related to the movement allotted by the protons following RF excitation. Free water refers to the water residing in the Haversian and Volkman's canals comprising the largest majority of the pore network in cortical bone. Pore volume is shown to increase with age and disease and lead to a decline in bone mechanical properties. Thus changes in free water measures in these pores provides a unique surrogate measure in MRI. [248-250]

This water pool, as a result, has the longest T_2 because the water is allowed the most movement within its microenvironment. For the collagen-bound water, three distinct compartments have been identified including water bridges between distant alpha-helices where a direct hydrogen bond cannot be formed, cleft water within the grooves of the triple helix and interfacial monolayer water comprising the hydration layer of the collagen. [251, 252] The portion of bone water that is collagen bound is typically higher than the amount of free water, however accessing the collagen-bound water is more difficult due to the shorter T_2 inherent to bound water fractions in bone.[253] Collagen's three stranded arrangement of alpha-helices lends itself to MR imaging as it is stabilized by a ladder of hydrogen bonds in addition to the support provided by the steroelectronic effect, hydroxylation and cross-linking. [254] Collagen protons have the most inherently short T_2 of all the bone components due in part because collagen is so highly anisotropic in structure. Thus collagen MR imaging creates the largest challenge but, perhaps, would provide the greatest payoff where there is currently no available *in vivo* technique to quantify this in bone. [255]

The ability to non-invasively detect and quantify the contribution of bone water (bound and free) and collagen content, *in vivo*, is of great interest to the orthopaedic community at large. Bone water, matrix-bound and free, represent a large contributor to bone matrix strength and ductility. [29, 209, 256-258] Work by Nyman and colleagues has pointed to the association of age-related fragility with a decrease in matrix-bound water fractions.[29, 39] Further, changes in matrix water and collagen content go undetected using conventional radiography illustrating a significant diagnostic gap in the management of bone health.

Ultra-short echo time imaging

Initially described by Bergin et al. in 1991 and "rediscovered" by Robson et al. in 2003, the ability of 2D radial UTE to visualize sub millisecond T_2 species was realized and its utility in bone was emphasized. [41, 259, 260] The UTE sequence employs a short, rectangular RF pulse with a generally small flip angle (< 30°) while the phase encoding gradients are switched off (Figure 2.1B). [259] Following the RF pulse, the phase encoding gradients are switched on and radial k-space data sampling is initiated. The shortest gap in time between RF excitation and signal acquisition is limited by the hardware in the UTE sequence including transmission/reception switching and gradient coil switching. Taken together, these delays, albeit short and on the order of a few microseconds, are still measurable and limit UTE's ability to capture all protons without some signal attenuation. Unlike ZTE and SWIFT (discussed in the next two sections), UTE can be acquired in 2D with the use of half-pulse sequences and in 3D.[259] UTE has been used with increasing popularity clinically and pre-clinically and now comes as a pre-loaded sequence by most vendors. Perhaps as a result of its increasing availability, many studies have evaluated the efficacy of UTE for imaging of short T_2 species such as tendons, cortical bone, myelin, teeth and ligaments pre-clinically and clinically at a variety of magnet strengths from 1.5T through 11.7T and has even been combined with ^{31}P imaging to characterize mineral content.[40, 261-264]

For bone, the majority of UTE MR analysis has centered around the T_2 quantification of bone water (total or bulk) and bi-component water populations (describing the T_2 contribution from the bound and free water pools in bone). Bone therapeutics that modulate the non-mineral phase of bone are being identified and UTE has been employed with success in describing the non-invasive alterations to bone water as a result of these therapeutics.[162, 265] One such example is raloxifene, a selective estrogen modulator for the treatment of post-menopausal osteoporosis which works by mimicking the beneficial effects of estrogen in the bone.[124] Unlike bone preserving drugs like bisphosphonates, raloxifene decreases fracture rate with little to no observed improvements in BMD and studies have pointed to a non-cell-mediated increase in bone matrix water fractions to explain this phenomena. [124, 160-162, 266] Allen et al. sought to evaluate bone water *in vivo* through application of UTE to evaluate the bi-component water populations using the T_2 decay in canine bone treated with raloxifene for 6 months or left untreated.[162] Canines were imaged *in vivo* at 3T where cortical analysis demonstrated that raloxifene treatment increased the bound water pool by 14% and decreased the free water pool by 20% compared to vehicle control animals.

UTE applications in bone has progressed to *in vivo* clinical imaging. Work by Techawiboonwong et al. was one of the first to report the efficacy of resolving bone water using UTE *in vivo* at a clinical field strength (3T) with a TE of 70 μs.[267] The authors evaluated bone water (as one contribution, bulk) in the tibia in three patient populations and observed a 135% increase in bone water in patients with renal osteodystrophy compared to pre-menopausal women and a 43% increase compared to post-menopausal women. A hallmark of this work was that there was no statistical difference in volumetric BMD of the renal osteodystrophy group compared to any other group highlighting the utility of MRI to provide bone quality information beyond BMD.

At clinical field strengths, UTE has been successful in resolving the bi-component water populations in bone by directly detecting the T_2 values from bound and free water fractions. [268-270] This is an important consideration as the water fractions could be disproportionately affected due to aging, disease or treatment. Further progressing the *in vivo* UTE work in bone is Rajapaske et al. who demonstrated that pore size information via the cortical bone porosity volumetric map generated using UTE (porosity index, described by Li et al.), validated against CT, could be described in a cohort of postmenopausal women.[271, 272]

The utility of UTE to measure bone collagen has been investigated. In a recent study by Ma et al., it was determined that 3D UTE at 3T could capture both bound and free water protons but was unable to image protons from the collagen pool via freeze dried and D_2O-H_2O exchanged bone tissue studies.[255] Results from the study indicate that protons from the bound and free water are the sole sources of UTE signal and protons of the native collagen molecule are undetectable using UTE. The results were in contrast to findings by Siu et al. where solution of collagen, derived via a food grade bovine hide collagen powder, at varying concentrations were imaged using a spectroscopic technique at 7T, and a fraction of the collagen signal was observed via broadened spectral linewidths.[273] However, the spectral techniques are not compatible with *in vivo* imaging thus effective bone collagen imaging remains to be realized. It is likely that UTE was unable to capture the shortest T_2 in bone coming from collagen (~0.1 ms) due to the short transmit/receive switching time causing the small TE (< 5 ms) that remains inherent to UTE. Collagen bone image analysis should be investigated using ZTE and SWIFT techniques which nearly and totally eliminate the TE, respectively.

Zero echo time imaging

Similar to UTE, ZTE sequences also rely on initiating data acquisition as soon as possible following RF excitation.[274] ZTE works by switching on the readout gradients prior to RF excitation in contrast to UTE where the gradients are switched on following RF excitation (Figure 2.1C). [275] This series of events, in theory, allows the center of k-space to be sampled at an effective TE of zero. Because the hardware still switches from transmit to receive there is still a nominal TE dictated by the transmit/receive deadtime (although much shorter than that of

UTE) and using ZTE, the center of k-space is not actually sampled (instead a minimum k-space radius is acquired). The result is a loss of the first few data points in the specimen's acquisition window, however k-space filling techniques through reconstruction algorithms have been described to recapture or reconstruct the image in the absence of these data.[276-279] Compared to UTE, ZTE is able to achieve a greater signal-to-noise ratio and increase scan time efficiency, but unlike UTE, ZTE can only be acquired in 3D because the frequency encoding gradient is turned on during RF excitation.[280]

ZTE has been employed, *ex vivo* at 7T, to directly depict the microstructure of trabecular bone in a bovine specimen.[281] Comparisons to µCT demonstrated excellent agreement between the two modalities with the bone volume fraction assessed as 0.34 and 0.36 for MRI and CT data, respectively. Weiger et al. demonstrated the utility of ZTE when applying fat, water, and fat and water suppression using a sheep knee joint at 4.7T; with no suppression (thus collecting signal from both short and long T_2 species in the joint) there was little contrast between bone, marrow, cartilage and muscle.[282] When applying simultaneous fat and water suppression, ZTE contrast in the bone was similar to that of µCT. The authors postulate that ZTE MRI may hold the potential to directly determine bone mineral density without the use of ionizing radiation.

Application of ZTE *in vivo* at clinical strengths is not well explored due to the prerequisite of a modified gradient system that has a fast transmit and receive switch rate which is essential in ZTE. A few sites have been able to overcome the hardware restraints and offer insight to ZTE's potential clinical utility in bone. At clinical 3T, Breigner et al. reported that ZTE MRI provided "CT-like" contrast in bone with strong intermodality agreement between clinical (osteoarthritis, Bankart and Hill-Sachs lesions, subchondral cysts) and morphological measures (version, vault depth, erosion) in their patient cohort suggesting the ZTE could be considered in lieu of CT. [283] Wiesinger and Delso et al. have described ZTE in skull imaging and its utility has been further realized by Sekine et al. and others when combined with positron emission tomography (PET) for MRI-PET of the bone.[284-287] Promising work is being conducted to manufacture a gradient system for clinical use that reconciles extreme gradient strength with rapid transmit/receive switching speed that is required for ZTE.[288]

SWeep Imaging with Fourier Transformation

SWeep Imaging with Fourier Transformation (SWIFT) was introduced by Idiyatullin and Garwood et al. in 2006 as a novel fast and quiet MR sequence with a zero effective TE that is sensitive to short T_2 species and even biomaterials.[289] SWIFT is not dictated by the transmit/receive deadtime like UTE and ZTE; instead the SWIFT uses gapping of hyperbolic secant pulses which allows for a simultaneous signal excitation and acquisition which is acquired inside the gaps (Figure 2.1D).[290] The hyperbolic secant pulses supply the large bandwidth that is required to both simultaneously excite the protons during the frequency encoding gradient step all while providing pulse lengths long enough to allow the required gapping. In SWIFT, the gradients are always on and are adjusted during acquisition to radially sample k-space. SWIFT makes use of dummy scans which “force” spins into a steady state making the applications of SWIFT nearly endless. Further, SWIFT is a favorable technique as it is less sensitive to RF field inhomogeneity. The “SWeep” in SWIFT is because the sequence uses swept RF excitation using continuous wave NMR [289] but at a far higher sweep rate. The technique uses radial sampling of k-space and the Fourier slice theorem, or the “IFT”.

Compared to UTE, the broadband excitation pulses in SWIFT allow it to excite very off-resonance isochromats (ensembles of spins experiencing the same field) which means areas where susceptibility differences exist, such as the bone/marrow, bone/air and metal implant interfaces are reduced. Compared to ZTE, there is much less opportunity for lost or misplaced data at the center of k-space due to the gradient switching. The readout gradients in SWIFT do not need to be zeroed between TR therefore SWIFT is almost entirely silent. SWIFT is less taxing on the gradient hardware compared to both UTE and ZTE; however, SWIFT is far more demanding on the RF system due to the fast-switching.

SWIFT has been applied in various applications which require short T_2 species detection such as localizing iron oxide nanopartical (IONP)-labeled stem cells grafted in myocardium, resolving morphological features of human teeth, calcification detection in the brain following injury and detection of breast cancer metastasis to the lung (a short T_2 species). [291-294] Promising to our proposed research, SWIFT enabled the duel assessment of spontaneous chondral (soft tissue) and subchondral (short T_2 species) defect repair in an equine model following 12 months of healing using SNR as a biological outcome. [295] Further and promising was the high correlation between SWIFT-derived and µCT-derived bone volume fractions (r=0.83). Initial proof of concept studies applying SWIFT to detect changes in bone have been favorable. Sukenari and colleagues employed SWIFT, compared to conventional MRI, at 7.4T to probe alterations in *ex vivo* cortical bone following OVX and reported that SWIFT was more sensitive to early post-operative changes using SNR as a biological outcome.[296] Application of SWIFT to diabetes-induced rat model of bone loss demonstrated that excised tibiae scanned with SWIFT and µCT were able to detect cortical bone changes using SNR prior to a decline in BMD detected via µCT. [297] With SWIFT, cancer-induced osteogenesis and osteolytic alterations in bone microarchitecture were detected in tibia of young mice scanned *ex vivo*.[298] The authors describe that with SWIFT, it was possible to gain high-quality and high resolution images of the bone tumor boarders plus the surrounding bone and soft tissues with one rapid scan (78 µm isotropic resolution achieved in 10 minutes) without exposure to ionizing radiation.

Multi-Band SWeep Imaging with Fourier Transformation

In MRI, bandwidth refers to the range of frequencies, measured in Hz, involved in transmit (RF excitation) or receive (signal acquisition) steps. In conventional SWIFT, the transmit bandwidth must match the receive bandwidth which usually ranges from 31-125 kHz. This is because the RF pulse is applied during the readout gradient thus the bandwidth must be broad enough to cover the entire field of view (FOV) at the readout bandwidth. Due to technical constraints on achieving the effectively zero TE, regular SWIFT has an upper limit on bandwidth through coil ring down (time delay following excitation to mitigate receiver overload) and transmit/receive switching time constraints. Lower bandwidths can be problematic when resolving all excited short T_2 signals in the presence of long T_2 signals (common to *in vivo* biological imaging) which can result in off-resonance effects, particularly susceptibility artifact, presenting as blurring in radial imaging. Susceptibility artifact refers to the different magnetic susceptibility in a tissue or implant which cause magnetic field gradients at the interfaces. This is especially prevalent in bone where the cortices have the largest biological pool of strongly diamagnetic calcium salt and share a number of biological boarders with much less diamagnetic tissues such as muscle, fat, marrow and the periosteum; the strong contrast in tissue composition can result in magnetic field distortions.

Typically, susceptibility artifact can be minimized by lowering the TE or increasing the bandwidth but these options are not feasible with SWIFT which already acquires a zero TE and has an inherent upper limit on bandwidth. To address the bandwidth limitation, multi-band SWIFT (MBSWIFT) has been introduced by Idiyatullin et al. in 2015 where the theory behind the sequence can be appreciated in detail. [299] In short, MBSWIFT makes use of sidebands which are generated through gapping the RF pulse. Both regular SWIFT and MBSWIFT excite bands outside of the FOV, but only MBSWIFT makes use of the multiple excitation bands where SWIFT uses the baseband. As a result, MBSWIFT can achieve high excitation bandwidth with increased efficiency (small average power) and in theory, reduce or mitigate the susceptibility at the cortical bone interfaces during *in vivo* imaging. Compared to ZTE sequences achieving a similar resolution, MBSWIFT can include more pulse elements per gradient orientation and allows for an increased flip angle to be utilize at a given RF amplitude. [299]

In the original description, proof of concept images were acquired in the human mandible, compared to ZTE, where a visual reduction in blurring and an increase in sharpness can be appreciated in the MBSWIFT images. [299] MBSWIFT demonstrated a strong decrease in magnetic susceptibility artifact around the materials used for the wire leads (non-ferromagnetic metal) used during deep brain stimulation in rats. [300] Further, MBSWIFT provided contrast in the brain comparable to the current functional MRI gold standard sequence (spin-echo echo planar imaging) while significantly reducing image distortion around the leads. We believe MBSWIFT would have incredible application in bone imaging which has yet to be described. As such, MBSWIFT was utilized in Chapter 5 of this dissertation.

Quantitative magnetic resonance imaging

The development of MRI in the clinical field was first aimed at obtaining suitable images of the anatomical structures and has become known as “conventional” and “qualitative” MRI. Conventional MRI images rely on signal intensity in arbitrary units which cannot be compared across sites or even scanning sessions making quantitative longitudinal analysis of disease progression and drug intervention unfeasible. [301] Furthermore, these conventional MR images are assessed radiographically meaning they are qualitatively interpreted by a radiologist or trainee. Quantitative MRI represents the next step in the evolution of MRI offering a host of information over the purely anatomical assessment of conventional MR. However, quantitative techniques are in their infancy in that they require validation for their prognostic, diagnostic and response assessment value and are not well adopted clinically due to technical hurdles; quantitative MRI techniques require manual or semi-manual segmentation of the region of interest for analysis which can be time consuming and are susceptible to inter- and intra-rater variability. Although not the focus of the dissertation work, efforts to reduce or diminish the time cost of segmentation including description of automated segmentation routines for MR and the use of machine learning are being developed. [302, 303]

Quantitative MRI using mapping techniques has gained considerable interest in the musculoskeletal imaging field for its sensitivity and specificity to macromolecular content such as PG, GAG, collagen and its organization, water exchange, water diffusion and tissue susceptibility in the magnetic field (the measure of the extend a substance becomes magnetized when placed in an external magnetic field, nearly all biological tissues are diamagnetic and have susceptibility). Quantitative MRI mapping is comparable across subjects, imaging sites and time points because measurements are absolute. [304] Quantitative mapping techniques have been explored at length in osteoarthritis; much work has been done to validate the techniques in cartilage at pre-clinical and clinical field strengths. [305-307] But cartilage is but one piece of the musculoskeletal imaging puzzle where the joint is comprised of many short T_2 species such as ligament, tendon, endochondral cartilage and bone. Application of a quantitative MRI technique with a conventional MRI sequence as the readout would not be feasible in these tissues for reasons discussed; thus applying a UTE or ZTE technique as the MR readout sequence is necessary to achieve quantitative MR values in these species.

T_1 relaxation mapping

In MRI, the image contrast is based on spatial variations in T_1 and $T_{2,}$ among other parameters, which reflect molecular properties including chemical state of water and its mobility which in turn reflects the local macromolecular environment. T_1 relaxation times have shown to differ within normal tissue (such as depth-dependently in cartilage) [308, 309] and with disease [310-312] demonstrating promise as a quantitative imaging biomarker for its sensitivity to tissue-specific relaxation properties. It has been suggested that variation in T_1 may reflect the underlying physiology and composition of the mineral phase in bone. [313] When imaging bone using solid state ^{31}P MRI, Wu et al. reported that subtle molecular or crystalline structural differences was observed as large differences in T_1 relaxation values highlighting the discriminating power of T_1 relaxation using ^{31}P MRI.[313]

In addition to the capability of imaging ultra-short T_2 species, SWIFT has the capacity to provide quantitative maps of relaxation constants. With SWIFT, swept radiofrequency excitation drives the spin system into a steady state and equilibrium magnetization can be reached without applied magnetization preparation. When magnetization preparation blocks are embedded within the SWIFT sequence, SWIFT can achieve nearly pure proton density-weighted images, and depending on where the blocks are placed, different kinds of clinically meaningful contrasts can be produced. [289, 314] While magnetization preparation blocks can be used in SWIFT to achieve various contrasts, the image contrast can also be optimized by adjusting the flip angle close to the Ernst angle where signal intensity reaches its peak for a given $T_{1.}$ [289] This provides an opportunity to derive T_1 relaxation maps by varying the flip angle in small steps at and around the Ernst angle, referred to as the variable flip angle (VFA) method. [315] Because SWIFT has almost zero T_2 weighting, the sequence can provide a pure and true T_1 relaxation map and VFA using SWIFT has gained interest.

Wang et al. described the utility of VFA SWIFT in estimating T_1 relaxation values in varying concentrations of aqueous iron oxide nanoparticles in suspension and observed measures were in excellent agreement with spectroscopy. [316] Nissi et al. calculated T_1 relaxation values using VFA SWIFT and an inversion recovery fast spin echo sequence in doped with known concentrations of Gd-DTPA^2 and determined the methods to derive T_1 were in good agreement. Next, the authors evaluated the sensitivity of the methods to detect differences in T_1 between and native and trypsin-treated (to disrupt collagen) bovine cartilage-bone specimens and observed the VFA SWIFT shifted toward a shorter T_1 in the osteochondral specimens reflecting the higher sensitivity to short T_2 spins located at the cartilage/bone junction. [317] In a feasibility study, Sukenari et al. extended the VFA SWIFT method to derive T_1 relaxation times in five excised rat tibiae scanned *ex vivo* at 7.4T where T_1 maps were successfully derived in cortical bone. [318] Building on these works, we sought to apply the VFA method using MBSWIFT *in vivo*. We believe that MBSWIFT's ability to achieve a zero TE coupled with reduced susceptibility artifact at the bone/marrow and bone/muscle borders and inherent insensitivity to motion makes the technique highly desirable for quantification of *in vivo* T_1 values in bone.

Fat fraction mapping and water fraction mapping

In MRI, fat and water protons behave differently resulting in different magnetic properties which can be both visually exploited for qualitative assessment and quantitatively measured using knowledge of their chemical differences in the magnetic field "fat-water chemical shift".[319] Fat are large molecules (compared to water) existing primarily as long chain triglycerides, where triglycerides are the lipid in bone marrow. [319] Fat molecules move slowly in their local microenvironment due in part to this “bulky” composition with the applied external magnetic field. Further, the majority of fat’s hydrogen atoms are located in the long aliphatic side chains near electroneutral carbon atoms (electron clouds) leaving the protons in the fat molecule relatively “magnetically shielded” from the outside externally applied magnetic field. [320] Because of the slow rotation of the fat molecule, fat gives rise to T_1 values which are much shorter than that of water. For example at 1.5 T field strength, fat has an approximate $T_1 \sim 250$ ms while the T_1 of water is ~ 4000 ms. Biologically, fat and water often reside in separate anatomic compartments and can easily be imaged using MRI. However, in structures such as the bone which is made up of fat-containing bone marrow which can change as a function of disease, there is a desire to separate these signals either for contrast enhancement or for quantification. One such method to separate the fat and water components is through “suppression” done by exploiting knowledge of the fat-water chemical shift. [321]

Water molecules contain an oxygen atom which is strongly electronegative which permits the hydrogen nuclei to pull away from the electron cloud through deshielding. The hydrogen protons are exposed to the local magnetic field and resonate faster than the electron cloud-shielded fat molecules creating a difference in resonance frequencies. This difference in resonance frequencies, however, increases with increasing magnetic field strength thus a scaling factor taking into consideration of the changing Larmor frequency must be applied. The difference between fat and water is measured as 3.5 parts per million (ppm or $\times 10^{-6}$). At 9.4T, the field strength used in this work, the fat-water frequency difference is calculated as:

Equation 2.10

$$\Delta f = (400\ \text{MHz})(3.5 \times 10^{-6}) = 1400\ \text{Hz}$$

1400 Hz is thus the frequency distance between the water and fat peak at 9.4T; because fat processes slower than water, the main fat peak is found at -1400 Hz and water at 0 Hz (Figure 2.2). Based on this field strength-dependent value, frequency selective saturation RF pulses can be applied at the frequency of fat to saturate its contribution to the MR signal described in detail by Delfuat et al. [321] An advantage of fat saturation is that it can be applied to any MR imaging technique and effective fat suppression is more achievable at higher field strengths, such as in the present work, where the resonant frequencies are better separated. As such, fat saturation using SWIFT can be obtained by applying a hyperbolic secant (HS4) inversion pulse (1-kHz bandwidth) centered at the fat resonance frequency (-1400 Hz) after every specified *N* views.[289] Similarly, water saturation can be achieved by applying a HS4 saturation pulse at the water frequency.

Biologically, fat cells are both highly dynamic and physiologically active having metabolic, endocrine, haematological and immune roles. Alterations in number and/or size of adipose cells may be directly related to disease and could be related to inflammation and even malignant infiltration in the bone. It has been observed that adipose cells can secrete growth factors and matrix proteins that interact with the skeletal system.[322] The accumulation of fat within an organ or within the bone marrow is known as ectopic fat deposits and there is a growing appreciation for its role in disease pathogenesis.[323] Specifically, bone marrow adipose cells are observed to have a role in regulation of hematopoiesis, bone turnover and metabolism and the alteration/derangement of marrow adipose cells are observed in metabolic bone diseases such as osteoporosis in addition to obesity and diabetes. [213] Through the exploitation of the MRI signal to saturate fat and water, fat fraction (FF) maps, or the proportion of signal derived from fat protons can be calculated and may have a role as a quantitative imaging-based biomarker in bone.[219] The FF can therefore be derived by taking the signal in the image that arises from fat protons divided by the sum of the signal from fat + water protons:

Equation 2.11

$$FF = fat/(water + fat) * 100$$

Similarly, the water fraction (WF) can be exploited by:

Equation 2.12

$$WF = water/(water + fat) * 100$$

where fat is the magnitude of the fat image where water was saturated and water is the water image where fat was saturated. The significance of mapping WF in the cortical bone can be appreciated in the section entitle, “Short T_2 species” in this chapter.

Bone mineral density using magnetic resonance imaging

In contrast to the methods to derive BMD described in detail in earlier in this chapter, 3D MRI may be a valuable tool to derive volumetric BMD while concurrently providing meaningful soft tissue signal. While imaging mineral and other solids is regarded as beyond the scope of conventional MRI, Ho et al. demonstrated the feasibility of conventional proton imaging to compute voxel-wise BMD by exploiting signal intensity. [324] The authors used proton-density weighted in-phase images of water and fat derived from chemical-shift T_{2*}- IDEAL MRI where the fat-water separation was used to compute an inverse BMD measure and results significantly correlated to CT.[324] The calculation method for the author’s BMD measure based on signal intensity is described in detail in Chapter 5 of this dissertation. The advent of phosphorous solid state nuclear MR imaging (P^{31}) have allowed for the direct signal from phosphorous making MRI-derived BMD calculations a possibility. [261, 313] However P^{31} MRI is even more limited in spatial resolution because of the lower gyromagnetic ratio associated with the phosphorous molecule. We believe ZTE MRI as such, could be used in place of phosphorous imaging to directly resolve BMD using CHA phantom standards (Chapter 5).

Conclusions

As such, characterization of disease progression and treatment efficacy for metabolic bone diseases is complicated by the lack of imaging modality able to safely monitor material-level and biochemical changes *in vivo* without the use of ionizing radiation. To improve upon the current bone imaging landscape and the near ubiquitous reliance on x-ray based BMD, we tested the efficacy of a 3D ZTE-MRI approach, MBSWIFT, in an estrogen-deficient (OVX) model of osteoporosis during growth in Chapter 5 of this thesis. Here we describe the utility of MBSWIFT to characterize not only the mineral phase of bone, but additional material-level bone components which contribute to overall bone quality.

Figures

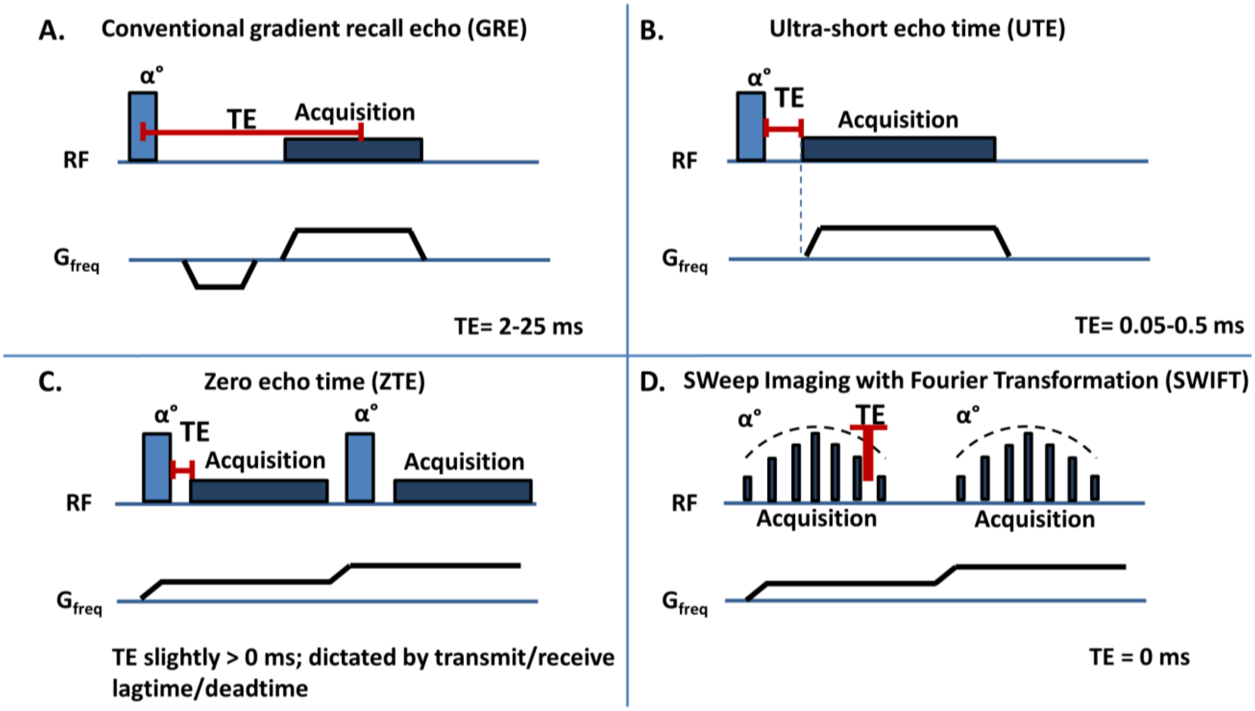

Figure 2.1: Simplified pulse sequence diagram.
Diagram emphasizes echo time (TE) for A.) conventional gradient recall echo (GRE) sequence, B.) ultra-short echo time (UTE) sequence, C.) zero echo time (ZTE) sequence and D.) SWeep Imaging with Fourier Transformation (SWIFT). RF= radiofrequency; G=gradient and α° denotes the flip angle of the RF excitation pulse.

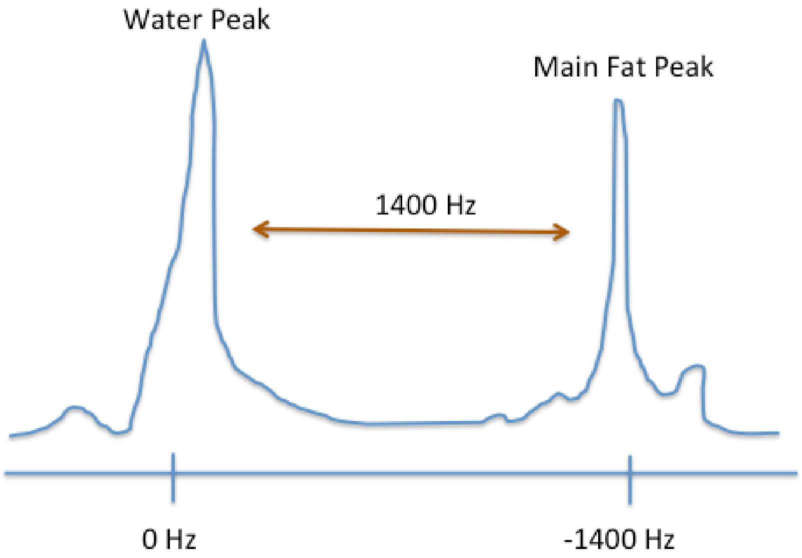

Figure 2.2: Schematic of water and fat peaks acquired at 9.4T.
The fat-water chemical shift is found to be 1400 Hz based on the Larmor frequency of 400 MHz at 9.4T field strength.

Tables

Table 2.1: T_2 relaxation times for musculoskeletal tissue.

Musculoskeletal Tissue	Approximate T_2 Relaxation Time (ms)	Refs
Cartilage	10-35	[325-327]
Endochondral Junction	2-9	[327]
Tendon	1-2	[328-330]
Meniscus	5-11	[331, 332]
Temporomandibular Disc	8-28	[333]
Cortical Bone	0.2-0.8	[268]
Periosteum	5-11	[41]
Free Water	>1	[334, 335]
Bound Water	0.3-0.4	[334, 335]
Collagen	0.1	[40, 273]
Dried Cortical Bone	0.22	[268]

Chapter 3 Gene Expression Profile and Acute Gene Expression Response to Sclerostin Inhibition in Pediatric Osteogenesis Imperfecta Bone

Introduction

Osteogenesis imperfecta (OI) is a rare and severe congenital bone dysplasia characterized by low bone mass and poor bone quality with increased pathological fracture risk. [1] OI is both genetically and clinically heterogeneous; the bone dysplasia can currently be categorized into 18+ genetically unique types ranging in severity from mild forms with minor skeletal clinical manifestations to perinatally lethality. [3, 56, 336] Further complicating the disease are the different possible modes of inheritance (dominant, recessive or X-linked gene mutations) and variability associated with the affected genetic loci resulting in the range of phenotypic presentation. [337] Further, patients with the same OI-causing mutation can present with different clinical phenotypes. [4] In up to 85% of cases, OI is caused from a mutation in the *COL1A1* or *COL1A2* gene encoding the α1 or α2 chain of type I collagen respectively, resulting in an underproduction of normal collagen or secretion of defective collagen chains depending on the mutation. [63, 64, 338] Further modifications due to glycine substitutions in the Gly-X-Y collagen repeat in the *COL1A1* or *COL1A2* gene have been observed which result in moderate-to-severe phenotypic forms of OI from the structural defect in the collagen triple helix. [338] More recently, other genes localized in the matrix, endoplasmic reticulum (ER), ER-golgi, and nucleus have been identified in the pathogenesis of OI and make up the remaining 15% of cases. [3, 63, 67-69, 87, 339-345] This spectrum of genotype-phenotype variability has made both diagnosis and management of the disease challenging; as such, no cure for OI exists, there is no

United States Food and Drug Administration or European Medicines Agency approved pharmacological treatment and consensus on an appropriate treatment strategy has yet to be identified. [55, 346]

Pharmacologic treatment strategies for OI have evolved from approaches developed to treat osteoporosis, a metabolic bone disease. These strategies which aim to elicit an increase in bone mass, improve architecture and decrease fracture risk often result in a variable clinical response when applied to OI. Current clinical pharmacological approaches to manage OI relies on anti-resorptive bisphosphonates, yet bisphosphonates have demonstrated variable patient outcomes depending on OI phenotype, severity and bone site. [6, 70] Further, long-term bisphosphonate use in pediatric OI is a concern due to its suppression of bone turnover and the drug's long half-life which leads to long-term residence in the bone. [73] Inconsistent clinical pediatric OI results have also been reported with Denosumab, a RANKL inhibitor, and concerns regarding hypercalciuria development during active therapy observed in pre-clinical studies have limited its clinical use. [77, 79, 80] More recently, bone-forming sclerostin antibody (SclAb) has emerged as a promising alternative or adjuvant to existing therapies and acts by inhibiting sclerostin, a negative regulator of bone formation. SclAb has elicited significant increases in bone mineral density (BMD) and quality during clinical trials for post-menopausal osteoporosis [13, 85] and stimulated markers of bone formation, reduced resorption and increased lumbar spinal areal BMD in adults with moderate OI (limited to type I, III, or IV). [21] Despite these findings, effects in the pediatric OI population and across all OI types remain unknown. Different OI phenotypes appear to respond differently to therapies. Pre-clinically, the bone-forming response to SclAb has varied in magnitude from strong in the moderate knock-in Brtl+/- murine model, moderate in the recessive severe Crtap$^{/--}$ murine model, and a lesser bone-forming response in the dominant severe Col1a1$^{jrt/+}$ murine model. [15-18, 20] Therefore, factors that contribute to the heterogeneity of the disorder, including skeletal morphology and individual patient gene expression profile may play an important role in the patient's response to therapy.

Understanding the transcriptional response to treatment in the diseased target tissue is of great interest. Gene expression response following SclAb treatment has been reported rat models of post-menopausal osteoporosis and in female Balb/c mice, [347-350] highlighting the unique signaling events and compensatory response occurring in the osteoblast lineage as a result of SclAb. However, patterns of gene expression response due to treatment in human OI bone tissue remains unknown and difficult to assess clinically. We sought to evaluate gene expression profiles in native pediatric OI bone tissue and describe the acute gene expression response to SclAb treatment across OI patients with severe and moderate phenotypes. We explore how the patient's untreated cellular condition and the bone's baseline morphological phenotype contribute to treatment response during acute sclerostin inhibition.

Materials and Methods

Study design

Seven pediatric OI and five pediatric non-OI patients undergoing surgical orthopaedic intervention were recruited for this Institutional Review Board-approved study and informed consent was obtained from the subject and/or legal guardian. Detailed patient demographics including OI type and bone harvest location can be appreciated in Table 3.1. Native bone typically discarded as surgical waste was collected immediately to media (αMEM/10% fetal bovine serum (FBS)) and placed on ice for experiment preparation. Patient bone tissue was divided into a Falcon 12-well microplate (Corning Inc., Corning, New York) with each well containing 3 mL of media and maintained in culture at 37°C. Each well contained one solid bone isolate ~2 mm^3 in size and each patient yielded up to 14 usable bone isolates (Table 3.1**).**

Prepared bone was randomly assigned to an untreated (UN), treated with a low dose of SclAb (TRL, 2.5 µg/mL), or treated with a high dose of SclAb (TRH, 25 µg/mL) condition. Each patient had enough bone tissue to repeat each UN, TRL, TRH condition 2-4 times. Wells containing tissue and media were dosed directly with SclAb on days two and four and all samples were removed on day five to 1 mL of TRIzol reagent (Invitrogen, Carlsbad, CA) and kept at -80°C until RNA isolation occurred. For all conditions, media was changed on day two and four immediately prior to treatment. One bone sample from each patient was fixed immediately in 10% neutral buffered formalin (NBF) for 24 hours, decalcified in 10% ethylenediaminetetracetic acid (EDTA) for 15-20 days, paraffin processed and stained with hematoxylin and eosin (H&E) to determine bone morphology using established procedures. [351] A detailed schematic can be appreciated in Figure 3.1A.

A subset of bone tissue from patients OI3, OI4 and OI6 were collected to media and immediately implanted subcutaneously on the dorsal surface of an athymic mouse representing our xenograft model to evaluate the effects of SclAb in a host-derived system more closely recapitulating the *in vivo* microenvironment (Figure 3.1B). Fourteen bone samples in total were implanted and mice were randomly assigned to an untreated or SclAb treated group. Treatment was administered to the host (mouse) subcutaneously at 25 mg/kg, two times a week for either 2 or 4 weeks where the mice were euthanized. All mice received calcein (30 mg/kg, intraperitoneal (i.p.) injection), administered seven days before sacrifice and alizarin (30 mg/kg, i.p.) administered one day prior to sacrifice, to follow new bone formation. Implanted mice underwent µCT imaging (Bruker Skyscan 1176, Bruker BioSpin, Belgium) 24 hours following implantation and immediately following euthanasia using an X-ray voltage of 50 kV, current of 800 uA and a 0.5 mm aluminum filter. Scans were reconstructed at an 18 µm isotropic voxel size and calibrated with the use of two manufacturer provided hydroxyapatite standards. The bone implant was manually segmented followed by a series of several automated processes so that only implant was extracted and analyzed for longitudinal changes (presented as a percent change from pre- to post- scans) for bone surface (CTAn Version 1.15.4.0, Bruker Biospin, Belgium). Following imaging, OI bone tissue implants were removed from the host and plastic processed for histomorphometric analysis using standard laboratory procedure. All experimental animal procedures were approved by the University of Michigan Committee for the Use and Care of Animals.

Bone tissue preparation and RNA extraction

Total RNA was extracted from each bone isolate by first pulverizing each bone in 1 mL TRIzol using a high-speed tissue homogenizer (Model 1000; ThermoFisher Scientific). Each bone isolate underwent three 20-second cycles of homogenization and was placed on ice between cycles. The bone's total nucleic acid content was isolated using 0.2 mL of 24:1 chloroform:isoamyl alcohol per 1 mL of TRIzol, centrifuged at 12000 g for 15 minutes at 4°C where the supernatant containing the RNA fraction was removed by pipetting. RNA was then purified using the RNeasy Mini Kit (Qiagen, Valencia, California) followed by DNA digestion with an RNase-Free DNase Set (Qiagen) using manufacturer provided instruction. Finally, total RNA was eluted in 30 µL of RNase-free water. For quality control, RNA concentration extracted from each bone isolate was determined using NanoDrop 2000 (ThermoFisher Scientific) followed by assessment of RNA quality using a bioanalyzer (Model 2100, Pico Kit; Agilent Technologies, Santa Clara, California) to generate an RNA integrity number (RIN). In order to maximize nucleic acid content from each patient condition, RNA from each well condition (UN, TRL, TRH) per patient with an RNA integrity number (RIN) number of 5.5 or greater were pooled to yield 200 ng per condition and a new concentration value was determined using the NanoDrop. The RIN number of 5.5 was chosen due to the rarity of the human tissue and few samples did not meet this threshold; two non-OI and four OI bone samples had RIN values below 5.5 and were excluded from analysis and not pooled as they did not meet our quality standard for the study. The average RIN number was 8.8; pooled non-OI patient bone RIN values ranged from 6.3-10 and OI patient bone from 6.7-9.9. Extracted RNA was stored at -80°C until further processing.

TaqMan qPCR analysis

The expression levels of 10 genes related to the canonical and non-canonical *Wnt* signaling pathway and one endogenous control were quantified using TaqMan quantitative real-time polymerase chain reaction (RT-qPCR) (Table 3.2**)**. Specifically, downstream *Wnt* targets (*WISP1*, *TWIST1*), inhibitory regulators of bone formation (*SOST*, *DKK1*), markers of osteoblastogenesis (*SP7*, *RUNX2*), osteoblast markers (*BGLAP*, *COL1A1*), and markers of osteoclast differentiation and activity (*OPG*, *RANKL*) were evaluated. The panel represents a subset of markers in the bone remodeling cycle many of which have been identified as key targets for SclAb therapy in prior animal studies.[347-349, 352] Due to the rarity of the OI bone tissue and the size of the available harvested bone (which affected the amount of total nucleic acid we were able to extract), we chose to analyze only one housekeeping gene (*HPRT1*), which has documented in the literature as a stable gene across experimental conditions in human bone studies. [353, 354]

Pooled, purified RNA samples underwent reverse transcription using qScript cDNA SuperMix (Quanta Biosciences, Gaithersburg, MD) followed by thermocycling (C1000 Thermal Cycler, Bio-Rad Laboratories, Hercules, California) according to manufacturer recommendations. TaqMan Gene Expression Master Mix (Applied Biosystems) was combined with cDNA and validated TaqMan primer (Applied Biosystems, Foster City, California) and loaded into a 96-well microfluidic array card (Applied Biosystems, Foster City, California). Each array card permitted for two patients' (one OI, one non-OI) samples (UN, TRL, TRH, each) and five primers plus the housekeeping primer simultaneously with twelve array cards in total evaluated. All reactions were run in duplicate and a no-template control and no-reverse transcription control were utilized. Array cards were centrifuged at 4°C (Legend XTR (with custom TaqMan array card bucket); Sorvall, Waltham, Massachusetts), sealed and ran in accordance to recommendations from the manufacturer.

Amplification plots were generated and expression of *SOST, DKK1, COL1A1, BGLAP, OPG, RANKL, RUNX2, TWIST1, WISP1*, and the housekeeping gene *(HPRT1)* were quantified. For cellular untreated analysis to understand phenotypic expression levels and treatment response analysis, baseline and threshold settings were adjusted to obtain an accurate threshold cycle (CT) that was standard across all patients (OI 1-7 and non-OI 1-5) and conditions (UN, TRL, TRH) per each individual gene of interest. Comparative CT method (ΔΔCT) was used to calculate fold change expression levels by normalizing data to endogenous *HPRT1* by averaging the duplicates of the gene of interest and the duplicate of the housekeeping gene for each patient per condition.[355] Experiments in which duplicate reactions deviated by four or more cycles (CT) were deemed a failed reaction due to technical error and thus excluded.

The individual OI patient UN condition was normalized to the average non-OI UN condition (control) to quantify variability in untreated gene expression and describe genotypic variability present among OI patients irrespective of OI clinical phenotype. We then quantified the individual patient response to SclAb by normalizing each individual patient's treatment condition (TRL, TRH) to that patient’s untreated condition to assess treatment response variation among individual patient tissue. Next, we evaluated the response to SclAb by clinical phenotype by averaging the treatment condition (TRL, TRH) normalized to the average untreated condition within each OI type (Type III, Type III/IV, Type IV). Finally we normalized each mean treatment condition (TRL, TRH) within OI type to the mean untreated non-OI control allowing observations on whether SclAb treatment returned gene expression to non-OI untreated control levels.

Statistical analysis

All data were analyzed using GraphPad Prism v7 (GraphPad Software, La Jolla, California). Gene expression results are shown as mean ± standard error of the mean (SEM). Differences in individual OI untreated gene expression, individual OI treatment response and mean treatment response within OI type were statistically evaluated via a paired t-test using the respective ΔCT values as described in detail by Yuan et al. [356] A two-way ANOVA (non-repeated measures) with patient type (OI Type III, OI Type III/IV, OI Type IV or Non-OI) and treatment (UN, TRL, TRH) as factors was used to determine differences in treatment response to SclAb by patient group. Follow-up Dunnett’s post-hoc analysis was used where appropriate in order to compare average OI patient condition outcomes back to the average non-OI untreated controls. TaqMan probes have validated amplification specificity, sensitivity and efficiency; as such fold changes from the TaqMan assays (up or down) of 1.5 or greater that were identified as being statistically significant ($p < 0.05$) via paired t-test or two-way ANOVA met our criteria for denoting differences in gene expression levels. [357]

Results

Bone samples harvested from OI patients were of cortical and trabecular origin, while harvested non-OI bone, derived from tibial reamings during anterior cruciate ligament (ACL) reconstruction, were morselized (Figure 3.2).Patient bone yield varied, ranging from 5-14 usable samples; patients with lower sample yield ultimately resulted in lower nucleic acid concentration which did not allow the evaluation of all conditions and/or all genes of interest. For these patients, an abbreviated panel of genes were evaluated or the TRL condition was omitted. When a gene or condition was omitted, missing fold-change values were denoted herein by “insufficient nucleic acid content” in the figures where appropriate.

Untreated gene expression was heterogeneous among OI patients

Untreated expression levels for all ten genes in each individual OI patient normalized to the average untreated non-OI control condition was conducted to understand genotypic variability among OI patients. Untreated expression varied among the OI patients regardless of bone morphological or Sillence type Figure 3.3. OI bone generally demonstrated lower expression of downstream *Wnt* targets (*WISP1, TWIST1*). Inhibitory regulators (*SOST* and *DKK1*) were variable between OI. *SOST* expression for patient OI1 was significantly greater compared to non-OI controls (+5.54 fold difference). Osteoblast marker genes (*SP7, RUNX2*) and osteoblast progenitor marker genes (*BLGAP, COL1A1*) were heterogeneous among OI patients and were generally expressed below non-OI levels with some exceptions. Patient OI5 (Type III/IV OI) demonstrated both high levels of inhibitory regulator *DKK1* and osteoclast precursor *RANKL* and high expression levels of osteoblast and progenitor (*SP7, BGLAP*) markers well above both non-OI controls and OI patients.

Individual OI patient response to SclAb varied in magnitude

Individual patient response to SclAb was evaluated using a low and high dose to understand response variability among patients. Differences in treatment response among OI patients can be appreciated in Figure 3.4 where significance within each patient between conditions (UN, TRL, TRH) is denoted by stars and brackets. SclAb induced an upregulation in downstream *Wnt* targets (W*ISP1, TWIST1*) and an upregulation (compensatory response) in inhibitory regulators (*SOST, DKK1*). The greatest magnitude of upregulation was observed in treated OI cortical-derived bone tissue (OI2, OI3, OI6) for these targets. A bone-forming response to treatment observed by an upregulation of osteoblast activity was observed in nearly all OI patient samples regardless of bone type (trabecular, cortical) or OI Type (III, III/IV). For *SP7*, treatment response was improved (through a greater upregulation) using the TRH dose compared to the TRL. For *RUNX2*, *BGLAP* and *COL1A1*, a dose dependent effect was less pronounced among OI patients in these osteoblast-related genes.

Response to treatment appeared related to untreated gene expression levels

Patient's untreated gene expression appears to influence the magnitude of response to SclAb treatment, specifically for osteoblast and osteoblast progenitor genes *COL1A1*, *RUNX2*, *SP7* and *BGLAP* (Figure 3.5). Data suggests that patients with the highest untreated osteoblast expression were least responsive to the acute SclAb treatment. This can be appreciated in the case of patient OI2 with high untreated expression of *SP7* (Figure 3.3) and down regulation (TRL) and nominal upregulation (TRH) with SclAb treatment (Figure 3.4). A similar observation was made in patient OI5 for *BGLAP* and patient OI1 for *RUNX2* and *COL1A1* genes (Figure 3.3 and Figure 3.4). The converse was true; patients with low untreated expression were the most responsive in bone formation markers to SclAb treatment (Figure 3.5). This can be appreciated in patients OI3, OI6 and OI7 who had the lowest untreated expression of *SP7* (Figure 3.3) and the greatest magnitude of upregulation with SclAb treatment (Figure 3.4). This observation was true regardless of dose for patient OI3 and OI6 and for low dose (TRL) for OI7. Similar observations were made for patient OI7 for genes *RUNX2, BGLAP*, *COL1A1* and for patient OI5 for *RUNX2* and *COL1A1* (Figure 3.3 and Figure 3.5). Further, individual patients with low untreated expression of downstream *Wnt* target *TWIST1* and inhibitory regulators *DKK1* and *SOST* relative to the untreated average non-OI controls demonstrated the largest magnitude of upregulation following SclAb treatment. The increased compensatory response with of inhibitory regulators *DKK1* and *SOST* with treatment in patients OI3 and OI6 correlated with low untreated expression of these targets (untreated expression Figure 3.3, treatment response Figure 3.4).Conversely, high untreated expression for these same genes demonstrated a moderate-to-low treatment response with SclAb (patient OI5, Figure 3.3 and Figure 3.4) compared to other OI patients with more moderate-to-low untreated expression levels.

Response to SclAb was also differential by patient's clinical Sillence type classification

Next, mean SclAb treatment response was stratified by the patient's clinical Sillence classification by averaging the gene expression data from OI Type III, OI Type III/IV and OI Type IV patients, respectively (Figure 3.6). Gene expression response to SclAb was heterogeneous among clinical OI phenotypes. OI Type III patients demonstrated a greater upregulation in *TWIST1*, *BGLAP* and *RUNX2* with treatment while OI Type III/IV had a greater magnitude of upregulation for *WISP1*, *SOST* and *COL1A1*. OI Type IV patients demonstrated the greatest upregulation in *DKK1*, *SP7* and a comparable response in *BGLAP* for OI Type III patients. There was no statistical significance reached in gene expression response within OI type.

Results from two-way ANOVA (non-repeated measures) and follow-up Dunnett's post-hoc testing for each gene of interest comparing average treatment condition (UN, TRL, TRH) within patient OI type (Type III, Type IV, or Non-OI) normalized to average non-OI untreated condition can be appreciated in Figure 3.7A-B. Results revealed a significant effect of patient type for downstream *Wnt* target *TWIST1*, inhibitory regulators *SOST* and *DKK1* and osteoblastogenesis marker *RUNX2*. Additionally, a significant effect of treatment and a significant interaction between treatment and OI patient type was observed for *SOST* (Figure 3.7A). OI Type III patients were the only patent conditions which differed significantly from the non-OI untreated controls following SclAb treatment (Figure 3.7B). Specifically, following treatment OI Type III patients had a significantly greater upregulation in *TWIST1* (TRL and TRH), *SOST*, (TRL and TRH), and *DKK1* (TRL) above non-OI untreated control levels. Following acute SclAb treatment, osteoblast and osteoblast precursor markers of *SP7*, *RUNX2*, *BGLAP* and *COL1A1* were upregulated to- or above non-OI untreated control levels in patients with type III OI.

In vivo treatment confirmed a bone forming response to SclAb

The subset of OI bone tissue from patients OI3, OI4 and OI6 implanted into our xenograft model demonstrated increases in µCT measures of percent change bone surface (BS) following SclAb treatment at 2 (OI3, OI4, OI6) and 4 weeks (OI4) (Figure 3.8A). Two week treated implants demonstrated the most robust increase in bone surface (+ 29%) followed by four weeks of treatment which increased on average by +12%. Untreated implants demonstrated a mean -3% decrease in BS following the implantation duration at two weeks and a slight increase (+10%) following untreated implantation at four weeks. Histomorphometry corroborated µCT findings. Implants following two and four weeks of treatment demonstrated robust calcein and alizarin fluorochrome labeling compared to the untreated implants which had minimal non-specific calcein labeling only (Figure 3.8B).

Discussion

In this study we explored the impact of genotypic patient diversity to bone-forming SclAb in native OI patient bone cells within their native extracellular environment using a panel of 10 key *Wnt*-related bone targets. Gene expression was heterogeneous across untreated conditions both between and within the patient's phenotypical clinical classification. Acute SclAb treatment induced upregulation of osteoblast activity in nearly all OI patients regardless of bone origin (trabecular, cortical) or OI Type (III, III/IV, or IV) but varied in magnitude. When the average condition response by OI type was normalized to the average non-OI untreated controls, SclAb upregulated osteoblast marker and progenitor genes in OI Type III patients to- or above non-OI untreated control levels. Acute inhibition of sclerostin induced an upregulation of inhibitory regulators (*SOST, DKK1*) similar to prior reports in animal models treated with SclAb. The patient's untreated gene expression appeared to influence the magnitude of response to SclAb treatment, specifically for osteoblast and osteoblast progenitor genes *COL1A1*, *RUNX2*, *SP7* and *BGLAP*. We observed that OI patients with low untreated expression of a gene targeted by SclAb generally demonstrated a greater magnitude of response (upregulation) with treatment. Conversely, patients with higher untreated gene expression elicited moderate to minimal upregulation with sclerostin inhibition. Gene expression at the time of treatment may provide new insights in predicting treatment response and guide clinical decision making in OI.

Our findings in human pediatric OI tissue share similarities with studies monitoring gene expression treatment response to SclAb in animal models of bone loss. Nioi et al. evaluated expression changes in 84 confirmed canonical *Wnt* target genes in OVX rats treated with SclAb and reported significant upregulation in a focused set of *Wnt* targets: *Wisp1*, *Twist1*, *Bglap*, *Gja1* and *Mmp2*. The authors reported the most consistent SclAb treatment response was observed in the *Wisp*/*Twist* cluster. [349] In our work, SclAb induced an upregulation of *WISP1* and *TWIST1* with the strongest response in OI Type III patients and patients demonstrating low untreated expression in the *WISP*/*TWIST* cluster. *WISP1* and *TWIST1* hold important roles in modulating osteogenesis and cell function. *WISP1* has been described to act as a negative regulator of osteoclastogenesis and its upregulation following SclAb treatment may point to its proposed anti-resorptive effects. [358] While *TWIST1*'s function is not as well defined, the gene is thought to serve as a negative regulator of *RUNX2* and an upregulation in *TWIST1* is suggestive of *RUNX2* inhibition (a marker of bone formation). [359] Supporting *TWIST1*'s proposed role, Patient OI1 demonstrated a large upregulation in *TWIST1* and a concurrent downregulation of *RUNX2* with treatment (Figure 3.4). It has additionally been proposed that *TWIST1* may be responsible for the inhibition of osteoblast apoptosis by suppressing *TNF-α* but *TNF-α* was not quantified in the present study. [360]

SclAb stimulates a rapid increase in bone formation in preclinical models [15, 17, 361, 362] and increases markers of bone formation, increases BMD, [12] decreases vertebral fracture risk [13] and increases trabecular and cortical bone mass [11] in patients with low bone mass. Nioi et al. observed that *Bglap* and *Col1a1* were significantly upregulated in osteoblast lineage cells following one dose of SclAb in an OVX rat model, indicating that the bone forming response at the gene level can be both acute and robust. [349] In our short-term treatment scheme using human bone isolates, our results are supportive of Nioi et al. and others where we observed that SclAb treatment elicited an early bone-forming response through upregulation of *COL1A1* and *BGLAP* in nearly all treated OI patient tissue. [349, 352, 363] This upregulation following short-term treatment reflects initial stages of bone anabolism consistent with an eventual increase in osteoblast differentiation. Taken together with the *WISP1* upregulation, a negative regulator of osteoclastogenesis, our results in human tissue suggest an increase in bone forming activity and evidence of a concurrent decrease in resorptive activity. We observed an upregulation in *RANKL* (albeit slight) and down regulation in *OPG*. These results align with Stolina et al. where no changes in *Rankl* or *Opg* were observed following SclAb treatment in aged OVX rats. [350] However, Stolina et al. evaluated *Rankl* and *Opg* expression following long-term treatment, not short-term as in the present study, where treatment-induced bone forming gains may have begun to attenuate as previously described. [361, 364, 365] Alternatively, it is possible that the inconsistent results in our *in vitro* model compared to animal models treated with SclAb may be due in part to the unloaded condition experienced during culture which may have led to *RANKL* upregulation.[366] We acknowledge, however, that the OI condition may also mirror disuse. Future studies could evaluate the *in vitro* treatment response in human OI tissue under *in vitro* loading conditions in order to induce mechanotransduction in the bone to determine the impact on *RANKL* and *OPG*. [367]

Following long-term SclAb treatment, bone formation begins to attenuate or decrease, suggesting a period where the bone begins to self-regulate the anabolic action. [348, 361, 363-365] It has been proposed that the dampening effects following long-term SclAb treatment may be due to a large and acute upregulation in inhibitory regulators of bone formation (*SOST*, *DKK1*). [347] We observed a similar upregulation of *SOST* and *DKK1* with SclAb treatment. A similar upregulation of a compensatory response to sclerostin inhibition has been reported in OVX rats and female Balb/c mice treated with SclAb. [347-350] Like our study, this compensatory response has been documented in the acute phase of treatment with significant upregulation observed following a single dose of SclAb. [347] Because SclAb acts to prevent the interaction of sclerostin with LRP5, not by blocking the production of sclerostin, it has been suggested that a signaling event may occur to increase secretion of sclerostin following the initial blocking of LRP5 binding. [8] This event may lead to an increase in inhibitory regulators leading to the observed compensatory upregulation in *SOST* and *DKK1* we observed in order to regulate the concurrent early bone-formation gains.

While SclAb elicited increases in osteoblast and osteoblast progenitor markers and increases in inhibitory regulators in our OI patient tissue, the magnitude of this response varied across patients. Variability in treatment response has been observed clinically with no clear causation documented and no metric to predict which patients will positively respond to a therapy and which patient will require a completely different treatment approach to mitigate the effects of the disease. OI type, phenotypic severity and age provide valuable guides when determining a treatment plan but identification of factors that contribute to differential treatment response would be advantageous. For example, following two years of Pamidronate treatment in children with Type III and Type IV OI, Zacharin et al. reported no statistical correlation in age, phenotypic severity, or predicted collagen mutation on treatment response. [70] While nearly all patients in the study demonstrated improvements in BMD, magnitude of BMD gains differed between and within patients of the same OI type. We demonstrated that SclAb response statistically differed between OI Type (III, IV, III/IV) in key inhibitory genes (*SOST, DKK1, TWIST1*) and for osteoblast markers (*RUNX2*). Specifically, patients with OI Type III, considered the most severe form of children who survive through the neonatal period, demonstrated the greatest upregulation in these markers with treatment. It is understood that severity of the disease can vary within OI type. When treatment response was evaluated between individual patients, the magnitude of response differed *within* patients of the same OI classification suggesting factors beyond phenotype may be responsible for differential treatment response.

We postulate that the patient's genetic expression/cellular phenotype at the onset of treatment may hold valuable, predictive information regarding treatment response. When normalized to the average non-OI untreated control, we observed a differential expression in all genes evaluated among the seven OI patients. This variability in the untreated condition was present irrespective of OI type or bone origin. Interestingly, when OI patient tissue was treated with SclAb, untreated expression of bone formation markers appeared to impact the magnitude of response during our short-term treatment *in vitro*. Bone with the lowest relative untreated expression of osteoblast and osteoblast precursor markers *SP7*, *RUNX2*, *COL1A1* and *BGLAP* were particularly impacted demonstrating the greatest upregulation following treatment. The converse was true; patients with a high relative untreated expression of these markers, indicative of a bone forming response, were only moderately upregulated when treated with SclAb. From our results, we postulate that there is an upper limit for eliciting an early/rapid bone response with SclAb which is perhaps attributable to 1) the amount of available mesenchymal stem cells (MSCs) and quiescent bone lining cells [363, 368, 369] and 2) the available bone surface area for which osteoblasts can differentiate. We can reason that patients with high expression levels of osteoblast markers and osteoblast progenitors have "little room" for further formation where further minimal upregulation was observed. Second, there is a finite bone surface area in which SclAb can induce bone formation (without the use of co-treatment of bisphosphonate, for example [370, 371] and perhaps a maximization of bone forming surfaces in the sample had already occurred, further limiting bone response. Supportive of this reasoning, trabecular-derived bone (which inherently contains a greater MSC population and has more surface area compared to cortical-implants) demonstrated a greater capacity for acute response (upregulation in osteoblast markers and precursors) and demonstrated the greatest increase in µCT-derived bone surface when treated in our xenograft pilot. Future work should further evaluate these potential factors and their role in determining the magnitude of treatment response.

The *in vitro* environment provides a safe and reductionist method to evaluate human tissue response to SclAb but the environment is limited in both biokinetic and metabolic factors inherent to the *in vivo* environment. Through a proof of concept pilot, we extended treatment to human bone from three OI patients *in vivo* using a xenograft model to evaluate the bone forming response to SclAb in an environment that more closely recapitulates the patient environment. We implanted both cortical-derived (patient OI3 and OI6) and trabecular-derived tissue (OI4) and observed a greater magnitude of response to SclAb in trabecular-derived implants following two weeks of treatment in both µCT and histomorphometry outcomes. For patient OI4, trabecular-derived implants, this response appeared to attenuate following four weeks of treatment where µCT changes measured from pre- to post- treatment decreased in magnitude compared to the two week treated implants from the same patient. Because of the limited bone tissue we received from patients OI3 and OI6, we did not allocate tissue to the four week treated time point (instead, using the tissue for *in vitro* analysis), so we did not evaluate treatment response in the cortical implants at four weeks. Prior evaluation of this xenograft model in our lab demonstrates that cortical-derived bone with minimal human marrow cells at the time of implantation requires longer implantation duration to elicit a bone-forming response (data not shown). When the parallel cortical-derived bone tissue from patient's OI3 and OI6 were treated acutely *in vitro*, we did observe an upregulation in osteoblast markers (particularly *SP7*) and an upregulation (compensatory response) in inhibitory regulators *SOST* and *DKK1* indicating a treatment response. We believe the in vivo treatment duration for these cortical-derived implants may have been too short (two weeks) to induce an analogous gene expression response to what was observed *in vitro* in this cortical bone tissue. Future analysis using the proposed xenograft model should evaluate gene expression response analogous to the panel reported in the present study to determine the effects of SclAb in the host-derived microenvironment in comparison to the *in vitro* response.

Conclusions

Using solid tissue isolates from human OI bone patients culture *in vitro*, SclAb activates downstream *Wnt* targets of *WISP1* and *TWIST1* and induces a compensatory response in *SOST* and *DKK1* expression, consistent with pre-clinical studies of ovariectomized rats and *SOST* and *DKK1* in female Balb/c mice. In all patient samples, a bone-forming response to treatment was observed but the magnitude of this response was variable. While OI type and bone origin (cortical, trabecular) were influential in response, the level of untreated gene expression appeared to greatly influence the magnitude of response to SclAb in native human OI bone tissue. Clinical heterogeneity is a hallmark of OI; understanding a patient's genetic, cellular and morphological bone phenotype may play a crucial role in predicting treatment response and could help guide clinical decision making.

Figures

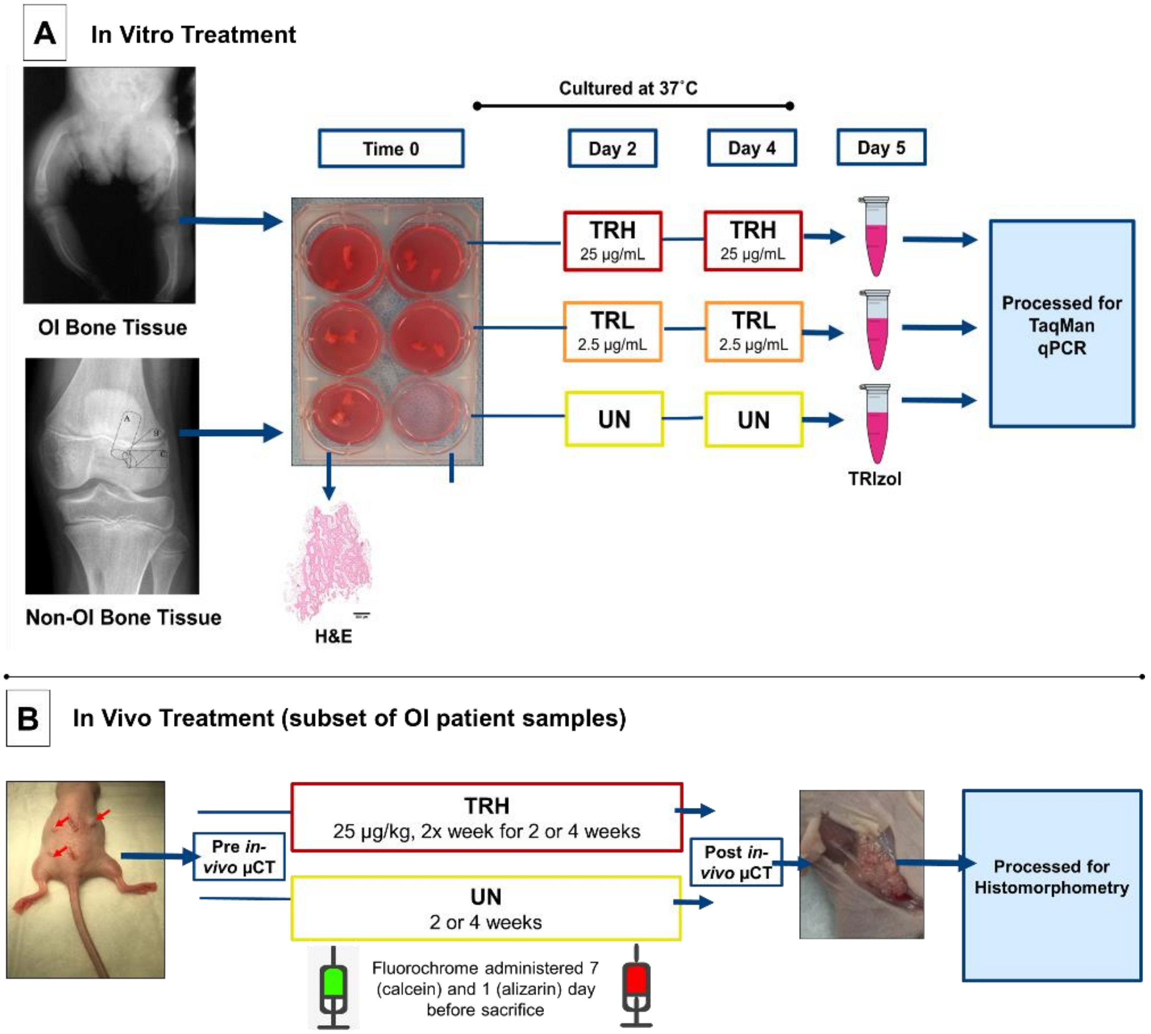

Figure 3.1: Study schematic.

A) Cortical and trabecular bone samples (~2 mm^3) from osteogenesis imperfecta (OI) patients and morselized bone samples from non-OI control patients typically discarded as surgical waste during corrective orthopaedic procedures were collected to media and randomly assigned: untreated (UN), low-dose SclAb (TRL, 2.5 µg/mL), or high-dose SclAb (TRH, 25 µg/mL) group and maintained in culture (37ºC). Treatment occurred on day 2 and 4 and samples were removed on day 5 for RNA extraction. One bone sample per patient was formalin-fixed upon harvest for baseline hematoxylin and eosin (H&E). B) A subset of OI bone tissue (14 samples from 3 OI patients) was immediately implanted subcutaneously on the dorsal surface (~2 mm^3 in size) of an athymic mouse representing our xenograft model. Implanted mice were randomly assigned to an UN or high dose (TRH, 25 µg/kg) group for 2 or 4 weeks where SclAb treatment was administered via subcutaneous injection 2 times a week. All mice received calcein and alizarin fluorochrome injections 7 and 1 day prior to sacrifice, respectively. Mice were imaged via µCT 24 hours after implantation and immediately following sacrifice. Following imaging, implanted OI bone tissue was removed from the host and plastic processed for dynamic histomorphometry analysis.

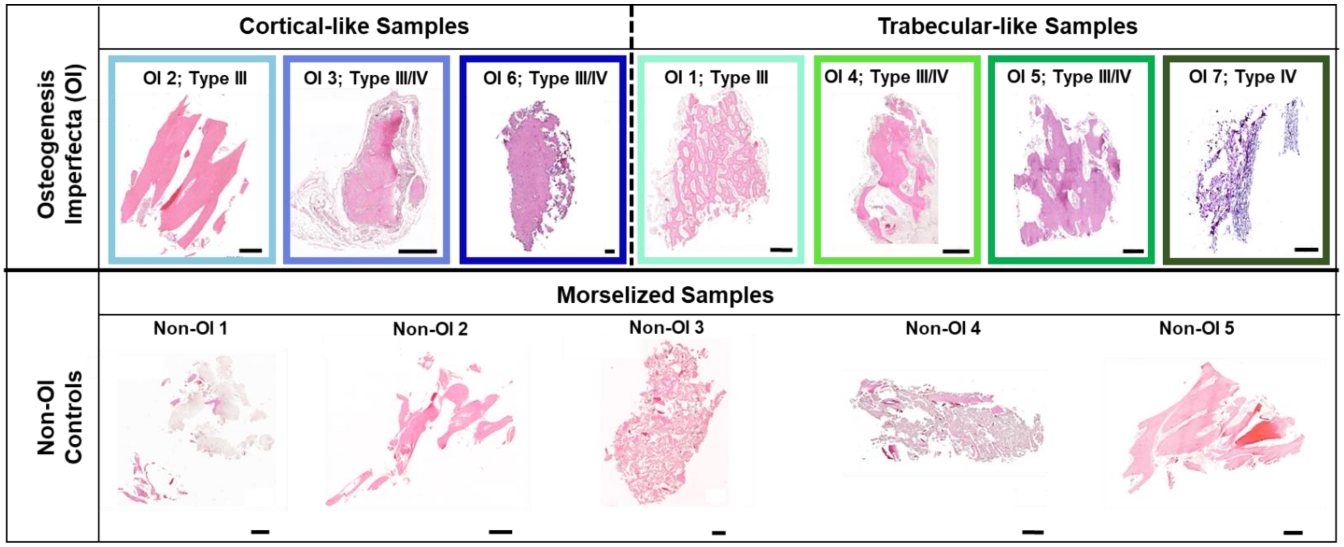

Figure 3.2: Patient donor bone tissue morphology for OI and non-OI patients evaluated using hematoxylin and eosin (H&E).

For the OI patients, tissue ranged from cortical (OI 2, OI 3, OI 6) and trabecular (OI 1, OI 4, OI 5, OI 7) bone tissue. In all cases, non-OI control bone tissue (bottom) was morselized due to the method it was removed during anterior cruciate ligament (ACL) reconstruction tibial tunnel placement (non-OI 1-5). Colored boxes surrounding OI patient samples correspond to subsequent figures depicting fold-change gene expression. Images were acquired at 20x. Scale bar= 500 µm.

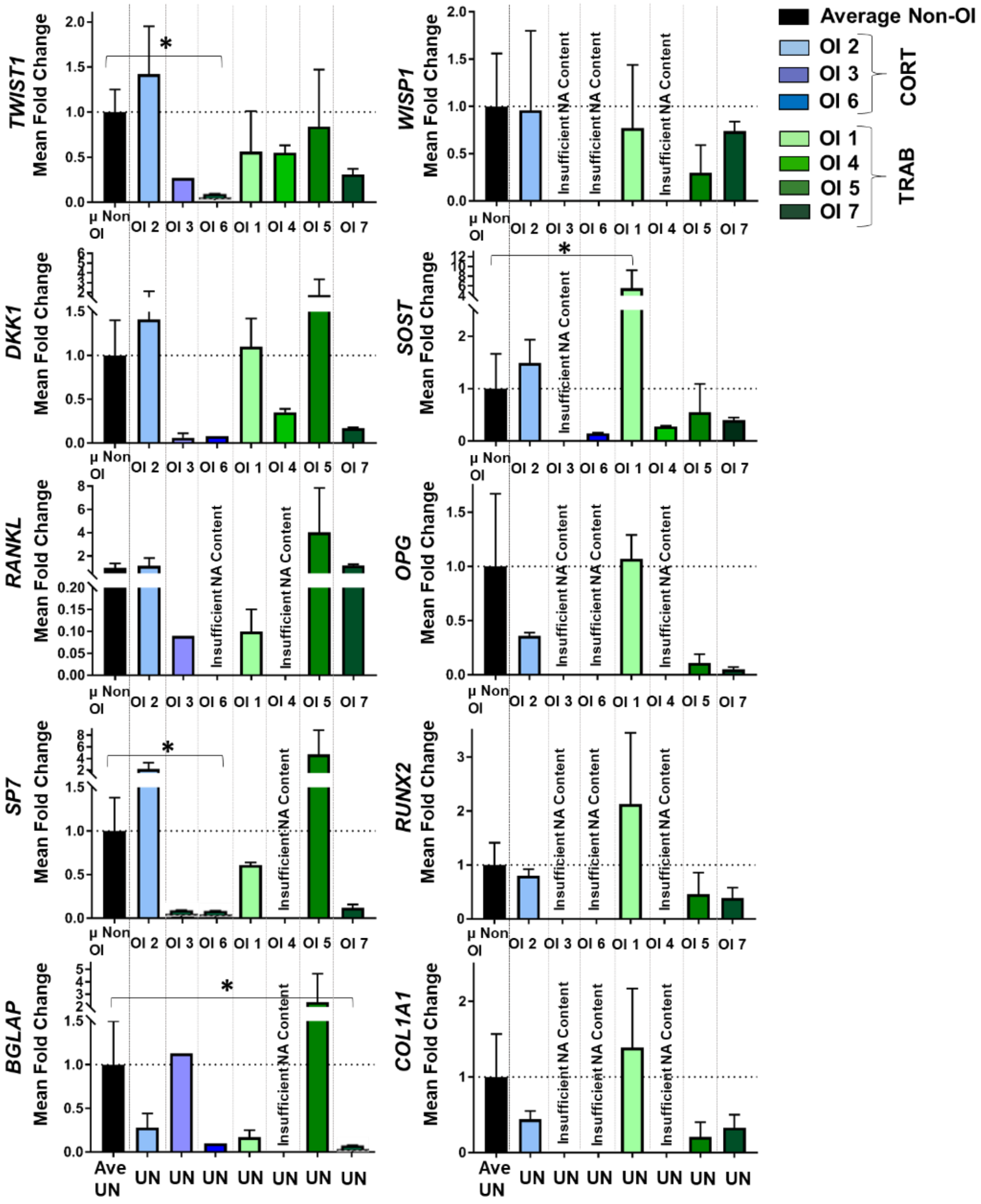

Figure 3.3: Untreated gene expression was heterogeneous across osteogenesis imperfecta (OI) patients.

Quantification of fold-differences in the untreated expression of 10 genes of interest for each OI patient (n=7) normalized to the average untreated non-OI control patients (n=5) corrected by *HPRT1*. Height of bars represents fold-change derived from mean technical replicates and error bars represent standard error of the mean (SEM) derived from technical replicates of three pooled bone samples for the untreated condition for each OI patient. Untreated non-OI (black bar) is the average of these data from 5 patients. OI patients are organized by cortical-like bone samples (right, blue) and trabecular-like bone samples (left, green). [*] and brackets denote significant differences in OI expression compared to untreated controls at $p \leq 0.05$. Missing data due to insufficient nucleic acid content (NA) is indicated. UN= untreated; CORT=cortical-like samples; TRAB=trabecular-like samples.

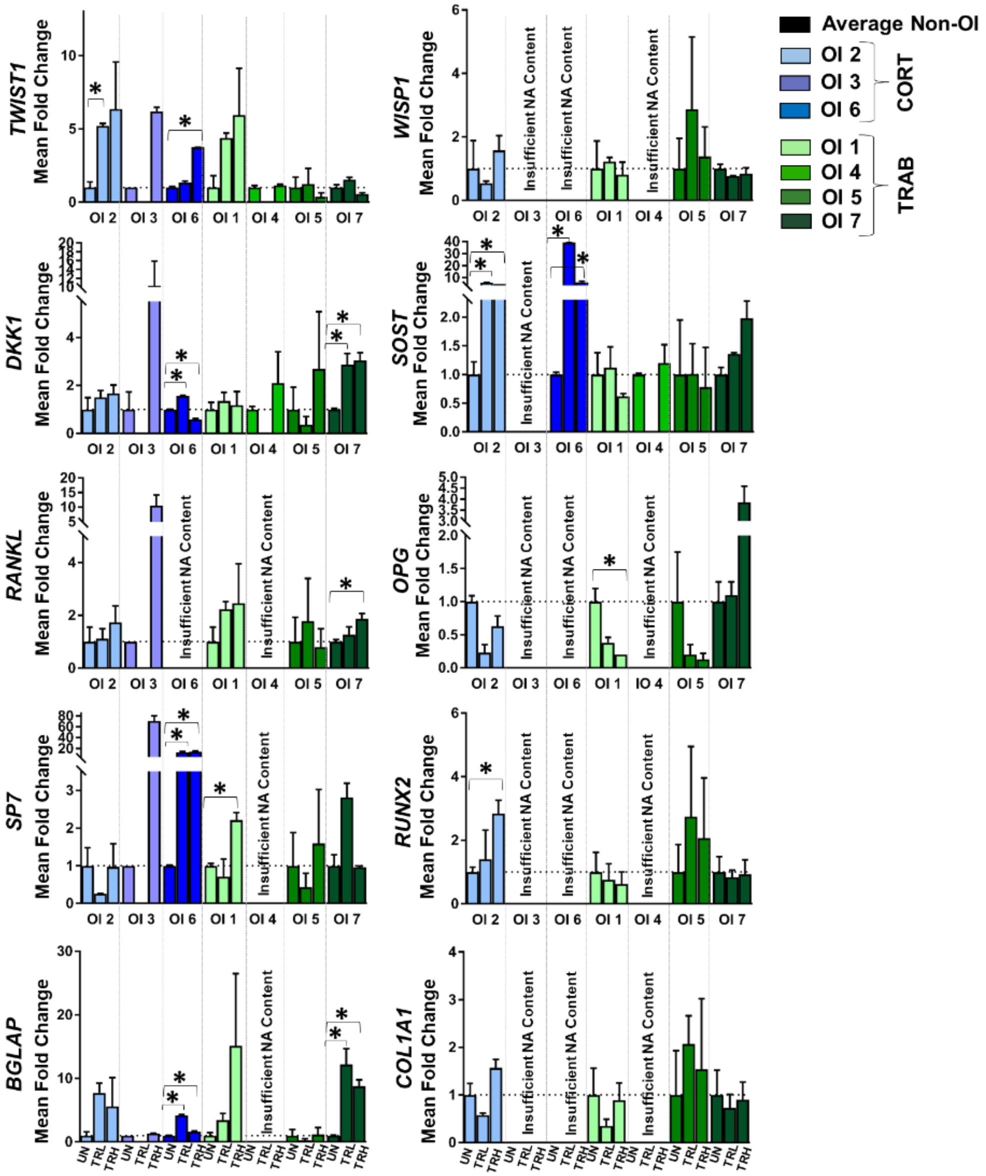

Figure 3.4: Response to SclAb varied in magnitude among individual osteogenesis imperfecta (OI) patients.

Quantification of fold-change expression of 10 genes of interest due to low (TRL) and high (TRH) dose SclAb treatment in vitro. Each OI patient's treated conditions were normalized to the individual patient's untreated condition, corrected by *HPRT1*. Height of bars represents relative fold-change derived from mean technical replicates and error bars represent standard error of the means (SEM) from technical replicates of three pooled bone samples for each condition (UN, TRL, TRH) for each OI patient (n=7). Data is organized by cortical-like patient samples (right, blue; OI 2, OI 3, OI 6) and trabecular-like patient samples (left, green; OI 1, OI 4, OI 5, OI 7). [*] and brackets denote significance within each patient due to treatment at $p \leq 0.05$. Missing data due to insufficient nucleic acid (NA) content is indicated. UN=untreated; TRL=low dose treatment; TRH=high dose treatment; CORT=cortical-like samples; TRAB=trabecular-like samples.

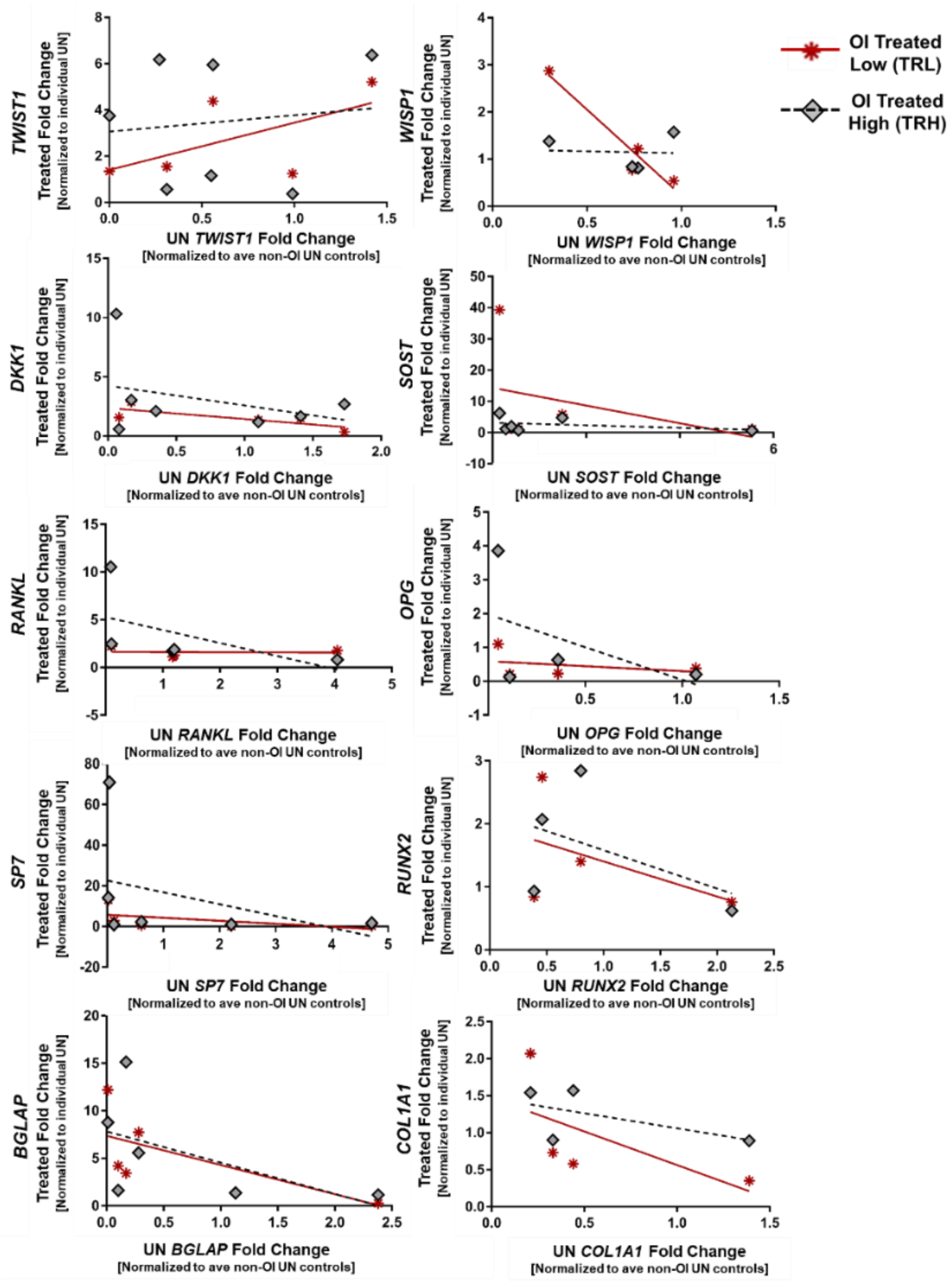

Figure 3.5: Untreated gene expression levels appear to impact magnitude of response to SclAb treatment.

SclAb treated fold change for 10 genes of interest plotted against the individual patient's untreated fold change by dose (treated low dose, TRL; treated high dose, TRH). In particular, magnitude of treatment response of osteoblast markers and precursors *COL1A1, RUNX2, SP7* and *BGLAP* appeared to be impacted by the OI patient's relative untreated expression of the osteoblast related genes. SclAb treated OI patient bone that demonstrated a large magnitude of upregulation generally presented with low untreated expression. Conversely, patient bone that demonstrated little to no upregulation in osteoblast markers with SclAb treatment change due to treatment generally demonstrated high relative untreated expression of the gene of interest. Data represents treatment fold-change relative to the individual patient's untreated condition (y-axis) plotted against the individual patient's untreated fold-change relative to the average non-OI control patients (x-axis). Specifically, each data point on the y-axis represents individual OI-patient SclAb treated bone sample (TRL=red stars; TRH=grey diamonds) fold-change derived from technical replicates of three pooled condition bone samples normalized to the individual patient's untreated condition. X-axis is the individual patient's untreated fold-change condition normalized to the average non-OI untreated controls. TRL=treated low dose; TRH=treated high dose; UN=untreated; ave=average.

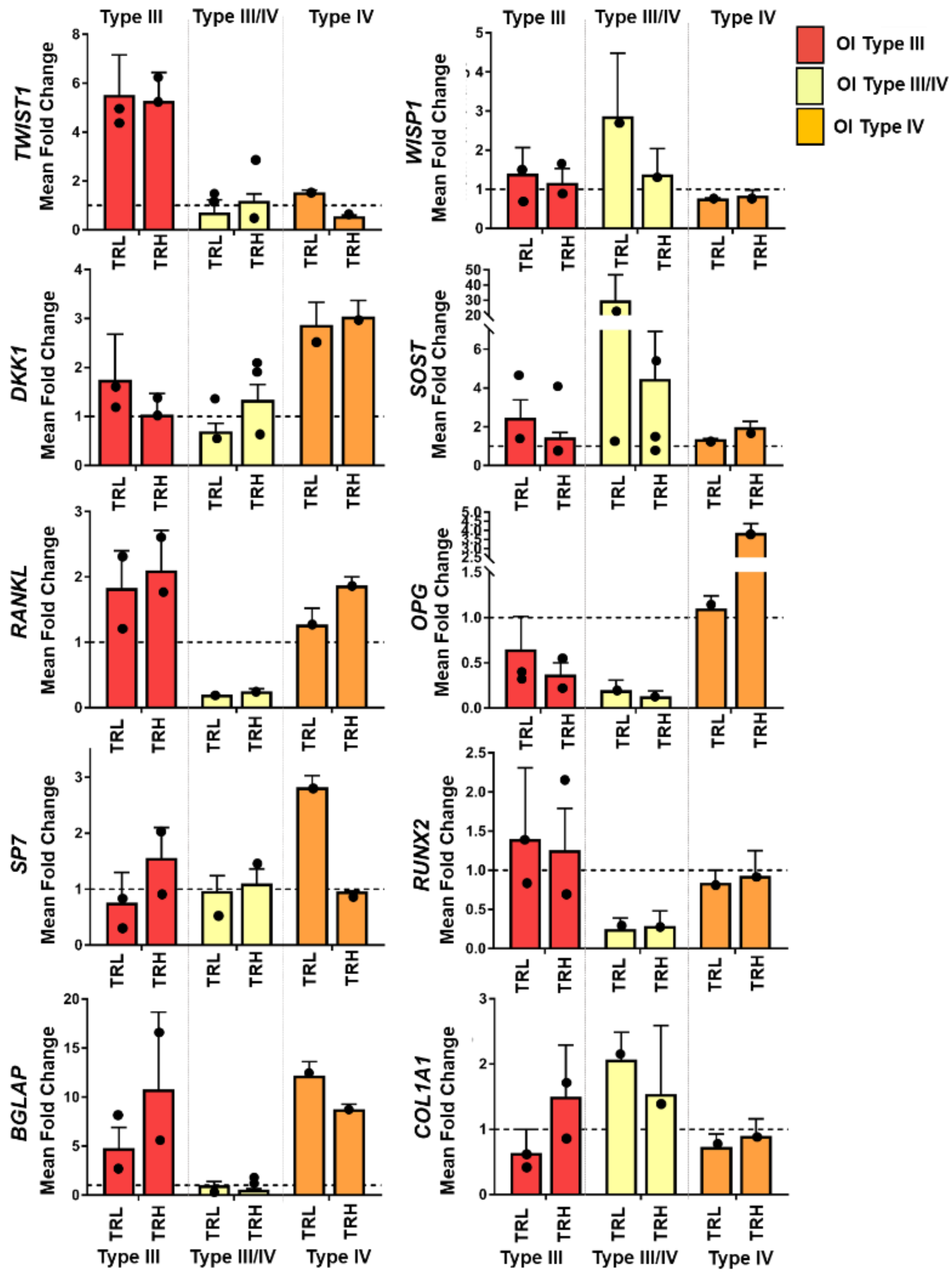

Figure 3.6: Response to SclAb was differential by patient's clinical phenotype classification. Average fold-change expression of 10 genes of interest due to low (TRL) and high (TRH) dose SclAb treatment by patient's OI Sillence type clinical classification. Multiple bone tissue samples were harvested from patients clinically classified by physical examination and genetic testing as either Type III (n=2), Type III/IV (n=4) or Type IV (n=1). Average treated conditions for each OI type were normalized to average untreated condition for that OI type, corrected by HPRT1. For example, average TRL for all OI Type III patients were normalized to the average OI Type III untreated (UN) condition. Height of bars represents relative fold-change derived from combined mean technical replicates for all patients of that OI Type (each patient's technical replicates were averaged over condition) and error bars represent standard error of the means (SEM) from averaged technical replicates which were derived from three pooled bone samples for each condition (UN, TRL, TRH) for each OI patient combined by OI type. Horizontal dotted

line represents 1, or the normalized untreated condition and average treatment response (TRL and TRH) are plotted. Black circles represent individual OI patient fold change for each condition and correspond to results presented in Figure 3.4. Black circles indicate variability in treatment response to acute SclAb present within bone tissue obtained from patients of the same clinical OI classification. No significance was observed between UN, TRL and TRH conditions within OI type but difference in magnitude of treatment response by either increase or decrease in mean fold change gene expression can be appreciated between OI type.

A Two-Way ANOVA results of average condition by OI type normalized to average non-OI untreated controls

	TWIST1	*WISP1*	*SOST*	*DKK1*	*RANKL*	*OPG*	*SP7*	*RUNX2*	*BGLAP*	*COL1A1*
Treatment	0.08	0.86	**0.02**	0.81	0.70	0.57	0.92	0.96	0.53	0.79
Patient Type	**<0.0001**	0.34	**<0.0001**	**0.0002**	0.36	0.57	0.06	**0.01**	0.17	0.37
Interaction	0.07	0.71	**0.03**	0.65	0.56	0.88	0.77	0.95	0.22	0.93

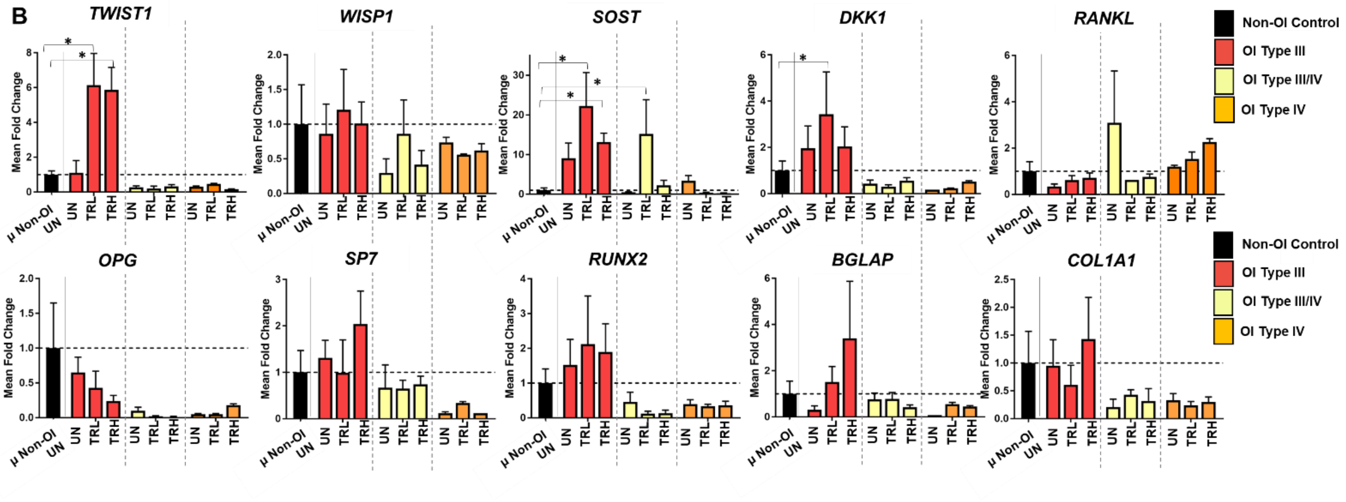

Figure 3.7: Acute SclAb treatment upregulated osteoblast related genes in OI Type III patients to- or above non-OI untreated control levels.

A) Two-way non-repeated measures ANOVA results for each gene of interest comparing average treatment condition (UN, TRL, TRH) within OI type (Type III, Type III/IV, Type IV) normalized to average non-OI untreated control condition. Treatment and patient type served as factors and table values are bolded when significance was reached. B) Quantification of fold-change expression levels of 10 genes of interest for average OI Type III, average OI Type III/IV, and average OI Type IV patients in their untreated (UN) and SclAb treated low (TRL) and high (TRH) conditions. The average OI patient conditions were normalized to the average non-OI untreated condition, corrected by *HPRT1*, in order to create a common scale for the three OI patient populations. Height of bars represents relative fold-change derived from the average of each patients conditional (UN, TRL, TRH) mean technical replicates and error bars represent standard error of the means (SEM) from these technical replicates of three pooled bone samples from each condition, for each patient. Data is organized by OI Type III patients (left, horizontal stripes) and OI Type IV patients (right, diagonal stripes). [*] and brackets denote significant difference from the non-OI untreated control using a Dunnett's post-hoc test at $p \leq 0.05$.

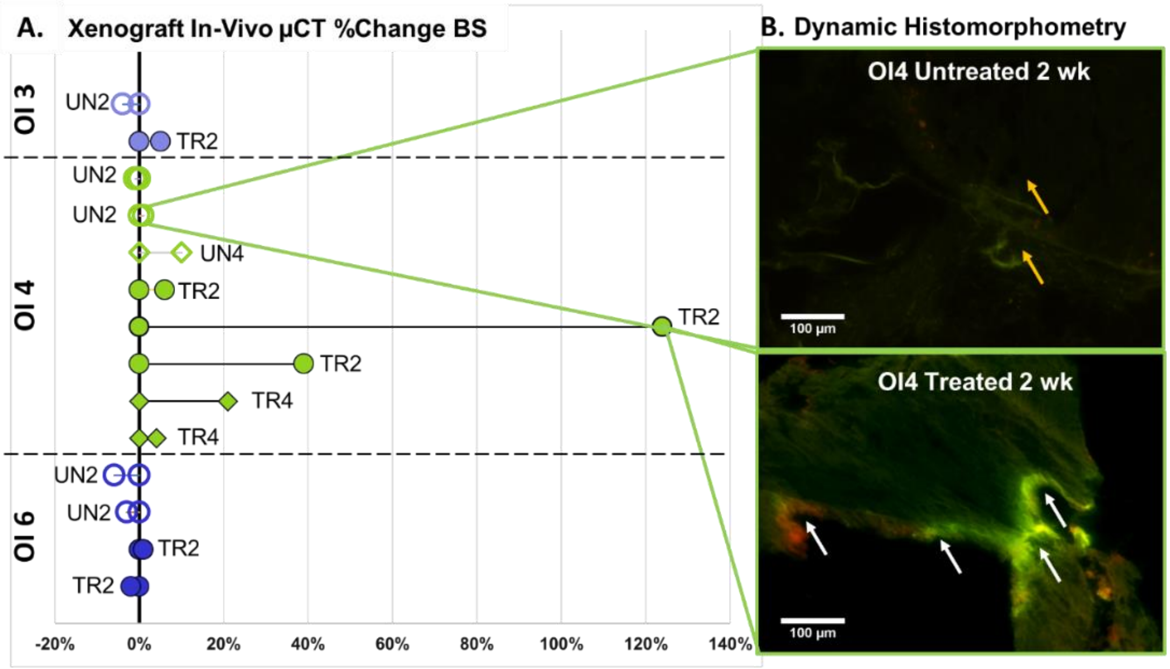

Figure 3.8: In vivo SclAb treatment confirmed a bone forming response.
Additional cortical-derived bone tissue from patient OI3 and OI6 and trabecular-derived bone tissue from patient OI4 were implanted subcutaneously into an athymic mouse representing our xenograft model system. A) OI implants treated with SclAb demonstrated increases in bone surface (BS) measured as a percent change from pre- to post- *in vivo* µCT following two weeks compared to untreated OI implants. The treatment response in these trabecular-derived implants began to attenuate following four weeks of SclAb treatment. B) Histomorphometry corroborated treatment-induced increases in BS at two weeks (bottom panel) demonstrating robust calcein (green) and alizarin (red) fluorochrome labeling (white arrows) compared to the untreated two week implants which had minimal non-specific calcein labeling only (yellow arrow). Fluorescent images acquired at 20x. Scale bar= 100 µm.

Tables

Table 3.1: Patient demographics and bone sample type.

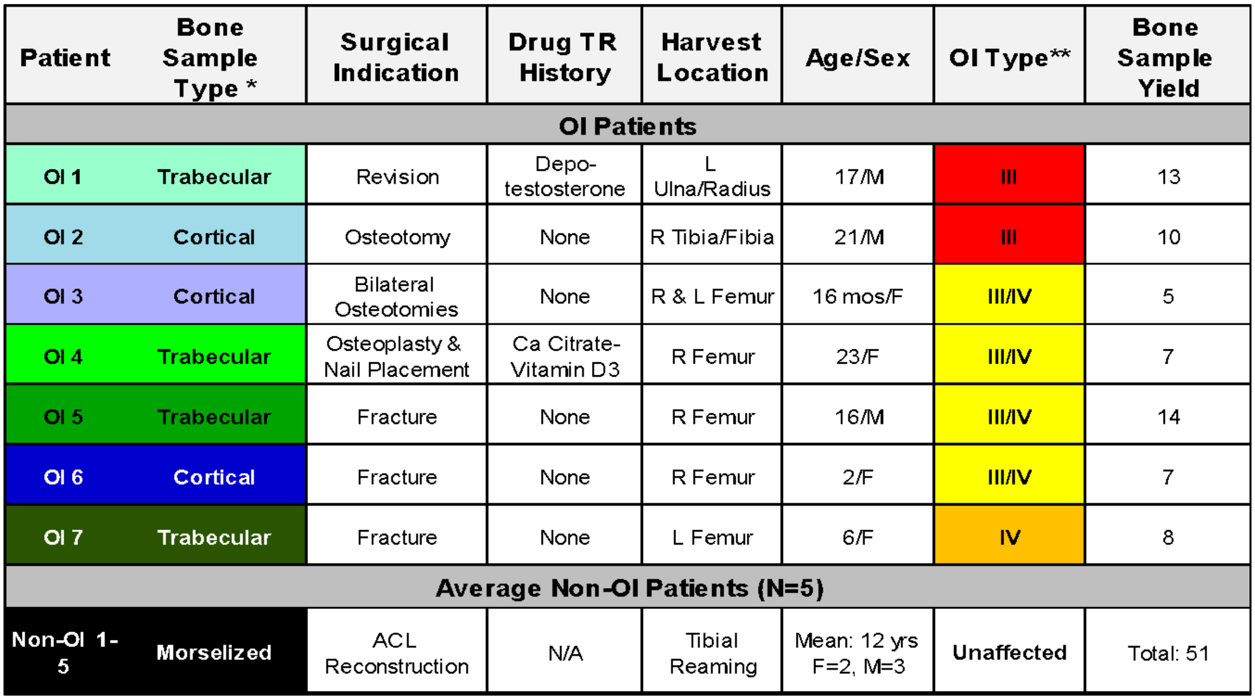

Patient	Bone Sample Type *	Surgical Indication	Drug TR History	Harvest Location	Age/Sex	OI Type**	Bone Sample Yield
OI Patients							
OI 1	Trabecular	Revision	Depo-testosterone	L Ulna/Radius	17/M	III	13
OI 2	Cortical	Osteotomy	None	R Tibia/Fibia	21/M	III	10
OI 3	Cortical	Bilateral Osteotomies	None	R & L Femur	16 mos/F	III/IV	5
OI 4	Trabecular	Osteoplasty & Nail Placement	Ca Citrate-Vitamin D3	R Femur	23/F	III/IV	7
OI 5	Trabecular	Fracture	None	R Femur	16/M	III/IV	14
OI 6	Cortical	Fracture	None	R Femur	2/F	III/IV	7
OI 7	Trabecular	Fracture	None	L Femur	6/F	IV	8
Average Non-OI Patients (N=5)							
Non-OI 1-5	Morselized	ACL Reconstruction	N/A	Tibial Reaming	Mean: 12 yrs F=2, M=3	Unaffected	Total: 51

Table 3.2: Target genes for qPCR analysis.

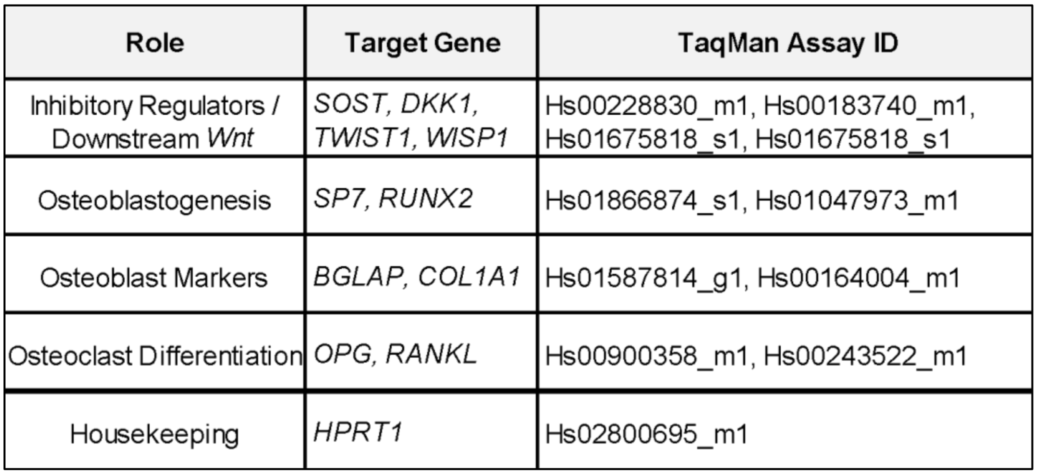

Role	Target Gene	TaqMan Assay ID
Inhibitory Regulators / Downstream *Wnt*	*SOST, DKK1, TWIST1, WISP1*	Hs00228830_m1, Hs00183740_m1, Hs01675818_s1, Hs01675818_s1
Osteoblastogenesis	*SP7, RUNX2*	Hs01866874_s1, Hs01047973_m1
Osteoblast Markers	*BGLAP, COL1A1*	Hs01587814_g1, Hs00164004_m1
Osteoclast Differentiation	*OPG, RANKL*	Hs00900358_m1, Hs00243522_m1
Housekeeping	*HPRT1*	Hs02800695_m1

Chapter 4 A Xenograft Model to Evaluate the Bone Forming Effects of Sclerostin Antibody in Human Bone Derived from Pediatric Osteogenesis Imperfecta Patients

Introduction

Osteogenesis imperfecta (OI) is a heritable collagen-related bone dysplasia characterized by low bone mass and poor bone quality with increased pathological fracture risk presenting most severely in childhood. OI occurs equally in males and females with an overall incidence of ~1:10,000-20,000 births. [1] The disease can be classified into 18 genetically unique types differing in modes of inheritance (dominant or recessive) and severity both within and between type. [3, 336] The hallmark genetic heterogeneity of OI may not only contribute to its growing variable clinical classifications but may also impact patient response to treatment.

The goal of OI treatment is to reduce fracture risk and increase bone mass and density. Numerous treatment options for OI have been proposed with inconsistent treatment response across patients where efficacy appears to be based, in part, on the underlying disease pathology [70, 77, 81, 82, 372]. Bisphosphonates, a class of drugs which reduce osteoclastic activity, represent the predominant treatment strategy over the past decade for OI, [5] yet bisphosphonates only partially correct the bone phenotype. [6, 7] The advent of monoclonal sclerostin antibody (SclAb) has gained interest as a bone-forming therapeutic suggesting a different treatment strategy through inhibition of endogenous sclerostin, a negative regulator of bone formation. [8] Clinical trials of SclAb have led to positive increases in bone quality and mechanical strength in post-menopausal osteoporosis [10-12, 84-86] and results are corroborated in OI animal models supportive of its use in OI. [15-20] In a phase II clinical trial in adults with a moderate phenotype of OI, SclAb stimulated markers of bone formation, reduced bone resorption and increased lumbar spine areal bone mineral density (aBMD), [21] yet results in pediatric OI patients across all types and severity remains unknown.

Clinical trials in the pediatric OI population are especially challenging due to low patient number and high disease variability coupled with a desire for treatment-naïve individuals. [22] As such there is wide-use and reliance on genetically modified mouse models to understand the impact of emerging bone therapeutics, yet a mouse model does not exist to mimic each unique OI mutation. Furthermore, studies have revealed divergent phenotypes in patients with identical, or near-identical genetic mutations. [4] Specifically for SclAb, varying magnitude of positive bone-forming response to therapy has been reported pre-clinically between mild, moderate, and severe phenotypic murine models of OI suggesting the impact of genotypic and phenotypic variability [15, 18-20] including baseline fragility, [20] pre-existing trabecular phenotype, [370] or other yet undescribed mechanisms, on treatment response. As new antiresorptive and anabolic agents are being investigated, the efficacy of these drugs within- and across all OI types and patients in the pediatric population should be better understood prior to clinical extension.

Based on these limitations, there exists a need for a model which represents the inherent phenotypic tissue-level, cellular and genetic variability of OI to safely evaluate emerging therapeutics prior to clinical extension. Human xenograft models in the form of heterotransplantation of human immortalized cancer cell lines into immunodeficient mice were first documented by Isaacson and Cattanach in 1962 and have continually been employed with success over the past five decades. [373] The advent of patient-derived xenograft systems represents a bench-to-bedside approach in cancer research to generate more clinically relevant preclinical models. Solid tumor isolates can be surgically harvested from the patient and subcutaneous implanted into the nude mouse to explore treatment in humanized tumors thus more closely recapitulating human disease. [374, 375] The use of solid tissue isolates has been extrapolated to bone where McCauley and colleagues evaluated the effects of anabolic intermittent parathyroid hormone (iPTH) on implanted neonate mouse tissue drawing on the interaction of host-derived osteoclasts and donor-derived osteoblasts in the model. [376, 377] Together, these earlier works motivate the exploration of a similar transplantation model to evaluate therapeutic interventions in OI. Here, we describe a patient-derived xenograft approach as an alternative to genetically modified OI mouse models through the procurement of pediatric OI bone tissue that is implanted directly into a biologically rich host-derived microenvironment where we can evaluate treatment efficacy of a bone-forming therapeutic in its target tissue.

Materials and Methods

Study design

Eight pediatric OI patients undergoing corrective orthopaedic surgery (osteotomy, open reduction-internal fixation, rodding, fracture intervention, implant exchange) and three age-matched non-OI patients with unaffected collagen status undergoing anterior cruciate ligament (ACL) reconstructive surgery provided informed consent for this Internal Review Board approved study (Table 4.1). These orthopaedic procedures yield bone fragments typically discarded as surgical waste which were collected at surgery (OI n=8/ non-OI n=3), immediately transferred to media (αMEM/10% fetal bovine serum) on ice and trimmed to roughly 3 mm^3. Samples were implanted subcutaneously (s.c.) on the dorsal surface of a 4-6 week athymic mouse ($Foxn^{nu}$ [002019]; The Jackson Laboratory, Bar Harbor, ME, USA) through a 1 cm posterior incision adjacent to the spinal column (Figure 4.1). Each mouse received up to three implants depending on patient yield with one non-implanted sample per patient fixed (10% neutral buffered formalin (NBF)) for baseline analysis. In total, 67 mice were implanted with 84 samples and 14 additional samples were fixed for baseline analysis. Donor OI bone tissue was either trabecular-like or cortical-like in morphology while healthy non-OI tissue always originated from tibial reamings and was received as morselized pieces approximately 1-2 mm^3 in size and implanted as a “conglomerate” of the smaller morselized pieces. Due to the nature of the OI procedures and how the bone samples were procured, we had no control over selection of anatomical site and bone type. Two mice implanted with one bone sample each died before the end of the implantation period due to formation of a bulbourethral gland cyst which was strain-dependent and unrelated to treatment, and one implant fell out from the surgical incision site before the end of the implantation period and thus were excluded from analysis. All experimental animal procedures were approved by the University of Michigan Committee for the Use and Care of Animals.

Bone was randomly divided for this three-stage study. In the first stage, implanted mice were randomly assigned to 1, 2, 4 and 12 week untreated groups to evaluate donor implant viability in the host during short and long-term implantation durations. Second, additional implanted mice were assigned to 2 and 4 week untreated and treated groups used to assess the bone-forming effects of SclAb treatment in the human explants. Mice received SclAb (SclAb VI, Amgen , Thousand Oaks, CA, USA 25 mg/kg s.c. 2QW) beginning one day following implantation for 2 or 4 weeks and compared to 2 and 4 week untreated controls. All mice received calcein (30 mg/kg, intraperitoneal (i.p.) injection), administered seven days before sacrifice and alizarin (30 mg/kg, i.p.) administered one day prior to sacrifice, to follow new bone formation. At sacrifice, implanted human bone and mouse right femora (RF) were dissected free of soft tissue and fixed overnight (10% NBF), rinsed for 10 minutes in dH_2O and placed in 70% ethanol at 4°C for in preparation for tissue processing. Implants and RF were divided for immunohistochemical and histological analysis (paraffin processed) or histomorphometry (plastic processed). The mouse (host) RF served as an internal control for all subsequent analyses described below.

To confirm efficacy of drug delivery to the implanted human bone at the initiation of treatment on day one following implantation, one mouse received calcein (30 mg/kg) and SclAb (25 mg/kg) s.c. 24 hours post-implantation. The mouse was euthanized 24 hours following the calcein and SclAb injections (48 hours post-implantation) and the human bone implant was prepared for non-decalcified fluorescence histology.

Finally, to provide information on the effects of bone tissue storage for the third stage of the study, tissue from two additional OI patients were collected to media and immediately stored at 4°C with one sample from each patient fixed immediately for baseline analysis. At five time points during a 48 hour period, bone fragments were removed from media and fixed to evaluate donor bone cell survival following storage.

Tissue preparation

Bone samples prepared for paraffin processing were decalcified in 10% ethylenediaminetetracetic acid (EDTA) with constant shaking for 15-20 days and complete decalcification was ensured by Faxitron imaging. Bone tissue was paraffin processed (Leica ASP 300 paraffin tissue processor), embedded and cut into 5 µm thick sections (Leica RM2255 microtome).

A subset of undecalcified bone samples and mouse RF were prepared for plastic processing using a Leica ASP300 tissue processor and placed in a series of methyl methacrylate (MMA) and dibutyl phthalate with progressively higher concentrations of benzoyl peroxide. Samples were manually embedded in partially polymerized polymethyl methacrylate

(PMMA) and allowed to cure at room temperature for up to ten days followed by hardening in a 37° C oven overnight. Bone explants were sectioned to 5 µm thickness (Leica RM2255 fitted with a disposable tungsten carbide blade) and slides were placed under compression for two days in a 37° C oven to allow section fixation to the slide. Embedded mouse RF were sectioned transversely with a low-speed saw (IsoMet, Beuhler, Lake Bluff, IL), polished using progressive grades of silicon carbide abrasive paper (1200, 2400, and 4000 grit) followed by a felt pad with a ¼ µm diamond slurry suspension (Struers Inc., Cleveland, OH) on the plane distal to the lateral third trochanter. All images were acquired using a Nikon Eclipse Ni-U microscope (Nikon Instruments Inc., Melville, NY).

Micro-computed tomography (µCT)

Bone morphology and microarchitecture of the implanted bone sample were analyzed using high resolution µCT (Bruker, Skyscan 1176) at two time points; a pre- scan acquired 24 hours following implantation under anesthesia and a post- scan acquired immediately following euthanasia. A third *ex vivo* scan of the implant and RF was acquired following removal from the host. *Ex vivo* scans of the excised implant and RF were acquired on the same system by placing the sample of interest in a 0.5 mL or 1.5 mL tubule filled with deionized water, respectively. All pre- and post- images were obtained at an X-ray voltage of 75 kV and current of 333 µA and *ex vivo* at an X-ray voltage of 50 kV and 500 µA current and all acquisitions used a 0.5 mm aluminum filter to ensure uniform beam energy. Reconstructed scans were calibrated with the use of two manufacturer-provided hydroxyapatite standards at either 18 µm (pre- and post-) or 9 µm (*ex vivo*) isotropic voxel size. Images were analyzed using the Skyscan CT-Analyzer software (CTAn, Bruker,Version 1.15.4.0).

For the implant, area surrounding the bone was segmented manually followed by several automated processes to extract only the implant from the image allowing for morphometric 3D analysis to be performed on the donor bone without assumptions on underlying bone structures of the host mouse (e.g. mouse spine, rib, sacrum). Due to the differential morphology of the donor bone tissue, the implant was subject to a specimen-specific threshold to obtain densitometry values. [378] Parameters including bone mineral density (BMD), tissue mineral density (TMD), bone volume fraction (BV/TV) and bone volume (BV) were quantified using manufacturer supplied algorithms (CTAn, Bruker, Belgium). Analysis was performed using percent change from pre- to post- *in vivo* scans for BMD (%changeBMD), TMD (%changeTMD), BV/TV (%changeBV/TV) and BV (%changeBV). Baseline values derived from pre- *in vivo* scans of BMD, TMD, BV/TV and BV were used to describe bone morphology at implantation.

To evaluate a systemic treatment response to SclAb, host right femora were analyzed for femoral geometry (trabecular thickness, cortical area and cortical thickness) and volumetric trabecular BMD (g/cm^3) by first isolating cortical and trabecular bone with fixed attenuation coefficient derived densitometry threshold values of 110 and 90 μ, respectively. The volumes of interest (VOIs) were created and assessed using an auto-segmentation method (CTAn) which separates cortical and trabecular bone automatically using a series of morphological and bitwise operations. A trabecular VOI was created proximal to the end of the distal growth plate spanning 1 mm in the z-direction. The cortical VOI was selected at the mid diaphysis distal to the lateral third trochanter spanning 2 mm in the z-direction.

Immunohistochemical analysis

Immunohistochemistry with fluorescence (IHC-F) was used to evaluate the presence of human-derived bone cells through staining for human mitochondria (hMito) at baseline and upon removal from the host following implantation durations of 1, 4 and 12 weeks and a subset of 2 and 4 week treated and untreated implants. Detection of host/donor contributions of sclerostin (SOST) and osterix (Osx) was performed using a dual IHC-F staining protocol where primary antigens of SOST/hMito, and on serial sections, Osx/hMito were immunolocalized. Staining of hMito was used in all instances to indicate donor-derived cells with the addition of SOST or Osx (using antibodies with validated sensitivity to both mouse and human antigens) in order to detect all instances of SOST and Osx expression (both mouse (host) and human (donor) derived) to derive host/donor relationship.

In brief, paraffin sections were deparaffinized in xylene and rehydrated through a descending alcohol series. For dual stained hMito/Osx, heat-mediated antigen retrieval was achieved by placing slides in 0.01 mol/L sodium citrate (pH 8.0) in a steamer (Black and Decker) for 15 minutes and sections were cooled to room temperature. For dual stained hMito/SOST, antigen retrieval using Proteinase K (2.5 µl in 100 mm Tris, pH 9.0, and 50 mm EDTA, pH 8.0) for 10 minutes at 37 °C followed by three washes with 0.1 m Tris-buffered saline (pH 7.4) containing 0.02% Tween-20. In all cases, endogenous peroxidase activity was quenched by a 10 minute immersion in 0.3% hydrogen peroxide. hMito/Osx sections were blocked with 5% donkey blocking serum mixed with 1% bovine serum albumin and 1xPBS plus 0.1% triton detergent. hMito/SOST sections were blocked in the same manner except for Tween-20 used in the place of triton.

Sections were incubated with the primary anti-hMito antibody (MAB1273, EMD Millipore) at a 1:200 dilution and either a primary polyclonal rabbit anti-Osx antibody (ab22552, Abcam; 1:400) or primary polyclonal rabbit anti-SOST antibody (bs-10200r, Bioss; 1:200) overnight at 4°C. For all cases, hMito was developed with a biotinylated mouse anti-rabbit secondary antibody (715-066-150, Jackson ImmunoResearch) at a 1:400 dilution, incubated at ambient temperature for one hour and followed by the addition of the Osx donkey anti-rabbit IgG secondary antibody conjugated to Alexafluor 488, (A-21206, Invitrogen; 1:400) or SOST goat anti-rabbit IgG secondary antibody conjugated with Alexafluor 488 (ABIN400260, antibodies-online; 1:250) for an additional hour at 37°C. Following washing, slides were incubated with an avidin conjugated peroxidase system (Vectastain Elite ABC Kit; Vector Laboratories) and developed with a tyramide signal amplification (TSA) substrate (Perkin Elmer) per the manufacturer's instructions to amplify the hMito signal. All slides were washed with a DAPI dilution and mounted using Prolong Gold Antifade Mountant (Life Technologies). Negative control sections underwent the same procedure, but primary antibodies were omitted. Species control sections were used to evaluate the specificity of the primary antibodies. Serial sections were stained with hematoxylin and eosin (H&E) for morphology guiding IHC-F findings using established procedures. [351] Dual, positive-stained cells indicate that either Osx or SOST is human (donor) derived while single Osx or SOST stained cells suggest host (mouse) contributions.

Dynamic and static histomorphometry

Undecalcified plastic-embedded implant sections were assessed for the presence and labeling characteristics of calcein and alizarin fluorochrome labeling on newly-formed bone surfaces in 2 and 4 week treated and untreated implants. Analysis of labeling was qualitative in nature due to the heterogeneity of the bone tissue (size, orientation, bone type). Serial implant sections were stained with Goldner's Masson Trichrome (GMT) for static histomorphometry assessment of cellular populations guiding fluorochrome labeling findings.

To further confirm bone-forming activity due to treatment in the host, dynamic histomorphometry of mouse RF including bone surface (BS), mineral apposition rate (MAR), mineralizing surface to bone surface (MS/BS) and bone formation rate (BFR) were performed at the mid-diaphysis on the periosteal and endosteal surfaces using the calcein and alizarin label according to standard nomenclature. [379] Fluorescent images of the prepared cross sections were acquired with a 10x objective of calcein (excitation 485/20 nm, emission: 540/25 nm) and alizarin (excitation: 557/55 nm, emission: 615 nm) and merged (NIS Elements Br, Nikon Instruments Inc., Melville, NY). Quantitative dynamic measurements were performed using ImageJ. Regions where a dual label was not present, MAR was treated as a missing value. To calculate BFR/BS in the cases with a missing MAR value, a value of 0.3 μm/day was assigned. This value has been used previously in our lab and is established in the literature for cases of missing MAR values. [17, 380]

Tartrate-resistant acidic phosphatase (TRAP) staining

A subset of decalcified paraffin embedded baseline (time-0), and 2 and 4 week treated and untreated implant sections were stained for tartrate-resistant acidic phosphatase (TRAP) activity, a marker of bone resorption, and counterstained with Fast Green according to manufacturer protocol (387A-1KT, Sigma, St. Louis, MO, USA). Slides were imaged using a bright-field light microscope (10x objective) and analysis was performed in ImageJ where osteoclast detection comprised TRAP-positive cells. [381] For each slide, the entire implant was treated as the ROI where the bone surface was measured followed by quantification of TRAP-positive cells. Measurements were expressed as the number of positive TRAP-stained osteoclastic cells per millimeter of bone surface (Oc.N./B.pm.) of the implant.

TUNEL assay for bone cell apoptosis

For the third stage of the study, a subset of OI bone samples were evaluated for cell survival by initiating TdT-mediated dUTP nick end labeling (TUNEL) assay for apoptosis. To evaluate the effects of tissue storage and determine the optimal time course for retrieval and implantation, trabecular bone from one OI patient and cortical bone from a separate OI patient (5 samples per patient, ~3 mm^3 each in size for a total of 10 bone samples) were collected to αMEM/10% FBS and immediately stored at 4°C. One bone sample per patient was formalin fixed immediately for baseline analysis (time-0) and the remaining bone tissue was removed from storage and formalin fixed at the following time points: 18, 24, 32, and 48 hours. The procedure was performed with a TUNEL staining kit (In Situ Cell Death Detection Kit, Roche, 11684817910) following instructions from the manufacturer. All fluorescent images were acquired at 20x using a Nikon Eclipse Ni-U microscope. Analysis was performed in ImageJ using the analyze particle function combined with the watershed pre-processing algorithm to better separate areas of dense cells (e.g. marrow cells). [382] In short, quantification of all nucleated cells (DAPI) and positive stained cells (TUNEL) were performed in a total tissue region of interest (ROI) that contained bone and bone marrow, a bone-only ROI, and a marrow-only ROI to determine if cell apoptosis rate differs between the marrow and bone. Results were presented as a percentage of total TUNEL/total DAPI. Serial standard H&E stained sections were used to morphologically guide ROI selection.

To determine the presence of bone cell apoptosis in our implanted human bone, excised implants 1, 4 and 12 weeks (untreated) were evaluated in the same manner using TUNEL assay to ensure bone cells remained viable throughout the proposed implantation duration.

Statistical analysis

Descriptive and inferential statistics for µCT implant outcomes, presented as a relative percent change derived from pre- and post- image acquisitions, were analyzed using SPSS v.22.0 (IBM, Armonk, NY). First, we describe the demographic, clinical and related characteristics of the implant including patient type (OI or non-OI), implant duration (2 or 4 week), treatment status (treated or untreated), baseline µCT values (BMD, TMD, BV/TV and BV) and bone type (trabecular, cortical or morselized) by using raw counts, measures of central tendency (e.g., mean, median or mode) and measures of data dispersion (e.g., 95% confidence intervals, standard deviations (SD)) where appropriate. Comparisons of baseline µCT BMD, TMD, BV/TV and BV between randomly assigned treated and untreated OI and treated and untreated non-OI groups using Student's t tests were undertaken to ensure group equality at implantation. Direct comparisons of µCT outcome measures were carried out with paired t-test for 2 and 4 week data within patient type (OI and non-OI). To understand the impact of bone type, univariate ANOVAs for 2 and 4 week analysis of %changeBMD, %changeTMD, %changeBV/TV, and %changeBV were used to detect a differential response in implant bone type (cortical, trabecular, morselized) to treatment (treated, untreated). This analysis also served to detect differential response due to implantation (using the untreated condition) between OI and non-OI control tissue at each time point. Bonferroni post-hoc analyses were conducted as appropriate.

Analysis of positive TRAP activity using the Oc.N./B.Pm. ratio was conducted on a subset of baseline (time-0), treated and untreated 2 and 4 week OI bone implants. The Oc.N./B.Pm. were analyzed using a regular one-way ANOVA with a Holm-Sidek test for multiple comparisons between implant groups. Results from the TUNEL assay for cell apoptosis following tissue storage were presented as a percentage of total positive TUNEL cells/total DAPI nucleated cells from trabecular- and cortical-derived bone and reported in the total tissue ROI, bone-only ROI and marrow-only ROI at five time points.

Mouse (host) dynamic histomorphometry outcomes (periosteal and endosteal MAR, MS/BS, and BFR/BS) and e*x vivo* µCT derived trabecular (BMD, trabecular thickness) and cortical (area, thickness) measurements were analyzed using a Two-Way ANOVA with treatment (treated vs. untreated) and duration (2 vs. 4 week) as factors to confirm a systemic effect of SclAb. Post-hoc t tests with a Tukey correction was conducted as appropriate (GraphPad Prism v7, GraphPad Software, La Jolla, CA, USA). In all cases, alpha was set at $p \leq 0.05$.

Results

Donor bone is bioaccessible, viable, and donor-derived bone cells are present for up to 12 weeks

A definitive calcein fluorochrome label was present on the OI bone surface (Figure 4.2A, white arrows) following one dose of calcein administered 24 hours following s.c. implantation. This suggests that SclAb can reach the target implant 24 hours following implantation. Results from TUNEL assay for apoptosis demonstrated minimal TUNEL-positive apoptotic cells following short (1 week) and intermediate (4 week, Figure 4.2B) durations. Following long-term implantation, nominal positive TUNEL cells were observed in osteocytes, marrow cells and bone lining cells (Figure 4.2C). The existence of viable, human-derived osteocyte-rich bone which expressed human-derived bone lining cells was observed upon harvest and maintained at intermediate durations (Figure 4.2D) through 12 weeks (Figure 4.2E) in OI and non-OI untreated implants (positive for hMito, red). Together, these results suggest that SclAb treatment can reach the target implant 24 hours following s.c. implantation, and xenografts present with human-derived bone cells at short, intermediate and long-term implantation durations with nominal bone cell apoptosis.

Balance of host-to-donor bone cell contribution is altered with duration and treatment

Qualitative analysis of hMito IHC-F revealed the presence of human-derived bone cells, but their occurrence decreased slightly with longer implantation durations (up to 12 weeks) (Figure 4.2D-E). Trabecular-derived bone presented with more positive hMito cells, including a greater number of hMito positive bone lining cells that remained present longer (12 weeks) compared to cortical-derived bone which had the fewest instances of viable hMito cells at 12 weeks (Figure 4.3). Similar to trabecular-derived implants, hMito positive bone cells were observed in greater quantities (both osteocyte and lining cells) in the morselized bone compared to cortical bone. No specific staining was observed in negative control sections and no species cross-reactivity was observed in mouse tissue controls ensuring the specificity of the hMito antibody (Figure 4.4A-B).

A subset of baseline (time-0), and 2 and 4 week treated and untreated OI and non-OI implants were dual IHC-F stained to probe for Osx (green) and hMito (red), and on serial sections, dual SOST (yellow) and hMito (red) to determine donor/host cell populations. Following both 2 and 4 week treatment durations, implants exhibited bone surfaces rich with human-derived Osx-expressing cells (Figure 4.5B and D) which became more robust with increasing treatment duration. Untreated implants expressed Osx on bone surfaces; however, expression was principally host-derived (i.e. positive for Osx but not hMito) (Figure 4.5A-C). In untreated implants, these host-derived Osx-expressing lining cells decreased between 2 and 4 weeks (Figure 4.5C) implantation duration regardless of bone type (trabecular, cortical, morselized), and in some cases, no Osx expressing lining cells were present by 4 weeks. Non-OI bone implants behaved similarly to OI as they contained more instances of human-derived Osx - expressing bone lining cells with treatment compared to untreated xenografts at the same time point. While most treated OI implants expressed primarily human-derived Osx, cortical xenografts from patient OI4 demonstrated surfaces which were rich with a combination of mouse-derived Osx-expressing cells, along with human-derived Osx-expressing cells, at both treated time points. Patients with less immunolocalized Osx expression at baseline generally demonstrated more robust Osx-expression, primarily human-derived, by 4 weeks of treatment Figure 4.6A). Conversely, high baseline Osx expression led to fewer Osx-expressing cells on implant bone surfaces for patient OI4 who also had a mix of mouse and human-derived Osx-expressing cells (reported, above) following four weeks of treatment (Figure 4.6A).

Donor SOST is expressed at baseline and throughout the 4 week period for all conditions (Figure 4.5E-H). Varying levels of SOST staining surrounding the osteocyte was observed at baseline and generally demonstrated an increase in staining following SclAb treatment (Figure 4.5F and H). Baseline SOST expression surrounding the osteocyte varied by patient ranging from minimal (OI4, non-OI1), moderate (OI5, OI6) to robust (non-OI1, non-OI3). Implants with minimal SOST expression at baseline generally demonstrated the greatest increase in staining levels surrounding the osteocyte following treatment compared to the untreated condition (e.g. OI4 implants, Figure 4.6B). This observed increase in staining appeared less robust in implants presenting with moderate and robust baseline SOST expression prior to the initiation of treatment. In all cases, osteocytes were human-derived with the exception of OI6 cortical-like implants, which demonstrated several instances of mouse-derived, SOST expressing osteocytes near bone surfaces at 4 week treated and untreated conditions (Figure 4.6C example in treated condition).

In vivo µCT confirms a variable bone-forming treatment effect

Baseline *in vivo* µCT confirmed there were no significant differences between baseline values of BMD, TMD, BV/TV and BV between treated and untreated two week + four week OI or treated and untreated two + four week non-OI groups (Figure 4.7A-D). This ensured equality between randomized groups and that no unintended bias was introduced at the time of implantation.

When OI implants were combined into treatment groups regardless of baseline morphology, treated OI implants were not significantly different from untreated OI implants in any percent change µCT outcome at two or four weeks despite numerically higher increases in all measures with SclAb treatment (Figure 4.8A-D). Non-OI implants elicited a significant treatment response for two week %changeTMD, %changeBV/TV, and four week %changeBV.

Given the large variation in the data, we performed a post-hoc analysis based on bone type. OI implants were both trabecular and cortical-derived while non-OI implants were all morselized bone. SclAb treatment response varied in magnitude by bone type at both two and four weeks (Figure 4.9A-D, bolded p-values indicate significant effect of bone type). In some conditions, implantation alone (untreated) continued to increase in bone formation which was differential by bone type (Figure 4.9A-D). Results from follow-up Bonferonni post-hoc analysis are denoted by brackets and stars when significance was reached between bone type. While not statistically significant, we observed a 7-fold increase in mean %changeBMD for trabecular OI groups between two and four weeks of treatment (2.24 vs. 18.47), a 0.5-fold increase for cortical OI groups (7.38 vs. 11.19) and a decrease in morselized non-OI groups (65.42 vs 40.61).

Untreated xenografts were not significantly different following two weeks of implantation. At four weeks, trabecular and morselized implant %changeBMD was significantly increased over cortical implants (Figure 4.9A). Interestingly, untreated trabecular implants trended for an increase in %changeBMD, TMD and BV/TV between two and four weeks while untreated cortical implants decreased between 2 and 4 weeks (Figure 4.9A-C).

Implant histomorphometry findings corroborate µCT results

Analysis of implant histomorphometry was qualitative due to tissue heterogeneity including variation in bone size, orientation and bone type and an inability to define a common sectioning plane. OI and non-OI SclAb-treated implants demonstrated positive formation of new bone presenting with more definitive calcein and alizarin labeling and greater inter-label width (Figure 4.10E and M) compared to weaker and non-specific labeling observed in untreated implants (Figure 4.10A and I). In general, labeling became more robust following 4 weeks of SclAb treatment compared to two weeks of treatment.

Osteoid seams were observed on serial sections stained with GMT and closely matched locations of calcein and alizarin-labeled surfaces in all implants (Figure 4.10B, F, J, N). Evaluation of Osx expression in the implants corroborated fluorochrome and GMT data by revealing a concurrent increase in osteoblast activity. In general, Osx expression on implanted bone surfaces was stronger in treated implants compared to untreated implants and increased in expression with treatment duration (Figure 4.10, C,G,K,O).

No significant changes in bone resorption following SclAb was observed in the implants

TRAP analysis was conducted on a subset of baseline, treated and untreated 2 and 4 wk implants. No significant changes in Oc.N./B.Pm., a measure indicative of bone resorption, was observed across all groups (Figure 4.11A-B).

Host mouse femora confirmed systemic bone-formation response to SclAb

Ex vivo μCT analysis of mouse RF confirmed a systemic bone-forming effect of treatment in the host (Figure 4.12A-E). Two-Way ANOVA results revealed a significant effect of treatment and duration for cortical area (treatment: $p<0.0001$, duration: $p<0.01$) and cortical thickness (treatment: $p<0.0001$, duration: $p<0.0001$) and a significant treatment effect for trabecular BMD ($p<0.001$) and trabecular thickness ($p=0.022$). Specifically, cortical area increased by +10% following 2 weeks ($p=0.06$) and +18% following 4 weeks ($p=0.0001$) of treatment. Cortical thickness increased by +9% ($p=0.02$) and +15% ($p<0.0001$) following 2 and 4 weeks of treatment, respectively. Trabecular BMD increased by +25% following treatment at 2 weeks ($p=0.06$) and +20% at 4 weeks ($p=0.008$) and trabecular thickness increased by +5% following treatment at 2 weeks ($p=0.89$) and +21% ($p=0.05$) at 4 weeks.

Dynamic histomorphometry measures of MAR, MS/BS, and BFR/BS on the periosteal and endosteal surfaces of the host RF (Figure 4.12F-G) further corroborated a systemic bone-forming effect of SclAb.

Bone tissue morphology dictates donor cell apoptosis rates following harvest and during storage

Trabecular and cortical OI bone revealed dissimilar rates of donor cell apoptosis following removal from the patient (baseline, time-0) through storage up to 48 hours at 4° C. TUNEL assay results from two patients can be appreciated in Figure 4.13A-K. Patient OI7 yielded trabecular-like bone while patient OI 8 yielded cortical-like bone (Table 4.1 for detailed patient demographics; both patients Type III OI). At baseline following harvest from the patient, trabecular bone experienced fewer positive apoptotic cells compared to the cortical bone (5% vs. 12%). Following 18 hours in storage, cortical bone underwent cell apoptosis in 54% of the total tissue including 63% of the bone and 38% of the marrow. At the same time point, trabecular bone demonstrated apoptosis in 19% of the total tissue with 14% of the bone and 20% of the marrow donor cells undergoing apoptosis. Both trabecular- and cortical-like bone demonstrated a linear increase in total tissue cell apoptosis with increasing storage time except for trabecular bone at 32 hours and cortical bone at 24 hours. In general, trabecular bone underwent a greater amount of apoptosis in the marrow ROI while cortical bone experienced a greater amount of apoptosis in the bone ROI following storage.

Discussion

There is currently no US Food and Drug Administration- or European Medicines Agency-approved therapy for the treatment of OI. Rather, current clinical OI management relies, in part, on off-label use of therapies targeting osteoporosis. Osteoporosis represents a metabolic disease of bone fragility, and therefore, patient response to therapy is not fully predictive of the clinical response in pediatric OI patients using the same interventions. [70, 76] Divergent clinical therapeutic responses in OI highlights the need for an appropriate model to evaluate bone drug efficacy prior to clinical extension. To address this deficiency, we describe a novel xenograft model using solid, OI patient-derived bone tissue harvested during corrective orthopaedic procedures which maintains human-derived bone cells within their native extracellular environment and preserves the genetic mutation unique to each patient. The model provides a controlled host-derived micro-environment to evaluate the *in vivo* bone-forming effects of SclAb in its target tissue without contraindications to the OI patient outside of pre-planned surgical intervention. Following bone implantation, TUNEL assays demonstrated that donor bone cells remain viable at short (1 week), intermediate (2-4 weeks) and long-term (12 week) durations. Implanted donor-derived bone tissue became bioaccessible to the host following 24 hours, indicating that systemic treatment is accessible by the xenograft tissue as early as day one in the model. Taken together, we administered SclAb systemically beginning 24 hours after implantation and evaluated implant treatment response at 2 and 4 weeks durations to maximize the likelihood that treatment targeted human-derived bone cells.

We used immunohistochemistry to evaluate the donor/host relationship of the implants with and without SclAb treatment. Most notably, there was a shift in donor/host origin of Osx expression with SclAb treatment in the human OI implants. We observed that treated implant surfaces were rich with human-derived Osx expressing cells while untreated implants demonstrated surfaces primarily expressing mouse-derived Osx expressing cells. This observation was determined using a dual-IHC approach where human-derived Osx was confirmed by the presence of cells positively stained for both hMito and Osx antibodies. TUNEL results reveal that nominal apoptosis occurs in the implant at 2 and 4 weeks, therefore the lack of human-derived Osx expressing cells in the untreated implant is likely not attributable to cell death. We hypothesize that SclAb treatment may have been able to preserve and differentiate the human-derived cells of the osteoblast lineage leading to the human-derived Osx expression observed in the treated xenografts. It is possible that untreated implant osteoblast precursors were present in the implant but did not differentiate to Osx-expressing lining cells and instead, mouse-derived osteoblasts were recruited to the untreated implant. Baseline Osx expression also appeared to dictate the magnitude of osteoblast response to treatment in the implants. For instance, bone from patient OI6 had very little Osx expression on bone surfaces prior to implantation; as soon as 2 weeks of SclAb treatment, all OI6 implant surfaces were rich in Osx expressing cells which were primarily human-derived. Conversely, patient OI4 had surfaces rich with Osx at baseline (Figure 4.6A). Of the two bone samples from patient OI4 treated for 2 weeks, one bone sample maintained some surfaces of strong Osx expression while the other bone sample had less human-Osx expression compared to baseline.

Human-derived SOST was expressed by osteocytes in both 2 and 4-week treated and untreated implants. At baseline, SOST expression was variable ranging from minimal positive SOST-expressing osteocytes to moderate and even robust in a few cases. Following treatment, immunolocalization of SOST surrounding the osteocyte appeared more robust compared to the positive immunolocalized levels surrounding untreated control osteocytes at the same timepoint. SclAb treatment acts by inhibiting SOST which is a negative regulator of bone formation. The drug itself possesses a post-translational effect; it blocks the effects of the protein rather than halting the expression of SOST by the osteocytes. Holdsworth et al. reported a significant upregulation, or compensatory response, of SOST as measured by RT-qPCR (TaqMan) analysis following both a single dose and long-term treatment with SclAb. [347] We postulate that this compensatory response following SclAb treatment may explain the increased levels of immunolocalized SOST surrounding the osteocytes in the treated OI implants. Future studies should evaluate SOST gene expression using qPCR approaches in the human bone following treatment to confirm SOST upregulation.

Osteoblast differentiation into matrix-embedded osteocytes is a complex and not well understood process which includes a gradual transition to osteoid-osteocytes before differentiating fully into osteocytes. [383] By two weeks we confirmed the presence of mouse-derived Osx-expressing lining cells on some of the human implants; while human osteoblasts remain active up to three months, [384] the lifespan of a murine osteoblast is ~10-20 days. [385] While numerous studies report bone deposition rates, the time between osteoblast-osteocyte transformation is still not well understood and range from three days in young rabbits, [386] 2-5 days in newborn rats, [387, 388] and 10-19 days on periodontal surfaces in newborn mice. [385] Expression of SOST is indicative of a mature osteocyte phenotype and is expressed as early as during the onset of mineralization of the osteoid. [389, 390] SOST expression has been confirmed at low levels in osteoblasts, [389] yet its presence in the osteoid-osteocyte in humans and mice remains in question. [390-392] We postulate that it is feasible for these mouse osteoblasts to begin the differentiation process and express SOST by our 4 week timepoint (14 days after we observed mouse Osx expression) where immunolocalization of SOST in patient OI 6 treated and untreated implants near the bone surface appeared to be mouse-derived (absence of positive hMito, Figure 4.6C). Future studies using transgenic mice tagging cells of the osteoblast lineage could evaluate the host-osteoblast fate in the human xenograft bone tissue to validate our findings.

Similar to our model, Pettway and McCauley et al. described an ectopic ossicle bone model system utilizing donor bone marrow stromal cells (BMSCs), expanded *in vitro*, and implanted into an athymic murine host. The model represents a system where mesenchymal components are from the donor and hemopoietic cells are from the host. [376, 377, 393, 394] The authors observed an increase in marrow cellularity following 1 week of iPTH treatment, an anabolic response by 3 weeks of treatment and plateau in treatment response following 7 weeks. The authors hypothesized that the plateau was indicative of a time point where the host was incapable of supplying viable mesenchymal cells. In our study, SclAb stimulated new bone formation in the implanted bone tissue which significantly differed in both magnitude and rate when implant bone type was considered. Specifically, trabecular and morselized implants continued to respond in µCT markers of bone formation with longer treatment durations while cortical implants responded early (2 weeks) and appeared to demonstrate a similar plateau as discussed by Pettway et al. following 4 weeks of treatment. We hypothesize that trabecular implants did not reach a treatment plateau by 4 weeks due to two factors. First, the increased geometric quantities of surface-to-volume ratio inherent to trabecular and morselized samples appear to hold a greater capacity for bone-forming response to SclAb treatment. [370, 395] Second, both the trabecular and morselized bone contained rich donor-derived marrow progenitor cells which we believe were capable of osteoblast differentiation upon SclAb treatment. Upon removal from the patient, only 6% of the trabecular marrow elements stained positive for TUNEL, leaving a large population of viable donor osteoprogenitor cells that have the capacity to form new bone with anti-sclerostin therapy having local effects on osteoblastogenesis. [389, 396-398] When implementing the proposed model, treatment durations should be altered by implant bone type depending on the hypothesis tested.

Literature supports that SclAb acts in part by decreasing bone resorption through a decrease in osteoclast number. [399-401] We did not observe a significant reduction in Oc.N./B.Pm. in OI implants treated with SclAb. Interestingly, the implants with the highest osteoclast number following treatment were also the same implants that contained the most robust human-derived Osx expression on bone surfaces. Our TRAP findings are in line with those reported by Spatz et al. and Williams et al. where partial and no significant changes in markers of bone resorption, respectively, following SclAb treatment after short-term treatment schemes (≤ 4 weeks) in pre-clinical murine models. [402, 403] Because our model involves implantation of donor bone tissue into a host microenvironment, it is conceivable that increased osteoclasts in the treated implants were mouse-derived. The presence of mouse-derived osteoclasts has been observed in humanized xenograft models of bone metastasis. [404] Further supporting that osteoclasts were mouse-derived (host), Pettway et al. observed increased osteoclast number in Zoldronic acid treated ossicles at levels above untreated ossicles while circulating serum TRAP in the treated host mouse was well below serum TRAP levels in the untreated host. [377, 405] Moreover, the increased Oc.N./B.Pm in the treated implants may have been influenced by the lack of mechanical stimuli of the subcutaneously implanted bone where skeletal unloading leads to increased markers of bone resorption. [406, 407]

Some bone tissue continued to increase in µCT outcome parameters due to implantation alone which appeared to be a result of osteoblast-derived contributions from the host. Pettway and McCauley et al. observed increases in bone size in both vehicle (VEH) and treated ossicles at longer implant durations (7 weeks and a 3 week group where treatment or VEH was initiated following 12 weeks of untreated implantation). [393] In our study, untreated trabecular-derived and morselized implants demonstrated a positive increase in %changeBMD, %changeTMD and %changeBV/TV between 2 and 4 weeks (while cortical implants trended for a decrease with increasing implantation duration). Histomorphometry corroborated results with increased inter-label width and more robust osteoid seams were demonstrated trabecular and morselized 4 week untreated xenografts. As early as 2 weeks of untreated implantation, bone surfaces were lined with mouse-derived Osx expressing cells which increased in magnitude by 4 weeks indicating the origin of bone formation in the untreated implants is due in part to host-derived components acting on the donor bone. We postulate that we did not observe the same increase in the cortical implants perhaps because cortical implants, in contrast to trabecular and morselized implants, inherently contained fewer human-derived BMSCs/marrow cells at harvest and had less bone surface area available for remodeling.

A strength of the implant model is its ability to evaluate the effects of treatment in its target tissue while possessing the ability to monitor changes in the endogenous host bone. This provides a necessary internal positive control for the proposed treatment effects of the bone-forming therapeutic being considered. We observed a significant increase in µCT and dynamic histomorphometry markers of bone formation in treated mice compared to untreated using the host right femora for analysis. Results in the mice were consistent with prior work performed in our lab evaluating the effects of SclAb treatment. [362]

The time between bone harvest and implantation is an important consideration for donor bone cell survival. We evaluated the effects of tissue storage at 4˚C over the course of 48 hours to guide decision making regarding implantation latency duration and the potential for tissue banking and shipping tissue between OI centers for future diagnostic and treatment studies. At baseline, at the time human bone was implanted in the proposed xenograft model, trabecular bone experienced less apoptosis in the total tissue and the marrow ROI compared to cortical bone. Further, trabecular bone tissue (from the bone-only ROI) demonstrated fewer instances of apoptotic cells over the 48 hours compared to cortical bone. Over time, however, marrow space for trabecular bone did demonstrate greater amount of positive TUNEL cells compared to the cortical bone by the 24 and 48 hour time points. Taken together, it appears that 18 hours of storage at 4˚ C may be the upper limit following removal from the patient and that trabecular derived bone may have a greater capacity for bone cell survival through 18 hrs.

Conclusions

In summary, we propose a xenograft model using solid bone tissue derived from OI patients as a means to evaluate treatment response to novel therapeutics. We demonstrate that patient bone remains viable during implantation, contains human-derived bone cells for up to 12 weeks of implantation, and is bioaccessible by the host as early as 24 hours and systemic SclAb treatment in the host elicits a bone-forming effect in the implant. Response to treatment was variable; bone morphology, treatment duration and baseline cellular phenotype likely play important contributing roles. When donor/host response was evaluated, donor SOST remains present in all conditions while SclAb treatment appeared to dictate Osx expression in the implants. Differences in response in this heterogeneous OI bone tissue is of interest and could lead to understanding which patients would respond best to therapy. The successful implementation of the model may provide a safe approach to evaluate drug efficacy in a disease state without contraindications to the patient.

Figures

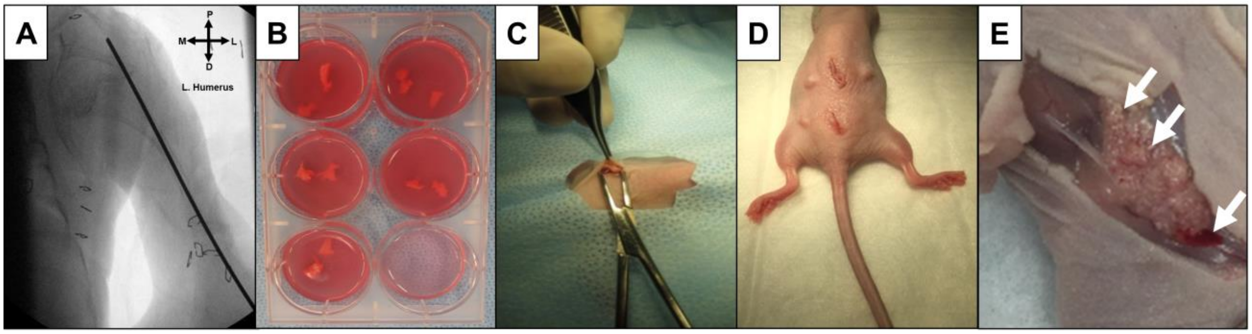

Figure 4.1: Bone tissue harvest and implantation process.
Radiograph from osteogenesis imperfecta (OI) patient OI 1, open reduction internal fixation (ORIF) surgery, left humerus (A). Bone samples typically discarded during orthopaedic surgery were collected into media (B), trimmed, and implanted subcutaneously on the dorsal side of a 4-6 week nude mouse through a 1 cm posterior incision adjacent to the spinal column in the lumbar region (C,D). Upon removal (E), implanted bone is rich with host blood vessels (white arrows). Each patient yielded ~3-20 samples.

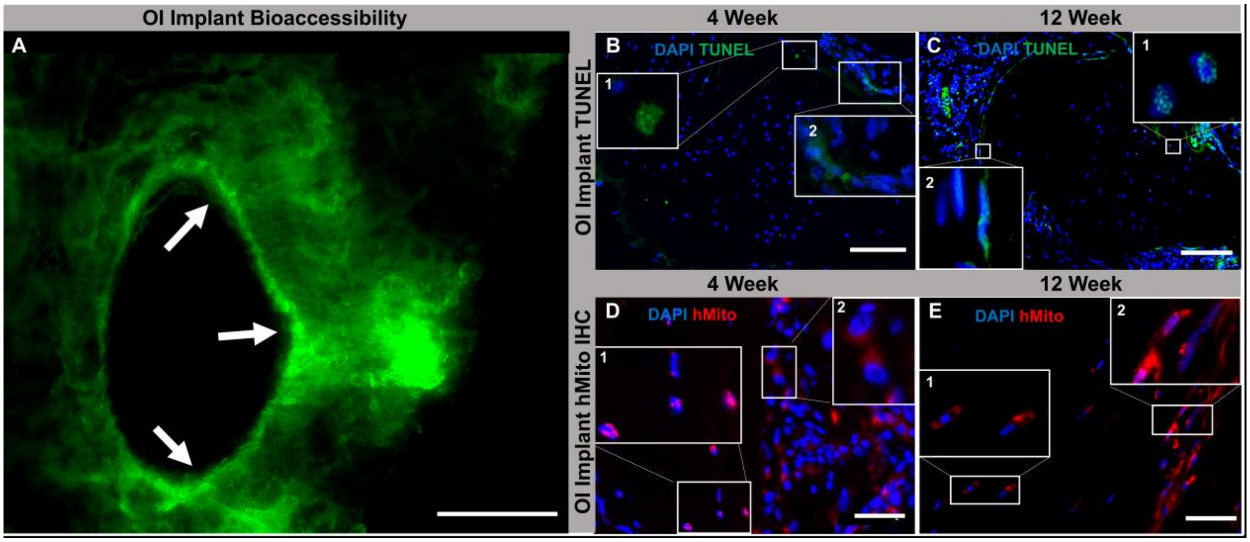

Figure 4.2: Donor bone is bioaccessible, viable, and donor-derived bone cells are present for up to 12 weeks.

Bioaccessibility, bone cell viability and presence of donor cells in the human-derived implant. One subcutaneous administration of calcein (30 mg/kg) to the host 24 hours following implantation demonstrated a definitive calcein label (green label, white arrow) present on the implant bone surface upon removal 24 hours after injection (A). TUNEL assay results following intermediate (B) and long-term (C) implantation duration (4 weeks and 12 weeks untreated) demonstrate minimal positive TUNEL cells (green; DAPI=blue) at each time point; insets (1) positive apoptotic osteocyte(s) and (2) example of positive apoptotic progenitor and lining cell populations. Immunolocalization (IHC) of donor derived cells using human mitochondria primary antigen (hMito=red; DAPI=blue) at 4 weeks (D) and 12 weeks (E) demonstrate human-derived osteocytes (inset 1) and bone rich with human-derived lining cells (inset 2) in the OI implant. A, D-E acquired at 40x (50 µm scale bar) from patient OI 3 (Type III OI) and patient OI 2 (Type I OI), respectively; B-C acquired at 20x (100 µm scale bar) from patient OI 1 (Type III OI). OI= osteogenesis imperfecta.

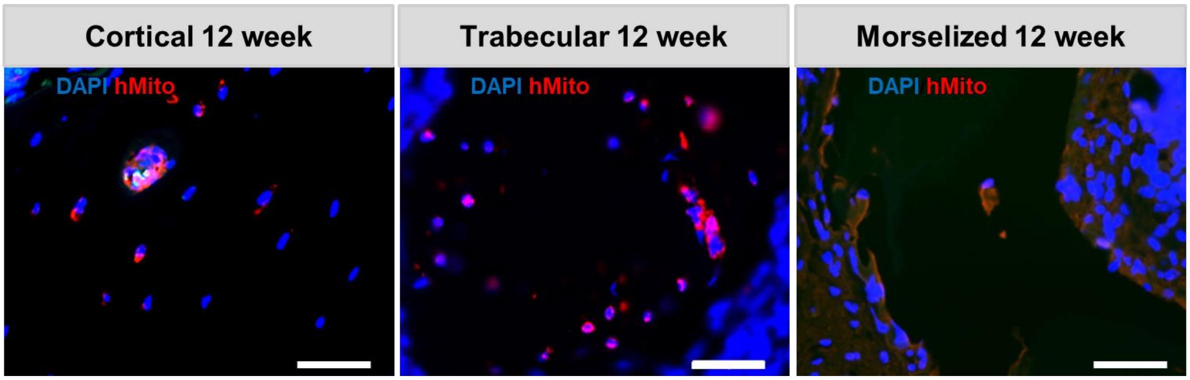

Figure 4.3: Immunolocalization of human mitochondria in osteogenesis imperfect (OI) and non-OI control bone implants following 12 weeks of implantation in the xenograft model.
In all cases, OI and non-OI control bone tissue presented with human-derived bone cells and bone lining cells that stained positive for human mitochondria (hMito, red) antibody following 12 weeks of implantation (the longest implantation time point). While all bone tissue stained positive for hMito, the amount of stain appeared to be dictated by bone type (cortical (left) or trabecular (middle) derived bone from OI patients and morselized (right) bone tissue from non-OI controls). OI cortical implant from patient OI 1, OI trabecular implant from patient OI 2 and non-OI morselized implant from patient non-OI 1. All images acquired at 40x magnification with a 50 µm scale bar.

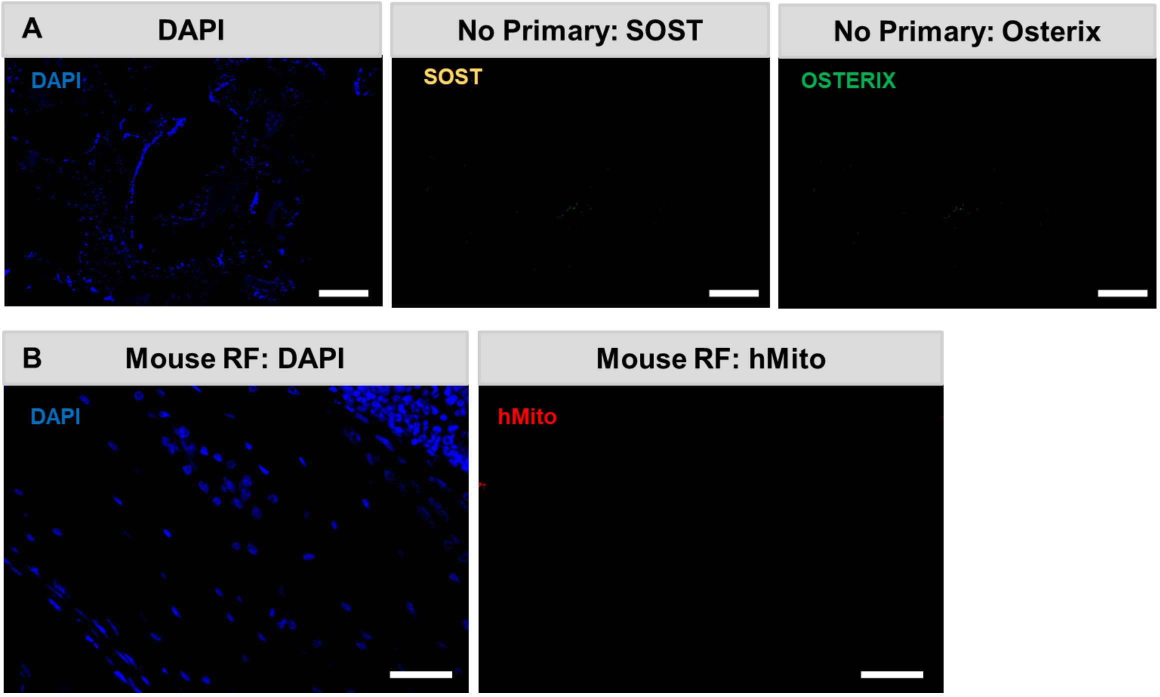

Figure 4.4: Results from immunohistochemistry control slides.
No specific staining was observed in osteogenesis imperfect (OI) bone tissue when primary antibodies for SOST or osterix was omitted (no primary control) (A). Top left depicts DAPI nuclear stained section (blue), top middle is the no primary control for SOST (yellow) and top right is the no primary control for osterix (green). Human osteogenesis imperfect bone tissue images from patient OI 1 obtained at 4x magnification with a 500 µm scale bar. No species cross-reactivity was observed in mouse (host) right femoral (RF) control tissue when stained with human mitochondria (hMito) primary antibody (B). Left panel depicts DAPI nuclear stain (blue) and right panel depicts no fluorescence from the hMito antibody (red) ensuring the specificity of the antibody. Mouse RF images obtained at 40x with a 50 µm scale bar.

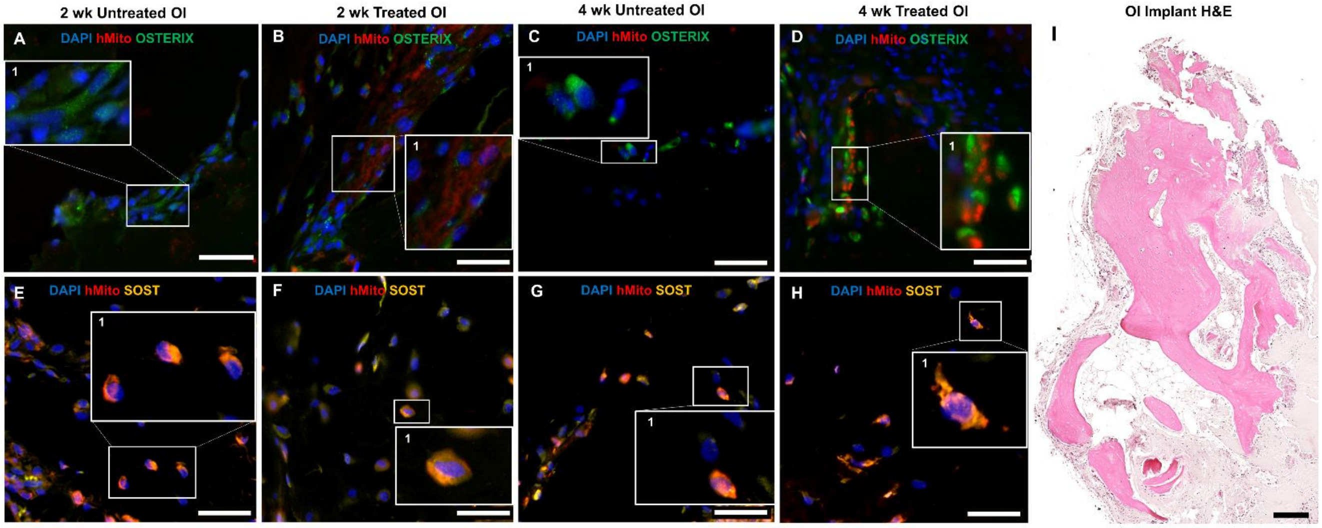

Figure 4.5: Immunohistochemistry with fluorescence (IHC-F) to assess donor/host relationship. Human osteogenesis imperfecta (OI) implants were dual IHC-F stained to probe for the presence of Osterix (Osx; green) and human mitochondria (hMito; red) (A-D) and on serial sections, Sclerostin (SOST; yellow) and hMito (red) (E-H). In all cases, hMito was used to indicate donor derived cells and Osx or SOST primary antibody (validated sensitivity to both mouse and human antigens) were used to probe all instances of expression (both host and donor). Zoomed insets (1) depict lining cells expressing Osx (A-D) and osteocytes expressing SOST (E-H). Images were acquired at 40x (50 µm scale bar). DAPI= nuclear stain (blue). Panel represents data from one OI patient (OI 6, Type III/IV OI) who yielded cortical-derived bone samples (I), hematoxylin and eosin (H&E) stained implant acquired at 20x with a 250 µm scale bar.

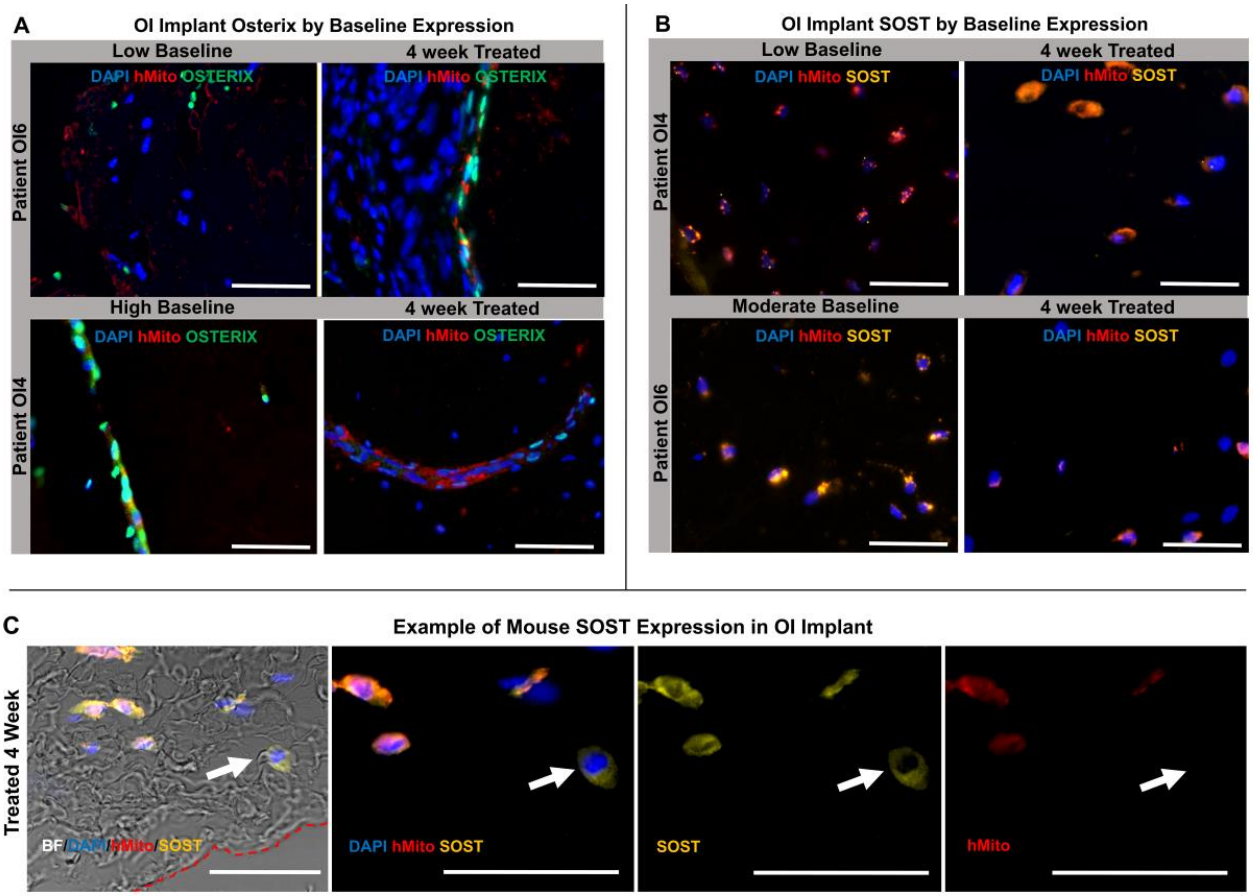

Figure 4.6: Influence of baseline human osterix (Osx) and SOST expression on treatment response in OI patient implants.

Low baseline Osx expression upon removal from the patient increased following 4 weeks of treatment and remained primarily donor-derived. An OI patient with high baseline Osx expression demonstrated minimal Osx expressing cells following 4 weeks of treatment (A). A similar pattern was observed with SOST expression; low baseline levels appeared to increase in expression following treatment while patients with robust baseline IHC SOST staining still had had osteocytes expressing SOST but staining levels were less pronounced (B). Tissue from one OI patient demonstrated the presence of host-derived (mouse) SOST-expressing osteocytes (example, white arrow) near the implant bone surface (red dashed line in brightfield (BF) image) following 4 weeks of treatment (C). In all cases, hMito (red) was used to indicate donor derived cells and Osx (green) or SOST (yellow) primary antibody (validated sensitivity to both mouse and human antigens) probed all expression regardless of species. Images were acquired at 40x (50 µm scale bar). OI= osteogenesis imperfecta; DAPI= nuclear stain (blue).

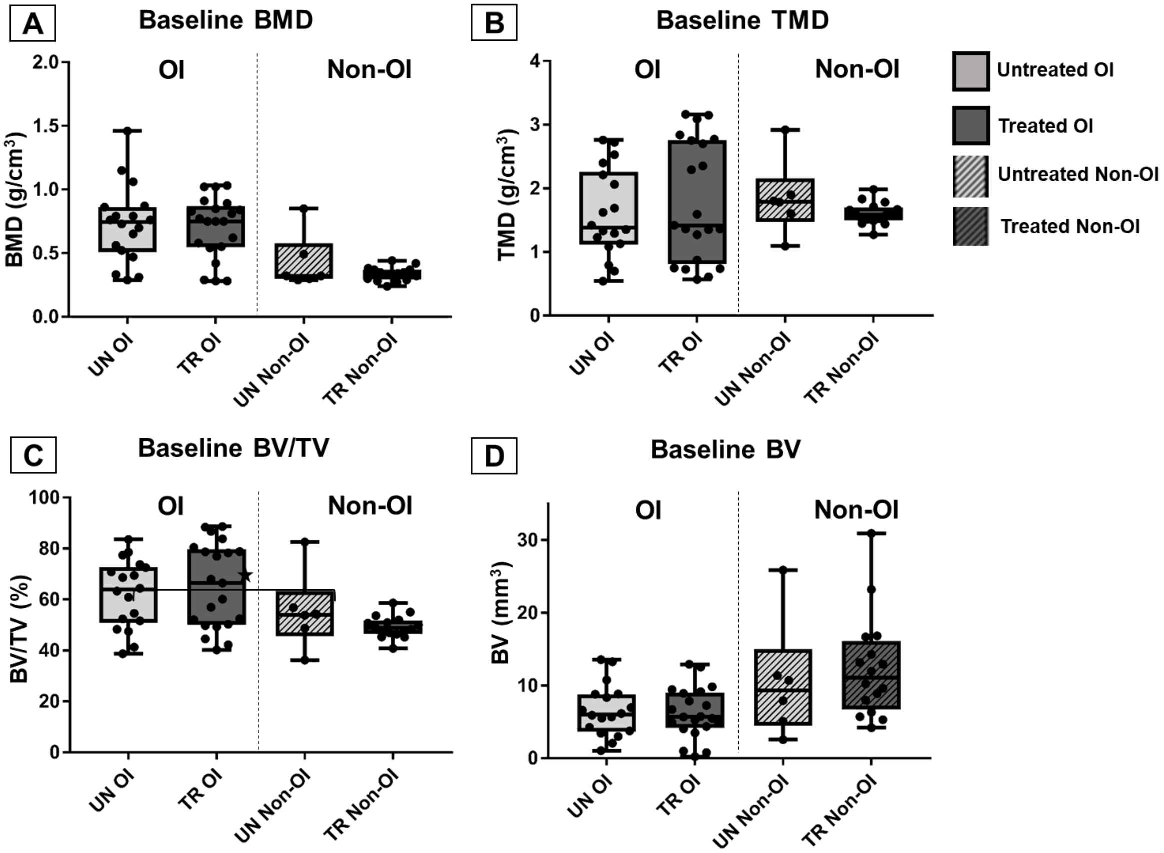

Figure 4.7 Baseline in vivo µCT confirmed no significant differences between µCT parameters at time of implantation.

In vivo µCT baseline BMD (A), TMD (B),BV/TV (C), and BV (D) acquired 24 hours following implantation are plotted for 2 + 4 week treated and untreated OI and non-OI groups. No significant differences in baseline BMD (A), TMD (B), BV/TV (C), and BV (D) between randomly assigned untreated and treated OI and untreated and treated non-OI implant groups was observed. Results indicate equality between randomly assigned treated and untreated patient groups at baseline prior to treatment initiation. OI= osteogenesis imperfecta; BMD = bone mineral density; TMD = tissue mineral density; BV/TV = bone volume fraction; BV = bone volume.

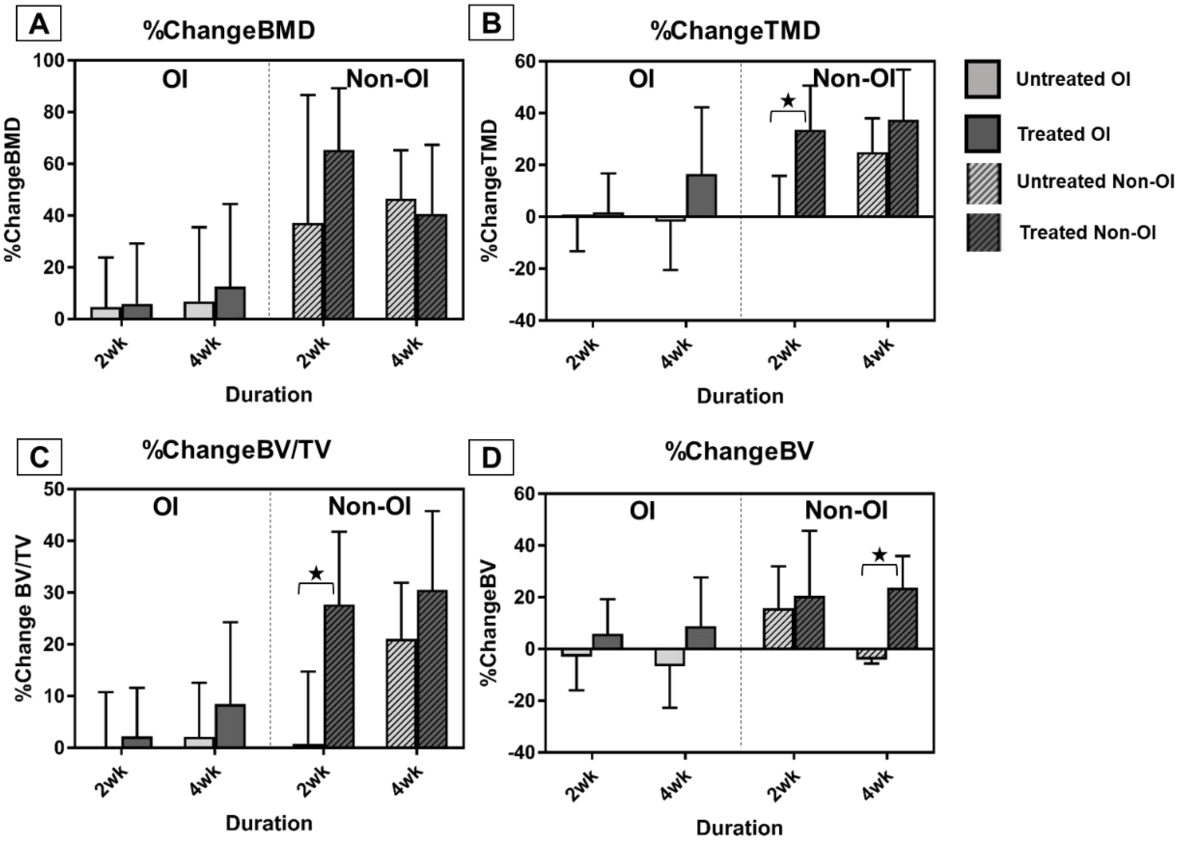

Figure 4.8: Longitudinal in vivo µCT outcomes for two and four week treated and untreated osteogenesis imperfect (OI) and non-OI implants.

Mean ± standard deviation of in vivo µCT derived %changeBMD (A), %changeTMD (B), %changeBV/TV (C) and %changeBV (D) for treated and untreated 2 and 4 week OI and non-OI implants. %change values were derived as the change from pre- µCT acquisition acquired 24 hours following implantation (baseline) and post- µCT acquired immediately following sacrifice. Direct comparisons of µCT outcome measures were carried out with paired test for 2 and 4 week data within patient type (OI and non-OI) where significance is denoted by brackets and stars. In all cases, statistical significance was set to $p<0.05$. OI= osteogenesis imperfecta; BMD = bone mineral density; TMD = tissue mineral density; BV/TV = bone volume fraction; BV = bone volume.

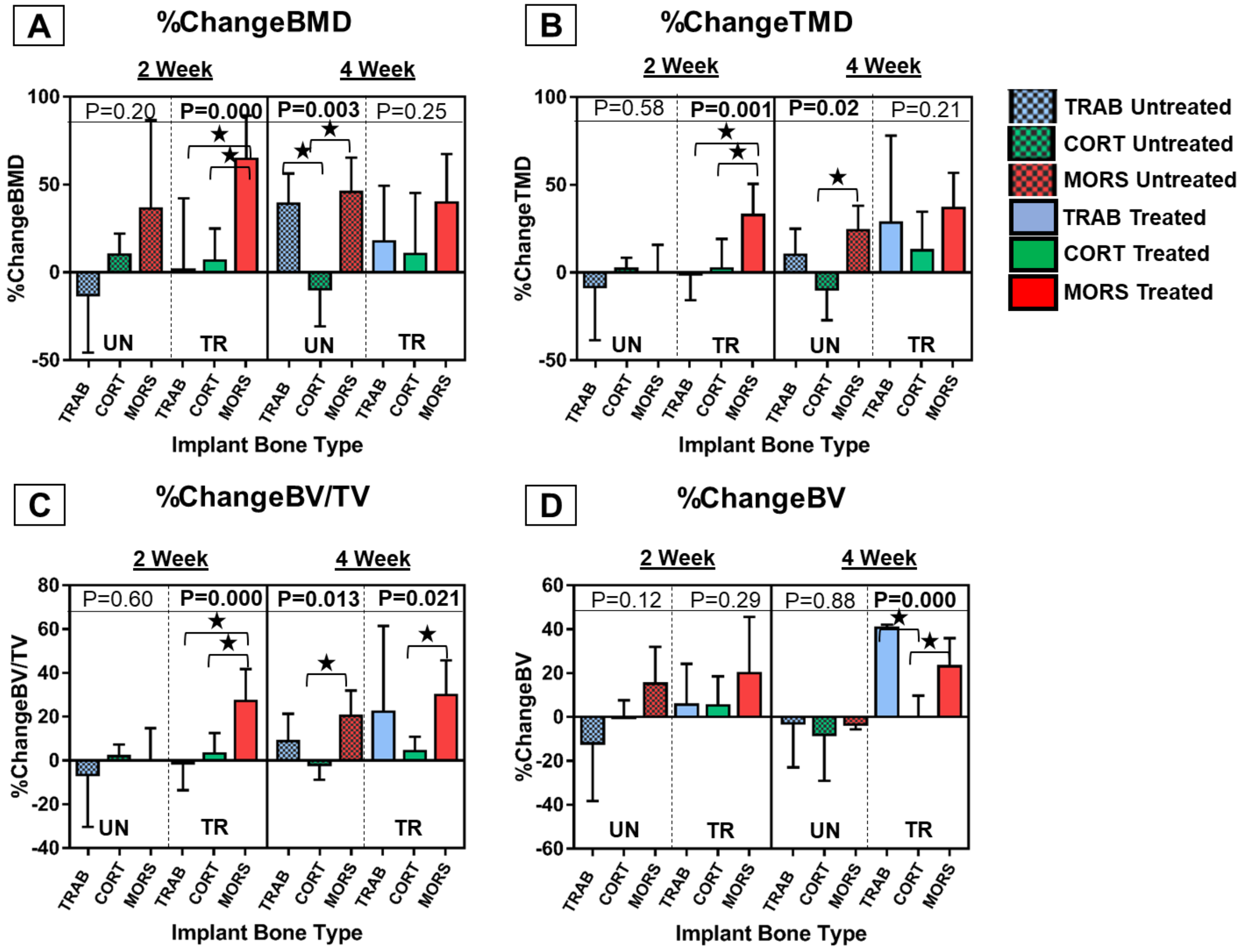

Figure 4.9: In vivo μCT confirms a variable bone-forming treatment effect that changes in magnitude by implant bone type.

ANOVA results with Bonferonni correction of *in vivo* implant μCT results by bone type for two and four week treated and untreated implants. Mean ± standard deviation of *in vivo* μCT derived parameters of %changeBMD (A), %changeTMD (B), %changeBV/TV (C) and %changeBV (D) for trabecular-derived implants, cortical-derived implants and morselized implants are plotted. ANOVA p-values are reported and bolded when a significant effect of bone type was detected at $p \leq 0.05$. Significance between bone type within condition, assessed via post-hoc analysis with a Bonferonni correction, is denoted by brackets and stars. Trabecular and cortical implants originated from OI patients while morselized implants originated from non-OI patients. OI= osteogenesis imperfecta; TRAB= trabecular; CORT= cortical; MORS= morselized; BMD = bone mineral density; TMD = tissue mineral density; BV/TV = bone volume fraction; BV = bone volume.

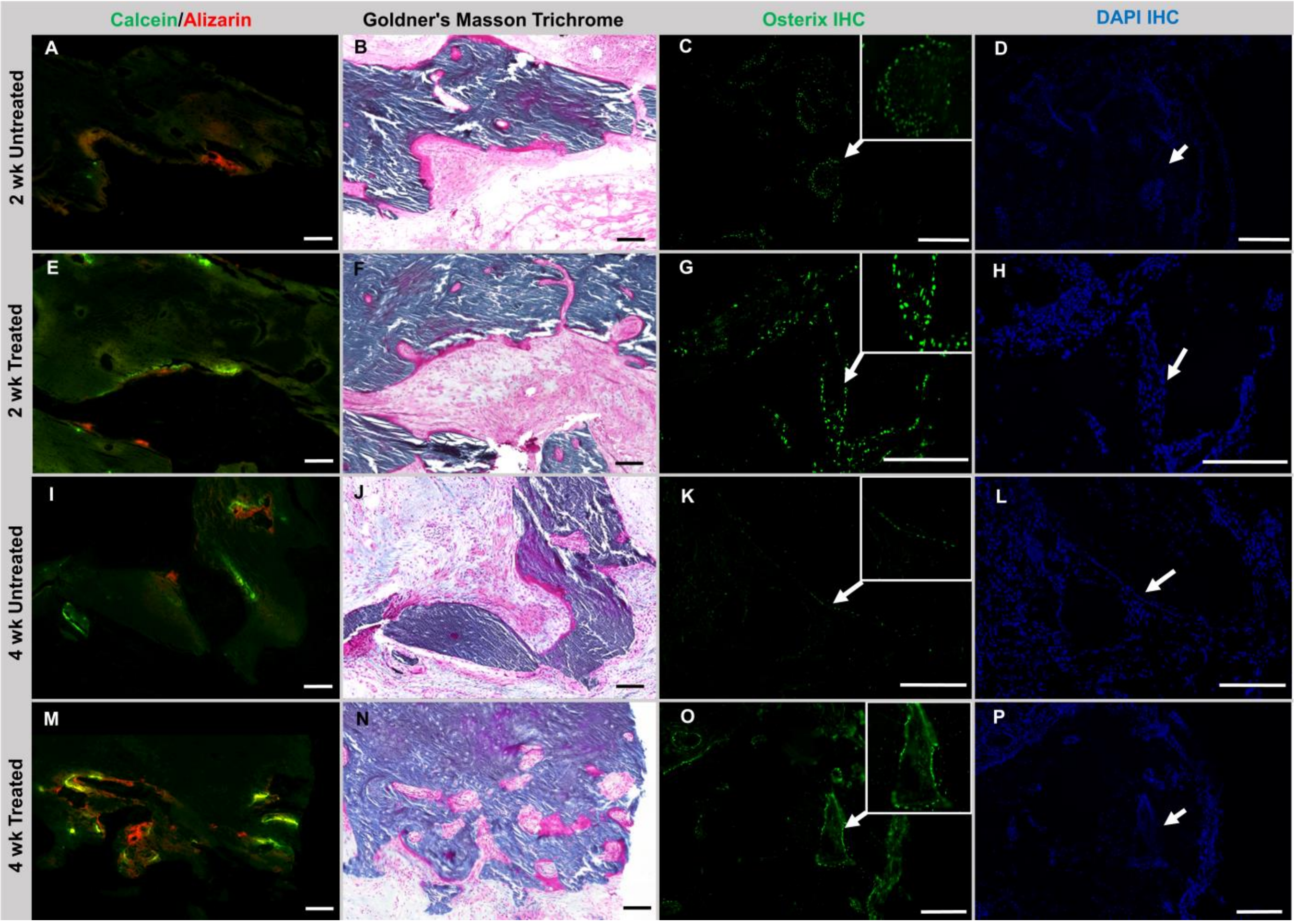

Figure 4.10: Implant histomorphometry findings and immunolocalization of osterix corroborate µCT results.

Calcein (green) and alizarin (red) fluorochrome bone labeling, serial Goldner's Masson trichrome (GMT), and immunohistochemistry (IHC) with fluorescence of osterix (green) and corresponding DAPI (blue) nuclear stained images for one patient at 2 (A-D) and 4 week (I-L) untreated, 2 (E-H) and 4 week (M-P) treated. SclAb treated implants presented with a definitive calcein and alizarin label and greater inter-label width (E,M) compared to weaker and non-specific labeling observed in untreated conditions (A,I). GMT osteoid seams corresponded to areas of fluorochrome labeling (B,F,J,N). Osterix expression on implant bone surfaces was strong in treated implants and increased with treatment duration (G, O). Untreated implants at 2 weeks displayed osterix on bone surfaces which diminished by 4 weeks untreated (C, K). Calcein/alizarin images and GMT were acquired at 10x (100 µm scale bar) and IHC images at 20x (250 µm scale bar). Panel represents data from one OI patient (OI 4, Type III OI, cortical-derived implant). Due to the tissue processing requirements for histomorphometry (undecalcified plastic processing) and immunohistochemistry (decalcified paraffin processing) images are parallel implants harvested from the same OI patient (OI 4).

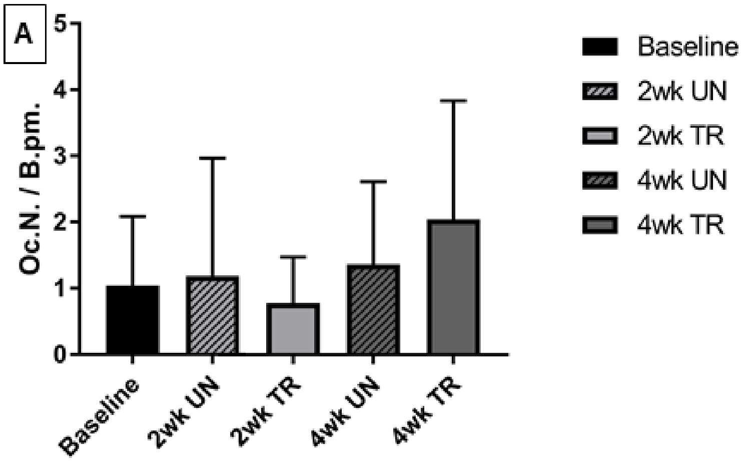

B

Condition	N	B.pm. (mm)	Oc.N.	Oc.N / B.pm.	SD
Baseline (time 0)	8	37.42	35.25	1.04	0.97
2 wk UN	4	30.05	18.50	1.19	1.54
2 wk TR	5	42.51	22.80	0.78	0.62
4 wk UN	5	46.62	41.00	1.37	1.12
4 wk TR	4	53.83	81.25	2.05	1.56

Figure 4.11: Sclerostin antibody did not significantly alter bone resorption in the implants. TRAP results from baseline (time 0) and 2 and 4 week SclAb-treated and untreated OI implants (A, B). No statistically significant differences were observed in measures of osteoclast number per bone perimeter (Oc.N./B.pm.) between groups. The Oc.N./B.pm. decreased below baseline and untreated levels following 2 weeks of SclAb treatment (not sig.) and increased above all other groups following 4 weeks of treatment. The entire implant bone surface was used as the region of interest (ROI). Statistical significance was set to $p \leq 0.05$. OI= osteogenesis imperfecta; UN= untreated; TR= treated; Oc.N.= osteoclast number; B.pm.= bone perimeter; SD= standard deviation.

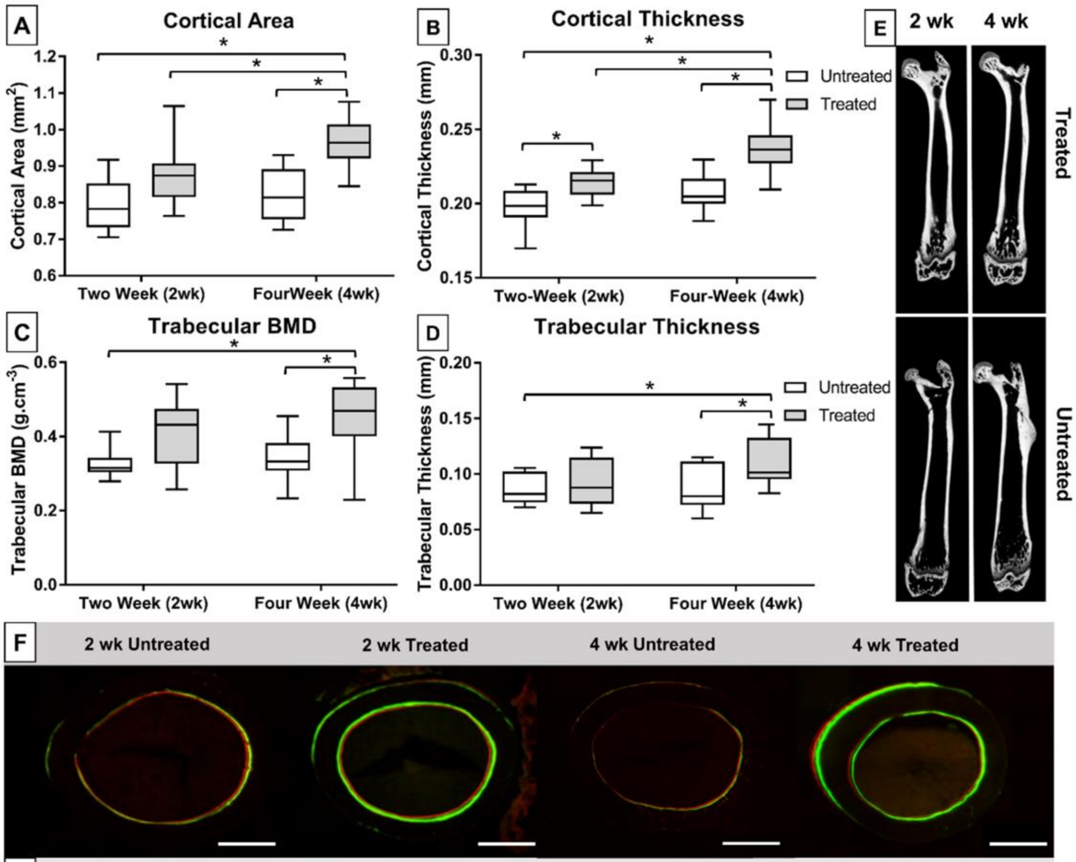

G

	2 wk Untreated (n=10)	2 wk Treated (n=16)	4 wk Untreated (n=8)	4 wk Treated (n=13)	Treatment p-value	Duration p-value	Interaction p-value
Endosteal							
MS/BS	0.64 ± 0.27	0.91 ± 0.16 *	0.68 ± 0.22	0.88 ± 0.15 +	**<0.001**	0.919	0.581
MAR	0.73 ± 0.25	1.35 ± 0.60 *,%	0.72 ± 0.31	0.93 ± 0.47	**<0.01**	0.158	0.171
BFR/BS	0.46 ± 0.27	1.27 ± 0.67 *,%	0.48 ± 0.22	0.84 ± 0.51	**<0.001**	0.205	0.149
Periosteal							
MS/BS	0.27 ± 0.19	0.55 ± 0.14 *	0.37 ± 0.22	0.52 ± 0.14 +	**<0.001**	0.497	0.210
MAR	0.49 ± 0.26	0.97 ± 0.40 *	0.60 ± 0.27	0.93 ± 0.47	**<0.001**	0.864	0.383
BRF/BS	0.13 ± 0.13	0.55 ± 0.30 *,%	0.24 ± 0.24	0.47 ± 0.20 +	**<0.0001**	0.845	0.185

Two-Way ANOVA results are bolded when significance is reached at p=0.05. Follow-up Tukey's post-hoc determined significance indicated by:
*TR 2 wk vs. UN 2 wk, +TR 4 wk vs. UN 2 wk, %TR 2 wk vs. UN 4 wk.

Figure 4.12: Host mouse femora confirmed a systemic bone-forming effect of SclAb treatment. Quantitative µCT analysis host (mouse) femora reveal a significant bone-forming response to SclAb treatment compared to untreated controls in measures of cortical area (A), thickness (B) and trabecular bone mineral density (BMD) (C) and thickness (D) at 2 and 4 weeks. Significance is indicated by brackets and stars (*) when reached ($p \leq 0.05$). Representative *ex vivo* µCT images of mouse femora at 2 and 4 week treated with SclAb (top) and untreated (bottom) (E). Treated 2 week n=14, untreated 2 week n=10, treated 4 week n= 13, untreated 4 week n=11. Representative cross-sectional dynamic histomorphometry images of femora demonstrate stronger calcein (green) and alizarin (red) labeling, including increased inter-label width, following 2 and 4 weeks of SclAb treatment compared to untreated controls (F). Results from endosteal and periosteal mineralizing surface/bone surface (MS/BS), mineral apposition rate (MAR) and bone formation rate/bone surface (BFR/BS) for all groups is presented as mean ± SD with statistical significance indicated ($p \leq 0.05$) (G). Dual label was not present on all surfaces (preventing MAR measurements in some cases) and was treated as a missing value. Treated 2 week n=16, untreated 2 week n=10, treated 4 week n= 13, untreated 4 week n=8. Images acquired at 20x (500 µm scale bar).

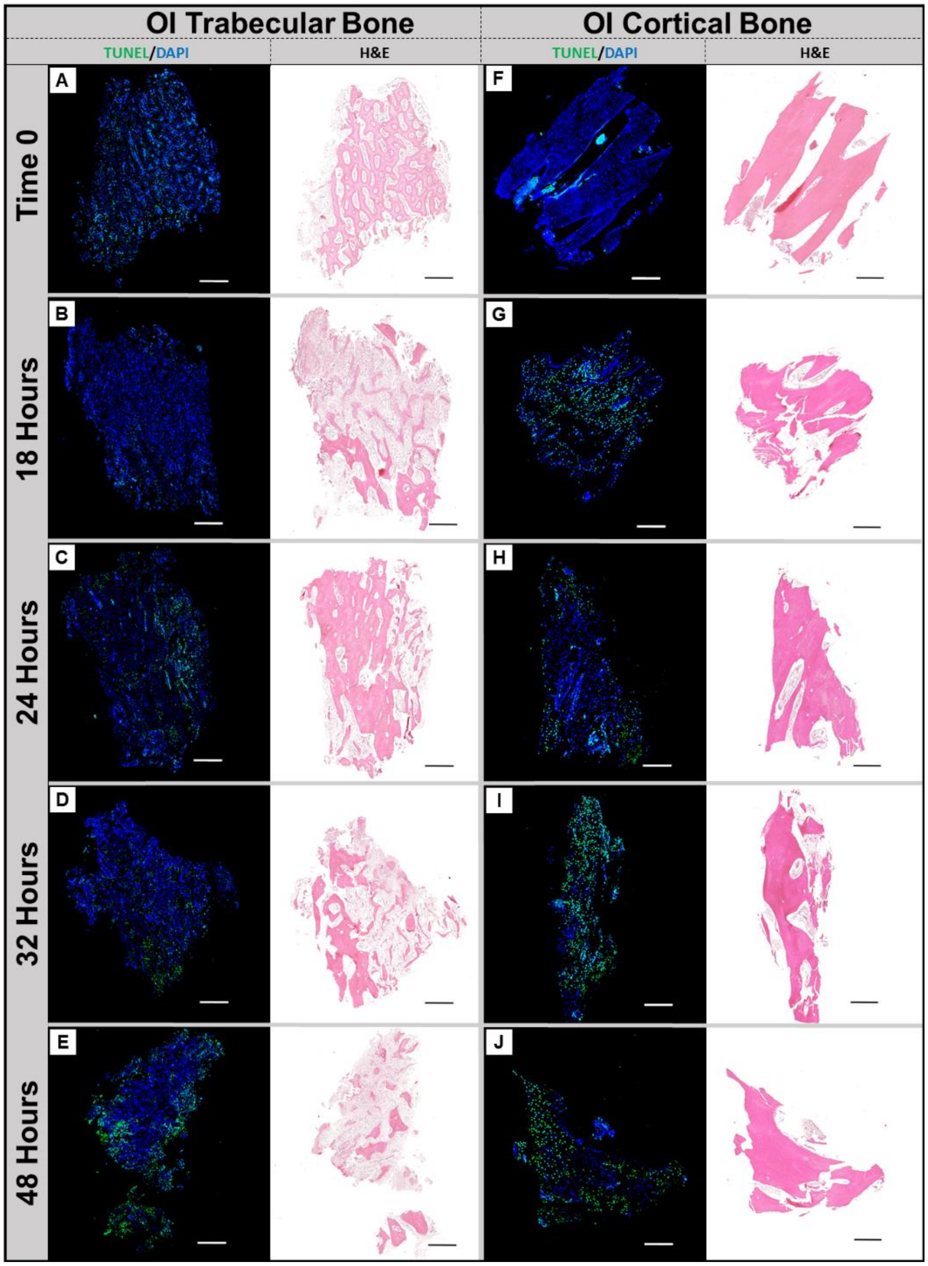

Storage Duration	OI Trabecular Bone			OI Cortical Bone		
	Total Tissue (tot.TUNEL/tot. DAPI)	Bone ROI (tot.TUNEL/tot. DAPI)	Marrow ROI (tot.TUNEL/tot. DAPI)	Total Tissue (tot.TUNEL/tot. DAPI)	Bone ROI (tot.TUNEL/tot. DAPI)	Marrow ROI (tot.TUNEL/tot. DAPI)
Time 0 (baseline)	5%	4%	6%	12%	3%	25%
18 Hours	19%	14%	20%	54%	63%	38%
24 Hours	64%	40%	82%	47%	45%	50%
32 Hours	33%	42%	30%	60%	70%	48%
48 Hours	61%	56%	62%	71%	95%	39%

Tot=total; ROI=region of interest

Figure 4.13: Bone tissue morphology dictates donor cell apoptosis rates in osteogenesis imperfect (OI) bone tissue following harvest and during storage.
OI patient trabecular-derived and cortical-derived bone was evaluated for donor cell apoptosis using a TUNEL assay at baseline and following storage four time points (18, 24, 32 and 48 hrs) in αMEM/10% FBS at 4° C. TUNEL assay results from trabecular bone (A-E) and cortical bone (F-J) (left) and serial hematoxylin and eosin (H&E, right) are displayed. Detailed TUNEL results, presented as a percent of total TUNEL positive cells/total DAPI stained cells for a total tissue ROI, bone only ROI and marrow only ROI for the trabecular and cortical bone at each time point is depicted (K). Positive TUNEL apoptotic cells are shown in green and DAPI nuclear stain (highlighting all cells) in blue. Trabecular bone was harvested from OI 7 (Type III OI) and cortical from OI 8 (Type III OI). All images acquired at 20x (500 µm scale bar).

Tables

Table 4.1: Pediatric osteogenesis imperfect (OI) and non-OI control patient demographics.

Patient	OI Type	Analysis Type	Surgical Indication	Drug TR History	Harvest Location	Age	Sex	Bone Sample Yield (baseline/implant)
OI								
OI 1	III	Xenograft	Open Reduction Internal Fixation	Depo-testosterone	L Humerus	17	M	1/9
OI 2	I	Xenograft	Implant Exchange	Vitamin D2	R Tibia	14	M	2/18
OI 3	III	Xenograft	Fracture	Ca Carbonate, Vitamin D2	R Humerus	17	F	1/11
OI 4	III	Xenograft	Bowing of Femur over Rod	Ca Carbonate, Vitamin D2	R Metaphyseal Femur	18	F	1/6
OI 5	III/IV	Xenograft	Bilateral, Multiple Osteotomies	None	R&L Femur	16 mo	F	1/2
OI 6	III/IV	Xenograft	Osteoplasty	Ca Citrate-Vitamin D3	R Femur	23	F	1/8
OI 7	III	Storage Pilot	Revision	Depo-testosterone	L Ulna/Radius	17	M	6 (Storage Pilot)
OI 8	III	Storage Pilot	Osteotomy	None	R Tibia/Fibia	21	M	6 (Storage Pilot)
Non-OI								
Non-OI 1	Unaffected	Xenograft	ACL Reconstruction	N/A	Tibial Reaming	15	F	4/9
Non-OI 2	Unaffected	Xenograft	ACL Reconstruction	N/A	Tibial Reaming	14	M	1/9
Non-OI 3	Unaffected	Xenograft	ACL Reconstruction	N/A	Tibial Reaming	10	M	2/12

Chapter 5 *In Vivo Quantitative Imaging Biomarkers of Bone Quality and Mineral Density using a Novel 3D Zero Echo Time Magnetic Resonance Imaging Approach*

Introduction

In bone diseases of altered remodeling such as osteoporosis, current clinical practice relies primarily on ionizing x-ray-based approaches to characterize the mineral phase of bone. [23-25, 27, 28] While mineral is the focus of x-ray based measures, it is understood that bone is a composite material composed of ~35-45% mineral crystals composed of hydroxyapatite, ~40% organic matrix including type I collagen, proteoglycan and glycosaminoglycan, and ~15-25% water existing as free (in Haversian and Volkmann's canals) and bound (hydrostatically to organic matrix constituents), by volume. [29] Each are critical components to bone quality and fragility and may change independently, or together, with disease progression and in response to treatment. [30, 31] Even so, there is a near ubiquitous reliance on bone mineral density (BMD) to predict mechanical properties and ultimately serve as an *in vivo* surrogate for treatment efficacy, while ignoring these other important contributors of bone strength. [23] However, the literature largely supports that BMD is an incomplete measure since it accounts for only ~60% of bone strength and may not adequately predict fracture risk. [32, 33]

Despite the prevalence of radiographic techniques that are used to predict fracture risk through alterations in BMD, it has become increasingly evident that additional factors, commonly referred to as markers of bone quality, play an important and unique role in governing the mechanical integrity of the bone and its overall health. [29, 227, 408, 409] Importantly, these factors are not interpretable from traditional radiographic imaging approaches, but rather rely on invasive or *ex vivo* techniques to quantify changes. For example, traditional pre-clinical targets typically involve end-stage tissue resection to perform histology. This requires study designs to include matched treatment/control groups (cross-sectional) limiting longitudinal *in vivo* analysis adding both cost and use of animal. [35, 36] Therefore, the ability to non-invasively measure biochemical processes and material-level changes *in vivo* as they relate to bone pathophysiology represents a powerful tool to guide therapeutic development and subsequent clinical trials [34] where the desire for non-destructive imaging biomarkers to characterize mineral in addition to the remaining material-properties is immense and equally unmet.

There are a number of clinically available imaging modalities whose application in bone appear promising but have not yet been fully exploited. [37, 38] One such clinically available modality, magnetic resonance imaging (MRI), is gaining interest for its sensitivity to biochemical composition and its rich dynamic range. However bone appears as a signal void in conventional MRI bone since it is unable to "capture" bone's inherently ultra-short transverse relaxation time (T_2) due to time domain constraints (echo time, TE and repetition time, TR). In bone, proton signal intensity is drawn from a limited hydrogen pool which includes water residing in microscopic Haversian canals and lacuno-canaliculi systems (free water, $T_2 > 1$ ms), matrix water bound to collagen (bound water, $T_2 << 1$ ms) and protons of the collagen backbone/sidechain ($T_2 < 0.1$ ms). [29, 39] The extremely short T_2 relaxation times for these three pools are directly related to the movement allotted by the protons following excitation in MRI. [40] In recent years, a number of remarkable advances have been proposed for both the qualitative and quantitative evaluation of short T_2 species with the advent of ultra-short echo time (UTE) MRI. [41, 42] However, UTE's minimal TE caused by transmit/receive switching time may miss the shortest T_2 proton pools in bone, specifically those associated with collagen.

Zero-echo time (ZTE) technologies such as 3D radial SWeep Imaging with Fourier Transformation (SWIFT) MRI can overcome this limitation providing sensitivity to highly ordered and mineralized tissue allowing for imaging of all compositional elements of bone [45, 410]. SWIFT is an entirely different class of ZTE; the time domain signals are acquired in a time-shared manner during a swept radio frequency (RF) excitation. [289] This results in virtually no acquisition delay (TE=0) allowing it to overcome the rapid signal loss due to low and restricted proton concentrations. [289] Initial proof-of-concept studies applying SWIFT to bone and calcified cartilage have been favorable. [295-298, 318] Due to technical constraints on achieving this nominal TE, conventional SWIFT has an upper limit on bandwidth (BW), or the range of frequencies (in Hz) allowed in the imaging signal. Lower BW may be insufficient in capturing all excited short T_2 species and can lead to an increase in susceptibility artifact. This is particularly problematic in bone where the cortices have the largest pool of strongly diamagnetic calcium salt in the body and shares its biological boarder with lesser diamagnetic tissues such as muscle, fat, marrow and the periosteum which can result in magnetic field distortions. To address the limitation on BW, multi-band SWIFT (MBSWIFT) has been introduced which makes use of sidebands generated by gapping the RF pulse. [299] As a result, MBSWIFT can achieve high excitation BW and in theory mitigate susceptibility artifact at the cortical bone interfaces during *in vivo* imaging.

MBSWIFT could have a novel and specific application in bone research where capturing the mineral and the remaining 40% of the tissue that confers quality and strength to bone is highly desired. Using MBSWIFT, we sought to describe a comprehensive (although not exhaustive) set of MRI biomarkers to characterize aspects of bone quality that go “missed” when using gold-standard bone imaging approaches (e.g., clinical DXA, pre-clinical µCT).

Specifically, we employed MBSWIFT to quantify cortical water, cortical matrix T_1 relaxation times (a tissue-specific biomarker where measures are related to tissue organization) and marrow fat longitudinally following ovariectomy in growing rats. Further, we established the efficacy of MBSWIFT to directly measure changes in BMD in comparison to µCT. Findings contribute to the overall goal of establishing a potential imaging strategy to simultaneously quantify material-level and biochemical alterations in bone safely, without the use of ionizing radiation.

Materials and Methods

Animal model and study design

All animal procedures were approved and conducted in accordance with the University's Institutional Animal Care & Use Committee (IACUC) in compliance with the Animal Care & Use Office (ACUO) guidelines. Seven female Sprague Dawley rats, six weeks old, were housed randomly (2-3 per cage) and fed a standard rat chow diet with access to tap water at libitum. All rats were subject to bilateral ovariectomy (OVX) following baseline imaging (described in detail in the next section). In short, bilateral OVX was performed using a dorsal approach through 2 cm incisions from the second to fifth lumbar vertebrae ventral to the rector spinae muscles below the last rib. Sutures were placed around the cranial portion of the uterus and uterine vessels and the ovaries and oviducts were excised.

To track longitudinal changes in bone following estrogen deficiency in the growing rats, *in vivo* imaging of the right proximal tibia included µCT, a conventional MRI sequence with the lowest achievable TE, and the experimental ZTE MBSWIFT MRI approach described in detail below. *In vivo* imaging occurred at baseline 48 hours prior to OVX procedure and at 2, 4, 10 and 12 weeks post-OVX surgery. All rats were euthanized following the 12 week imaging timepoint. Successful OVX was confirmed by assuring uterine horn atrophy during necropsy.

In vivo Magnetic Resonance Imaging (MRI)

In vivo high-field magnetic resonance imaging was performed with an Agilent 9.4T small animal imaging system (31 cm horizontal bore, Agilent Technologies Inc., Santa Clara, CA) running VnmrJ software (version 2.3 A) using a 33 mm diameter surface coil composed of materials (Teflon) not visible with ^{1}H MRI even when using MBSWIFT. This ensures that no unwanted signal would fold into the field of view (FOV) from the coil. Rats were anesthetized and imaged under 2% isoflurane inhalation and right tibiae were immobilized and secured so that the region of the proximal tibial growth plate was within the coil iso-center and aligned in the same direction for maintenance of a specific flip angle (FA) and to avoid radiofrequency (RF) non-uniformity.

A table of MRI scanning parameters for the study can be found in Table 5.1**.** MBSWIFT images were acquired at three FAs in order to derive T_1 relaxation times (using the variable flip angle method described in detail in the next section); one at the Ernst angle, one below and one above the Ernst angle. At each of the three FA, the following three saturation schemes were acquired; fat saturation, water saturation and no saturation. Fat saturation which was obtained by applying a hyperbolic secant (HS4)[289] saturation pulse of 1-kHz bandwidth centered at fat resonance frequency after every 16 views (MBSWIFT-FS). Water saturation was similarly applied at water resonance frequency (MBSWIFT-WS). Images without saturation were acquired with identical timing parameters (MBSWIFT-NS). The use of fat suppression with MBSWIFT (MBSWIFT-FS) removed almost all signal contributed by fat in the bone including the fatty bone marrow, whereas water saturation (MBSWIFT-WS) left only the signal arising from visible fat. All MBSWIFT acquisitions made use of 128 sidebands in order to achieve a bandwidth (bw) of 1395 Hz. 800 dummy projections were applied prior to the first spatial encoding and 32 dummy projections were applied before each spiral to ensure steady state was achieved in all

MBSWIFT acquisitions. Additional acquisition parameters specific to MBSWIFT not found in Table 5.1 include: number of projections (np) = 2048; number of spirals (nspirals) = 5; number of views (nv) = 2250. A conventional 3D gradient echo (3DGE) sequence was acquired with no saturation scheme at the lowest achievable TE for comparison (scan time = 5 m 13 s). Each MBSWIFT acquisition (using the saturation scheme at a given FA) took 56 seconds and a 30 second delay was observed between MBSWIFT acquisitions. In total nine MBSWIFT images and one 3DGE image were acquired for each animal at each imaging time point. Total *in vivo* scan time was 16 minutes 57 seconds per animal.

The MBSWIFT images were reconstructed using gridding and iterative FISTA algorithm [411] CMRRpack written in VnmrJ (Agilent Technologies, Santa Clara, CA, USA), LabVIEW (National Instruments, Austin, TX, USA) and Matlab (MathWorks, Natick, MA, USA) (http://www.cmrr.umn.edu/swift/). [412] Because of the 3D radial nature of MBSWIFT, the sequence is highly insensitive to motion so no motion correction was applied.

In vivo Micro-Computed Tomography (µCT)

In vivo µCT imaging (Bruker, Skyscan 1176) was acquired on the right proximal tibia at baseline (two days prior to OVX surgery) and week 2, 4, 10 and 12 post OVX surgery. Rats were imaged supine and the right tibia was secured to minimize motion. All *in vivo* images were obtained at an x-ray voltage of 70 Kv and current of 357 µA using a 1 mm aluminum filter to insure uniform beam hardening. Total scan time equaled 6 minutes 47 seconds. All scans were reconstructed at 35 µm isotropic voxel size using vendor-supplied software (NRecon, Bruker, Version 1.7.1.6.).

In vivo Image Analysis

All image analysis was performed using Matlab algorithms developed in-house. Full resolution µCT images (35 µm) were used to derive the trabecular and cortical segmentation masks for each animal (n=7) at each imaging timepoint (baseline, 2, 4, 10, 12 wk) and used as the standard volume of interest (VOI) for comparing µCT and MRI outcomes (described in the next section). Specifically, trabecular and cortical masks were created 2.5 mm distal to the growth plate and spanned 3 mm in the z-direction. The cortical mask included only cortical bone while the trabecular mask contained both marrow and trabecular bone encompassing the entire non-cortical region inside the tibia. Masks were contoured using an automated segmentation algorithm based on a pre-defined threshold to isolate the cortical mask and was followed by a set of morphological operations to extract the trabecular mask.

Image Registration

In order to quantify longitudinal changes following OVX in the cortical and tibial VOIs, the µCT images were registered to the MBSWIFT MR images for each rat at each time point using Elastix (version 4.8), an open-source registration algorithm with mutual information as an objective function and simplex as an optimizer (Figure 5.1).[413, 414] The registration was automatically performed and assumed rigid-body geometry (only rotation and translation) of the right tibia. The resulting transforms derived from each registration [each animal (n=7 at each timepoint for a total of 42 registrations)] were applied to the µCT-derived trabecular and cortical segmentation masks (which created the VOIs) on the experimental MBSWIFT MRI images which were identical to the µCT VOIs to guide quantitative imaging analysis (Figure 5.1G).

Signal to Noise Ratio (SNR)

Signal to noise ratio (SNR) was used to compare signal efficiency between the conventional 3DGE MRI and the experimental MBSWIFT-NS and MBSWIFT-FS across baseline *in vivo* acquisitions. Using the right proximal tibia, mean SNR was calculated in manually segmented cortical, marrow and muscle regions beginning 3 mm distal from the growth plate and spanning 5 slices distally. SNR was calculated using Equation 5.1:

Equation 5.1

$$SNR=SI_{mean}/SD_{noise}$$

where SI_{mean} is the mean signal in the region and SD_{noise} is the standard deviation of the background noise in the image.

Bone Mineral Density (BMD)

Trabecular and cortical volumetric BMD was calculated in the original μCT images reconstructed at 35 μm resolution and registered μCT (DS μCT) where resolution matched that of the MRI scans (156 μm). Scans were acquired with a known calcium hydroxyapatite density calibration phantom (CHA), a water phantom, and an air region. The mean attenuation coefficient of an air (μ_A) and water (μ_w) VOIs were determined and used to convert the image attenuation coefficient (μ_{ijk}) to Hounsfield units (HU) by applying a linear transformation of the data, Equation 5.2.

Equation 5.2

$$HU= \mu * M + B$$

where

$$M \text{ (or slope)} = 1000/(\mu_w - \mu_A)$$

$$B \text{ (or intercept)} = (-M* \mu_W)$$

Once in HU's, the mean HU of the CHA phantom (HU_{CHA}) VOI was calculated. The mean of the trabecular (HU_{TRAB}) and cortical (HU_{CORT}) VOIs was determined, from the vBMD for each was calculated using Equation 5.3.

Equation 5.3

$$\mathrm{vBMD}_{\mathrm{TRAB\ or\ CORT}} = \left\{\frac{[HU_{TRAB\ or\ CORT} \times \rho_{CHA}]}{HU_{CHA}}\right\}$$

The value 1.64 mg/mm^3 is the known concentration of CHA in the standard and HU_{CHA} is the average HU of the CHA standard.

Next, vBMD was derived in the MBSWIFT MRI images (MRI BMD) with the lowest flip angle (closest to pure proton density in MBSWIFT) and no saturation scheme using an analogous manner. MBSWIFT MRI scans were acquired with the same known calcium hydroxyapatite density calibration phantom, CHA, water phantom, and a region of air. An example MBSWIFT image of the CHA phantom can be seen in Figure 5.2. The mean gray scale index of air (GS_A) and water (GS_W) were determined. Images were converted to a HU value by applying the linear transform found in Equation 5.2 (using the mean MRI values for the air and water phantom). Using Equation 5.3, the volumetric BMD for the trabecular and cortical VOIs in the MRI were calculated.

Finally, using MBSWIFT-NS MRI image with the lowest flip angle, we employed a method using MRI signal intensity to estimate BMD (SI MRI BMD) first described by Ho et al. for comparison of our direct HU MRI BMD approach.[324] Using the CHA standard and water phantom, SI MRI BMD can be estimated using the signal model, adapted from Ho et al., in Equation 5.4.

Equation 5.4

$$\text{SI BMD}_{\text{TRAB or CORT}} = \left\{1 - \left[\frac{S_{TRAB\ or\ CORT} - S_{CHA}}{S_{WATER} - S_{CHA}}\right]\right\} \times \rho_{CHA}$$

where SI BMD is the estimated BMD based on signal intensity, $S_{\text{TRAB or CORT}}$ is the average signal of the VOI of interest, S_{WATER} is the average signal intensity for water and ρ_{CHA} is the known concentration of the CHA standard (1.64 mg/mm^3). In the original equation described by Ho et al., S_{WATER} can be any standardized region in which there is no mineral and there is a maximum signal in the region. In the original description, the authors used a region of subcutaneous fat; however, in our model of estrogen deficiency during growth we refrained from using an internal reference to ensure no unintended effect of estrogen deficiency in the fat region and instead chose a standardized water phantom.

Sensitivity to water loss in cortical bone subject to sequential drying

MBSWIFT sensitivity to changes in cortical water was evaluated under progressive dehydration using bone from three four month old female rats who had not undergone OVX. Immediately following sacrifice, bi-lateral tibia were removed and dissected free of soft tissue including removal of the periosteum. The proximal and distal ends were removed and marrow was flushed completely from the cortices. Using the left tibia (n=3), the prepared bone was patted dry and weighed in air with an electronic balance (Mettler-Toledo AE50, Columbus OH) at baseline. Dehydration was performed in an oven at 110°C while maintaining a constant vacuum. Weight was acquired every 5 minutes for the first 100 minutes and every 30 minutes thereafter until full dehydration was reached. Full dehydration was marked by a plateau in weight for at least three consecutive observations 30 minutes apart. Weight and time were plotted and dehydration time was determined for ¾ hydration, ½ hydration and full dehydration for each of the three tibiae calculated using the following equation:

Equation 5.5

$$\%\text{Water loss by weight} = (W_{\text{initial}} - W)/ W_{\text{initial}}$$

The initial bone wet weight is denoted by W_{initial} and W is the weight taken throughout the dehydration protocol.

Next, the contralateral tibias (n=3, right) were imaged *ex vivo* at baseline and following dehydration under oven/vacuum condition to reach ¾ hydration, ½ hydration and full dehydration using the imaging protocol described in detail above. Specifically, following baseline image acquisition, tibiae entered the 110°C oven under vacuum for the amount of time each contralateral tibia required to reach ¾ dehydration. Tibia were immediately imaged, returned to oven and the process was repeated until ½ hydration and full dehydration had been imaged. To mitigate any effects of transmit and receive gain changes over image acquisition at multiple time-points; a water phantom was imaged, in addition to the experimental tibia, as an internal control for B1 field changes. Weights were taken before and after imaging to ensure bone did not alter weight due to further dehydration in air by more than 0.05% which has been used in previous reports. [268] Water fraction maps were calculated (described in the next section) in the cortical bone VOI to evaluate MBSWIFT'S sensitivity to cortical water content loss during sequential drying.

Water Fraction and Fat Fraction MRI Maps

Signal fat fraction (FF) maps and water fraction (WF) were derived from consecutive MBSWIFT MR images acquired with fat saturation (MBSWIFT-FS), with water saturation

(MBSWIFT-WS) and no saturation scheme (MBSWIFT-NS) each using a nominal flip angle in order to achieve near proton-density image and minimize T_1 bias. The FF maps which distinguish signal arising from fat protons in the image, [415] were derived in Matlab from the following Equation 5.6:

Equation 5.6

$$FF = fat/(water + fat) * 100$$

where fat is the magnitude of the fat image where water was saturated (MBSWIFT-WS) and water is the water image where fat was saturated (MBSWIFT-FS). Water fraction (WF), signal arising from water protons, were calculated using Equation 5.7:

Equation 5.7

$$WF = water/(water + fat) * 100$$

MBSWIFT T_1 Relaxation using the Variable Flip Angle (T_1-VFA) Method

T_1 relaxation maps of the MBSWIFT-NS MRI using the variable flip angle method (T_1-VFA) were fitted using a voxel-by-voxel linear fitting relative to E_1 in Equation 5.9 based on the theoretical signal intensity (Equation 5.8) described by Treier et al.[315]

Equation 5.8

$$S = M_0 * (\sin \alpha * (1 - E_1) * E_2)/ (1 - E_1 * \cos \alpha)$$

S is the signal intensity that is a function of equilibrium longitudinal magnetization (M_0), relaxation times T_1, T_2, echo time (TE), repetition time (TR) and the flip angle (FA, α). In the linear form, we get:

Equation 5.9

$$S/\sin \alpha = E_1 * S/\tan \alpha + M_0 * (1 - E_1) * E_2$$

where

$$E_1 = \exp(-TR/T_1)$$

$$E_2 = \exp(-TE/T_2)$$

E_2, however, is set to 1 since the effective TE for MBSWIFT-NS acquisitions is 0. Since TR is kept constant and there is no input from TE, the measured signal changes from each FA is fit to a line characterized by slope $\alpha = E_1$ and intercept $b= M_0*(1-E_1)$ and T_1 values were calculated in the cortical and trabecular VOI. [315]

Signal intensity normalization

Signal normalization (SigNorm) of the MBSWIFT-NS images was performed in order to compare signal intensity changes due to OVX, longitudinally, across all animals in the study. Signal was normalized to a manually segmented region of the water phantom scanned during each acquisition. This fixed the water signal in the images to 1 and scaled the remaining signal (normalizing) in the image. The mean normalized signal intensity was calculated in the cortical and trabecular VOIs for analysis.

Histology

To support MRI outcomes, tibia from one additional rat euthanized at six weeks of age (no OVX, representing our baseline time point) and one rat from the 12 week post-OVX group were stained for marrow fat deposition using an Oil Red O- isopropanol method described by Lillie et al. [416] In short, tibia were removed free of soft tissue, fixed for 24 hours in 10% neutral buffered formalin, rinsed in tap water and embedded in OCT (Tissue-Tek; Sakura Finetek USA) in preparation for cryosectioning following standard laboratory procedure. Embedded non-decalcified tibia were sectioned longitudinally at 5 µm thickness on a cryostat (Leica CM30505, Nussloch, Germany) where sections were adhered using the Kawamoto tape method. [417] Oil Red O stained sections were imagined (brightfield) 20x magnification using a Nikon Eclipse Ni-U microscope (Nikon Instruments Inc., Melville, NY).

Statistical analysis

For comparison of *in vivo* signal efficiency, one-way analysis of variance (ANOVA) with Bonferonni correction were used to compare SNR between conventional 3DGE MRI with the lowest achievable TE, MBSWIFT-NS and MBSWIFT-FS for cortical, marrow and muscle VOIs.

Pearson correlation coefficients were used to test the linear association between μCT BMD measures at 35 μm resolution, DS μCT BMD measures at the resolution of the MRI (156 μm), the direct MRI BMD and the SI MRI BMD approach. Pearson correlation coefficients were also calculated to compare the two MRI methods to obtain BMD. Simple linear regressions were used to determine the predictive value of the BMD methods against μCT BMD measures at 35 μm resolution, our gold standard approach.

To determine MBSWIFT's sensitivity to changes in water during sequential drying during our dehydration protocol, a simple linear regression model was used to determine association between WF and gravimetric weight in the cortical bone. To evaluate the sensitivity of *in vivo* imaging outcomes to longitudinal changes in the cortical and trabecular VOIs following OVX, repeated measures ANOVA (RM-ANOVA) followed by Holm-Sidak's multiple comparison test was used to detect differences in imaging outcome parameters compared to baseline (pre-OVX). Specifically, we tested the sensitivity of μCT BMD, MRI BMD, WF, SigNorm and T_1 relaxation to detect changes following OVX in the cortical VOI. For the trabecular VOI, analysis was carried out using the following outcomes: μCT BMD, MRI BMD, FF and SigNorm. Finally, a simple linear regression model was used to determine association between these MRI derived outcomes compared to μCT BMD. Pearson correlation coefficients were also reported between each MRI outcome and μCT BMD. Graphpad Prism Version 8.0.2. was used for data analysis. In all cases, $P \leq 0.05$ was considered statistically significant.

Results

MBSWIFT achieved significantly greater signal to noise ratio (SNR) in the tibia compared to 3DGE MRI

Representative consecutive *in vivo* MRI acquisitions of the rat proximal tibia using 3DGE, MBSWIFT-NS, and MBSWIFT-FS acquired for the study (Figure 5.3A). For the cortical, marrow and muscle regions (Figure 5.3B,C) MBSWIFT-NS and MBSWIFT-FS achieved significantly greater SNR compared to 3DGE acquired with the lowest achievable TE. ANOVA results, including Bonferonni post-hoc analysis, can be appreciated in Figure 5.3D where significance is denoted by brackets and stars. Compared to the 3DGE MRI, we observed a +562% and +617% increase in SNR in the cortical bone using MBSWIFT-FS and MBSWIFT-NS, respectively. Marrow SNR increased by +197% (MBSWIFT-FS) and +199% (MBSWIFT-NS) and muscle SNR by +142% (MBSWIFT-FS) and +164% (MBSWIFT-NS) compared to the 3DGE acquisition. There were no significant differences in SNR between MBSWIFT-NS and MBSWIFT-FS in any region. Representative SNR color map overlays in the cortical region for each sequence can be appreciated in Figure 5.4.

MRI-derived BMD significantly correlated with μCT BMD measures

We observed a significant positive linear correlation between all methods used to derive BMD in both the cortical and trabecular VOIs where r- and p-values can be appreciated in Table 5.2. Specifically, cortical BMD derived from the full resolution μCT, our gold standard, demonstrated a strong linear correlation with each MRI BMD method (MRI BMD: $r = 0.67$; SI MRI BMD: $r = 0.65$). Correlations were statistically significant for trabecular BMD between µCT and MRI however, the direct MRI approach had a slightly decreased r value (0.58) compared to the SI MRI BMD method (r=0.62). BMD derived between µCT methods (full resolution µCT vs. DS µCT) were highly correlated (cortical: r=0.97; trabecular: r=0.90) and BMD between MRI methods (MRI vs. SI MRI BMD) were highly correlated (cortical: r=0.98; trabecular: r=0.97) (Table 5.2).

Linear regressions between BMD acquired using DS µCT, MRI BMD and SI MRI BMD against results from the full resolution µCT (gold standard) for the cortical and trabecular VOI were significant in all cases (Figure 5.5). Y-intercepts for trabecular BMD were significantly different ($p < 0.0001$) and can be appreciated in Figure 5.5.

Both MRI and µCT detected significant longitudinal increases in BMD

We evaluated longitudinal changes in cortical and trabecular BMD measured using full resolution µCT and MBSWIFT MRI BMD using RM ANOVAs (Figure 5.6A-B). For cortical BMD, RM ANOVA results for each modality was significant (µCT: $p<0.0001$; MRI: $p<0.0001$). Cortical BMD increased from baseline following OVX and follow-up Holm-Sidek's multiple comparison test determined this was significant by 2 weeks and was observed in both imaging modalities. For trabecular BMD, RM ANOVA results were significant for MRI ($p<0.0001$) but not for µCT ($p=0.06$). Trabecular BMD measured with MRI increased from baseline following OVX and was significantly different by 2 weeks post-OVX. Trabecular BMD measured using µCT was significantly increased from baseline by 10 weeks post-OVX.

MBSWIFT Cortical water fraction was sensitive to sequential drying

Correlations between *ex vivo* cortical MBSWIFT WF and water loss (measured as a % loss by volume) during sequential drying under oven/vacuum (Figure 5.7). As WF decreased, percent water loss by volume increased; this strong negative correlation was significant between the two measures (R=-0.98; p=0.01). Results indicate MBSWIFT WF is highly sensitive cortical water loss.

Cortical water fraction significantly decreased by 10 weeks and was negatively correlated with BMD

While BMD measures significantly increased in our model (likely as a result of growth overcoming estrogen-deficiency changes), we evaluated the utility of WF and SigNorm to detect additional bone quality changes in the cortical bone consistent with OVX. The longitudinal effects of OVX on cortical WF and SigNorm can be appreciated in Figure 5.8A. Both cortical WF and SigNorm significantly decreased longitudinally from baseline following OVX (RM ANOVA WF: $p<0.0001$; SigNorm: $p=0.02$). Post hoc testing revealed that the decrease in cortical WF and SigNorm was significantly different from baseline by 10 weeks post-OVX.

Associations between cortical WF and BMD and cortical SigNorm and BMD can appreciated in Figure 5.8B and Pearson's correlation coefficients can be found in Table 5.3. Cortical WF negatively correlated with cortical µCT BMD (r=-0.6; p=0.0002). While cortical SigNorm decreased marginally with increasing cortical BMD, this observation was not statistically significant (r=-0.32; p=0.06).

Prior studies using SNR as a biological outcome derived from conventional SWIFT in cortical bone following diabetes onset detected significant changes in SNR prior to change in BMD between controls.[297] The authors hypothesized that changing signal was due to changes in cortical water. As such, we evaluated the relationship between cortical SigNorm and WF and did not observe a relationship (r=0.09; p=0.6). Results suggest that changes in water do not fully explain changes in SigNorm over time following OVX indicating another pool of protons, perhaps collagen-related, may be contributing to changes in SigNorm.

Marrow fat fraction significantly increased by 10 weeks post OVX

Marrow fat measured as the FF in the trabecular VOI increased longitudinally following OVX (Figure 5.9A). RM ANOVA was significant ($p<0.0001$) and Holm's-Sidek post hoc determined that FF significantly increased from baseline by 10 weeks post-OVX. Undecalcified cryosections stained with Oil Red O support the finding where increased marrow fat deposition is observed in 12 week post-OVX sections (Figure 5.9C). While FF increased following OVX, normalized signal intensity values, SigNorm, in the trabecular VOI were relatively unchanged over time and no significant differences measured by the RM ANOVA was observed ($p=0.97$). There were no statistical associations between FF and trabecular BMD or between SigNorm and BMD (Figure 5.9B). Longitudinal changes in marrow fat from baseline through 12 weeks post-OVX for one rat can qualitatively be appreciated in Figure 5.9D.

Cortical matrix T_1 relaxation time decreased significantly by 10 weeks post-OVX

Mean T_1 relaxation measured using VFA-MBSWIFT increased two weeks following OVX and then began to decrease over time through the 12 week post-OVX timepoint which can be appreciated in Figure 5.10A. RM ANOVA results comparing T_1 relaxation times longitudinally were significant ($p=0.0005$) and Holm's-Sidek post hoc test for multiple comparisons determined that T_1 relaxation was significantly decreased from baseline by 10 weeks post-OVX. There was an observed negative relationship between T_1 relaxation times and BMD but this association was not significant ($p=0.08$). There was no statistical relationship between T_1 relaxation time and cortical WF (Figure 5.10B, Table 5.3). The decrease in cortical matrix T_1 relaxation time longitudinally following OVX can qualitatively be appreciated in Figure 5.10C.

Discussion

Because the high atomic mass number associated with calcium (Z=20) gives rise to a higher photoelectric absorption compared to that of soft tissue, there is a near ubiquitous reliance on ionizing x-ray based techniques to visualize the mineral phase of bone. [125] As a result, characterization of disease progression and treatment efficacy for metabolic bone diseases is complicated by the lack of imaging modality able to safely monitor material-level and biochemical changes *in vivo*. To improve upon x-ray based BMD, we tested the efficacy of a novel 3D ZTE-MRI approach, MBSWIFT, in an estrogen-deficient (OVX) model of osteoporosis during growth. This provided a rapidly changing system to evaluate our proposed MRI bone biomarkers of cortical WF, cortical matrix T_1 relaxation times, marrow FF, and trabecular and cortical normalized signal intensity (SigNorm) in addition to a proposed direct measure of BMD using MBSWIFT. MBSWIFT MRI-derived BMD correlated significantly with BMD measured using the gold standard, µCT, in the trabecular and cortical regions which significantly increased longitudinally over the duration of the study. Growth appeared to overcome estrogen-deficient changes in bone mass in our rat model yet MBSWIFT MRI detected significant changes consistent with estrogen deficiency by 10 weeks in cortical WF, cortical matrix organization (T_1 relaxation times) and marrow FF. Further, MBSWIFT derived cortical WF was strongly correlated to water loss during sequential drying indicating the technique is highly sensitive to small changes in cortical water. Findings point to MBSWIFT MRI’s ability to quantify BMD in good agreement with the gold standard µCT, and ability to detect biochemical and material-level alterations consistent with disease independent of the mineral phase suggesting, its value for bone imaging.

MBSWIFT MRI was able to achieve significantly greater SNR in the bone compared to conventional 3DGE using the lowest achievable TE. The greatest magnitude of signal improvement compared to 3DGE was in the cortical bone where a +562% and +617% increase in SNR was observed using MBSWIFT-NS and MBSWIFT-FS, respectively. This increase highlights the immense improvement in signal efficiency achievable in not only the extremely short T_2 cortical bone, but the concurrent signal improvement in the surrounding muscle and marrow achieved *in vivo*.

BMD is used clinically to classify the onset and extent of osteoporosis [418] and as a pre-clinical endpoint in osteoporosis related research. [419] Because MBSWIFT is able to achieve TE=0, we hypothesized that it would be sensitive to the mineral phase of bone which has a short T_2 ~ 10 μs,[40] and therefore could directly quantify BMD without the use of harmful ionizing radiation. We imaged a CHA standard and water along the rat tibia using MBSWIFT, converted the images to HU and quantified trabecular and cortical BMD. We compared this to the high resolution μCT (35 μm, the gold standard) in addition to DS μCT and SI MRI BMD based on signal intensity in the MRI images. [324] MBSWIFT BMD significantly correlated to both trabecular and cortical BMD acquired using the gold standard approach demonstrating its promise to resolve changes in BMD in good agreement with μCT.

MBSWIFT BMD was able to significantly detect longitudinal increases in cortical bone comparable to BMD measured by μCT. However, for the trabecular region, MRI BMD detected a significant increase by 2 weeks while μCT was not significantly elevated from baseline until week 10. In aged models of estrogen deficiency (OVX) bone loss, bone loss is greater and occurs more rapidly in trabecular bone compared to cortical bone. [420, 421] We believe the estrogen-related changes in the trabecular region may have been stronger therefore growth induced increases in BMD did not overcome estrogen deficiency bone loss until 10 weeks post-OVX (μCT). While MBSWIFT demonstrated significant correlations with μCT BMD in the trabecular region, the correlations were not 1:1 and the method in which signal is captured (by exciting protons) is different from attenuation of the tissue. Inspection of the regression plots in the trabecular VOI show that both MRI-derived approaches appear to overestimate BMD compared to µCT and there was almost no difference between MRI approaches to derive BMD. The contribution of signal from the marrow (fat and water) may have impeded the BMD values in the region. In contrast, µCT trabecular VOI shows tissue attenuation for the trabeculae and little signal contributions from the marrow and water. As such, the increased BMD values for the trabecular region may have been confounded by the increased dynamic range of the MRI image compared to that achieved using µCT. Even so, we believe the statistical correlations in both VOIs and sensitivity to longitudinal change, especially in the cortical VOI, support the utility of MBSWIFT to characterize the mineral phase of bone, *in vivo*, without the use of ionizing radiation.

In human subjects, Li et al. demonstrated the utility of UTE MRI-derived bulk water (total) measures at the mid diaphyseal of the tibia where positive correlations were observed with age and negative correlations with BMD.[271] Using MBSWIFT to quantify water fraction in the cortical region of the rat proximal tibia, we also observed a significant negative correlation between cortical water and BMD measured using µCT. While both bound and free water pools are contributing to the signal we are capturing in the MBSWIFT water fraction maps, the bone has a larger portion of water existing in the bound form located in matrix [335] found either loosely bound to collagen [40] or more tightly to the mineral. [422] Further, Du et al. reported that UTE MRI signal in human cortical bone was greater than 77.6% attributable to the bound water pool [423] therefore it is likely that the greater contribution of our measured water signal was from bound water. Using a solid-state NMR spectroscopy technique, Cao et al. suggested that protons bound to the matrix more closely relate to the matrix composition and can infer mineral density of bone. [424] The authors used a solid-state approach to achieve zero-TE where the most molecularly immobile components could be imaged including signal in the solid bone matrix (where authors used suppression of fluid signals, similar to our study, to exploit this). With MBSWIFT MRI, time-domain signals are acquired during a swept RF excitation in a time-shared manner thus achieving zero TE and there the technique has the ability to capture all protons in the bone including matrix bound water. [289] Bound water has shown to decrease with age in rats [425] and in human cadaveric femurs [39] and decrease in rats with high bone turnover rates in a model of chronic kidney disease.[426] Bone turnover rate is increased both during aging and with osteoporosis and can lead to deterioration of bone microarchitecture affecting bone quality[427] which may be observed independent of BMD. In the present study, we observed a significant decrease in cortical water by 10 weeks post-OVX, consistent with increased bone turnover due to estrogen deficiency, even while BMD continued to increase.

Free pore water concentration on the other hand may be a surrogate to measure cortical porosity. [39] Li et al. applied a saturation recovery scheme to selectively quantify pore water in *ex vivo* cadaveric tibia specimens and demonstrated that UTE MRI demonstrated strong positive correlations with both age and μCT porosity.[428] It has been previously shown that porosity increases as a result of age and this change accounts for over 70% of reduction of strength in bone. [248, 429] Using ^{1}H NMR, Horch et al. observed that bound water positively correlated with peak stress while free water (pore) negatively correlated using human cortical bone specimens. [209] The ability to separate these water pools using *in vivo* acquisitions is desirable and work has been done using bi-component analysis of cortical water pools acquired by UTE both preclinically and in humans at clinical field strengths. [270, 335, 430] In the present study, we were limited in this analysis because MBSWIFT is inherently only able to capture TE=0; thus the curve fitting technique used to derive the bi-component water populations using variable TE's is not feasible. Future work using MBSWIFT with saturation schemes at the pore and bound peak should be applied to derive water contributions from each pool.

Traditional x-ray-based approaches also fall short in characterizing bone marrow fat. There is a strong relationship between increased marrow fat observed in patient biopsies with osteoporosis [214, 431, 432] suggesting its promise as an imaging target for the disease. Conventional MRI has demonstrated utility in quantifying marrow fat *in vivo*,[433-435] but conventional MRI is unable to provide additive information regarding the surrounding mineral and other material-level properties in bone. In the present study using MBSWIFT, we detected an increase in marrow FF longitudinally following OVX. This increase was statistically significant from baseline by 10 weeks supportive of clinical experience of increased bone marrow fat in osteoporotic bone samples. [214, 431, 432] Prior studies have suggested that fatty marrow is associated with reduced trabecular bone mass. Studies have demonstrated a negative relationship between lower bone density measured by DXA and higher fat content measured by conventional MRI, [434-437] where it has been suggested that low BMD may result in increased differentiation of mesenchymal stem cells to adipocytes instead of osteoblasts. [438, 439] However, in our study we did not observe a statistical relationship between increasing FF and µCT BMD in the growing rats following OVX (r=0.27; p=0.21). It has been reported that both DXA and CT are vulnerable to incorrect reading of BMD in the presence of large increases in marrow fat. [440, 441] Even so, we reason the lack of association was likely more attributable to the continued growth of the animal influencing the increased BMD in our study. We believe the detectable increase in FF observed independent of increasing BMD in our growing animals following OVX highlights the discriminating power of MBSWIFT measured FF, supported by histology (Figure 5.9) suggesting its additive utility as an imaging biomarker of increased bone turnover due to disease and estrogen deficiency.

T_1 relaxation times hold promise as a quantitative imaging biomarker based on tissue-specific relaxation properties because T_1 reflects the energy flow between spins and their local microenvironment. T_1 relaxation times have shown to be sensitive to small variations in healthy tissue [308, 309] and more importantly, is able to distinguish changes due to disease. [309, 310, 312, 442] Until the advent of UTE and ZTE MRI, T_1 relaxation times of short T_2 species such as bone has been unattainable. Since the description of SWIFT, Wang et al. described its utility of conventional SWIFT using the variable flip angle (VFA) method to measure T_1 relaxation times in aqueous suspensions of iron oxide nanoparticle in excellent agreement with spectroscopic measures [316] and others have applied *ex vivo* VFA SWIFT to quantify T_1 relaxation times in osteochondral specimens.[317] We applied the VFA method using MBSWIFT to reduce susceptibility artifact at the cortical borders where we calculated volumetric T_1 relaxation times *in vivo*. We observed the cortical matrix T_1 relaxation times increased immediately after baseline and then decreased longitudinally and were statistically different from baseline by 10 weeks. While cortical water also decreased longitudinally in the study, there was no statistical association between decreasing T_1 and decreasing cortical WF. Interestingly, while not statistically significant, T_1 relaxation time decreased with increasing BMD. Nissi et al. observed that T_1 relaxation times decreased closer to the more mineralized region in the cartilage bone interface reflecting the higher sensitivity to short T_2 spins located at the cartilage/bone interface. [317] Using 3D solid state phosphorus-31 NMR projection imaging ,Wu et al. reported that subtle molecular or crystalline structural differences in the mineral were reflected as large changes in T_1 highlighting the discriminating power of the parameter to its local environment.[313] We hypothesize that the significant decrease in VFA MBSWIFT T_1 reflects its ability to directly image the changing bone matrix composition. This included an increase in mineral density and changes in the collagen environment including cross link concentration and collagen morphology both of which are observed in osteoporosis [409, 443, 444] and would affect the mobility of protons measured during longitudinal relaxation (T_1) resulting in shorter T_1 relaxation times.

SNR itself has been used as a biological outcome measure in studies applying regular SWIFT, acquired *ex vivo*, in cortical bone. Sukenari and Minami et al. each determined SNR was positively correlated with new bone area measured using histomorphometry in rats with diabetes and following OVX and weakly correlated to increasing BMD following OVX. [296, 297] For Sukenari et al., 12 week old rats were subject to OVX or SHAM and cortical BMD was measured using DXA; both OVX and SHAM animals increased cortical BMD through 12 weeks but increases were less for OVX animals. The authors evaluated correlations between cortical SNR and BMD and determined that it was significant but weakly positive ($p=0.04$, $R^2=0.066$) suggesting that SNR detected additional bone quality measures not captured by BMD but the authors did not measure any additional SWIFT outcomes.[297] Using 8 week old male rats, Minami et al. induced diabetes via streptozotocin injection and monitored BMD changes using µCT compared to control animals and observed that BMD increased longitudinally in both groups but lesser so in diabetic rats. [297] While this difference was not detected until 8 weeks, SWIFT SNR detected a significant difference from controls by two weeks. Results were promising yet additional SWIFT measures were not evaluated to determine the source of this change (water, collagen) and correlations between SNR and BMD were not evaluated.

While we did not use SNR as a biological outcome in our study, we did use a signal intensity normalization (SigNorm) method to evaluate MBSWIFT signal changes following OVX. Cortical SigNorm significantly decreased by 10 weeks following OVX and demonstrated a negative non-significant relationship with the increasing BMD in our study (p=0.06, R=-0.32). While Sukenari and Minami suggested the source of their decreased signal was due to changes in water content following OVX and diabetes onset, respectively, when we evaluated the relationship between SigNorm and WF, we did not observe a relationship (p=0.59, R=0.09). We believe the results suggest a different contributing proton pool is responsible for this decrease in signal such as perhaps collagen which should be directly evaluated in future studies.

Conclusions

There are currently no accepted approaches to measure bone quality, non-invasively, in the clinical setting. [127] We believe MBSWIFT may hold enormous pre-clinical and clinical potential by overcoming MRI’s inability to directly image the mineral phase of bone *in vivo* while simultaneously providing quantitative bone quality measures. MBSWIFT significantly detected longitudinal increases in BMD comparable to BMD measured by µCT and significantly correlated to BMD acquired using the gold standard approach. Results support the utility of MBSWIFT to characterize the mineral phase of bone, longitudinally, without ionizing radiation. While BMD increased following OVX, likely as a result of growth, the proposed MBSWFIT MRI biomarkers targeting additional measures of bone quality significantly detected changes in the bone at 10 weeks that were consistent with estrogen-deficiency following OVX without the use of harmful ionizing radiation. Results support the promise of ZTE MRI techniques to non-invasively image bone *in vivo*.

Figures

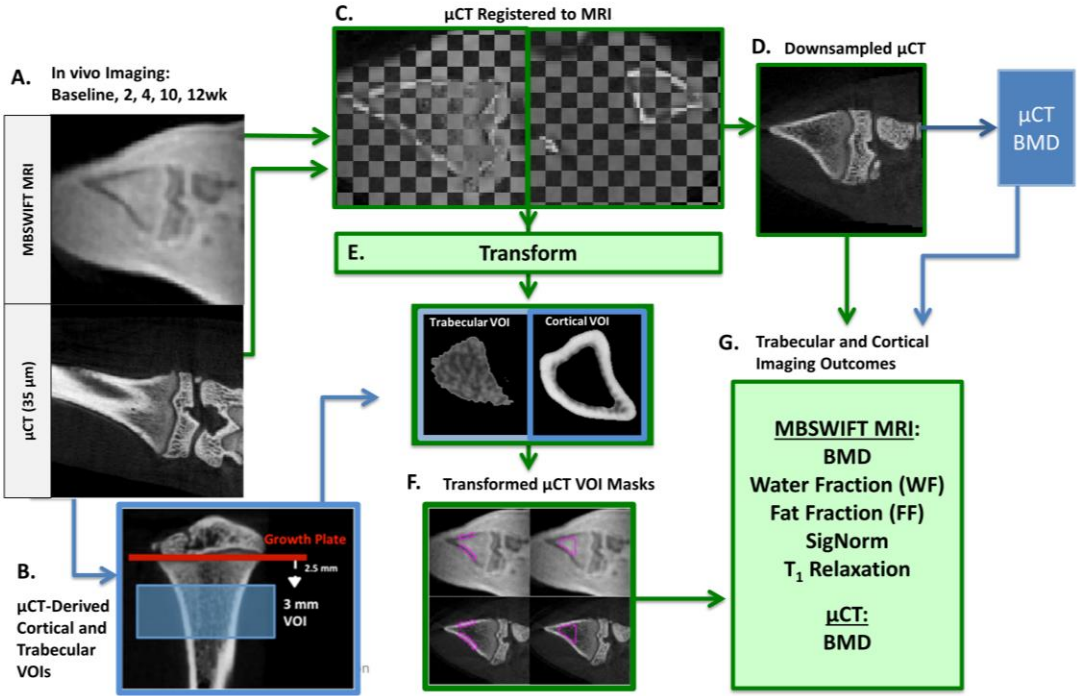

Figure 5.1 Image post-processing workflow.
A) Representative coronal slices from scans performed using *in vivo* Multi-Band SWeep Imaging with Fourier Transformation MRI (MBSWIFT, 156 µm resolution) and µCT (35 µm resolution) of the right proximal tibia acquired at baseline and post ovariectomy (OVX). B) Trabecular and cortical segmentation masks were derived using µCT images at each time point. Masks began 2.5 mm distal from the growth plate spanning 3 mm distally and created the volume of interest (VOI) for analysis. Cortical masks included only cortical bone and trabecular masks contained both marrow and trabecular bone encompassing the entire non-cortical region inside the tibia. C) µCT was registered to the experimental MBSWIFT MRI assuming a rigid body transformation and checkerboard images of the resultant registration were used as quality control for accuracy. D) Registered µCT image (156 µm) was used for further analysis. E) The transform from each registration for each animal (n=7 animals at 6 time points for a total of 42 registrations) was applied to corresponding trabecular and cortical VOIs. F) Transformed VOIs were used across imaging modalities to guide image analysis (G). Total registration time ~ 1 minute and 3 seconds and VOI transformation took ~47 seconds.

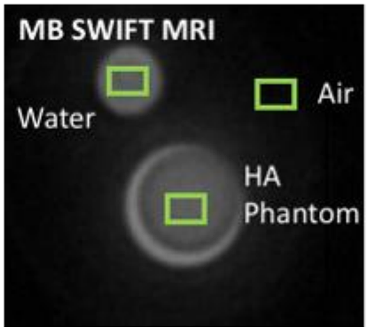

Figure 5.2: Calcium hydroxyapatite phantom acquired using MBSWIFT MRI.
Example image of the calcium hydroxyapatite (HA) phantom in water acquired using MBSWIFT MRI with no saturation scheme. Calibration phantom and a separate water phantom were acquired under the same experimental parameters. Regions of water and air were used to convert the MR images to Hounsfield units and the HA phantom was used to derive bone mineral density. MBSWIFT= Multi-Band SWeep Imaging with Fourier Transformation.

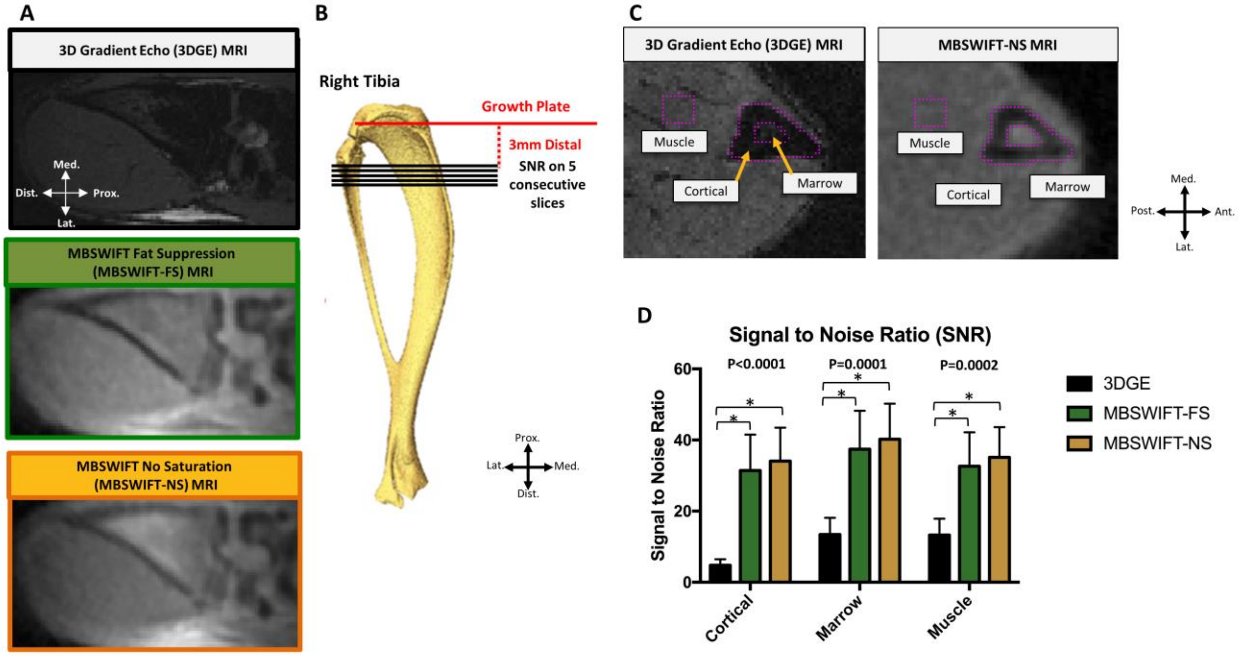

Figure 5.3: *In vivo* MRI signal to noise ratio (SNR) measures are improved with MBSWIFT. A) We compared the signal efficiency using SNR between the conventional 3D gradient echo (3DGE, top) with the lowest achievable TE, Multi-Band SWeep Imaging with Fourier Transformation with no saturation scheme (MBSWIFT-NS, middle), and MBSWIFT with fat suppression (MBSWIFT-FS). B) SNR was measures were taken in the right tibia beginning 3 mm distal from the growth plate and spanned 5 consecutive slices distally. C) SNR mean ± standard deviation was reported using manually-drawn regions in the muscle, cortical and marrow (outlined in pink). D) Results from ANOVA with Bonferonni correction are depicted; ANOVA p-values are reported and bolded when significance was detected and bracket and stars indicate significant post-hoc differences. In all cases, MBSWIFT achieved significantly greater SNR in each region. There were no significant differences in SNR between MBSWIFT-NS and MBSWIFT-FS. Significance was set at $p \leq 0.05$.

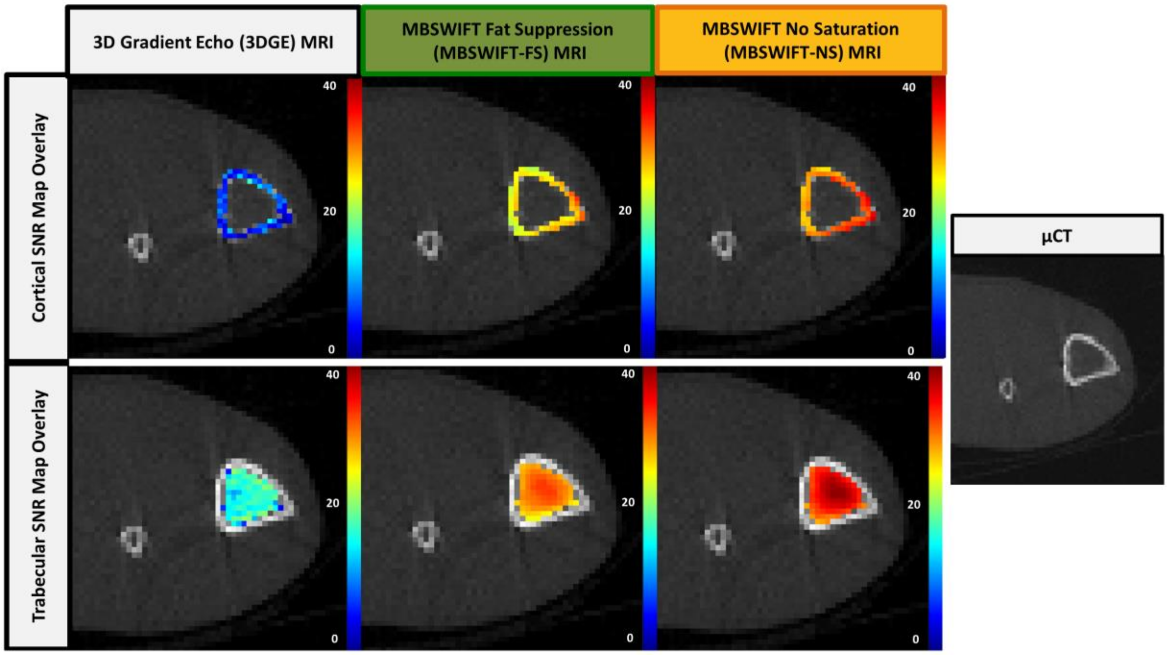

Figure 5.4: Example signal to noise ratio (SNR) colormap overlay between MRI sequences for one rat.
Cortical and trabecular SNR colormaps overlaid onto µCT image for the 3D gradient echo (3DGE) MRI acquired with the lowest achievable TE, Multi-Band SWeep Imaging with Fourier Transformation with no saturation (MBSWIFT-NS) and fat suppression (MBSWIFT-FS) demonstrate the signal efficiency gained in each VOI using 3D zero time MRI approach. Example in vivo acquisitions from one rat at baseline (axial view). Overlay colormap range: 0-40 SNR.

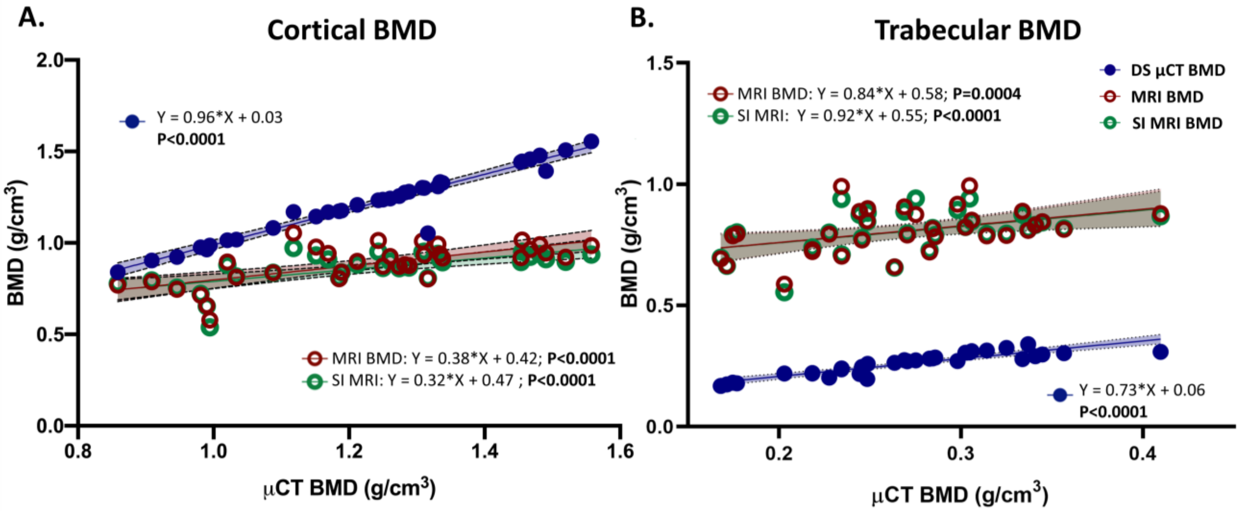

Figure 5.5: Relationship between MRI-derived bone mineral density (BMD) and μCT BMD (gold standard).

The x-axis is BMD calculated from the full resolution μCT and on the y-axis is BMD derived from the following experimental approaches: 1) downsampled μCT (DS μCT BMD, blue), 2) MBSWIFT MRI converted to Hounsfield units using a calcium hydroxyapatite phantom (MRI BMD, red) and 3) MBSWIFT using the signal intensity method described by Ho et al. (SI MRI BMD, green). The relationship between μCT derived BMD and experimentally derived BMD (MRI, SI MRI and DS μCT) was statistically significant in both the cortical (A) and trabecular (B) VOIs in all cases (denoted by bolded p-values next to the respective regression equation on the plot). The y-intercept between BMD methods in the trabecular VOI were statistically different. For each BMD method, regression lines (solid) and coefficients (dotted with shaded fill) are shown with the 95% confidence intervals. Significance was set at $p \leq 0.05$. MBSWIFT = Multi-Band SWeep Imaging with Fourier Transformation where the no suppression acquisition was used for calculation. R values from correlations can be found in Table 5.2.

A. µCT-derived BMD

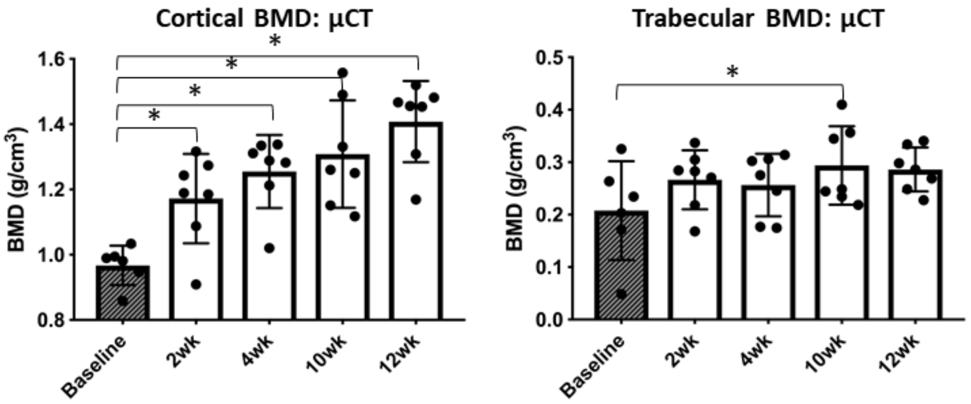

B. MBSWIFT-derived BMD

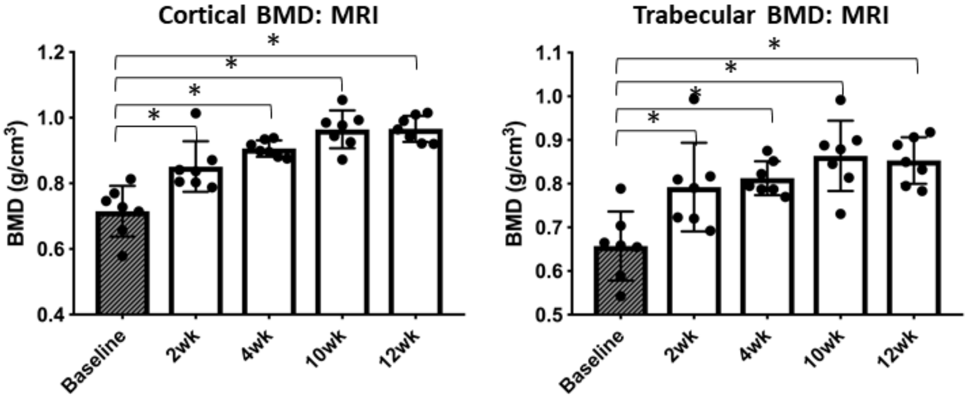

Figure 5.6: Longitudinal *in vivo* cortical and trabecular bone mineral density (BMD).
Cortical and trabecular BMD (mean ± SD) measured at the proximal tibia at baseline through 12 weeks post ovariectomy (OVX) in seven growing rats using µCT (A) and MBSWIFT MRI (B). For A-B, BMD was calculated by converting images to Hounsfield units and deriving BMD using calcium hydroxyapatite standard (CHA). Repeated measures ANOVA results were significant in cortical µCT BMD ($p<0.0001$), and cortical and trabecular MRI BMD ($p<0.0001$, $p<0.0001$, respectively) but not for trabecular µCT BMD ($p=0.06$). Holm-Sidak's multiple comparison test was used to detect differences in BMD compared to baseline (pre-OVX) and significance is denoted by brackets and stars. Significance was set at $p \leq 0.05$. MBSWIFT = Multi-Band SWeep Imaging with Fourier Transformation where the no suppression acquisition was used for calculation.

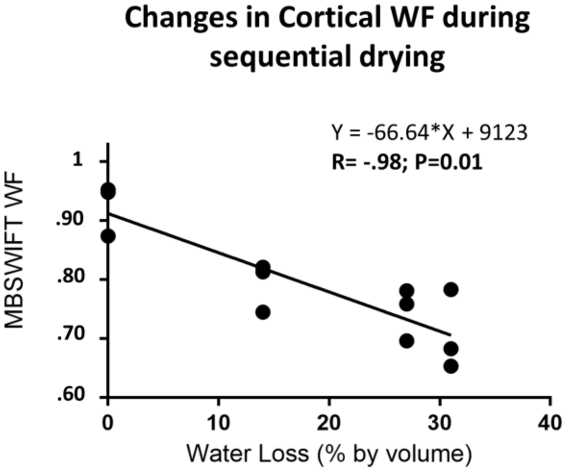

Figure 5.7: MBSWIFT WF is sensitive to cortical water loss during sequential drying. As MBSWIFT MRI water fraction (WF) decreased, percent water loss by volume increased; this strong negative correlation was significant between the two measures (R=-0.98; p=0.01). Results indicate MBSWIFT WF is highly sensitive cortical water loss. MBSWIFT= multi-band SWeep Imaging with Fourier Transformation.

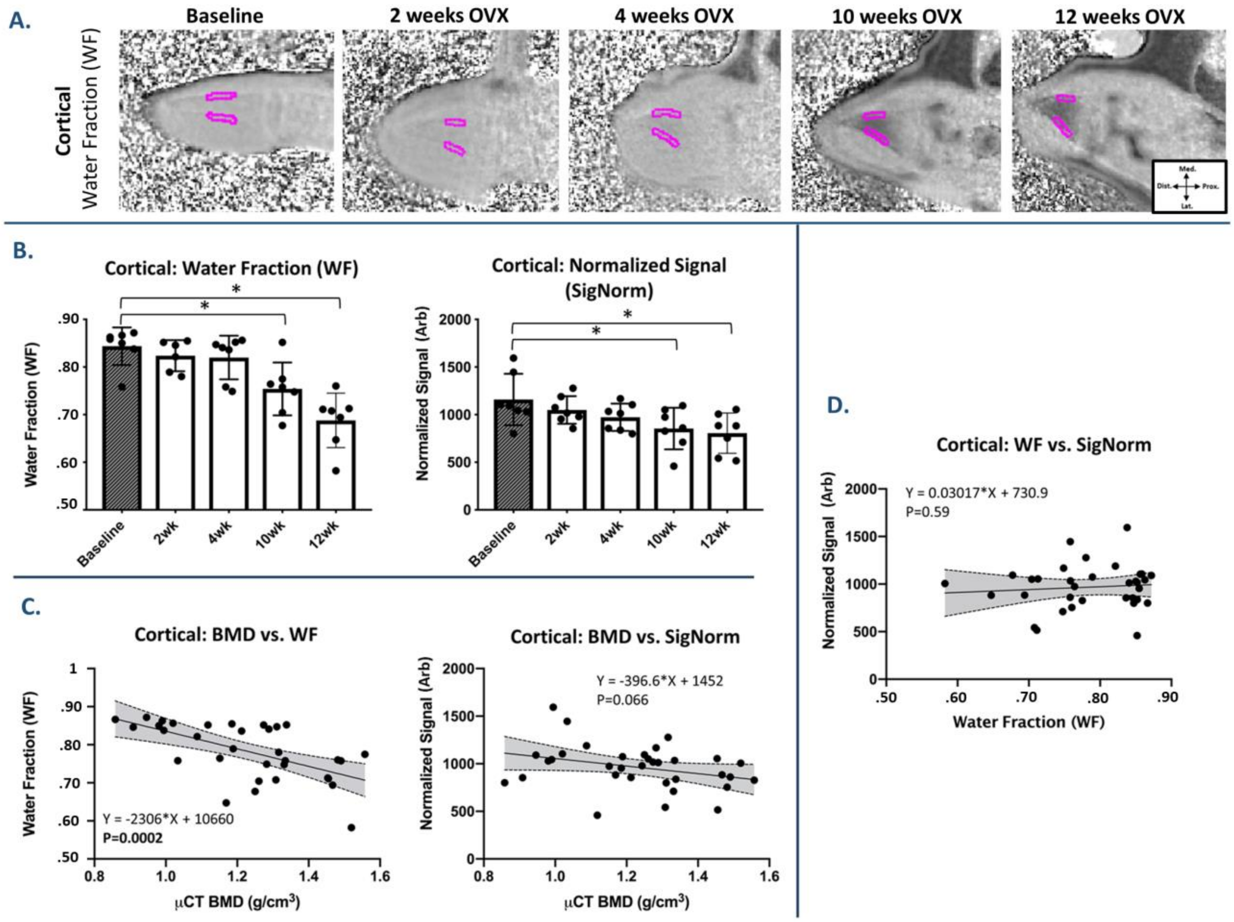

Figure 5.8: Longitudinal cortical MRI water fraction and normalized signal outcomes following OVX and their relationship with BMD.

A) *In vivo* coronal water fraction (WF) images with cortical VOI overlay at baseline through 12 weeks post-OVX. Cortical WF decreased longitudinally following OVX (reaching significance from baseline by 10 weeks) which can be appreciated by the loss of signal within the cortical region. B) Both cortical WF and normalized signal (SigNorm) decreased following OVX reaching significance from baseline by 10 weeks post-OVX (denoted by brackets and stars). C) Cortical WF and BMD were significantly negatively correlated. Cortical BMD and SigNorm demonstrated a negative non-significant association. D) Measures of cortical WF and SigNorm were not associated suggesting protons other than water contribute to the observed decrease in signal intensity measured using SigNorm. This would be feasible due to MBSWIFT's ability to achieve TE=0 thus is sensitive to all protons in the matrix. Significance was set at $p \leq 0.05$. Representative longitudinal WF images are from one rat. MBSWIFT= Multi-Band SWeep Imaging with Fourier Transformation; VOI=volume of interest.

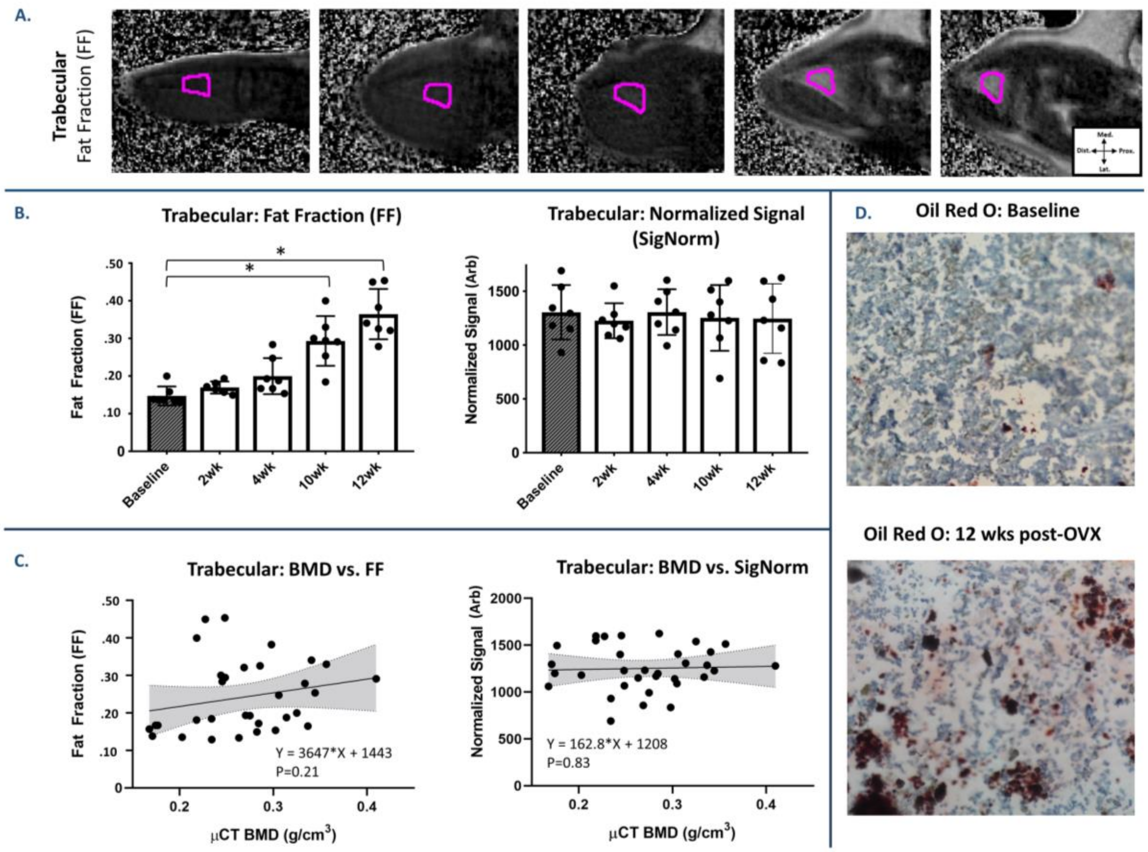

Figure 5.9: Longitudinal changes in trabecular MRI marrow fat fraction and normalized signal following OVX were unrelated to changes in BMD.
A) *In vivo* coronal fat fraction (FF) images with trabecular VOI overlay at baseline through 12 weeks post-OVX. FF increased longitudinally following OVX (reaching significance from baseline by 10 weeks) which can be appreciated by the increasing signal (white) within the trabecular region over time. B) FF and normalized signal (SigNorm) in the trabecular VOI plotted as mean ± SD measured at the proximal tibia at baseline through 12 weeks post ovariectomy (OVX). FF increased following OVX; RM ANOVA was significant and follow-up post hoc indicated that the measure was significantly increased from baseline by 10 weeks post-OVX. There were no significant longitudinal changes observed in SigNorm. C) There was no statistical association between FF and trabecular BMD and between trabecular BMD and SigNorm. D) Bright field images of tibial marrow region stained using Oil Red O at baseline (top, no OVX) and following 12-weeks post OVX (bottom) depict increases in lipid deposit (red) following OVX. Significance was set at $p \leq 0.05$. Representative longitudinal FF images are from one rat. MBSWIFT= Multi-Band SWeep Imaging with Fourier Transformation; VOI=volume of interest.

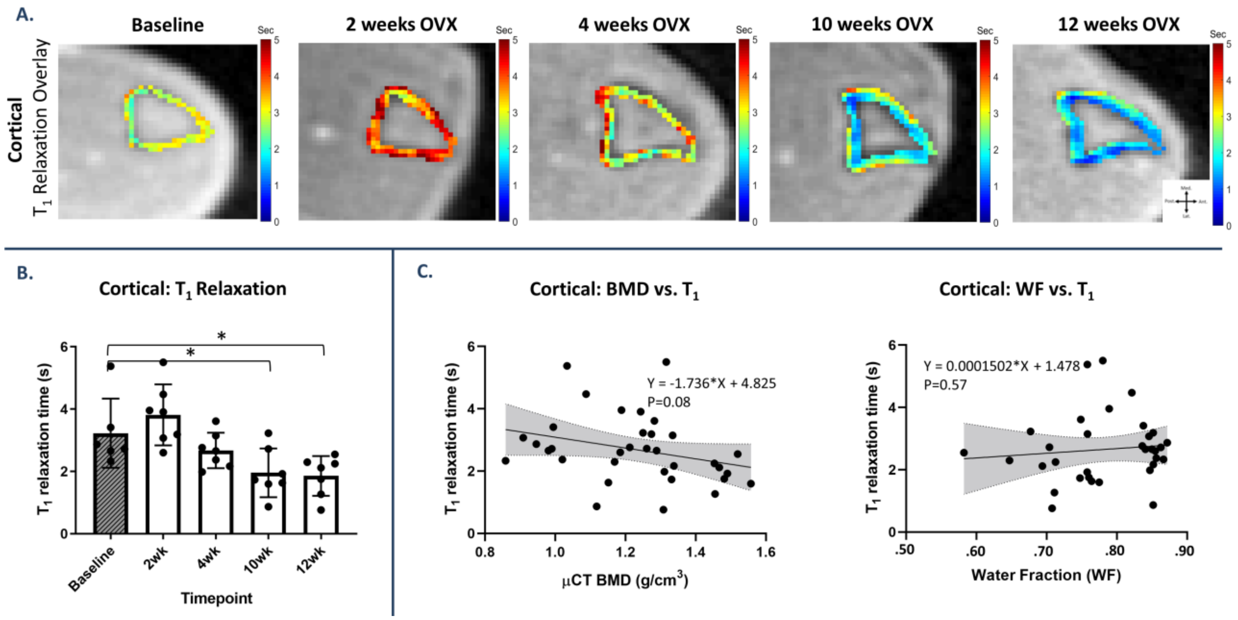

Figure 5.10: Cortical matrix T_1 relaxation times decrease significantly following OVX in growing rats.

A) Representative axial tibia MBSWIFT images with cortical T_1 relaxation map overlay for one rat at baseline through 12 weeks post-OVX. B) Mean ± SD of T_1 relaxation times in the cortical VOI measured using VFA-MBSWIFT at baseline through 12 weeks post-OVX (n=7). RM ANOVA with a Holm-Sidak post-hoc test determined T_1 relaxation times significantly decreased from baseline by 10 weeks post-OVX (brackets and stars). C) Regression plots show associations between cortical µCT-derived BMD and cortical T_1 relaxation (right) and between cortical water fraction (WF) and T_1 relaxation (left). Cortical BMD and T_1 relaxation demonstrated a negative relationship which was not significant. There was no statistical association between T_1 relaxation and WF. In all cases, $p \leq 0.05$. VFA-MBSWIFT= variable flip angle Multi-Band SWeep Imaging with Fourier Transformation MRI (used to acquire volumetric T_1 relaxation time measures); VOI= volume of interest; BMD= bone mineral density; WF = water fraction; OVX= ovariectomy.

Tables

Table 5.1:MRI scan parameters.

Sequence	**Saturation**	**Flip Angle (°)**	**TE (ms)**	**TR (ms)**	**Ave**	**Matrix**	**FOV (mm^3)**	**Voxel Size (μm^3)**	**Time**
3DGE	*No Saturation*	20	2.41	4.78	1	256x256x256	40	156	5 m 13 s
MBSWIFT	*No Saturation*	2	~0	3.37	1	256x256x256	40	156	56 s
		4	~0	3.37	1	256x256x256	40	156	56 s
		6	~0	3.37	1	256x256x256	40	156	56 s
MBSWIFT	*Fat Saturation*	2	~0	3.37	1	256x256x256	40	156	56 s
		4	~0	3.37	1	256x256x256	40	156	56 s
		6	~0	3.37	1	256x256x256	40	156	56 s
MBSWIFT	*Water Saturation*	2	~0	3.37	1	256x256x256	40	156	56 s
		4	~0	3.37	1	256x256x256	40	156	56 s
		6	~0	3.37	1	256x256x256	40	156	56 s

TE= echo time; TR= repetition time; Ave= number of averages; FOV= field of view. Resolution was isotropic in all cases.

Table 5.2: Summary of Pearson Correlations between imaging modalities used to obtain bone mineral density (BMD).

VOI	**Imaging Method for BMD**	**Correlation Coefficient [r]**	**P-value**
Cortical	µCT vs. DS µCT	0.97	<0.0001
	µCT vs. MRI BMD	0.67	<0.0001
	µCT vs. SI MRI BMD	0.65	<0.0001
	MRI BMD vs. SI MRI BMD	0.98	<0.0001
Trabecular	µCT vs. DS µCT	0.73	<0.0001
	µCT vs. MRI BMD	0.58	<0.0001
	µCT vs. SI MRI BMD	0.62	<0.0001
	MRI BMD vs. SI MRI BMD	0.97	<0.0001

VOI= volume of interest; DS= down sampled; SI= signal intensity; BMD= bone mineral density

Table 5.3: Summary of Pearson Correlations between MBSWIFT MRI outcomes and μCT derived BMD.

VOI	**μCT BMD vs. SWIFT MRI Outcome**	**Correlation Coefficient [r]**	**P-value**
Cortical	μCT BMD vs. WF	-0.6	0.0002
	μCT BMD vs. SigNorm	-0.32	0.066
	μCT BMD vs. T_1 Relaxation	-0.3	0.08
Trabecular	μCT BMD vs. FF	0.27	0.21
	μCT BMD vs. SigNorm	0.04	0.82

VOI=Volume of interest; BMD=bone mineral density; WF=water fraction; SigNorm=normalized signal intensity; FF=fat fraction.

Chapter 6 Conclusions

This thesis established a novel model to understand individual patient treatment response to an emerging therapeutic, sclerostin antibody (SclAb) prior to clinical exposure in osteogenesis imperfecta (OI) and described an alternative *in vivo* imaging strategy to quantify matrix-level and biochemical changes characteristic of OI and other bone diseases without the use of harmful ionizing radiation.

Based on the findings from these studies, the following conclusions, limitations and future studies are presented:

Gene Expression Profile and Acute Gene Expression Response to Sclerostin Inhibition in Pediatric Osteogenesis Imperfecta Bone

Conclusions

- Gene expression of *Wnt* and *Wnt*-related targets varied among untreated OI patient bone emphasizing the hallmark heterogeneity of the disease.
- SclAb induces downstream *Wnt* targets *WISP1* and *TWIST1* and a compensatory response in *Wnt* inhibitors *SOST* and *DKK1* in pediatric OI bone tissue. This observation is consistent with previous reports of an acute compensatory upregulation of similar factors in pre-clinical osteoporosis models and female Balb/c mice treated with SclAb.
- While all patients demonstrated an upregulation in osteoblast and osteoblast progenitor markers with treatment, the response was heterogeneous among individual patients.
- We observed a relationship between untreated gene expression levels and magnitude of treatment response for osteoblast and osteoblast precursors. Patients with low untreated expression demonstrated the greatest magnitude of upregulation with treatment while patients with higher untreated expression demonstrated a smaller upregulation with treatment.

- When patients were grouped by Sillence type, response varied by clinical phenotype with Type III patients demonstrating the greatest upregulation in osteoblast-related markers.
- *In vivo* implanted OI patient bone tissue demonstrated a bone forming response to SclAb with the greatest response from trabecular-derived OI tissue.

We conclude that understanding patients' genetic, cellular, and morphological bone phenotypes may play a crucial role in predicting treatment response, thus aiding clinical decision making for pharmacological intervention to address fragility in OI.

Limitations

We recognize several limitations to the present study. We evaluated expression levels in OI patient bone tissue removed during corrective orthopaedic procedure using qPCR to quantify a panel of key genes involved in bone metabolism. We are therefore, evaluating a specific point in time for these patients; it is both feasible and likely that expression levels will continue to change with growth and in consequence to environmental factors in this pediatric population. We were unable to standardize bone harvest site in the present study; instead, this rare pediatric bone tissue was taken as surgical waste from patients undergoing corrective orthopaedic procedure. As indication for surgery varied across patients, so did the site of bone harvest. We did consider bone morphological type (trabecular- or cortical-derived) in our evaluation of treatment response. As such, it is feasible that expression levels varied by bone site within the same patient and site variation likely played a role in the untreated expression levels observed between OI patients and the magnitude of treatment response. Even so we believe this variation was not a critical factor when evaluating treatment response *within* the patient where treatment response was normalized to that patient's untreated gene expression. The amount of nucleic acid concentration, which was dependent on the amount of bone tissue harvested, limited the number of genes we were able to evaluate using TaqMan qPCR in some patients. This also inhibited the number of conditions we were able to evaluate; as such future studies should include a baseline or “time 0” condition where bone removed from the patient is immediately processed for qPCR. This should also be performed because the act of culturing the bone itself may have altered gene expression; culture lacks all the growth factors inherent to in vivo and therefore may have influenced untreated expression.

Future Studies

In the present study, did not use a humanized form of SclAb to treat the OI patient bone. Instead, OI bone was treated using a pre-clinical version of SclAb (SclAb VI, Amgen , Thousand Oaks, CA) typically used in murine studies. Even so, we observed increases in markers of bone formation across all human bone tissue above untreated levels indicative of a bone forming response to treatment. Future studies could compare the efficiency of humanized SclAb (such as romosozumab/blosozumab) with the murine SclAb used in the present study to determine if magnitude of gene expression response is altered between formulations. If efficiency was increased using the humanized formulation, this would inform future studies applying the proposed methodology to quantify patient response.

While our focus was on an abbreviated panel of genes (a key panel we identified from prior pre-clinical work using SclAb), future studies should build on this work through RNA-sequencing (RNA-seq) of the treated rare OI tissue. RNA-seq provides more data overall and makes it possible to detect previously unknown transcripts, isoforms, junctions and evaluate genes in pathways where the user has little baseline knowledge on location that may be implicated by treatment. [445, 446]

A Xenograft Model to Evaluate the Bone Forming Effects of Sclerostin Antibody in Human Bone Derived from Pediatric Osteogenesis Imperfecta Patients

Conclusions

- The proposed xenograft model was efficacious in assessing effects of SclAb in bone cells harboring the causative OI defect.
- Treatment administered systemically to the host (mouse) can be initiated as early as 24 hours following implantation where donor bone becomes bioaccessible.
- Patient-derived osteocytes expressing human SOST and lining cells are present and remain viable up to 12 weeks of implantation in the host.
- SclAb recruits human-derived, osterix expressing lining cells to the implant surface while untreated implants had surfaces with host-derived osterix expressing cells.
- OI patients with low baseline osterix expression demonstrated robust human-derived osterix-expression after treatment while high baseline osterix expression demonstrated smaller expression gains with treatment.
- Magnitude of treatment response differed depending on implant bone type (trabecular or cortical derived OI bone) where trabecular implants demonstrated the strongest bone-forming response by four weeks measured by µCT and corroborated using histomorphometry.
- Host right femora confirmed a systemic response to SclAb in line with prior reports and served as a positive internal control for treatment in the proposed xenograft model.

Findings support the use of the xenograft model using solid bone isolates to explore the effects of novel bone-targeted therapies. We believe the findings will impact our understanding of SclAb therapy in pediatric OI tissue through establishing the efficacy of this treatment in human cells prior to extension to the clinic.

Limitations

There are several limitations to the study. First, the study was limited by low pediatric patient numbers (eight OI patients were enrolled) which was inevitable due to the rarity of the disease. [1] However, each patient yielded up to 20 implantable bone samples which allowed us to evaluate numerous treated and untreated implantation durations in a patient-matched manner. When patient bone yield was low, it limited our ability to allocate bone to every outcome measure (varying implantation durations and treatment durations) while maintaining an adequate size of the sample to implant (~3 mm^3). To mitigate this, outcome measures were prioritized to address our primary hypothesis that human OI bone can respond to SclAb *in vivo*, by focusing on µCT, immunohistochemistry, and histomorphometry in 2 and 4-week treated and untreated groups. Evaluation of the effects of tissue storage has shed light on the appropriate latency period between harvest and implantation. To increase patient numbers in future studies using this model, it may be possible to receive bone samples from other institutions within an 18 hour period following removal from the OI patient, based on results from the time course evaluation using TUNEL assay for apoptosis. Due to the rarity of the disease and our interest in investigating the impact of heterogeneity on treatment response, bone was harvested from all-comers undergoing orthopaedic surgical intervention which ranged from fracture repair, osteotomy and hardware removal and included tissue from various locations in the body (humerus, radius, femur, tibia) which intraskeletally undergo varying rates of remodeling. [447, 448] The non-OI group contained homogenized bone tissue harvested in otherwise healthy individuals from tibial tunnel reamings during ACL reconstructive procedure and implanted as a morselized trabecular bone mass. The bone collected for the study was bone that would have typically been discarded as surgical waste therefore it was not possible to standardize harvest location and bone type (cortical/trabecular). While this may have inhibited some more standardized analyses, it could be argued that a strength of the model is its ability to evaluate changes in heterogeneous, rare tissue and allowed us to evaluate the presence of a differential response to treatment and implantation in the model we described. Finally, it is accepted that sclerostin expression is altered under loading conditions and during unloading.[449] While the model allows for *in vivo* evaluation of the tissue, it is not fully analogous to the patient as the implanted bone tissue does not experience any normal loading condition.

Future Studies

The xenograft model described in this work gives rise to several ways we can explore emerging therapeutics in its target tissue. The model can first be extrapolated to other rare bone tissue, harvested from corrective orthopaedic procedure or through iliac crest biopsy, and implanted into the athymic mouse for study. Treatment is not limited to SclAb; the advent of novel therapeutics exploiting new pathways can and should be explored in the target tissue prior clinical extension. Our model provides a safe model where human bone can be treated with no contraindication to the patient. While the xenograft model was used in the framework of evaluating a novel anabolic bone therapy to treat a rare bone disease, the model may find utility in the study of human bone metastasis. The model in this work demonstrates that a human bone isolate can be successfully implanted into the host mouse and remain viable, with donor derived elements up to twelve weeks. This would allow a clinically relevant scenario where tumor propagation can be studied in native bone tissue.

Next, the untreated OI implants in the study demonstrated bone surfaces where osterix expression was primarily mouse (host) derived at two and four weeks (where treated implants had surfaces that expressed human-derived osterix). By four weeks, we observed a few instances of mouse-derived SOST below the bone surface in the untreated OI implants. This presents a unique scenario in which to 1) study inter-species signaling of the osteocytes and 2) determine if bone quality in the matrix improves in a scenario where mouse osteoblasts which are not defective in collagen are laid down into the bone matrix as osteocytes. This would require increasing implantation duration to increase the amount of mouse-derived osteoblasts which differentiate to osteocytes in the implant. It would be interesting to determine response of sclerostin to mechanical loading in a human bone implant with embedded mouse osteocytes that express mouse SOST compared to a human derived implant expressing only human SOST. This evaluation would explore if mechanosensing and signaling between bone cells of different species would be possible.

Literature supports that SclAb acts in part by decreasing bone resorption through a decrease in osteoclast number [399-401]. However, we did not observe a significant change in bone resorption with SclAb treatment, compared to baseline and untreated controls, at two or four weeks. In our study, bone resorption was quantified using TRAP staining on OI bone implant sections and we did not quantify host serum TRAP levels. Further, the TRAP staining technique we employed did not differentiate between donor/host osteoclasts (like what was performed using immunohistochemistry where concurrent staining for human mitochondria allowed us to determine if expression was donor or host derived). Therefore we were unable to determine if the lack of decrease in implant bone resorption with treatment was due to an increase of resorptive activity from the host acting on the implant. Future work using the xenograft model should evaluate the contributions of sclerostin inhibition (from SclAb) between circulating SOST (host) and local (human) to observe where the antibody is binding. Studies should understand if circulating mouse sclerostin can bind to local human cells; this observation could be performed by fluorescent tagging the antibody molecule. However, one should be cautious with tagging in this scenario since tagging molecules inevitably changes the size and may make it difficult-to-impossible for circulating SOST to make its way to the matrix.

While an upregulation in osteoblast and osteoblast precursor markers were observed in Chapter 3 with acute SclAb treatment and acute response *in vivo* was observed in Chapter 3, we were not able to evaluate where and what type of new bone was being deposited. This would be of great interest to further understand the effects of bone morphology and clinical phenotype on treatment response to SclAb. Further, evaluation of the quality of new bone deposited across all OI genotypes during anabolic treatment would interesting. It has been argued that, because OI is a collagen related bone disorder where osteoblasts can lay down defective collagen, increasing the amount of this bone (defective) may not be mechanically advantageous. Future studies could utilize *in situ* hybridization of osteocalcin and perhaps calcium-tagging of OI bone isolates treated in culture to visualize location and quality of new bone deposition.

Finally, future analysis using the proposed xenograft model should evaluate gene expression response analogous to the panel reported in Chapter 3 to determine the transcriptional effects of SclAb in the host-derived microenvironment in comparison to the *in vitro* treatment response. It is understood that *in vitro* provides a controlled environment to study the effects of SclAb in target OI tissue but lacks biokinetic and metabolic factors inherent to the *in vivo* environment. These factors, as such, likely influence gene expression response and are integral to further understanding factors contributing to an eventual bone-forming response in human tissue.

In Vivo Quantitative Imaging Biomarkers of Bone Quality and Mineral Density using a Novel 3D Zero Echo Time Magnetic Resonance Imaging Approach

Conclusions

- The direct quantification of BMD using ZTE MRI is strongly correlated to BMD acquired using µCT in both the cortical and trabecular regions.
- Longitudinally, both MRI and µCT BMD detected significant increases from baseline by two weeks post-OVX in the cortical bone

- While BMD increased longitudinally in the animals likely as a result of growth competing with estrogen deficiency-induced changes in the mineral phase, proposed MRI biomarkers were sensitive to OVX-related changes by 10 weeks post-surgery.
- Specifically, MRI detected a significant decrease in cortical water and significant increase in marrow fat by 10 weeks post-OVX.
- We achieved volumetric T_1 relaxation mapping in the cortical regions of the bone using the variable flip angle (VFA) method and observed a significant decrease in T_1 by 10 weeks post-OVX.
- During sequential drying, as cortical water decreased (measured using ZTE MRI), percent water loss by volume increased; this strong negative correlation was significant between the two measures ($R=-0.98$; $p=0.01$). Results indicate the experimental ZTE MRI sequence is highly sensitive cortical water loss.
- Findings point to the experimental ZTE MRI's ability to detect biochemical and material-level alterations occurring in the system following estrogen deficiency independent of changes in mineral.

In conclusion, the experimental zero echo time (ZTE) MRI sequence, MBSWIFT, significantly detected longitudinal increases in BMD comparable to BMD measured by µCT and significantly correlated to BMD acquired using the gold standard approach. Results support the utility of ZTE MRI to characterize the mineral phase of bone without ionizing radiation. While BMD increased following OVX, likely as a result of growth, the proposed ZTE MRI biomarkers targeting additional measures of bone quality significantly detected changes in the bone at 10 weeks that were consistent with estrogen-deficiency following OVX.

Limitations

In the present study, we may have been limited by the age of our animals at the time of OVX (six weeks old) where the rats were reproductively mature yet still growing.[450] The continued growth appeared to compete with estrogen deficiency-induced changes in the mineral phase where BMD significantly increased longitudinally over the course of the study. The impact of growth on OVX-related changes has been highlighted in other studies. Turner et al. observed that rats ovariectomized at seven weeks of age demonstrated a significantly increased bone formation rate at the tibial diaphysis by four weeks compared to SHAM.[451] The authors did not observe osteopenic changes in the OVX animals and reasoned that increasing radial growth overshadowed increases in endosteal resorption. In another study, rats ovariectomized at 10 weeks of age significantly increased bone formation in the tibia (measured at 5 weeks post-OVX) and the authors postulated estrogenic antagonism may have been overshadowed by the stimulatory effects of growth hormone.[452] It should be restated that our use of OVX in growing rats satisfied the goal of the present study where we sought to compare imaging modalities, including the sensitivity of their outcomes, longitudinally in a system of changing bone mass and material composition. While BMD increased over time in our growing rats following OVX, our proposed ZTE MRI was able to characterize BMD in a manner which significantly correlated to µCT and MRI provided additive quantitative outcomes about bone quality in a manner consistent with estrogen deficiency. The present study was not cross sectional and we did not use a SHAM operated control group for comparison. Instead, we focused on the sensitivity of MRI to detect longitudinal *in vivo* changes following OVX compared to measures acquired at baseline. A SHAM group, however, may have permitted OVX-related changes in BMD to be detected over time even during growth. Lietner et al. demonstrated that SHAM-operated 3 month old female rats longitudinally increased bone growth (significantly) by 10% at four weeks. [453] In the OVX rats, the authors determined that this growth rate “dampened” BMD results measured longitudinally from baseline. When the authors compared the OVX rats to the SHAM operated group, a significant decrease in OVX BMD compared to SHAM was observed. [453]

There is increasing interest in characterizing microarchitecture, in addition to BMD, as it relates to bone health and biomechanics[454-456] which is almost ubiquitously measured using high-resolution µCT pre-clinically and HR-pQCT in clinical studies.[457] Compared to µCT, proton-based MRI is limited by the *in vivo* spatial resolution it is able to achieve while maintaining a sufficient signal to noise ratio (SNR) and limited its ability to resolve microarchitecture of the trabeculae, for example. Resolution is directly proportional to the number of pixels and therefore can be improved by decreasing the FOV and increasing the matrix size. However, this comes at a tradeoff to SNR where SNR is inversely proportional to the basic resolution (or, directly proportional to pixel size). While not evaluated in the present study, we believe measures of cortical thickness in our rat tibia would be possible but the potential for partial-volume averaging, which could over- or underestimate the binarized thickness of the cortices, is a concern at decreased resolution. We instead focused on the ZTE MRI's ability to resolve mineral density, in addition to other bone quality outcomes, in the rat proximal tibia. Using our 156 µm *in vivo* MBSWIFT MR images we were able to achieve significant correlation in BMD measures between high resolution (35 µm) µCT (r = 0.67 for cortical region and r = 0.62 for trabecular region). Future work should focus on increasing resolution in the proposed ZTE MR images to determine if resolving cortical thickness and eventually trabecular microarchitecture of the rat bone is attainable while maintaining a sufficient SNR to obtain meaningful biomarker measures in the bone.

Future Studies

Building on the patient-specific xenograft approach in Chapter 4 combined with ZTE MRI using MBSWIFT in Chapter 5, an introduction of superparamagnetic iron oxide (SPIO) nanoparticle-labeled cancer cells in an ectopic orthotopic hybrid model of bone metastasis could be used to guide MR tracking of cell fate in the spirit of Paget's seed/soil hypothesis. Novel to the approach is the use of a 3D radial ZTE MRI sequence which will decrease iron blooms because of the k-space sampling trajectory and allow 1) the possibility of tracking of individual cells because of the more discrete iron blooms and 2) allow for the local bone environment to remain visible (due to reduced artifact from iron particles because of increased signal intensity possible novel to this acquisition approach).[291] Using MBSWIFT for this application, bone quality measures in the local microenvironment could be simultaneously obtained. Only now can the local surrounding bone environment be probed for the earliest biochemical alterations by resolving T_1 relaxation using the variable flip angle (VFA) method described in Chapter 5 in addition to marrow fat, cortical water fraction and BMD, without the use of ionizing radiation. Imaging findings could be correlated to serum markers of metabolic bone turnover indicative of metastasis. Now that we can quantify the earliest changes due to bone metastasis (MBSWIFT imaging biomarkers) using a non-invasive imaging approach, we can apply dual modality techniques at the earliest sign of metastasis to 1) deliver emerging drugs locally using microbubbles and 2) test novel ablation techniques which exploit sound and light (photothermal therapy (PTT) and high-intensity ultrasound ablation) to identify biological factors that bifurcate patients (tumors) from being responders versus non-responders.

Numerous studies have highlighted the ability to quantify bi-component water populations in the cortical bone using ultra short echo time (UTE) MRI. [269, 271, 458] The importance of each water population and its role in understanding mechanical strength is understood and as such, reporting these values as they relate to bone health using MRI is of great interest.[29] We reported cortical water fraction, or the fraction of signal in the image coming from water, but were unable to derive bound and free populations using the MBSWIFT technique. While MBSWIFT is able to achieve TE=0, the sequence cannot increase TE and is only able to acquire TE=0. This is unlike UTE, a gradient echo approach, where the TEs can be sequentially increased and multiple echoes acquired and fit to resolve the short and long T_2 components. Future studies using MBSWIFT could discriminate between water pools by utilizing saturation schemes at the bound and free water peaks. The water fraction arising from each pool could then be quantified.

Each imaging modality suffers from its own limitations and boasts its unique set of strengths; by combining non-invasive modalities to create an omni-modality approach we can reap the benefits, biologically, of complementary information. As such, there is a clear and unique role in incorporating photoacoustic imaging (PA) and MRI. Through activatable next generation gadolinium metallalofullerene combined with a photothermal agent with near infrared (NIR) absorbance (previously described [459]) the agent can be utilized in a dual-modality scenario, PA with MRI, where photothermal therapy (PTT) can be achieved and the activatable MRI contrast of the tumor environment can guide quantification. Unique to this proposed study would be the addition of ZTE MRI, such as MBSWIFT, where local environments with short T_2s, such as bone and lung, could explored. By developing a real-time registration or “fusing” of PA data to MR images, we can increase clinical efficacy providing immediate information from PA where MRI can provide a morphological reference coupled with voxel-wise mapping (of an imaging biomarker such as T_1 proposed in the present study) in the local environment without harmful ionizing radiation.

Bibliography

1. Van Dijk, F.S. and D.O. Sillence, *Osteogenesis imperfecta: clinical diagnosis, nomenclature and severity assessment.* Am J Med Genet A, 2014. **164A**(6): p. 1470-81.
2. Sillence, D.O., A. Senn, and D.M. Danks, *Genetic heterogeneity in osteogenesis imperfecta.* J Med Genet, 1979. **16**(2): p. 101-16.
3. Marini, J.C., et al., *Osteogenesis imperfecta.* Nat Rev Dis Primers, 2017. **3**: p. 17052.
4. Marini, J.C., et al., *Consortium for osteogenesis imperfecta mutations in the helical domain of type I collagen: regions rich in lethal mutations align with collagen binding sites for integrins and proteoglycans.* Hum Mutat, 2007. **28**(3): p. 209-21.
5. Reyes, C., et al., *Risks and Benefits of Bisphosphonate Therapies.* J Cell Biochem, 2016. **117**(1): p. 20-8.
6. Hald, J.D., et al., *Bisphosphonates for the prevention of fractures in osteogenesis imperfecta: meta-analysis of placebo-controlled trials.* J Bone Miner Res, 2015. **30**(5): p. 929-33.
7. Dwan, K., et al., *Bisphosphonate therapy for osteogenesis imperfecta.* Cochrane Database Syst Rev, 2014(7): p. CD005088.
8. Ke, H.Z., et al., *Sclerostin and Dickkopf-1 as therapeutic targets in bone diseases.* Endocr Rev, 2012. **33**(5): p. 747-83.
9. Delgado-Calle, J., A.Y. Sato, and T. Bellido, *Role and mechanism of action of sclerostin in bone.* Bone, 2017. **96**: p. 29-37.
10. Genant, H.K., et al., *Effects of Romosozumab Compared With Teriparatide on Bone Density and Mass at the Spine and Hip in Postmenopausal Women With Low Bone Mass.* J Bone Miner Res, 2017. **32**(1): p. 181-187.
11. Graeff, C., et al., *Administration of romosozumab improves vertebral trabecular and cortical bone as assessed with quantitative computed tomography and finite element analysis.* Bone, 2015. **81**: p. 364-9.
12. McClung, M.R., et al., *Romosozumab in postmenopausal women with low bone mineral density.* N Engl J Med, 2014. **370**(5): p. 412-20.
13. Cosman, F., et al., *Romosozumab Treatment in Postmenopausal Women with Osteoporosis.* N Engl J Med, 2016. **375**(16): p. 1532-1543.
14. Keaveny, T.M., et al., *Greater Gains in Spine and Hip Strength for Romosozumab Compared With Teriparatide in Postmenopausal Women With Low Bone Mass.* J Bone Miner Res, 2017. **32**(9): p. 1956-1962.
15. Sinder, B.P., et al., *Sclerostin antibody improves skeletal parameters in a Brtl/+ mouse model of osteogenesis imperfecta.* J Bone Miner Res, 2013. **28**(1): p. 73-80.
16. Sinder, B.P., et al., *Effect of anti-sclerostin therapy and osteogenesis imperfecta on tissue-level properties in growing and adult mice while controlling for tissue age.* Bone, 2016. **84**: p. 222-229.

17. Sinder, B.P., et al., *Rapidly growing Brtl/+ mouse model of osteogenesis imperfecta improves bone mass and strength with sclerostin antibody treatment.* Bone, 2015. **71**: p. 115-23.
18. Grafe, I., et al., *Sclerostin Antibody Treatment Improves the Bone Phenotype of Crtap(-/-) Mice, a Model of Recessive Osteogenesis Imperfecta.* J Bone Miner Res, 2016. **31**(5): p. 1030-40.
19. Jacobsen, C.M., et al., *Targeting the LRP5 pathway improves bone properties in a mouse model of osteogenesis imperfecta.* J Bone Miner Res, 2014. **29**(10): p. 2297-306.
20. Roschger, A., et al., *Effect of sclerostin antibody treatment in a mouse model of severe osteogenesis imperfecta.* Bone, 2014. **66**: p. 182-8.
21. Glorieux, F.H., et al., *BPS804 Anti-Sclerostin Antibody in Adults With Moderate Osteogenesis Imperfecta: Results of a Randomized Phase 2a Trial.* J Bone Miner Res, 2017. **32**(7): p. 1496-1504.
22. Kozloff, K.M., *Osteogenesis Imperfecta: A Need to Understand Divergent Treatment Outcomes in a Disorder Rich in Heterogeneity.* J Bone Miner Res, 2019.
23. Kanis, J.A., *Diagnosis of osteoporosis and assessment of fracture risk.* Lancet, 2002. **359**(9321): p. 1929-36.
24. Moore, M.S., et al., *The role of dual energy x-ray absorptiometry in aiding the diagnosis of pediatric osteogenesis imperfecta.* Am J Orthop (Belle Mead NJ), 1998. **27**(12): p. 797-801.
25. Renaud, A., et al., *Radiographic features of osteogenesis imperfecta.* Insights Imaging, 2013. **4**(4): p. 417-29.
26. Genant, H.K., et al., *Noninvasive assessment of bone mineral and structure: state of the art.* J Bone Miner Res, 1996. **11**(6): p. 707-30.
27. Tremoleda, J.L., et al., *Imaging technologies for preclinical models of bone and joint disorders.* EJNMMI Res, 2011. **1**(1): p. 11.
28. Schambach, S.J., et al., *Application of micro-CT in small animal imaging.* Methods, 2010. **50**(1): p. 2-13.
29. Granke, M., M.D. Does, and J.S. Nyman, *The Role of Water Compartments in the Material Properties of Cortical Bone.* Calcif Tissue Int, 2015. **97**(3): p. 292-307.
30. Fonseca, H., et al., *Bone quality: the determinants of bone strength and fragility.* Sports Med, 2014. **44**(1): p. 37-53.
31. Bala, Y. and E. Seeman, *Bone's Material Constituents and their Contribution to Bone Strength in Health, Disease, and Treatment.* Calcif Tissue Int, 2015. **97**(3): p. 308-26.
32. Marshall, D., O. Johnell, and H. Wedel, *Meta-analysis of how well measures of bone mineral density predict occurrence of osteoporotic fractures.* BMJ, 1996. **312**(7041): p. 1254-9.
33. Ammann, P. and R. Rizzoli, *Bone strength and its determinants.* Osteoporos Int, 2003. **14 Suppl 3**: p. S13-8.
34. Vanderheyden, J.L., *The use of imaging in preclinical drug development.* Q J Nucl Med Mol Imaging, 2009. **53**(4): p. 374-81.
35. Kagadis, G.C., et al., *In vivo small animal imaging: current status and future prospects.* Med Phys, 2010. **37**(12): p. 6421-42.
36. Cunha, L., et al., *Preclinical imaging: an essential ally in modern biosciences.* Mol Diagn Ther, 2014. **18**(2): p. 153-73.

37. Chang, G., et al., *MRI assessment of bone structure and microarchitecture.* J Magn Reson Imaging, 2017. **46**(2): p. 323-337.
38. Renaud, G., et al., *In vivo ultrasound imaging of the bone cortex.* Phys Med Biol, 2018. **63**(12): p. 125010.
39. Nyman, J.S., et al., *Measurements of mobile and bound water by nuclear magnetic resonance correlate with mechanical properties of bone.* Bone, 2008. **42**(1): p. 193-9.
40. Horch, R.A., et al., *Characterization of 1H NMR signal in human cortical bone for magnetic resonance imaging.* Magn Reson Med, 2010. **64**(3): p. 680-7.
41. Robson, M.D. and G.M. Bydder, *Clinical ultrashort echo time imaging of bone and other connective tissues.* NMR Biomed, 2006. **19**(7): p. 765-80.
42. Siriwanarangsun, P., et al., *Ultrashort time to echo magnetic resonance techniques for the musculoskeletal system.* Quant Imaging Med Surg, 2016. **6**(6): p. 731-743.
43. Kular, J., et al., *An overview of the regulation of bone remodelling at the cellular level.* Clin Biochem, 2012. **45**(12): p. 863-73.
44. Fratzl-Zelman, N., et al., *Decreased bone turnover and deterioration of bone structure in two cases of pycnodysostosis.* J Clin Endocrinol Metab, 2004. **89**(4): p. 1538-47.
45. Wehrli, F.W., et al., *Quantitative MRI for the assessment of bone structure and function.* NMR Biomed, 2006. **19**(7): p. 731-64.
46. Hadjidakis, D.J. and Androulakis, II, *Bone remodeling.* Ann N Y Acad Sci, 2006. **1092**: p. 385-96.
47. Bonewald, L.F., *The amazing osteocyte.* J Bone Miner Res, 2011. **26**(2): p. 229-38.
48. Boyce, B.F., et al., *The osteoclast, bone remodelling and treatment of metabolic bone disease.* Eur J Clin Invest, 2012. **42**(12): p. 1332-41.
49. Bonewald, L.F., *Osteocytes as dynamic multifunctional cells.* Ann N Y Acad Sci, 2007. **1116**: p. 281-90.
50. Parfitt, A.M., *Targeted and nontargeted bone remodeling: relationship to basic multicellular unit origination and progression.* Bone, 2002. **30**(1): p. 5-7.
51. Santos, A., A.D. Bakker, and J. Klein-Nulend, *The role of osteocytes in bone mechanotransduction.* Osteoporos Int, 2009. **20**(6): p. 1027-31.
52. Feng, X. and J.M. McDonald, *Disorders of bone remodeling.* Annu Rev Pathol, 2011. **6**: p. 121-45.
53. Baljet, B., *Aspects of the history of osteogenesis imperfecta (Vrolik's syndrome).* Ann Anat, 2002. **184**(1): p. 1-7.
54. Marini, J.C., *Osteogenesis imperfecta: comprehensive management.* Adv Pediatr, 1988. **35**: p. 391-426.
55. Martin, E. and J.R. Shapiro, *Osteogenesis imperfecta:epidemiology and pathophysiology.* Curr Osteoporos Rep, 2007. **5**(3): p. 91-7.
56. Sillence, D.O. and D.L. Rimoin, *Classification of osteogenesis imperfect.* Lancet, 1978. **1**(8072): p. 1041-2.
57. Rauch, F. and F.H. Glorieux, *Osteogenesis imperfecta.* Lancet, 2004. **363**(9418): p. 1377-85.
58. Glorieux, F.H., et al., *Type V osteogenesis imperfecta: a new form of brittle bone disease.* J Bone Miner Res, 2000. **15**(9): p. 1650-8.
59. Cho, T.J., et al., *A single recurrent mutation in the 5'-UTR of IFITM5 causes osteogenesis imperfecta type V.* Am J Hum Genet, 2012. **91**(2): p. 343-8.

60. Barnes, A.M., et al., *Deficiency of cartilage-associated protein in recessive lethal osteogenesis imperfecta.* N Engl J Med, 2006. **355**(26): p. 2757-64.
61. Cabral, W.A., et al., *Prolyl 3-hydroxylase 1 deficiency causes a recessive metabolic bone disorder resembling lethal/severe osteogenesis imperfecta.* Nat Genet, 2007. **39**(3): p. 359-65.
62. Warman, M.L., et al., *Nosology and classification of genetic skeletal disorders: 2010 revision.* Am J Med Genet A, 2011. **155A**(5): p. 943-68.
63. Cheung, M.S. and F.H. Glorieux, *Osteogenesis Imperfecta: update on presentation and management.* Rev Endocr Metab Disord, 2008. **9**(2): p. 153-60.
64. Forlino, A., et al., *New perspectives on osteogenesis imperfecta.* Nat Rev Endocrinol, 2011. **7**(9): p. 540-57.
65. Ben Amor, I.M., et al., *Skeletal clinical characteristics of osteogenesis imperfecta caused by haploinsufficiency mutations in COL1A1.* J Bone Miner Res, 2013. **28**(9): p. 2001-7.
66. Ha-Vinh, R., et al., *Phenotypic and molecular characterization of Bruck syndrome (osteogenesis imperfecta with contractures of the large joints) caused by a recessive mutation in PLOD2.* Am J Med Genet A, 2004. **131**(2): p. 115-20.
67. Morello, R., et al., *CRTAP is required for prolyl 3- hydroxylation and mutations cause recessive osteogenesis imperfecta.* Cell, 2006. **127**(2): p. 291-304.
68. Christiansen, H.E., et al., *Homozygosity for a missense mutation in SERPINH1, which encodes the collagen chaperone protein HSP47, results in severe recessive osteogenesis imperfecta.* Am J Hum Genet, 2010. **86**(3): p. 389-98.
69. Alanay, Y., et al., *Mutations in the gene encoding the RER protein FKBP65 cause autosomal-recessive osteogenesis imperfecta.* Am J Hum Genet, 2010. **86**(4): p. 551-9.
70. Zacharin, M. and J. Bateman, *Pamidronate treatment of osteogenesis imperfecta--lack of correlation between clinical severity, age at onset of treatment, predicted collagen mutation and treatment response.* J Pediatr Endocrinol Metab, 2002. **15**(2): p. 163-74.
71. Ward, L.M., et al., *Alendronate for the treatment of pediatric osteogenesis imperfecta: a randomized placebo-controlled study.* J Clin Endocrinol Metab, 2011. **96**(2): p. 355-64.
72. Gertz, B.J., et al., *Clinical pharmacology of alendronate sodium.* Osteoporos Int, 1993. **3 Suppl 3**: p. S13-6.
73. Drake, M.T., B.L. Clarke, and S. Khosla, *Bisphosphonates: mechanism of action and role in clinical practice.* Mayo Clin Proc, 2008. **83**(9): p. 1032-45.
74. McClung, M.R., et al., *Denosumab in postmenopausal women with low bone mineral density.* N Engl J Med, 2006. **354**(8): p. 821-31.
75. Hoyer-Kuhn, H., et al., *Two years' experience with denosumab for children with osteogenesis imperfecta type VI.* Orphanet J Rare Dis, 2014. **9**: p. 145.
76. Li, G., et al., *Systematic review of the effect of denosumab on children with osteogenesis imperfecta showed inconsistent findings.* Acta Paediatr, 2018. **107**(3): p. 534-537.
77. Hoyer-Kuhn, H., et al., *Safety and efficacy of denosumab in children with osteogenesis imperfect--a first prospective trial.* J Musculoskelet Neuronal Interact, 2016. **16**(1): p. 24-32.
78. Ward, L., et al., *Osteogenesis Imperfecta Type VI in Individuals from Northern Canada.* Calcif Tissue Int, 2016. **98**(6): p. 566-72.
79. Ferrari-Lacraz, S. and S. Ferrari, *Do RANKL inhibitors (denosumab) affect inflammation and immunity?* Osteoporos Int, 2011. **22**(2): p. 435-46.

80. Trejo, P., F. Rauch, and L. Ward, *Hypercalcemia and hypercalciuria during denosumab treatment in children with osteogenesis imperfecta type VI.* J Musculoskelet Neuronal Interact, 2018. **18**(1): p. 76-80.
81. Marini, J.C., et al., *Positive linear growth and bone responses to growth hormone treatment in children with types III and IV osteogenesis imperfecta: high predictive value of the carboxyterminal propeptide of type I procollagen.* J Bone Miner Res, 2003. **18**(2): p. 237-43.
82. Orwoll, E.S., et al., *Evaluation of teriparatide treatment in adults with osteogenesis imperfecta.* J Clin Invest, 2014. **124**(2): p. 491-8.
83. Vahle, J.L., et al., *Skeletal changes in rats given daily subcutaneous injections of recombinant human parathyroid hormone (1-34) for 2 years and relevance to human safety.* Toxicol Pathol, 2002. **30**(3): p. 312-21.
84. McClung, M.R. and A. Grauer, *Romosozumab in postmenopausal women with osteopenia.* N Engl J Med, 2014. **370**(17): p. 1664-5.
85. Recker, R.R., et al., *A randomized, double-blind phase 2 clinical trial of blosozumab, a sclerostin antibody, in postmenopausal women with low bone mineral density.* J Bone Miner Res, 2015. **30**(2): p. 216-24.
86. Recknor, C.P., et al., *The Effect of Discontinuing Treatment With Blosozumab: Follow-up Results of a Phase 2 Randomized Clinical Trial in Postmenopausal Women With Low Bone Mineral Density.* J Bone Miner Res, 2015. **30**(9): p. 1717-25.
87. Forlino, A. and J.C. Marini, *Osteogenesis imperfecta.* Lancet, 2016. **387**(10028): p. 1657-71.
88. Reginster, J.Y. and N. Burlet, *Osteoporosis: a still increasing prevalence.* Bone, 2006. **38**(2 Suppl 1): p. S4-9.
89. *NIH Consensus Development Panel on Osteoporosis Prevention, Diagnosis, and Therapy, March 7-29, 2000: highlights of the conference.* South Med J, 2001. **94**(6): p. 569-73.
90. Kannegaard, P.N., et al., *Excess mortality in men compared with women following a hip fracture. National analysis of comedications, comorbidity and survival.* Age Ageing, 2010. **39**(2): p. 203-9.
91. Kado, D.M., et al., *Vertebral fractures and mortality in older women: a prospective study. Study of Osteoporotic Fractures Research Group.* Arch Intern Med, 1999. **159**(11): p. 1215-20.
92. Burge, R., et al., *Incidence and economic burden of osteoporosis-related fractures in the United States, 2005-2025.* J Bone Miner Res, 2007. **22**(3): p. 465-75.
93. Kalkan, R. and P. Tulay, *The Interactions between Bone Remodelling, Estrogen Hormone and EPH Family Genes.* Crit Rev Eukaryot Gene Expr, 2018. **28**(2): p. 135-138.
94. Cosman, F., et al., *Clinician's Guide to Prevention and Treatment of Osteoporosis.* Osteoporos Int, 2014. **25**(10): p. 2359-81.
95. Hannan, M.T., et al., *Risk factors for longitudinal bone loss in elderly men and women: the Framingham Osteoporosis Study.* J Bone Miner Res, 2000. **15**(4): p. 710-20.
96. Chen, H., et al., *Age-related changes in trabecular and cortical bone microstructure.* Int J Endocrinol, 2013. **2013**: p. 213234.
97. Colangelo, L., et al., *Understanding and managing secondary osteoporosis.* Expert Rev Endocrinol Metab, 2019: p. 1-12.

98. Bianchi, M.L., et al., *Bone health in children and adolescents with chronic diseases that may affect the skeleton: the 2013 ISCD Pediatric Official Positions.* J Clin Densitom, 2014. **17**(2): p. 281-94.
99. Bianchi, M.L., *Osteoporosis in children and adolescents.* Bone, 2007. **41**(4): p. 486-95.
100. Kulkarni, M.L. and K.S. Keshavamurthy, *Juvenile idiopathic osteoporosis.* Indian Pediatr, 2004. **41**(7): p. 737-40.
101. Idris, A.I., *Ovariectomy/orchidectomy in rodents.* Methods Mol Biol, 2012. **816**: p. 545-51.
102. Turner, R.T., B.L. Riggs, and T.C. Spelsberg, *Skeletal effects of estrogen.* Endocr Rev, 1994. **15**(3): p. 275-300.
103. Imai, Y., et al., *Estrogens maintain bone mass by regulating expression of genes controlling function and life span in mature osteoclasts.* Ann N Y Acad Sci, 2009. **1173 Suppl 1**: p. E31-9.
104. Christiansen, C. and R. Lindsay, *Estrogens, bone loss and preservation.* Osteoporos Int, 1990. **1**(1): p. 7-13.
105. Thompson, D.D., et al., *FDA Guidelines and animal models for osteoporosis.* Bone, 1995. **17**(4 Suppl): p. 125S-133S.
106. Mosekilde, L., *Assessing bone quality--animal models in preclinical osteoporosis research.* Bone, 1995. **17**(4 Suppl): p. 343S-352S.
107. Wronski, T.J., M. Cintron, and L.M. Dann, *Temporal relationship between bone loss and increased bone turnover in ovariectomized rats.* Calcif Tissue Int, 1988. **43**(3): p. 179-83.
108. Saville, P.D., *Changes in skeletal mass and fragility with castration in the rat; a model of osteoporosis.* J Am Geriatr Soc, 1969. **17**(2): p. 155-66.
109. Ibbotson, K.J., et al., *Contrasting effects of parathyroid hormone and insulin-like growth factor I in an aged ovariectomized rat model of postmenopausal osteoporosis.* J Bone Miner Res, 1992. **7**(4): p. 425-32.
110. Matt, D.W., et al., *Chronological changes in fertility, fecundity and steroid hormone secretion during consecutive pregnancies in aging rats.* Biol Reprod, 1986. **34**(3): p. 478-87.
111. Martin, R.B. and J. Ishida, *The relative effects of collagen fiber orientation, porosity, density, and mineralization on bone strength.* J Biomech, 1989. **22**(5): p. 419-26.
112. Leichter, I., et al., *The relationship between bone density, mineral content, and mechanical strength in the femoral neck.* Clin Orthop Relat Res, 1982(163): p. 272-81.
113. Hansson, T., B. Roos, and A. Nachemson, *The bone mineral content and ultimate compressive strength of lumbar vertebrae.* Spine (Phila Pa 1976), 1980. **5**(1): p. 46-55.
114. Lang, S.M., et al., *Correlation of mechanical properties of vertebral trabecular bone with equivalent mineral density as measured by computed tomography.* J Bone Joint Surg Am, 1988. **70**(10): p. 1531-8.
115. Currey, J.D., *The effect of porosity and mineral content on the Young's modulus of elasticity of compact bone.* J Biomech, 1988. **21**(2): p. 131-9.
116. Burstein, A.H., et al., *Contribution of collagen and mineral to the elastic-plastic properties of bone.* J Bone Joint Surg Am, 1975. **57**(7): p. 956-61.
117. Martin, R.B. and D.L. Boardman, *The effects of collagen fiber orientation, porosity, density, and mineralization on bovine cortical bone bending properties.* J Biomech, 1993. **26**(9): p. 1047-54.

118. Landis, W.J., *The strength of a calcified tissue depends in part on the molecular structure and organization of its constituent mineral crystals in their organic matrix.* Bone, 1995. **16**(5): p. 533-44.
119. Boskey, A.L., *Bone mineral and matrix. Are they altered in osteoporosis?* Orthop Clin North Am, 1990. **21**(1): p. 19-29.
120. Martin, B., *Aging and strength of bone as a structural material.* Calcif Tissue Int, 1993. **53 Suppl 1**: p. S34-9; discussion S39-40.
121. Neer, R.M., et al., *Effect of parathyroid hormone (1-34) on fractures and bone mineral density in postmenopausal women with osteoporosis.* N Engl J Med, 2001. **344**(19): p. 1434-41.
122. Harris, S.T., et al., *Effects of risedronate treatment on vertebral and nonvertebral fractures in women with postmenopausal osteoporosis: a randomized controlled trial. Vertebral Efficacy With Risedronate Therapy (VERT) Study Group.* JAMA, 1999. **282**(14): p. 1344-52.
123. Chesnut, C.H., 3rd, et al., *Effects of oral ibandronate administered daily or intermittently on fracture risk in postmenopausal osteoporosis.* J Bone Miner Res, 2004. **19**(8): p. 1241-9.
124. Ettinger, B., et al., *Reduction of vertebral fracture risk in postmenopausal women with osteoporosis treated with raloxifene: results from a 3-year randomized clinical trial. Multiple Outcomes of Raloxifene Evaluation (MORE) Investigators.* JAMA, 1999. **282**(7): p. 637-45.
125. Mahesh, M., *The Essential Physics of Medical Imaging, Third Edition.* Med Phys, 2013. **40**(7).
126. *Clinical indications for bone mass measurements. A report from the Scientific Advisory Board of the National Osteoporosis Foundation.* J Bone Miner Res, 1989. **4 Suppl 2**: p. 1-28.
127. Sozen, T., L. Ozisik, and N.C. Basaran, *An overview and management of osteoporosis.* Eur J Rheumatol, 2017. **4**(1): p. 46-56.
128. Sheu, A. and T. Diamond, *Bone mineral density: testing for osteoporosis.* Aust Prescr, 2016. **39**(2): p. 35-9.
129. Johnell, O., et al., *Predictive value of BMD for hip and other fractures.* J Bone Miner Res, 2005. **20**(7): p. 1185-94.
130. Bachrach, L.K., *Acquisition of optimal bone mass in childhood and adolescence.* Trends Endocrinol Metab, 2001. **12**(1): p. 22-8.
131. Gordon, C.M., et al., *2013 Pediatric Position Development Conference: executive summary and reflections.* J Clin Densitom, 2014. **17**(2): p. 219-24.
132. Mora, S. and V. Gilsanz, *Establishment of peak bone mass.* Endocrinol Metab Clin North Am, 2003. **32**(1): p. 39-63.
133. Grover, M. and L.K. Bachrach, *Osteoporosis in Children with Chronic Illnesses: Diagnosis, Monitoring, and Treatment.* Curr Osteoporos Rep, 2017. **15**(4): p. 271-282.
134. Ward, L.M., V.N. Konji, and J. Ma, *The management of osteoporosis in children.* Osteoporos Int, 2016. **27**(7): p. 2147-2179.
135. Feldkamp, L.A., et al., *The direct examination of three-dimensional bone architecture in vitro by computed tomography.* J Bone Miner Res, 1989. **4**(1): p. 3-11.
136. Faulkner, K.G., et al., *Cross-calibration of liquid and solid QCT calibration standards: corrections to the UCSF normative data.* Osteoporos Int, 1993. **3**(1): p. 36-42.

137. Lang, T.F., *Quantitative computed tomography.* Radiol Clin North Am, 2010. **48**(3): p. 589-600.
138. Kaneko, T.S., et al., *Relationships between material properties and CT scan data of cortical bone with and without metastatic lesions.* Med Eng Phys, 2003. **25**(6): p. 445-54.
139. Keyak, J.H., et al., *Reduction in proximal femoral strength due to long-duration spaceflight.* Bone, 2009. **44**(3): p. 449-53.
140. Jiang, Y., et al., *Application of micro-CT assessment of 3-D bone microstructure in preclinical and clinical studies.* J Bone Miner Metab, 2005. **23 Suppl**: p. 122-31.
141. MacNeil, J.A. and S.K. Boyd, *Improved reproducibility of high-resolution peripheral quantitative computed tomography for measurement of bone quality.* Med Eng Phys, 2008. **30**(6): p. 792-9.
142. MacNeil, J.A. and S.K. Boyd, *Accuracy of high-resolution peripheral quantitative computed tomography for measurement of bone quality.* Med Eng Phys, 2007. **29**(10): p. 1096-105.
143. Cummings, S.R., et al., *Bone density at various sites for prediction of hip fractures. The Study of Osteoporotic Fractures Research Group.* Lancet, 1993. **341**(8837): p. 72-5.
144. Keaveny, T.M., et al., *Age-dependence of femoral strength in white women and men.* J Bone Miner Res, 2010. **25**(5): p. 994-1001.
145. Sornay-Rendu, E., et al., *Rate of forearm bone loss is associated with an increased risk of fracture independently of bone mass in postmenopausal women: the OFELY study.* J Bone Miner Res, 2005. **20**(11): p. 1929-35.
146. Prentice, A., T.J. Parsons, and T.J. Cole, *Uncritical use of bone mineral density in absorptiometry may lead to size-related artifacts in the identification of bone mineral determinants.* Am J Clin Nutr, 1994. **60**(6): p. 837-42.
147. Zemel, B.S., et al., *Height adjustment in assessing dual energy x-ray absorptiometry measurements of bone mass and density in children.* J Clin Endocrinol Metab, 2010. **95**(3): p. 1265-73.
148. Manolagas, S.C., S. Kousteni, and R.L. Jilka, *Sex steroids and bone.* Recent Prog Horm Res, 2002. **57**: p. 385-409.
149. Turner, R.T., et al., *Animal models for osteoporosis.* Rev Endocr Metab Disord, 2001. **2**(1): p. 117-27.
150. Kozloff, K.M., et al., *Brittle IV mouse model for osteogenesis imperfecta IV demonstrates postpubertal adaptations to improve whole bone strength.* J Bone Miner Res, 2004. **19**(4): p. 614-22.
151. Fratzl-Zelman, N., et al., *Mineral particle size in children with osteogenesis imperfecta type I is not increased independently of specific collagen mutations.* Bone, 2014. **60**: p. 122-8.
152. Roschger, P., et al., *Evidence that abnormal high bone mineralization in growing children with osteogenesis imperfecta is not associated with specific collagen mutations.* Calcif Tissue Int, 2008. **82**(4): p. 263-70.
153. Paterson, C.R., S.J. McAllion, and J.W. Shaw, *Clinical and radiological features of osteogenesis imperfecta type IVA.* Acta Paediatr Scand, 1987. **76**(4): p. 548-52.
154. Paterson, C.R. and P.A. Mole, *Bone density in osteogenesis imperfecta may well be normal.* Postgrad Med J, 1994. **70**(820): p. 104-7.
155. Wekre, L.L., E.F. Eriksen, and J.A. Falch, *Bone mass, bone markers and prevalence of fractures in adults with osteogenesis imperfecta.* Arch Osteoporos, 2011. **6**: p. 31-8.

156. Cummings, S.R., et al., *Improvement in spine bone density and reduction in risk of vertebral fractures during treatment with antiresorptive drugs.* Am J Med, 2002. **112**(4): p. 281-9.
157. Black, D.M., et al., *The effects of parathyroid hormone and alendronate alone or in combination in postmenopausal osteoporosis.* N Engl J Med, 2003. **349**(13): p. 1207-15.
158. Bjarnason, N.H., et al., *Six and twelve month changes in bone turnover are related to reduction in vertebral fracture risk during 3 years of raloxifene treatment in postmenopausal osteoporosis.* Osteoporos Int, 2001. **12**(11): p. 922-30.
159. Sarkar, S., et al., *Relationships between bone mineral density and incident vertebral fracture risk with raloxifene therapy.* J Bone Miner Res, 2002. **17**(1): p. 1-10.
160. Gallant, M.A., et al., *Bone cell-independent benefits of raloxifene on the skeleton: a novel mechanism for improving bone material properties.* Bone, 2014. **61**: p. 191-200.
161. Aref, M., et al., *In vivo reference point indentation reveals positive effects of raloxifene on mechanical properties following 6 months of treatment in skeletally mature beagle dogs.* Bone, 2013. **56**(2): p. 449-53.
162. Allen, M.R., et al., *In Vivo UTE-MRI Reveals Positive Effects of Raloxifene on Skeletal-Bound Water in Skeletally Mature Beagle Dogs.* J Bone Miner Res, 2015. **30**(8): p. 1441-4.
163. Bivi, N., et al., *Structural features underlying raloxifene's biophysical interaction with bone matrix.* Bioorg Med Chem, 2016. **24**(4): p. 759-67.
164. Ammann, P., et al., *Strontium ranelate treatment improves trabecular and cortical intrinsic bone tissue quality, a determinant of bone strength.* J Bone Miner Res, 2007. **22**(9): p. 1419-25.
165. Meunier, P.J., et al., *The effects of strontium ranelate on the risk of vertebral fracture in women with postmenopausal osteoporosis.* N Engl J Med, 2004. **350**(5): p. 459-68.
166. Nielsen, S.P., et al., *Influence of strontium on bone mineral density and bone mineral content measurements by dual X-ray absorptiometry.* J Clin Densitom, 1999. **2**(4): p. 371-9.
167. Fogelman, I. and G.M. Blake, *Strontium ranelate for the treatment of osteoporosis.* BMJ, 2005. **330**(7505): p. 1400-1.
168. Vande Velde, G., et al., *Longitudinal in vivo microcomputed tomography of mouse lungs: No evidence for radiotoxicity.* Am J Physiol Lung Cell Mol Physiol, 2015. **309**(3): p. L271-9.
169. Bretin, F., et al., *Monte Carlo simulations of the dose from imaging with GE eXplore 120 micro-CT using GATE.* Med Phys, 2015. **42**(10): p. 5711-9.
170. Taschereau, R., P.L. Chow, and A.F. Chatziioannou, *Monte carlo simulations of dose from microCT imaging procedures in a realistic mouse phantom.* Med Phys, 2006. **33**(1): p. 216-24.
171. Arentsen, L. and S. Hui, *Characterization of rotating gantry micro-CT configuration for the in vivo evaluation of murine trabecular bone.* Microsc Microanal, 2013. **19**(4): p. 907-13.
172. *The 2007 Recommendations of the International Commission on Radiological Protection. ICRP publication 103.* Ann ICRP, 2007. **37**(2-4): p. 1-332.
173. Lochmuller, E.M., et al., *Can novel clinical densitometric techniques replace or improve DXA in predicting bone strength in osteoporosis at the hip and other skeletal sites?* J Bone Miner Res, 2003. **18**(5): p. 906-12.

174. Eckstein, F., et al., *Reproducibility and side differences of mechanical tests for determining the structural strength of the proximal femur.* J Bone Miner Res, 2004. **19**(3): p. 379-85.
175. Mettler, F.A., Jr., et al., *Effective doses in radiology and diagnostic nuclear medicine: a catalog.* Radiology, 2008. **248**(1): p. 254-63.
176. Damilakis, J., et al., *Radiation exposure in X-ray-based imaging techniques used in osteoporosis.* Eur Radiol, 2010. **20**(11): p. 2707-14.
177. Stagi, S., et al., *Peripheral quantitative computed tomography (pQCT) for the assessment of bone strength in most of bone affecting conditions in developmental age: a review.* Ital J Pediatr, 2016. **42**(1): p. 88.
178. Alwood, J.S., et al., *Heavy ion irradiation and unloading effects on mouse lumbar vertebral microarchitecture, mechanical properties and tissue stresses.* Bone, 2010. **47**(2): p. 248-55.
179. Alwood, J.S., et al., *Low-dose, ionizing radiation and age-related changes in skeletal microarchitecture.* J Aging Res, 2012. **2012**: p. 481983.
180. Willey, J.S., et al., *Risedronate prevents early radiation-induced osteoporosis in mice at multiple skeletal locations.* Bone, 2010. **46**(1): p. 101-11.
181. Kondo, H., et al., *Oxidative stress and gamma radiation-induced cancellous bone loss with musculoskeletal disuse.* J Appl Physiol (1985), 2010. **108**(1): p. 152-61.
182. Alwood, J.S., et al., *Ionizing Radiation Stimulates Expression of Pro-Osteoclastogenic Genes in Marrow and Skeletal Tissue.* J Interferon Cytokine Res, 2015. **35**(6): p. 480-7.
183. Sodickson, A., et al., *Recurrent CT, cumulative radiation exposure, and associated radiation-induced cancer risks from CT of adults.* Radiology, 2009. **251**(1): p. 175-84.
184. Ammann, P., et al., *Bone density and shape as determinants of bone strength in IGF-I and/or pamidronate-treated ovariectomized rats.* Osteoporos Int, 1996. **6**(3): p. 219-27.
185. Balena, R., et al., *The effects of 2-year treatment with the aminobisphosphonate alendronate on bone metabolism, bone histomorphometry, and bone strength in ovariectomized nonhuman primates.* J Clin Invest, 1993. **92**(6): p. 2577-86.
186. Viguet-Carrin, S., P. Garnero, and P.D. Delmas, *The role of collagen in bone strength.* Osteoporos Int, 2006. **17**(3): p. 319-36.
187. Depalle, B., et al., *Influence of cross-link structure, density and mechanical properties in the mesoscale deformation mechanisms of collagen fibrils.* J Mech Behav Biomed Mater, 2015. **52**: p. 1-13.
188. Saito, M. and K. Marumo, *Collagen cross-links as a determinant of bone quality: a possible explanation for bone fragility in aging, osteoporosis, and diabetes mellitus.* Osteoporos Int, 2010. **21**(2): p. 195-214.
189. Bailey, A.J., et al., *Biochemical changes in the collagen of human osteoporotic bone matrix.* Connect Tissue Res, 1993. **29**(2): p. 119-32.
190. Paschalis, E.P., et al., *Bone fragility and collagen cross-links.* J Bone Miner Res, 2004. **19**(12): p. 2000-4.
191. Wallace, J.M., et al., *Type I collagen exists as a distribution of nanoscale morphologies in teeth, bones, and tendons.* Langmuir, 2010. **26**(10): p. 7349-54.
192. Strupler, M., et al., *Second harmonic imaging and scoring of collagen in fibrotic tissues.* Opt Express, 2007. **15**(7): p. 4054-65.

193. Villa, M.M., et al., *Visualizing osteogenesis in vivo within a cell-scaffold construct for bone tissue engineering using two-photon microscopy.* Tissue Eng Part C Methods, 2013. **19**(11): p. 839-49.
194. Campagnola, P., *Second harmonic generation imaging microscopy: applications to diseases diagnostics.* Anal Chem, 2011. **83**(9): p. 3224-31.
195. Wilson, R.H., et al., *Review of short-wave infrared spectroscopy and imaging methods for biological tissue characterization.* J Biomed Opt, 2015. **20**(3): p. 030901.
196. Lee, H.D., et al., *Label-free photoacoustic microscopy for in-vivo tendon imaging using a fiber-based pulse laser.* Sci Rep, 2018. **8**(1): p. 4805.
197. Mountain, K.M., et al., *The functional microstructure of tendon collagen revealed by high-field MRI.* Magn Reson Med, 2011. **66**(2): p. 520-7.
198. Kakkad, S., et al., *Collagen fibers mediate MRI-detected water diffusion and anisotropy in breast cancers.* Neoplasia, 2016. **18**(10): p. 585-593.
199. Wang, X., et al., *The role of collagen in determining bone mechanical properties.* J Orthop Res, 2001. **19**(6): p. 1021-6.
200. Zioupos, P., J.D. Currey, and A.J. Hamer, *The role of collagen in the declining mechanical properties of aging human cortical bone.* J Biomed Mater Res, 1999. **45**(2): p. 108-16.
201. Nyman, J.S., et al., *The influence of water removal on the strength and toughness of cortical bone.* J Biomech, 2006. **39**(5): p. 931-8.
202. Nyman, J.S., et al., *Partial removal of pore and loosely bound water by low-energy drying decreases cortical bone toughness in young and old donors.* J Mech Behav Biomed Mater, 2013. **22**: p. 136-45.
203. Yan, J., et al., *Fracture toughness and work of fracture of hydrated, dehydrated, and ashed bovine bone.* J Biomech, 2008. **41**(9): p. 1929-36.
204. Kahler, B., M.V. Swain, and A. Moule, *Fracture-toughening mechanisms responsible for differences in work to fracture of hydrated and dehydrated dentine.* J Biomech, 2003. **36**(2): p. 229-37.
205. Lucksanasombool, P., et al., *Fracture toughness of bovine bone: influence of orientation and storage media.* Biomaterials, 2001. **22**(23): p. 3127-32.
206. Robinson, R.A., *Bone tissue: composition and function.* Johns Hopkins Med J, 1979. **145**(1): p. 10-24.
207. Jonsson, U., H. Ranta, and L. Stromberg, *Growth changes of collagen cross-linking, calcium, and water content in bone.* Arch Orthop Trauma Surg, 1985. **104**(2): p. 89-93.
208. Bousson, V., et al., *Cortical bone in the human femoral neck: three-dimensional appearance and porosity using synchrotron radiation.* J Bone Miner Res, 2004. **19**(5): p. 794-801.
209. Horch, R.A., et al., *Non-invasive predictors of human cortical bone mechanical properties: T(2)-discriminated H NMR compared with high resolution X-ray.* PLoS One, 2011. **6**(1): p. e16359.
210. Ong, H.H., A.C. Wright, and F.W. Wehrli, *Deuterium nuclear magnetic resonance unambiguously quantifies pore and collagen-bound water in cortical bone.* J Bone Miner Res, 2012. **27**(12): p. 2573-81.
211. Nomura, S., et al., *Interaction of water with native collagen.* Biopolymers, 1977. **16**(2): p. 231-46.

212. Yerramshetty, J.S. and O. Akkus, *The associations between mineral crystallinity and the mechanical properties of human cortical bone.* Bone, 2008. **42**(3): p. 476-82.
213. Scheller, E.L. and C.J. Rosen, *What's the matter with MAT? Marrow adipose tissue, metabolism, and skeletal health.* Ann N Y Acad Sci, 2014. **1311**: p. 14-30.
214. Meunier, P., et al., *Osteoporosis and the replacement of cell populations of the marrow by adipose tissue. A quantitative study of 84 iliac bone biopsies.* Clin Orthop Relat Res, 1971. **80**: p. 147-54.
215. Martin, R.B. and S.L. Zissimos, *Relationships between marrow fat and bone turnover in ovariectomized and intact rats.* Bone, 1991. **12**(2): p. 123-31.
216. Nuttall, M.E. and J.M. Gimble, *Is there a therapeutic opportunity to either prevent or treat osteopenic disorders by inhibiting marrow adipogenesis?* Bone, 2000. **27**(2): p. 177-84.
217. Agrawal, K., et al., *Evaluation of MR Spectroscopy and Diffusion-Weighted MRI in Postmenopausal Bone Strength.* Cureus, 2015. **7**(9): p. e327.
218. Schwartz, A.V., et al., *Vertebral bone marrow fat associated with lower trabecular BMD and prevalent vertebral fracture in older adults.* J Clin Endocrinol Metab, 2013. **98**(6): p. 2294-300.
219. Hu, H.H., et al., *ISMRM workshop on fat-water separation: insights, applications and progress in MRI.* Magn Reson Med, 2012. **68**(2): p. 378-88.
220. Burr, D.B., *Bone material properties and mineral matrix contributions to fracture risk or age in women and men.* J Musculoskelet Neuronal Interact, 2002. **2**(3): p. 201-4.
221. Burr, D.B., *Why bones bend but don't break.* J Musculoskelet Neuronal Interact, 2011. **11**(4): p. 270-85.
222. Bouxsein, M.L., *Bone quality: where do we go from here?* Osteoporos Int, 2003. **14 Suppl 5**: p. S118-27.
223. Oxlund, H., et al., *Reduced concentrations of collagen cross-links are associated with reduced strength of bone.* Bone, 1995. **17**(4 Suppl): p. 365S-371S.
224. Bailey, A.J., et al., *Age-related changes in the biochemical properties of human cancellous bone collagen: relationship to bone strength.* Calcif Tissue Int, 1999. **65**(3): p. 203-10.
225. Wallace, J.M., et al., *Inbred strain-specific response to biglycan deficiency in the cortical bone of C57BL6/129 and C3H/He mice.* J Bone Miner Res, 2009. **24**(6): p. 1002-12.
226. Silva, M.J., et al., *Decreased collagen organization and content are associated with reduced strength of demineralized and intact bone in the SAMP6 mouse.* J Bone Miner Res, 2006. **21**(1): p. 78-88.
227. Sheu, Y. and J.A. Cauley, *The role of bone marrow and visceral fat on bone metabolism.* Curr Osteoporos Rep, 2011. **9**(2): p. 67-75.
228. Di Iorgi, N., et al., *Update on bone density measurements and their interpretation in children and adolescents.* Best Pract Res Clin Endocrinol Metab, 2018. **32**(4): p. 477-498.
229. Bloch, F., *Nuclear induction.* Physical Reviews, 1946. **70**: p. 460-474.
230. Purcell, E.M.T., H.C. Pound, R. V. , *Resonance Absorption by Nuclear Magnetic Moments in a Solid.* Phys Rev, 1946. **69**: p. 37-8.
231. Lauterbur, P.C., *Image formation by induced local interactions. Examples employing nuclear magnetic resonance. 1973.* Clin Orthop Relat Res, 1989(244): p. 3-6.

232. Mansfield, P.G., P.K., *NMR 'diffraction' in solids?* J Phys C Solid State Phys, 1973. **6**(22): p. 422-426.
233. Ernst, R.R.A., W.A., *Application of Fourier Transform Spectroscopy to Magnetic Resonance.* Rev Sci Instr, 1966. **37**(1): p. 93-102.
234. Damadian, R., M. Goldsmith, and L. Minkoff, *NMR in cancer: XVI. FONAR image of the live human body.* Physiol Chem Phys, 1977. **9**(1): p. 97-100, 108.
235. Dixon, R.L. and K.E. Ekstrand, *The physics of proton NMR.* Med Phys, 1982. **9**(6): p. 807-18.
236. Bushberg, J.T., *The essential physics of medical imaging*. 3rd ed. 2012, Philadelphia: Wolters Kluwer Health/Lippincott Williams & Wilkins. xii, 1030 p.
237. Bloch, F., *The Principle of Nuclear Induction.* Science, 1953. **118**(3068): p. 425-30.
238. Damadian, R., *Tumor detection by nuclear magnetic resonance.* Science, 1971. **171**(3976): p. 1151-3.
239. Wehrli, F.W., *Structural and functional assessment of trabecular and cortical bone by micro magnetic resonance imaging.* J Magn Reson Imaging, 2007. **25**(2): p. 390-409.
240. Majumdar, S., *Magnetic resonance imaging of trabecular bone structure.* Top Magn Reson Imaging, 2002. **13**(5): p. 323-34.
241. Wehrli, F.W., et al., *Mechanical implications of estrogen supplementation in early postmenopausal women.* J Bone Miner Res, 2010. **25**(6): p. 1406-14.
242. Carballido-Gamio, J., et al., *Generation of an atlas of the proximal femur and its application to trabecular bone analysis.* Magn Reson Med, 2011. **66**(4): p. 1181-91.
243. Han, M., et al., *Variable flip angle three-dimensional fast spin-echo sequence combined with outer volume suppression for imaging trabecular bone structure of the proximal femur.* J Magn Reson Imaging, 2015. **41**(5): p. 1300-10.
244. Chang, G., et al., *MRI of the hip at 7T: feasibility of bone microarchitecture, high-resolution cartilage, and clinical imaging.* J Magn Reson Imaging, 2014. **39**(6): p. 1384-93.
245. Chang, G., et al., *Finite element analysis applied to 3-T MR imaging of proximal femur microarchitecture: lower bone strength in patients with fragility fractures compared with control subjects.* Radiology, 2014. **272**(2): p. 464-74.
246. Haase, A., et al., *FLASH imaging: rapid NMR imaging using low flip-angle pulses. 1986.* J Magn Reson, 2011. **213**(2): p. 533-41.
247. Reichert, I.L., et al., *Magnetic resonance imaging of periosteum with ultrashort TE pulse sequences.* J Magn Reson Imaging, 2004. **19**(1): p. 99-107.
248. McCalden, R.W., et al., *Age-related changes in the tensile properties of cortical bone. The relative importance of changes in porosity, mineralization, and microstructure.* J Bone Joint Surg Am, 1993. **75**(8): p. 1193-205.
249. Bell, K.L., et al., *A novel mechanism for induction of increased cortical porosity in cases of intracapsular hip fracture.* Bone, 2000. **27**(2): p. 297-304.
250. Bousson, V., et al., *CT of the middiaphyseal femur: cortical bone mineral density and relation to porosity.* Radiology, 2000. **217**(1): p. 179-87.
251. Fullerton, G.D. and M.R. Amurao, *Evidence that collagen and tendon have monolayer water coverage in the native state.* Cell Biol Int, 2006. **30**(1): p. 56-65.
252. Fullerton, G.D., et al., *An NMR method to characterize multiple water compartments on mammalian collagen.* Cell Biol Int, 2006. **30**(1): p. 66-73.

253. Techawiboonwong, A., H.K. Song, and F.W. Wehrli, *In vivo MRI of submillisecond T(2) species with two-dimensional and three-dimensional radial sequences and applications to the measurement of cortical bone water.* NMR Biomed, 2008. **21**(1): p. 59-70.
254. Shoulders, M.D. and R.T. Raines, *Collagen structure and stability.* Annu Rev Biochem, 2009. **78**: p. 929-58.
255. Ma, Y.J., et al., *Can ultrashort-TE (UTE) MRI sequences on a 3-T clinical scanner detect signal directly from collagen protons: freeze-dry and D2 O exchange studies of cortical bone and Achilles tendon specimens.* NMR Biomed, 2016. **29**(7): p. 912-7.
256. Bae, W.C., et al., *Quantitative ultrashort echo time (UTE) MRI of human cortical bone: correlation with porosity and biomechanical properties.* J Bone Miner Res, 2012. **27**(4): p. 848-57.
257. Granke, M., et al., *Identifying Novel Clinical Surrogates to Assess Human Bone Fracture Toughness.* J Bone Miner Res, 2015. **30**(7): p. 1290-300.
258. Granke, M., et al., *Change in porosity is the major determinant of the variation of cortical bone elasticity at the millimeter scale in aged women.* Bone, 2011. **49**(5): p. 1020-6.
259. Robson, M.D., et al., *Magnetic resonance: an introduction to ultrashort TE (UTE) imaging.* J Comput Assist Tomogr, 2003. **27**(6): p. 825-46.
260. Bergin, C.J., J.M. Pauly, and A. Macovski, *Lung parenchyma: projection reconstruction MR imaging.* Radiology, 1991. **179**(3): p. 777-81.
261. Anumula, S., et al., *Ultra-short echo-time MRI detects changes in bone mineralization and water content in OVX rat bone in response to alendronate treatment.* Bone, 2010. **46**(5): p. 1391-9.
262. Krug, R., et al., *Ultrashort echo time MRI of cortical bone at 7 tesla field strength: a feasibility study.* J Magn Reson Imaging, 2011. **34**(3): p. 691-5.
263. Du, J., et al., *Qualitative and quantitative ultrashort echo time (UTE) imaging of cortical bone.* J Magn Reson, 2010. **207**(2): p. 304-11.
264. Reichert, I.L., et al., *Magnetic resonance imaging of cortical bone with ultrashort TE pulse sequences.* Magn Reson Imaging, 2005. **23**(5): p. 611-8.
265. Allen, M.R., et al., *Effects of combination treatment with alendronate and raloxifene on skeletal properties in a beagle dog model.* PLoS One, 2017. **12**(8): p. e0181750.
266. Allen, M.R., et al., *Raloxifene enhances vertebral mechanical properties independent of bone density.* Bone, 2006. **39**(5): p. 1130-1135.
267. Techawiboonwong, A., et al., *Cortical bone water: in vivo quantification with ultrashort echo-time MR imaging.* Radiology, 2008. **248**(3): p. 824-33.
268. Biswas, R., et al., *Ultrashort echo time (UTE) imaging with bi-component analysis: bound and free water evaluation of bovine cortical bone subject to sequential drying.* Bone, 2012. **50**(3): p. 749-55.
269. Du, J., et al., *Ultrashort echo time imaging with bicomponent analysis.* Magn Reson Med, 2012. **67**(3): p. 645-9.
270. Manhard, M.K., et al., *In Vivo Quantitative MR Imaging of Bound and Pore Water in Cortical Bone.* Radiology, 2015. **277**(1): p. 221-9.
271. Li, C., et al., *Cortical bone water concentration: dependence of MR imaging measures on age and pore volume fraction.* Radiology, 2014. **272**(3): p. 796-806.
272. Rajapakse, C.S., et al., *Volumetric Cortical Bone Porosity Assessment with MR Imaging: Validation and Clinical Feasibility.* Radiology, 2015. **276**(2): p. 526-35.

273. Siu, A.G., et al., *Characterization of the ultrashort-TE (UTE) MR collagen signal.* NMR Biomed, 2015. **28**(10): p. 1236-44.
274. Kuethe, D.O., N.L. Adolphi, and E. Fukushima, *Short data-acquisition times improve projection images of lung tissue.* Magn Reson Med, 2007. **57**(6): p. 1058-64.
275. Madio, D.P. and I.J. Lowe, *Ultra-fast imaging using low flip angles and FIDs.* Magn Reson Med, 1995. **34**(4): p. 525-9.
276. Grodzki, D.M., P.M. Jakob, and B. Heismann, *Ultrashort echo time imaging using pointwise encoding time reduction with radial acquisition (PETRA).* Magn Reson Med, 2012. **67**(2): p. 510-8.
277. Kuethe, D.O., et al., *Transforming NMR data despite missing points.* J Magn Reson, 1999. **139**(1): p. 18-25.
278. Weiger, M., et al., *ZTE imaging in humans.* Magn Reson Med, 2013. **70**(2): p. 328-32.
279. Weiger, M., F. Hennel, and K.P. Pruessmann, *Sweep MRI with algebraic reconstruction.* Magn Reson Med, 2010. **64**(6): p. 1685-95.
280. Weiger, M., K.P. Pruessmann, and F. Hennel, *MRI with zero echo time: hard versus sweep pulse excitation.* Magn Reson Med, 2011. **66**(2): p. 379-89.
281. Weiger, M., M. Stampanoni, and K.P. Pruessmann, *Direct depiction of bone microstructure using MRI with zero echo time.* Bone, 2013. **54**(1): p. 44-7.
282. Weiger, M., et al., *ZTE imaging with long-T2 suppression.* NMR Biomed, 2015. **28**(2): p. 247-54.
283. Breighner, R.E., et al., *Technical Developments: Zero Echo Time Imaging of the Shoulder: Enhanced Osseous Detail by Using MR Imaging.* Radiology, 2018. **286**(3): p. 960-966.
284. Chen, Y. and H. An, *Attenuation Correction of PET/MR Imaging.* Magn Reson Imaging Clin N Am, 2017. **25**(2): p. 245-255.
285. Sekine, T., et al., *Clinical Evaluation of Zero-Echo-Time Attenuation Correction for Brain 18F-FDG PET/MRI: Comparison with Atlas Attenuation Correction.* J Nucl Med, 2016. **57**(12): p. 1927-1932.
286. Delso, G., et al., *Clinical evaluation of zero-echo-time MR imaging for the segmentation of the skull.* J Nucl Med, 2015. **56**(3): p. 417-22.
287. Wiesinger, F., et al., *Zero TE MR bone imaging in the head.* Magn Reson Med, 2016. **75**(1): p. 107-14.
288. Weiger, M., et al., *A high-performance gradient insert for rapid and short-T2 imaging at full duty cycle.* Magn Reson Med, 2018. **79**(6): p. 3256-3266.
289. Idiyatullin, D., et al., *Fast and quiet MRI using a swept radiofrequency.* J Magn Reson, 2006. **181**(2): p. 342-9.
290. Garwood, M. and L. DelaBarre, *The return of the frequency sweep: Designing adiabatic pulses for contemporary NMR.* Journal of Magnetic Resonance, 2001. **153**(2): p. 155-177.
291. Zhou, R., et al., *SWIFT detection of SPIO-labeled stem cells grafted in the myocardium.* Magn Reson Med, 2010. **63**(5): p. 1154-61.
292. Idiyatullin, D., et al., *Dental magnetic resonance imaging: making the invisible visible.* J Endod, 2011. **37**(6): p. 745-52.
293. Lehto, L.J., et al., *Detection of calcifications in vivo and ex vivo after brain injury in rat using SWIFT.* Neuroimage, 2012. **61**(4): p. 761-72.

294. Kobayashi, N., et al., *SWIFT MRI enhances detection of breast cancer metastasis to the lung.* Magn Reson Med, 2015. **73**(5): p. 1812-9.
295. Rautiainen, J., et al., *Osteochondral repair: evaluation with sweep imaging with fourier transform in an equine model.* Radiology, 2013. **269**(1): p. 113-21.
296. Sukenari, T., et al., *Cortical bone water changes in ovariectomized rats during the early postoperative period: Objective evaluation using sweep imaging with Fourier transform.* J Magn Reson Imaging, 2015. **42**(1): p. 128-35.
297. Minami, M., et al., *Usefulness of Sweep Imaging With Fourier Transform for Evaluation of Cortical Bone in Diabetic Rats.* J Magn Reson Imaging, 2018. **48**(2): p. 389-397.
298. Luhach, I., et al., *Rapid ex vivo imaging of PAIII prostate to bone tumor with SWIFT-MRI.* Magn Reson Med, 2014. **72**(3): p. 858-63.
299. Idiyatullin, D., C.A. Corum, and M. Garwood, *Multi-Band-SWIFT.* J Magn Reson, 2015. **251**: p. 19-25.
300. Lehto, L.J., et al., *MB-SWIFT functional MRI during deep brain stimulation in rats.* Neuroimage, 2017. **159**: p. 443-448.
301. Pauleit, D., et al., *O-(2-[18F]fluoroethyl)-L-tyrosine PET combined with MRI improves the diagnostic assessment of cerebral gliomas.* Brain, 2005. **128**(Pt 3): p. 678-87.
302. Yang, Z., et al., *Automatic bone segmentation and bone-cartilage interface extraction for the shoulder joint from magnetic resonance images.* Phys Med Biol, 2015. **60**(4): p. 1441-59.
303. Pedoia, V., S. Majumdar, and T.M. Link, *Segmentation of joint and musculoskeletal tissue in the study of arthritis.* MAGMA, 2016. **29**(2): p. 207-21.
304. Metere, R., et al., *Simultaneous Quantitative MRI Mapping of T1, T2* and Magnetic Susceptibility with Multi-Echo MP2RAGE.* PLoS One, 2017. **12**(1): p. e0169265.
305. Joseph, G.B., et al., *Texture analysis of cartilage T2 maps: individuals with risk factors for OA have higher and more heterogeneous knee cartilage MR T2 compared to normal controls--data from the osteoarthritis initiative.* Arthritis Res Ther, 2011. **13**(5): p. R153.
306. Li, X. and S. Majumdar, *Quantitative MRI of articular cartilage and its clinical applications.* J Magn Reson Imaging, 2013. **38**(5): p. 991-1008.
307. Surowiec, R.K., E.P. Lucas, and C.P. Ho, *Quantitative MRI in the evaluation of articular cartilage health: reproducibility and variability with a focus on T2 mapping.* Knee Surg Sports Traumatol Arthrosc, 2014. **22**(6): p. 1385-95.
308. Wiener, E., C.W. Pfirrmann, and J. Hodler, *Spatial variation in T1 of healthy human articular cartilage of the knee joint.* Br J Radiol, 2010. **83**(990): p. 476-85.
309. Berberat, J.E., et al., *Assessment of interstitial water content of articular cartilage with T1 relaxation.* Magn Reson Imaging, 2009. **27**(5): p. 727-32.
310. Nissi, M.J., et al., *Proteoglycan and collagen sensitive MRI evaluation of normal and degenerated articular cartilage.* J Orthop Res, 2004. **22**(3): p. 557-64.
311. Kawel, N., et al., *T1 mapping of the myocardium: intra-individual assessment of post-contrast T1 time evolution and extracellular volume fraction at 3T for Gd-DTPA and Gd-BOPTA.* J Cardiovasc Magn Reson, 2012. **14**: p. 26.
312. Heye, T., et al., *MR relaxometry of the liver: significant elevation of T1 relaxation time in patients with liver cirrhosis.* Eur Radiol, 2012. **22**(6): p. 1224-32.
313. Wu, Y., et al., *Evaluation of bone mineral density using three-dimensional solid state phosphorus-31 NMR projection imaging.* Calcif Tissue Int, 1998. **62**(6): p. 512-8.

314. Zhang, J., et al., *Capturing fast relaxing spins with SWIFT adiabatic rotating frame spin-lattice relaxation (T1rho) mapping.* NMR Biomed, 2016. **29**(4): p. 420-30.
315. Treier, R., et al., *Optimized and combined T1 and B1 mapping technique for fast and accurate T1 quantification in contrast-enhanced abdominal MRI.* Magn Reson Med, 2007. **57**(3): p. 568-76.
316. Wang, L., et al., *T(1) estimation for aqueous iron oxide nanoparticle suspensions using a variable flip angle SWIFT sequence.* Magn Reson Med, 2013. **70**(2): p. 341-7.
317. Nissi, M.J., et al., *Measurement of T1 relaxation time of osteochondral specimens using VFA-SWIFT.* Magn Reson Med, 2015. **74**(1): p. 175-184.
318. Sukenari, T., et al., *Investigation of the Longitudinal Relaxation Time of Rat Tibial Cortical Bone Using SWIFT.* Magn Reson Med Sci, 2017. **16**(4): p. 351-356.
319. Ren, J., et al., *Composition of adipose tissue and marrow fat in humans by 1H NMR at 7 Tesla.* J Lipid Res, 2008. **49**(9): p. 2055-62.
320. Bley, T.A., et al., *Fat and water magnetic resonance imaging.* J Magn Reson Imaging, 2010. **31**(1): p. 4-18.
321. Delfaut, E.M., et al., *Fat suppression in MR imaging: techniques and pitfalls.* Radiographics, 1999. **19**(2): p. 373-82.
322. Coelho, M., T. Oliveira, and R. Fernandes, *Biochemistry of adipose tissue: an endocrine organ.* Arch Med Sci, 2013. **9**(2): p. 191-200.
323. Thomas, E.L., et al., *Whole body fat: content and distribution.* Prog Nucl Magn Reson Spectrosc, 2013. **73**: p. 56-80.
324. Ho, K.Y., et al., *Measuring bone mineral density with fat-water MRI: comparison with computed tomography.* J Magn Reson Imaging, 2013. **37**(1): p. 237-42.
325. Dunn, T.C., et al., *T2 relaxation time of cartilage at MR imaging: comparison with severity of knee osteoarthritis.* Radiology, 2004. **232**(2): p. 592-8.
326. Bae, W.C., et al., *UTE MRI of the Osteochondral Junction.* Curr Radiol Rep, 2014. **2**(2): p. 35.
327. Du, J., et al., *Dual inversion recovery ultrashort echo time (DIR-UTE) imaging and quantification of the zone of calcified cartilage (ZCC).* Osteoarthritis Cartilage, 2013. **21**(1): p. 77-85.
328. Gardin, A., et al., *T2 * relaxation time in Achilles tendinosis and controls and its correlation with clinical score.* J Magn Reson Imaging, 2016. **43**(6): p. 1417-22.
329. Anz, A.W., et al., *MRI T2 mapping of the asymptomatic supraspinatus tendon by age and imaging plane using clinically relevant subregions.* Eur J Radiol, 2014. **83**(5): p. 801-5.
330. Ganal, E., et al., *Quantitative MRI characterization of arthroscopically verified supraspinatus pathology: comparison of tendon tears, tendinosis and asymptomatic supraspinatus tendons with T2 mapping.* Knee Surg Sports Traumatol Arthrosc, 2016. **24**(7): p. 2216-24.
331. Paproki, A., et al., *Automated T2-mapping of the Menisci From Magnetic Resonance Images in Patients with Acute Knee Injury.* Acad Radiol, 2017. **24**(10): p. 1295-1304.
332. Rauscher, I., et al., *Meniscal measurements of T1rho and T2 at MR imaging in healthy subjects and patients with osteoarthritis.* Radiology, 2008. **249**(2): p. 591-600.
333. Schmid-Schwap, M., et al., *Biochemical analysis of the articular disc of the temporomandibular joint with magnetic resonance T2 mapping: a feasibility study.* Clin Oral Investig, 2014. **18**(7): p. 1865-71.

334. Diaz, E., et al., *Ultrashort echo time spectroscopic imaging (UTESI): an efficient method for quantifying bound and free water.* NMR Biomed, 2012. **25**(1): p. 161-8.
335. Chen, J., et al., *Evaluation of bound and pore water in cortical bone using ultrashort-TE MRI.* NMR Biomed, 2015. **28**(12): p. 1754-1762.
336. Kang, H., A.C.S. Aryal, and J.C. Marini, *Osteogenesis imperfecta: new genes reveal novel mechanisms in bone dysplasia.* Transl Res, 2017. **181**: p. 27-48.
337. Kaneto, C.M., et al., *Gene expression profiling of bone marrow mesenchymal stem cells from Osteogenesis Imperfecta patients during osteoblast differentiation.* Eur J Med Genet, 2017. **60**(6): p. 326-334.
338. Brodsky, B., *Structural consequences of glycine missense mutations in osteogenesis imperfecta*, in *Osteogenesis Imperfecta: A Translational Approach to Brittle Bone Disease*, S. JR., Editor. 2013, Elsevier. p. 115-124.
339. Lindert, U., et al., *MBTPS2 mutations cause defective regulated intramembrane proteolysis in X-linked osteogenesis imperfecta.* Nat Commun, 2016. **7**: p. 11920.
340. Symoens, S., et al., *Deficiency for the ER-stress transducer OASIS causes severe recessive osteogenesis imperfecta in humans.* Orphanet J Rare Dis, 2013. **8**: p. 154.
341. Volodarsky, M., et al., *A deletion mutation in TMEM38B associated with autosomal recessive osteogenesis imperfecta.* Hum Mutat, 2013. **34**(4): p. 582-6.
342. van Dijk, F.S., et al., *PPIB mutations cause severe osteogenesis imperfecta.* Am J Hum Genet, 2009. **85**(4): p. 521-7.
343. Martinez-Glez, V., et al., *Identification of a mutation causing deficient BMP1/mTLD proteolytic activity in autosomal recessive osteogenesis imperfecta.* Hum Mutat, 2012. **33**(2): p. 343-50.
344. Mendoza-Londono, R., et al., *Recessive osteogenesis imperfecta caused by missense mutations in SPARC.* Am J Hum Genet, 2015. **96**(6): p. 979-85.
345. Becker, J., et al., *Exome sequencing identifies truncating mutations in human SERPINF1 in autosomal-recessive osteogenesis imperfecta.* Am J Hum Genet, 2011. **88**(3): p. 362-71.
346. Morello, R., *Osteogenesis imperfecta and therapeutics.* Matrix Biol, 2018. **71-72**: p. 294-312.
347. Holdsworth, G., et al., *Dampening of the bone formation response following repeat dosing with sclerostin antibody in mice is associated with up-regulation of Wnt antagonists.* Bone, 2018. **107**: p. 93-103.
348. Taylor, S., et al., *Time-dependent cellular and transcriptional changes in the osteoblast lineage associated with sclerostin antibody treatment in ovariectomized rats.* Bone, 2016. **84**: p. 148-159.
349. Nioi, P., et al., *Transcriptional Profiling of Laser Capture Microdissected Subpopulations of the Osteoblast Lineage Provides Insight Into the Early Response to Sclerostin Antibody in Rats.* J Bone Miner Res, 2015. **30**(8): p. 1457-67.
350. Stolina, M., et al., *Temporal changes in systemic and local expression of bone turnover markers during six months of sclerostin antibody administration to ovariectomized rats.* Bone, 2014. **67**: p. 305-13.
351. Feldman, A.T. and D. Wolfe, *Tissue processing and hematoxylin and eosin staining.* Methods Mol Biol, 2014. **1180**: p. 31-43.

352. Ma, Y.L., et al., *Time course of disassociation of bone formation signals with bone mass and bone strength in sclerostin antibody treated ovariectomized rats.* Bone, 2017. **97**: p. 20-28.
353. Taihi, I., et al., *Validation of Housekeeping Genes to Study Human Gingival Stem Cells and Their In Vitro Osteogenic Differentiation Using Real-Time RT-qPCR.* Stem Cells Int, 2016. **2016**: p. 6261490.
354. Rauh, J., A. Jacobi, and M. Stiehler, *Identification of stable reference genes for gene expression analysis of three-dimensional cultivated human bone marrow-derived mesenchymal stromal cells for bone tissue engineering.* Tissue Eng Part C Methods, 2015. **21**(2): p. 192-206.
355. Livak, K.J. and T.D. Schmittgen, *Analysis of relative gene expression data using real-time quantitative PCR and the 2(-Delta Delta C(T)) Method.* Methods, 2001. **25**(4): p. 402-8.
356. Yuan, J.S., et al., *Statistical analysis of real-time PCR data.* BMC Bioinformatics, 2006. **7**: p. 85.
357. Scientific, T., *Gene expression assay performance guaranteed with the TaqMan assays qPCR guarantee program.* . Applied Biosystems White Paper, 2015. **docs.appliedbiosystems.com/pebiodocs/088754.pdf**.
358. Maeda, A., et al., *WNT1-induced Secreted Protein-1 (WISP1), a Novel Regulator of Bone Turnover and Wnt Signaling.* J Biol Chem, 2015. **290**(22): p. 14004-18.
359. Yousfi, M., F. Lasmoles, and P.J. Marie, *TWIST inactivation reduces CBFA1/RUNX2 expression and DNA binding to the osteocalcin promoter in osteoblasts.* Biochem Biophys Res Commun, 2002. **297**(3): p. 641-4.
360. Yousfi, M., et al., *Twist haploinsufficiency in Saethre-Chotzen syndrome induces calvarial osteoblast apoptosis due to increased TNFalpha expression and caspase-2 activation.* Hum Mol Genet, 2002. **11**(4): p. 359-69.
361. Boyce, R.W., Q.T. Niu, and M.S. Ominsky, *Kinetic reconstruction reveals time-dependent effects of romosozumab on bone formation and osteoblast function in vertebral cancellous and cortical bone in cynomolgus monkeys.* Bone, 2017. **101**: p. 77-87.
362. Sinder, B.P., et al., *Adult Brtl/+ mouse model of osteogenesis imperfecta demonstrates anabolic response to sclerostin antibody treatment with increased bone mass and strength.* Osteoporos Int, 2014. **25**(8): p. 2097-107.
363. Ominsky, M.S., et al., *Differential temporal effects of sclerostin antibody and parathyroid hormone on cancellous and cortical bone and quantitative differences in effects on the osteoblast lineage in young intact rats.* Bone, 2015. **81**: p. 380-391.
364. Boyce, R.W., et al., *Decreased osteoprogenitor proliferation precedes attenuation of cancellous bone formation in ovariectomized rats treated with sclerostin antibody.* Bone Rep, 2018. **8**: p. 90-94.
365. Li, X., et al., *Progressive increases in bone mass and bone strength in an ovariectomized rat model of osteoporosis after 26 weeks of treatment with a sclerostin antibody.* Endocrinology, 2014. **155**(12): p. 4785-97.
366. Moriishi, T., et al., *Osteocyte network; a negative regulatory system for bone mass augmented by the induction of Rankl in osteoblasts and Sost in osteocytes at unloading.* PLoS One, 2012. **7**(6): p. e40143.
367. Michael Delaine-Smith, R., et al., *Preclinical models for in vitro mechanical loading of bone-derived cells.* Bonekey Rep, 2015. **4**: p. 728.

368. Kim, S.W., et al., *Sclerostin Antibody Administration Converts Bone Lining Cells Into Active Osteoblasts.* J Bone Miner Res, 2017. **32**(5): p. 892-901.
369. Ominsky, M.S., et al., *Tissue-level mechanisms responsible for the increase in bone formation and bone volume by sclerostin antibody.* J Bone Miner Res, 2014. **29**(6): p. 1424-30.
370. Olvera, D., et al., *Low Dose of Bisphosphonate Enhances Sclerostin Antibody-Induced Trabecular Bone Mass Gains in Brtl/+ Osteogenesis Imperfecta Mouse Model.* J Bone Miner Res, 2018. **33**(7): p. 1272-1282.
371. Perosky, J.E., et al., *Single dose of bisphosphonate preserves gains in bone mass following cessation of sclerostin antibody in Brtl/+ osteogenesis imperfecta model.* Bone, 2016. **93**: p. 79-85.
372. Land, C., et al., *Osteogenesis imperfecta type VI in childhood and adolescence: effects of cyclical intravenous pamidronate treatment.* Bone, 2007. **40**(3): p. 638-44.
373. Isaacson, J., Cattanach BM., *[Report]*. Mouse News Lett, 1962. **27**: p. 31.
374. Morton, C.L. and P.J. Houghton, *Establishment of human tumor xenografts in immunodeficient mice.* Nat Protoc, 2007. **2**(2): p. 247-50.
375. Aparicio, S., M. Hidalgo, and A.L. Kung, *Examining the utility of patient-derived xenograft mouse models.* Nat Rev Cancer, 2015. **15**(5): p. 311-6.
376. Pettway, G.J. and L.K. McCauley, *Ossicle and vossicle implant model systems.* Methods Mol Biol, 2008. **455**: p. 101-10.
377. Pettway, G.J., et al., *Parathyroid hormone mediates bone growth through the regulation of osteoblast proliferation and differentiation.* Bone, 2008. **42**(4): p. 806-18.
378. N., O., *A threshold selection method from gray-level histograms.* IEEE Trans Systems, Man, and Cybernetics, 1979. **91**: p. 62-66.
379. Dempster, D.W., et al., *Standardized nomenclature, symbols, and units for bone histomorphometry: a 2012 update of the report of the ASBMR Histomorphometry Nomenclature Committee.* J Bone Miner Res, 2013. **28**(1): p. 2-17.
380. Hauge, E., L. Mosekilde, and F. Melsen, *Missing observations in bone histomorphometry on osteoporosis: implications and suggestions for an approach.* Bone, 1999. **25**(4): p. 389-95.
381. Ballanti, P., et al., *Tartrate-resistant acid phosphate activity as osteoclastic marker: sensitivity of cytochemical assessment and serum assay in comparison with standardized osteoclast histomorphometry.* Osteoporos Int, 1997. **7**(1): p. 39-43.
382. Schneider, C.A., W.S. Rasband, and K.W. Eliceiri, *NIH Image to ImageJ: 25 years of image analysis.* Nat Methods, 2012. **9**(7): p. 671-5.
383. Franz-Odendaal, T.A., B.K. Hall, and P.E. Witten, *Buried alive: how osteoblasts become osteocytes.* Dev Dyn, 2006. **235**(1): p. 176-90.
384. Manolagas, S.C., *Birth and death of bone cells: basic regulatory mechanisms and implications for the pathogenesis and treatment of osteoporosis.* Endocr Rev, 2000. **21**(2): p. 115-37.
385. McCulloch, C.A. and J.N. Heersche, *Lifetime of the osteoblast in mouse periodontium.* Anat Rec, 1988. **222**(2): p. 128-35.
386. Owen, M. and S. Macpherson, *Cell Population Kinetics of an Osteogenic Tissue. Ii.* J Cell Biol, 1963. **19**: p. 33-44.

387. Kember, N.F., *Cell division in endochondral ossification. A study of cell proliferation in rat bones by the method of tritiated thymidine autoradiography.* J Bone Joint Surg Br, 1960. **42B**: p. 824-39.
388. Young, R.W., *Cell proliferation and specialization during endochondral osteogenesis in young rats.* J Cell Biol, 1962. **14**: p. 357-70.
389. Winkler, D.G., et al., *Osteocyte control of bone formation via sclerostin, a novel BMP antagonist.* EMBO J, 2003. **22**(23): p. 6267-76.
390. Poole, K.E., et al., *Sclerostin is a delayed secreted product of osteocytes that inhibits bone formation.* FASEB J, 2005. **19**(13): p. 1842-4.
391. Irie, K., et al., *Matrix mineralization as a trigger for osteocyte maturation.* J Histochem Cytochem, 2008. **56**(6): p. 561-7.
392. van Bezooijen, R.L., et al., *Sclerostin is an osteocyte-expressed negative regulator of bone formation, but not a classical BMP antagonist.* J Exp Med, 2004. **199**(6): p. 805-14.
393. Pettway, G.J., et al., *Anabolic actions of PTH (1-34): use of a novel tissue engineering model to investigate temporal effects on bone.* Bone, 2005. **36**(6): p. 959-70.
394. Schneider, A., et al., *Skeletal homeostasis in tissue-engineered bone.* J Orthop Res, 2003. **21**(5): p. 859-64.
395. Marcus R, F.D., Dempster DW, Luckey M, Cauley JA. , *Skeletal heterogeneity and the purposes of bone remodeling: implications for the understanding of osteroporosis.* 4th ed. 2013: Academic Press, MA, USA.
396. Ohgushi, H., V.M. Goldberg, and A.I. Caplan, *Repair of bone defects with marrow cells and porous ceramic. Experiments in rats.* Acta Orthop Scand, 1989. **60**(3): p. 334-9.
397. Nakahara, H., V.M. Goldberg, and A.I. Caplan, *Culture-expanded human periosteal-derived cells exhibit osteochondral potential in vivo.* J Orthop Res, 1991. **9**(4): p. 465-76.
398. Hoeppner, L.H., F.J. Secreto, and J.J. Westendorf, *Wnt signaling as a therapeutic target for bone diseases.* Expert Opin Ther Targets, 2009. **13**(4): p. 485-96.
399. Ominsky, M.S., et al., *Two doses of sclerostin antibody in cynomolgus monkeys increases bone formation, bone mineral density, and bone strength.* J Bone Miner Res, 2010. **25**(5): p. 948-59.
400. Li, X., et al., *Sclerostin antibody treatment increases bone formation, bone mass, and bone strength in a rat model of postmenopausal osteoporosis.* J Bone Miner Res, 2009. **24**(4): p. 578-88.
401. Tian, X., et al., *Sclerostin antibody increases bone mass by stimulating bone formation and inhibiting bone resorption in a hindlimb-immobilization rat model.* Bone, 2011. **48**(2): p. 197-201.
402. Spatz, J.M., et al., *Sclerostin antibody inhibits skeletal deterioration due to reduced mechanical loading.* J Bone Miner Res, 2013. **28**(4): p. 865-74.
403. Williams DK, P.S., Schryver E, Akel NS, Shelton RS, Webber J, Swain FL, Schmidt J, Suva LJ, Gaddy D. , *Sclerostin Antibody Treatment Stimulates Bone Formation to Normalize Bone Mass in Male Down Syndrome Mice.* JBMR Plus, 2018. **2**(1): p. 48-55.
404. Thibaudeau, L., et al., *A tissue-engineered humanized xenograft model of human breast cancer metastasis to bone.* Dis Model Mech, 2014. **7**(2): p. 299-309.
405. Reszka, A.A. and G.A. Rodan, *Mechanism of action of bisphosphonates.* Curr Osteoporos Rep, 2003. **1**(2): p. 45-52.
406. Bikle, D.D., T. Sakata, and B.P. Halloran, *The impact of skeletal unloading on bone formation.* Gravit Space Biol Bull, 2003. **16**(2): p. 45-54.

407. Cabahug-Zuckerman, P., et al., *Osteocyte Apoptosis Caused by Hindlimb Unloading is Required to Trigger Osteocyte RANKL Production and Subsequent Resorption of Cortical and Trabecular Bone in Mice Femurs.* J Bone Miner Res, 2016. **31**(7): p. 1356-65.
408. Donnelly, E., *Methods for assessing bone quality: a review.* Clin Orthop Relat Res, 2011. **469**(8): p. 2128-38.
409. Wallace, J.M., et al., *Distribution of type I collagen morphologies in bone: relation to estrogen depletion.* Bone, 2010. **46**(5): p. 1349-54.
410. Idiyatullin, D., et al., *Continuous SWIFT.* J Magn Reson, 2012. **220**: p. 26-31.
411. Beck, A. and M. Teboulle, *Fast gradient-based algorithms for constrained total variation image denoising and deblurring problems.* IEEE Trans Image Process, 2009. **18**(11): p. 2419-34.
412. Corum, C., Moeller, S., Idiyatullin, D., Garwood, M., *Signal processing and image reconstruction for SWIFT* Proceedings of the Fifteenth Meeting of the International Society for Magnetic Resonance in Medicine. , 2007: p. 1669.
413. Shamonin, D.P., et al., *Fast parallel image registration on CPU and GPU for diagnostic classification of Alzheimer's disease.* Front Neuroinform, 2013. **7**: p. 50.
414. Klein, S., et al., *elastix: a toolbox for intensity-based medical image registration.* IEEE Trans Med Imaging, 2010. **29**(1): p. 196-205.
415. Bray, T.J., et al., *Fat fraction mapping using magnetic resonance imaging: insight into pathophysiology.* Br J Radiol, 2018. **91**(1089): p. 20170344.
416. Lillie, R.D., *Supersaturated solutions of fat stains in dilute isopropanol for demonstration of acute fatty degenerations not shown by Herxheimer technique.* Arch Pathol, 1943. **36**: p. 432.
417. Kawamoto, T., *Use of a new adhesive film for the preparation of multi-purpose fresh-frozen sections from hard tissues, whole-animals, insects and plants.* Arch Histol Cytol, 2003. **66**(2): p. 123-43.
418. Kanis, J.A., *Assessment of fracture risk and its application to screening for postmenopausal osteoporosis: synopsis of a WHO report. WHO Study Group.* Osteoporos Int, 1994. **4**(6): p. 368-81.
419. Francisco, J.I., et al., *Relationship between age, skeletal site, and time post-ovariectomy on bone mineral and trabecular microarchitecture in rats.* J Orthop Res, 2011. **29**(2): p. 189-96.
420. Johnston, C.C., Jr., et al., *Early menopausal changes in bone mass and sex steroids.* J Clin Endocrinol Metab, 1985. **61**(5): p. 905-11.
421. Stepan, J.J., et al., *Bone loss and biochemical indices of bone remodeling in surgically induced postmenopausal women.* Bone, 1987. **8**(5): p. 279-84.
422. Cho, G., Y. Wu, and J.L. Ackerman, *Detection of hydroxyl ions in bone mineral by solid-state NMR spectroscopy.* Science, 2003. **300**(5622): p. 1123-7.
423. Du, J., et al., *Assessment of cortical bone with clinical and ultrashort echo time sequences.* Magn Reson Med, 2013. **70**(3): p. 697-704.
424. Cao, H., et al., *Quantitative bone matrix density measurement by water- and fat-suppressed proton projection MRI (WASPI) with polymer calibration phantoms.* Magn Reson Med, 2008. **60**(6): p. 1433-43.
425. Uppuganti, S., et al., *Age-related changes in the fracture resistance of male Fischer F344 rat bone.* Bone, 2016. **83**: p. 220-232.

426. Allen, M.R., et al., *Changes in skeletal collagen cross-links and matrix hydration in high- and low-turnover chronic kidney disease.* Osteoporos Int, 2015. **26**(3): p. 977-85.
427. Shetty, S., et al., *Bone turnover markers: Emerging tool in the management of osteoporosis.* Indian J Endocrinol Metab, 2016. **20**(6): p. 846-852.
428. Li, C., et al., *Cortical Bone Water Concentration: Dependence of MR Imaging Measures on Age and Pore Volume Fraction.* Radiology, 2016. **280**(2): p. 653.
429. Martin, R.B., *Determinants of the mechanical properties of bones.* J Biomech, 1991. **24 Suppl 1**: p. 79-88.
430. Manhard, M.K., et al., *In Vivo Quantitative MR Imaging of Bound and Pore Water in Cortical Bone.* Radiology, 2015. **277**(3): p. 927.
431. Verma, S., et al., *Adipocytic proportion of bone marrow is inversely related to bone formation in osteoporosis.* J Clin Pathol, 2002. **55**(9): p. 693-8.
432. Justesen, J., et al., *Adipocyte tissue volume in bone marrow is increased with aging and in patients with osteoporosis.* Biogerontology, 2001. **2**(3): p. 165-71.
433. Li, X., et al., *Quantification of vertebral bone marrow fat content using 3 Tesla MR spectroscopy: reproducibility, vertebral variation, and applications in osteoporosis.* J Magn Reson Imaging, 2011. **33**(4): p. 974-9.
434. Griffith, J.F., et al., *Vertebral bone mineral density, marrow perfusion, and fat content in healthy men and men with osteoporosis: dynamic contrast-enhanced MR imaging and MR spectroscopy.* Radiology, 2005. **236**(3): p. 945-51.
435. Griffith, J.F., et al., *Vertebral marrow fat content and diffusion and perfusion indexes in women with varying bone density: MR evaluation.* Radiology, 2006. **241**(3): p. 831-8.
436. MacEwan, I.J., et al., *Proton density water fraction as a biomarker of bone marrow cellularity: validation in ex vivo spine specimens.* Magn Reson Imaging, 2014. **32**(9): p. 1097-101.
437. Shen, W., et al., *MRI-measured pelvic bone marrow adipose tissue is inversely related to DXA-measured bone mineral in younger and older adults.* Eur J Clin Nutr, 2012. **66**(9): p. 983-8.
438. Quarto, R., D. Thomas, and C.T. Liang, *Bone progenitor cell deficits and the age-associated decline in bone repair capacity.* Calcif Tissue Int, 1995. **56**(2): p. 123-9.
439. Rickard, D.J., et al., *Isolation and characterization of osteoblast precursor cells from human bone marrow.* J Bone Miner Res, 1996. **11**(3): p. 312-24.
440. Gluer, C.C., et al., *Vertebral mineral determination by quantitative computed tomography (QCT): accuracy of single and dual energy measurements.* J Comput Assist Tomogr, 1988. **12**(2): p. 242-58.
441. Blake, G.M., et al., *Effect of increasing vertebral marrow fat content on BMD measurement, T-Score status and fracture risk prediction by DXA.* Bone, 2009. **44**(3): p. 495-501.
442. Kawel, N., et al., *T1 mapping of the myocardium: intra-individual assessment of the effect of field strength, cardiac cycle and variation by myocardial region.* J Cardiovasc Magn Reson, 2012. **14**: p. 27.
443. Yamauchi, M., et al., *Cross-linking and new bone collagen synthesis in immobilized and recovering primate osteoporosis.* Bone, 1988. **9**(6): p. 415-8.
444. Wang, X., et al., *Age-related changes in the collagen network and toughness of bone.* Bone, 2002. **31**(1): p. 1-7.

445. Agarwal, A., et al., *Comparison and calibration of transcriptome data from RNA-Seq and tiling arrays.* BMC Genomics, 2010. **11**: p. 383.
446. Malone, J.H. and B. Oliver, *Microarrays, deep sequencing and the true measure of the transcriptome.* BMC Biol, 2011. **9**: p. 34.
447. Schlecht, S.H., et al., *Brief communication: the effects of disuse on the mechanical properties of bone: what unloading tells us about the adaptive nature of skeletal tissue.* Am J Phys Anthropol, 2012. **149**(4): p. 599-605.
448. Parfitt, A.M., *What is the normal rate of bone remodeling?* Bone, 2004. **35**(1): p. 1-3.
449. Robling, A.G., et al., *Mechanical stimulation of bone in vivo reduces osteocyte expression of Sost/sclerostin.* J Biol Chem, 2008. **283**(9): p. 5866-75.
450. Lewis, E.M., et al., *Sexual maturation data for Crl Sprague-Dawley rats: criteria and confounding factors.* Drug Chem Toxicol, 2002. **25**(4): p. 437-58.
451. Turner, R.T., J.J. Vandersteenhoven, and N.H. Bell, *The effects of ovariectomy and 17 beta-estradiol on cortical bone histomorphometry in growing rats.* J Bone Miner Res, 1987. **2**(2): p. 115-22.
452. Wronski, T.J., et al., *Skeletal alterations in ovariectomized rats.* Calcif Tissue Int, 1985. **37**(3): p. 324-8.
453. Leitner, M.M., et al., *Longitudinal as well as age-matched assessments of bone changes in the mature ovariectomized rat model.* Lab Anim, 2009. **43**(3): p. 266-71.
454. Perilli, E., et al., *Dependence of mechanical compressive strength on local variations in microarchitecture in cancellous bone of proximal human femur.* J Biomech, 2008. **41**(2): p. 438-46.
455. Rhee, Y., et al., *Assessment of bone quality using finite element analysis based upon micro-CT images.* Clin Orthop Surg, 2009. **1**(1): p. 40-7.
456. Seeman, E. and P.D. Delmas, *Bone quality--the material and structural basis of bone strength and fragility.* N Engl J Med, 2006. **354**(21): p. 2250-61.
457. Campbell, G.M. and A. Sophocleous, *Quantitative analysis of bone and soft tissue by micro-computed tomography: applications to ex vivo and in vivo studies.* Bonekey Rep, 2014. **3**: p. 564.
458. Horch, R.A., et al., *Clinically compatible MRI strategies for discriminating bound and pore water in cortical bone.* Magn Reson Med, 2012. **68**(6): p. 1774-84.
459. Wang, S., et al., *Gadolinium Metallofullerene-Polypyrrole Nanoparticles for Activatable Dual-Modal Imaging-Guided Photothermal Therapy.* ACS Appl Mater Interfaces, 2018. **10**(34): p. 28382-28389.